University of Strathclyde
Department of Electronic and Electrical Engineering

Converter Fault Diagnosis and Post-Fault Operation of a Doubly-Fed Induction Generator for a Wind Turbine

by

Warachart Sae-Kok
B.Eng., M.Eng.

A thesis presented in fulfilment of the requirements for the degree of

Doctor of Philosophy

2008

Dedication

To my father, my mother and my adoptive parents

Acknowledgement

Table of Contents

Abstract

Wind energy has become one of the most important alternative energy resources because of the global warming crisis. Wind turbines are often erected off-shore because of favourable wind conditions, requiring lower towers than on-shore. The doubly-fed induction generator is one of the most widely used generators with wind turbines. In such a wind turbine the power converters are less robust than the generator and other mechanical parts. If any switch failure occurs in the converters, the wind turbine may be seriously damaged and have to stop. Therefore, converter health monitoring and fault diagnosis are important to improve system reliability. Moreover, to avoid shutting down the wind turbine, converter fault diagnosis may permit a change in control strategy and/or reconfigure the power converters to permit post-fault operation.

This research focuses on switch fault diagnosis and post-fault operation for the converters of the doubly-fed induction generator. The effects of an open-switch fault and a short-circuit switch fault are analysed. Several existing open-switch fault diagnosis methods are examined but are found to be unsuitable for the doubly-fed induction generator. The causes of false alarms with these methods are investigated. A proposed diagnosis method, with false alarm suppression, has the fault detection capability equivalent to the best of the existing methods, but improves system reliability. After any open-switch fault is detected, reconfiguration to a four-switch topology is activated to avoid shutting down the system. Short-circuit switch faults are also investigated. Possible methods to deal with this fault are discussed and demonstrated in simulation. Operating the doubly-fed induction generator as a squirrel cage generator with aerodynamic power control of turbine blades is suggested if this fault occurs in the machine-side converter, while constant dc voltage control is suitable for a short-circuit switch fault in the grid-side converter.

List of Symbols and Abbreviations

Symbol	Definition	Unit
A	cross-sectional area of actuator disc	m^2
a	axial flow induced factor	-
a_1, b_1	fundamental cosine and sine coefficient of DFT	pu
B	friction coefficient	Nm/rad/s
C	capacitance	μF
c	scale parameter	-
c_p	power coefficient	-
e	back emf	V
F	force	Nm
f	frequency	Hz
f_{fault}	diagnostic variable for the Control Deviation Method	-
h	height	m
I_1	fundamental phase current	A, pu
I_v	phase current	A, pu
i	current	A, pu
J	moment of inertia	$kg\text{-}m^2$
K_p, K_i	proportional gain and integral gain	-
L	inductance	H
m	mass	kg

Symbol	Definition	Unit
N_s, N_r	per-phase effective number of turns of the stator and rotor windings	turn
n_s, n_r	synchronous speed and rotor speed	rpm
P	power	W
P_p, P_c	the number of pole-pairs of the power machine and control windings	-
P_{conv}, P_g, P_s, P_{total}	active powers of converter, grid-side converter, stator and generator	W, pu
P	number of pole pairs of the generator	-
p	pressure	N/m^2
Q_s, Q_g	reactive power of stator and grid-side converter	VAR, pu
R	resistance	Ω
s	per-unit slip	-
T	switching period	pu
T, T_s	sampling time	sec
T_e	electromagnetic torque	Nm
T_m^*	torque command for dc drive	pu
t	timing of any voltage vector	pu
u	voltage	V, pu
V_{dc}	dc voltage	V
v_w	programmed wind speed command	m/s
v^*	command voltage	pu
v	voltage	V, pu

Symbol	Definition	Unit
α	angle of attack	rad
β	pitch angle	rad
Γ	complete gamma function	-
γ_v	a diagnostic variable for the Modified Normalized DC Current Method of each phase current	-
γ	the ratio of the lower dc-link voltage to the total dc-link voltage	-
δ	angle between 10 command and 11 command	pu
ε	rotor angle	rad, pu
θ	angle	rad, pu
λ	tip speed ratio	-
λ	magnetic flux	wb, pu
λ_v	the absolute value of the each phase current	pu
μ	stator flux angle	rad, pu
μ_v	moving average value of each phase current	pu
ξ_v	a diagnostic variable for the Absolute Normalized DC Current Method of each phase current	-
ρ	air density	kg/m^3
σ, σ_s	total and stator leakage factor	-
σ	slope from slope method	-
τ	time constant	H/Ω
τ	fundamental period	pu
Ω	angular velocity of the blades	rad/s
ω	angular velocity	rad/s
ω	angular frequency	rad/s, pu
ω_r^*	speed command for speed loop control	pu

Superscript

e	synchronous reference frame	-
g	grid voltage reference frame	-

Symbol	Definition	Unit
Superscript		
r	rotor reference frame	-
s	stationary reference frame	-
si	current model in stationary reference frame	-
sv	voltage model in stationary reference frame	-
λs	stator flux reference frame	-
Subscript		
e	synchronous	-
f	filter	-
g	Grid	-
m	magnetising	-
r	Rotor	-
s	Stator	-
av	Average	-
$conv$	grid-side converter component	-
ms	stator magnetising	-
sl	Leakage	-
λs	stator flux	-
$convd$, $convq$	dq-axis grid-side converter component	
$g\alpha$, $g\beta$	$\alpha\beta$ -axis grid voltage component	-
gd, gq	dq-axis grid voltage component	-
$r\alpha$, $r\beta$	$\alpha\beta$ -axis rotor component	-
rd, rq	dq-axis rotor component	-
$s\alpha$, $s\beta$	$\alpha\beta$ -axis stator component	-
sd, sq	dq-axis rotor component	-

Abbreviation	Definition
ADC	analogue-to-digital converter
AI	artificial intelligent
BDFIG	brushless doubly-fed induction generator
BDFM	brushless doubly-fed induction machine
BDRG	brushless doubly-fed reluctance generator
BLDC	brushless dc machine
CDFIG	cascaded doubly-fed induction generator
DAC	digital-to-analogue converter
DFIG	doubly-fed induction generator
DFT	discrete Fourier transform
DSP	digital signal processor
DWT	discrete wavelet transform
EMI	electromagnetic interference
FPRF	fault power rating factor
GPIO	general purpose I/O
GSC	grid-side converter
HAWT	horizontal axis wind turbine
IGBT	insulate gate bipolar transistor
MSC	machine-side converter
MMF	magnetomotive force
PI	proportional-plus-integral controller
PLL	phase-locked loop
PMSG	permanent magnet synchronous generator
PMSM	permanent magnet synchronous motor
PWM	pulse width modulation
RAM	random access memory
SDFIG	standard doubly-fed induction generator
SF-DFIG	single frame cascaded doubly-fed induction generator
SOCF	silicon overrating cost factor
SVM	space vector modulation
VAWT	vertical axis wind turbine

Abbreviation	Definition
VSI	voltage source inverter
WRIM	wound rotor induction machine
WRSG	wound rotor synchronous generator

Preface

Condition monitoring and fault diagnosis have become increasing important for any electrical drives as well as in generation systems. It can improve the reliability of the drive system. For a wind turbine equipped with a doubly-fed induction generator (DFIG), back-to-back converters are the weakest part of the DFIG system. Failure of the converters may lead to unforeseen failure in other parts of the wind turbine system. This research aims at fault diagnosis for the converters used in the DFIG, which is installed in the wind turbine. To achieve the aim, an experimental system is built and tested to prove its application capability in meeting the main objective. An established control method is applied to the system. The effects of converter faults on the DFIG are analysed. The appropriate fault diagnosis should be identified and the appropriate operating strategies, after reconfiguration, should be established for the system. This thesis covers the necessary details of the simulation model and the experimental system of this research. The thesis is organised into 8 chapters.

Chapter 1 expresses the broad background of this research and introduces the motivation of this research, objectives and methodology and scope of the research.

Chapter 2 explains the general background of wind energy and the different concepts for wind turbines and generators as currently used.

Chapter 3 describes the basic theory of the doubly–fed induction generator. The various types of doubly-fed induction generators are discussed, followed by the dynamic equations and control methods which are required for this research.

Chapter 4 presents details of system simulation and its implementation. The detailed mathematical models, which are discussed, are applied in both simulation and experiment.

Chapter 5 reviews previous research on fault detection and diagnosis for a power converter used in an electrical drive. The problem of diode current during an open-switch fault, which has not been mentioned in the literature, is discussed in this chapter.

Chapter 6 deals with converter faults in a doubly-fed induction generator, used with a wind turbine. The effects of an open-switch fault and a short-circuit switch fault are discussed and analysed. Reference frame theory is applied to analyse the effect of an

open-switch fault in the machine-side converter of the DFIG. In this chapter, two problems with existing fault detection methods are discussed. One problem is solved by a method proposed initially, while both problems are finally solved by the second proposed method. The fault detection performance of both proposed methods are simulated and implemented experimentally to compare with those of the existing methods.

Chapter 7 describes action which could be taken after a converter fault is detected. Several fault tolerant converter topologies are reviewed and the four-switch topology, with dc-link midpoint connection, is selected and applicable to the DFIG. Another topology, called "constant dc-voltage control", is also proposed as an alternative topology for the DFIG after a short-circuit switch fault. Both methods are simulated and implemented experimentally and the results compared to prove the suitability of the reconfiguration topologies.

Chapter 8 presents the conclusions and suggestion for further research.

Chapter One

Introduction

1.1 Background

Renewable energy has become important for the world due to the crisis of global warming caused by fossil fuel consumption. Several types of renewable energy have been exploited, for example, wind energy, solar energy and tide wave energy. Wind energy has become widely exploited and has been used for more than a decade due to the maturity of the technology to convert energy from the wind to electrical energy. Wind energy is captured by means of wind turbines which convert the kinetic energy of the wind into rotational kinetic energy. This mechanical energy is transformed to electrical energy by means of an electrical generator. Generally, wind turbines are not erected alone, but are erected with other wind turbines over a wide area called a "wind farm". The best place to set up the wind farm must be windy throughout the year to allow harvesting energy from the wind as often as possible, and wind speeds must be high enough to turn the wind turbine to generate electricity. Several countries, especially in Europe [1.6-1.8] have been interested in wind energy and have invested in research and on building large wind turbines to capture as much energy as possible from the wind.

As well as the aerodynamic design of the turbine itself, the generator and its control are very important for maximising the energy captured from the wind and meeting requirement of the quality of the power output to the grid or the user. Two types of generators have been used commercially – the induction generator and the synchronous generator. A wound rotor synchronous generator (WRSG) is claimed to be commercially successful, but only by one company, named "Enercon"[1.1]. The largest wind turbine equipped with a synchronous generator is erected in Germany. It can generate up to 7 MW [1.2]. However, this type of generator requires power converters having a larger VA rating than the generator to guarantee the proper operation of the generator. Another type of synchronous generator is the permanent magnet synchronous generator (PMSG) which has a permanent magnet rotor. The

advantage of this generator is no rotor power loss because there is no rotor winding. However, the cost of permanent magnet is quite high. These two types of generator are normally used in the direct drive wind turbine where there is no gear box meaning that fewer parts to wear out.

The most widely used generator is the induction generator, especially the wound rotor type which is applied with converters at its rotor terminals. This generator is called a doubly-fed induction generator or DFIG. More than 70% of the wind turbines in the world are equipped with DFIGs [1.3]. Many wind turbines equipped with DFIGs are erected off-shore because, at sea, there are no obstacles to block the wind and the towers do not need to be as high as equivalent turbines erected on-shore. Two of the largest wind turbines equipped with DFIGs are erected off-shore in the North Sea off Scotland. They are manufactured by Repower [1.4].

The DFIG consists of a wound rotor induction machine, back-to-back converters, three-phase filters and a three-phase transformer. The stator of this generator is directly connected to the grid while the rotor is also connected to the grid via the back-to-back voltage source converters, three-phase filters and three-phase transformer. One advantage of the DFIG is that the VA rating of the power converters, three-phase filter and a three-phase transformer need be only a fraction of the generator VA rating. The wind turbine driven DFIG operates in a typical speed range of ± 33% [1.5] of its synchronous speed. Therefore, the converters required to drive the DFIG are just one-third of the generator VA rating. Reduction of the size of the converters and other components is the main advantage of the DFIG over other generator types. However this type of generator requires slip rings and brushes to connect the rotor windings to the converters. The slip rings and brushes require maintenance to keep their condition in the optimum level, which is a disadvantage of the DFIG. Slip rings and brushes are vital components in most of the generators running in conventional power stations and their characteristics and maintenance requirements are well known. Several research groups [1.9] have tried to invent a brushless type of DFIG to solve this problem. However, the technology in this field is not yet mature and prototypes have poorer performance than normal wound rotor induction machines.

The need for slip rings and brushes has been more than compensated by the reduction in converter size. Since many DFIGs are erected off-shore, condition monitoring and fault diagnosis is very important to help schedule maintenance and protect the wind turbine from damage. The usual power converters used for wind turbines are PWM voltage source converters, connected back-to-back, and made with IGBTs as are used in many electrical drives. Without appropriate action, the faults which can occur in the power converters will cause operation downtime and lost of revenue. Therefore, converter fault diagnosis and fault tolerant control are necessary to help prevent downtime, maintain generator availability and lost of revenue.

1.2. Motivation

PWM converters have become standard in industry due to their performance and efficiency. In industry, they are mainly applied to drive singly-fed induction motors and most of them operate from grid frequency. In a wind turbine with a DFIG, the power converters are connected to the rotor of the generator and the rotor frequency typically varies between 0% and 33% of grid frequency. Therefore, it is necessary to investigate how a fault in a converter, especially the machine-side converter, affects the operation of the generator and to determine whether existing methods proposed for detecting faults in converter-fed induction machines are applicable and suitable for the DFIG or not.

1.3. Objectives

This research deals with fault detection and post-fault operation for a wind turbine driven DFIG. The objectives of this research can be divided into two parts – control of the DFIG and fault diagnosis for the back-to-back converters. Meeting objectives involved the following step,

- design the experimental system of the DFIG,
- apply established control method to operate the DFIG,
- investigate the effects of faults, especially open-switch faults in the back-to-back converters on the generator and the generator system,
- propose and verify a method to solve the problems in the existing methods of fault detection when applied to the DFIG,

- investigate appropriate methods to operate the system after fault is detected.

1.4. Methodology and Scope of This Research

Several methods have been proposed and applied to control the DFIG. In this research, stator-flux vector control and voltage vector control are applied to the generator and the grid-side converter. Regarding control of the DFIG, the scope is simply to operate the DFIG properly and prove that under fluctuated input torque conditions, as met with wind turbines, the DFIG can operate successfully and is ready for the main objective of the research.

Regarding the main objective of this research, the scope is to be able to analyse the effects of converter faults on the DFIG system. Within this investigation, the proper fault diagnosis method, suitable for the DFIG should be identified and the proper post-fault operation methods established to operate the system.

Reference

1.1. http://www.enercon.de

1.2 'WINDBLATT'. ENERCON Magazine for wind energy, Issue 04, 2007

1.3. S. Soter and R. Wegener, 'Development of Induction Machines in Wind Power Technology'. Proceeding of IEEE International Electric Machines & Drives Conference, 2007, pp. 1490-1495.

1.4. http://www.repower.de

1.5. S. Müller, M. Deicke, and Rik W. DE Doncker, 'Doubly-Fed Induction Generator Systems for Wind Turbines A Viable Alternative to Adjust Speed Over a Wide Range at Minimal Cost'. IEEE Industry Application Magazine, May/June 2002, pp. 26-33.

1.6. http://www.awea.org/pubs/documents/globalmarket2004.pdf

1.7. http://www.bwea.com

1.8. http://www.windustry.org

1.9. P. C. Roberts, 'A Study of Brushless Doubly-Fed (Induction) Machines'. Ph.D. Dissertation, University of Cambridge, 2004.

Chapter Two

Wind Energy

This chapter deals with the nature and opportunities for wind energy. A general description of wind energy, relating to its availability, scale and probability of unevenness are given first. Knowledge of the wind is then applied to the conversion from wind energy to electrical energy by wind turbines. The general structure of wind turbines is briefly discussed and further reading can be found in the references [2.1-2.4]. Several types of wind turbines are compared, including how their control matches their design. Different choices for the generator used with wind turbines are then proposed, compared and discussed. Finally, the application of doubly-fed induction generators to wind turbines is discussed.

2.1 General Discussion of Wind

Wind energy is transformed from the heat energy from the sun that heats the earth. The air generally flows from cold areas to hot areas due to temperature and pressure differences [2.1-2.3]. The global or geographic wind is driven by these temperature differences and pressure differences and is not much affected by the surface of the earth. This type of wind dominates at altitude above 1000 meters [2.2]. The low level wind, called "surface wind", is influenced by the earth's surface at altitudes up to 100 meters [2.3]. It is affected by any obstacle and the roughness of the earth's surface which can slow down the wind or cause turbulence. This is the wind pattern that concerns wind energy production throughout the world. Different locations have different wind patterns; therefore, to build a wind turbine, knowledge of the local wind conditions is necessary.

During the daytime the land is heated by the sun more quickly than the sea, so the air on the land rises and the air from the sea flows to replace the hot air on the land - on shore wind. The opposite occurs at night time, where the sea releases heat more slowly than the land, so the air pressure above the sea is lower than above the land, resulting in air flow from the land to the sea – off-shore wind. Variation of wind speed can be classified into variation with time and variation due to location and

wind direction. Variation with time can be observed falling into three groups - synoptic, diurnal (daily time scale) and short-term (gust and disturbance, 10 minutes or less) as can be seen in the power spectrum density curve of wind speed in figure 2.1 [2.1]. The power spectrum density function describes the variation in average power with frequency, and for the wind observed at a specific location shows that the largest average power occurs due to speed varying over several days i.e. major weather changes, but that short time turbulence as experienced in a normal windy day is the next most significant variation.
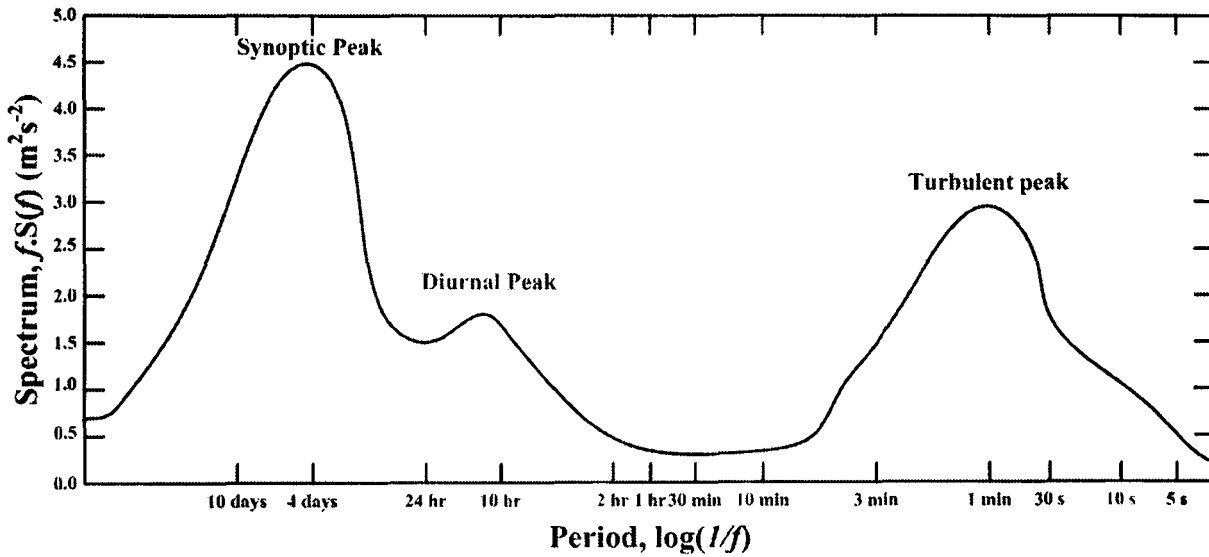
Figure 2.1 Wind spectrum based on work by van der Hoven

(Reproduced from [2.1])

It is quite difficult to predict the long-term wind speed, but is possible to predict the hourly wind speed over a year by statistical distribution. The Weibull distribution [2.1] has been used to represent the variation of the hourly wind speed over a year at any typical site. The distribution can be written as

$$F(U) = e^{\left(-\left(\frac{U}{c}\right)^k\right)},$$ (2.1)

where $F(U)$ is the fraction of time for which the hourly wind speed exceeds U, c is the scale parameter and k is the shape parameter.

The parameter c is related to the annual mean wind speed U by the relationship

$$U = c\Gamma\left(1 + \frac{1}{k}\right),$$

(2.2)

where Γ is the complete gamma function.

The mean wind speed in equation (2.2) can be written in integral form

$$\overline{U} = \int_0^\infty U f(U) dU .$$

(2.3)

Therefore, the probability density function can be derived as

$$f(U) = -\frac{dF(U)}{dU} = k\frac{U^{k-1}}{c^k} e^{\left(-\left(\frac{U}{c}\right)^k\right)} .$$

(2.4)

2.2 Energy form the Wind

Wind is an unpredictable energy source and it fluctuates. Moreover, the energy per unit mass is much less than water or steam which is used in hydro power and steam power plant respectively. Generally, air density at $15°C$ and at sea level is 1.225 kg/m^3, which is approximately 1000 time less than water (water density is 1000 kg/m^3). Therefore, to provide the same energy level wind energy requires a larger area than water. However, due to the energy crisis caused by the depletion of fossil fuels and the global warming problem, renewable energy is increasingly important to the world. Although hydro power is clean, it requires a large area to build a dam to store the water. This may require destruction of forest which would affect the environment and cause further problems. Wind energy is captured by change of momentum of the air flow. Based on fluid mechanics, wind power can be calculated by the mass flow model as shown in figure 2.2. The rate of change of air mass $\frac{dm}{dt}$, through a rotor disk area A can be written as follows,

$$\frac{dm}{dt} = \rho A U ,$$

(2.5)

where ρ is the air density and U is air velocity.

As shown in equation (2.5), assuming that the area is constant, the mass flow rate is a function of the air density and velocity.
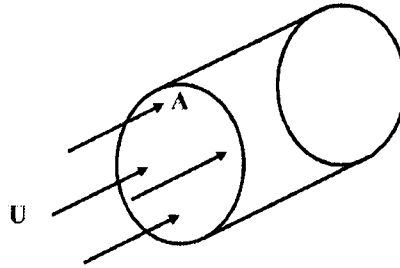
Figure 2.2 Flow of air through a rotor disk; A, area; U, wind velocity [2.2]

The wind power P_{wind} can be calculated from

$$P_{wind} = \frac{1}{2}\frac{dm}{dt}U^2 = \frac{1}{2}\rho A U^3,$$ (2.6)

and the wind power density is

$$\frac{P_{wind}}{A} = \frac{1}{2}\rho U^3.$$ (2.7)

2.3 Conversion from Wind Energy to Electrical Energy

The conservation of energy law states, "energy can neither be created nor destroyed, but can only be transformed from one form to other forms". This law applies to the conversion of wind energy to electrical energy. The equipment that is used to convert wind energy to other useful energy is called a "wind turbine". Generally, wind energy is in the form of translational kinetic energy. Assuming that a wind turbine system is lossless, once the wind blows the wind turbine, the translation kinetic energy is transformed to rotational kinetic energy which can rotate the turbine with the relationship as follows,

$$\frac{1}{2}mU^2 = \frac{1}{2}J\omega^2,$$ (2.8)

where J is the moment of inertia of the turbine and other rotational parts, and ω is the angular velocity.

The shaft of the wind turbine is directly or indirectly coupled to a generator which is used to convert rotational mechanical energy, transferred via the generator shaft, to electrical energy. In the case of indirect coupling, a gear box is installed between the turbine shaft and the generator shaft for the purpose of increasing the rotational speed to suit the generator. The details of different generator types will be discussed in a later section.

As stated in the conservation of energy law, 100% of wind power cannot be extracted from the wind. To explain this phenomenon, the concept of the actuator disc is taken into consideration. The device that is used to capture power from the wind called an actuator disc and the air-stream tube impinging on this actuator is shown in figure 2.3.
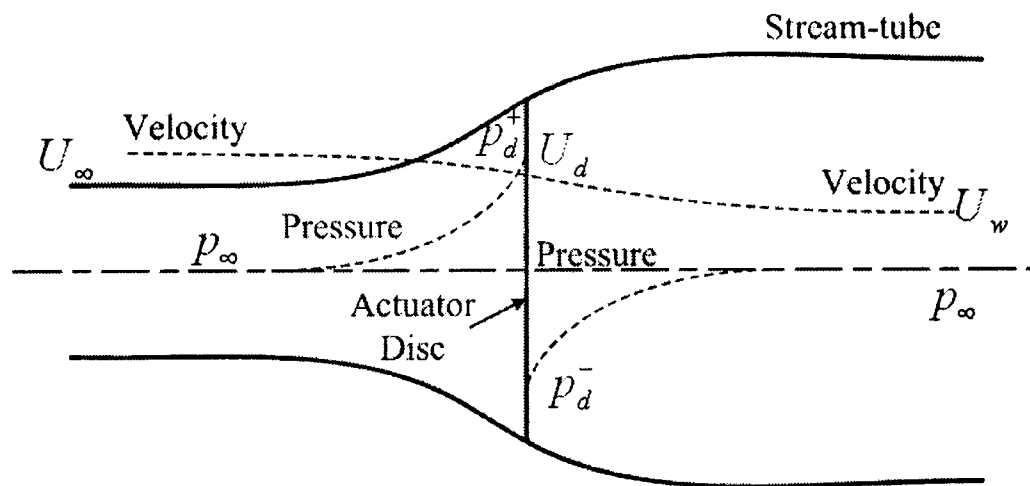
Figure 2.3 Energy extracted from actuator disc and stream-tube [2.1]

As shown in the figure, the cross-section area of the upstream tube (in front of the disc) is smaller than the cross-section area of the downstream tube (behind the disc). This expansion is due to the law that the air mass flow rate must be the same everywhere. Considering the air mass flow rate in terms of its density, cross-sectional area and its speed, therefore, the equation of the mass flow rate is

$$\rho A_\infty U_\infty = \rho A_d U_d = \rho A_w U_w,\qquad(2.9)$$

where subscripts ∞ refers to far upstream, d refers to the condition at the disc and w refers to the far wake (downstream).

[2.1] considered that the actuator disc induces a velocity variation which superimposes on the free-stream velocity. The stream-wise component of this induced flow at the disc is given by $-aU_\infty$, where a is the axial flow induced factor, or the inflow factor. Form this consideration, the net stream-wise velocity is as follows,

$$U_d = U_\infty(1-a).$$

(2.10)

The speed of the air that passes through the actuator disc is changed resulting in change of momentum which can be written in the form of velocity different times mass flow rate at the disc as follows,

$$\text{Rate of change of momentum} = (U_\infty - U_w)\rho A_d U_d.$$

(2.11)

The force that causes the change in momentum is due to difference of the pressure in the front of and behind the disc which can be written as follows,

$$(p_d^+ - p_d^-)A_d = (U_\infty - U_w)\rho A_d U_\infty(1-a).$$

(2.12)

This phenomenon can be explained by Bernoulli's equation by applied separately to the upstream and downstream section of the stream-tube. Bernoulli stated that, under steady-state condition, the summation of the kinetic energy, static pressure and gravitational potential energy is constant provided no work is done on or by the fluid. Hence, for the unit volume of the air [2.1],

$$\frac{1}{2}\rho U^2 + p + \rho g h = \text{constant}.$$

(2.13)

Considering upstream section,

$$\frac{1}{2}\rho_\infty U_\infty^2 + p_\infty + \rho_\infty g h_\infty = \frac{1}{2}\rho_d U_d^2 + p_d^+ + \rho_d g h_d,$$

(2.14)

and downstream section,

$$\frac{1}{2}\rho_\infty U_w^2 + p_\infty + \rho_\infty g h_\infty = \frac{1}{2}\rho_d U_d^2 + p_d^- + \rho_d g h_d.$$ (2.15)

Assuming that flow is incompressible ($\rho_\infty = \rho_d$) and horizontal height is equal ($h_\infty = h_d$), subtraction equations (2.15) from (2.14) results in

$$p_d^+ - p_d^- = \frac{1}{2}\rho\left(U_\infty^2 - U_w^2\right).$$ (2.16)

From equation (2.16), equation (2.12) can be written as follows,

$$\frac{1}{2}\rho\left(U_\infty^2 - U_w^2\right)A_d = \left(U_\infty - U_w\right)\rho A_d U_\infty\left(1 - a\right),$$ (2.17)

which also results in relationship between the U_w and U_∞, as follows,

$$U_w = \left(1 - 2a\right)U_\infty.$$ (2.18)

According to equations (2.12) and (2.18), the rate of work done by the force caused by pressure difference is given by

$$P_d = 2\rho A_d U_\infty^3 a\left(1 - a\right)^2.$$ (2.19)

Equation (2.19) can be rewritten in terms of P_∞ of equation (2.6) as follows,

$$P_d = c_p P_\infty = c_P \frac{1}{2}\rho A_d U_\infty^3,$$ (2.20)

where c_P is called "the power coefficient" and is equal to $4a\left(1 - a\right)^2$.

From equation (2.20), differentiating this equation to find the maximum point by letting the result be 0, the value a is equal to $\frac{1}{3}$ resulting in the maximum $c_P = \frac{16}{27} \approx 0.593$. This value is called "Betz limit".

Another coefficient which may be useful for the application of the wind turbine generator is called the "Thrust Coefficient". This value can be derived from the wind force equation which is equal to the wind power equation divided by wind speed. This coefficient is not directly useful for energy capture, but it is useful for design of the wind turbine blades and tower. As shown in equation (2.6), wind power is proportional to the cube of wind speed; therefore, the best place for a wind farm should be in a high wind speed region. Figure 2.4 shows the "wind speed map" of the UK. As shown in the figure, Scotland is in a high wind region and is therefore suitable for wind farms.

Annual mean wind speed
at 25m above ground level [m/s]

> 10
9 - 10
8 - 9
7 - 8
6 - 7
5 - 6
< 5

km 25   0   125 km

Copyright ETSU for the DTI 1999

Figure 2.4 Wind map of the UK [2.23]

2.3.1 Wind Turbines

Wind turbines have been used in the past for different purposes. An early model was designed in Tibet, for religious reasons, based on a scoop-drag type device [2.10] which today is used as an anemometer. Wind turbines were used for corn grinding in Holland and other countries. This ancestor of today's wind turbine had a horizontal axis and four blades. Today's wind turbines can be broadly classified into two types

by the alignment of its rotor axis – vertical axis wind turbines (VAWT) and horizontal axis wind turbines (HAWT), as shown in figure 2.5

(a)   (b)
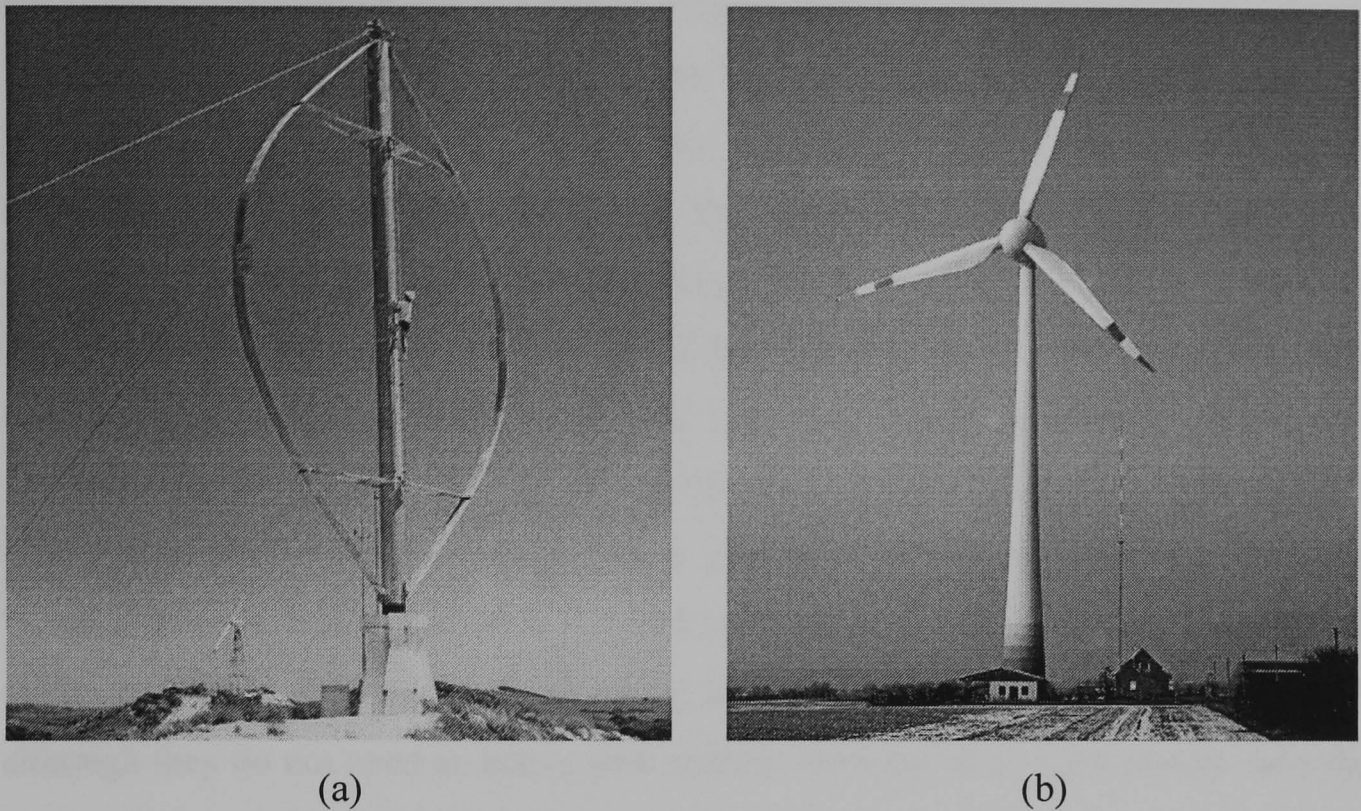
Figure 2.5 (a) Darrieus vertical axis wind turbine and (b) horizontal axis wind turbine

Considering figure 2.6, this represents an airfoil in the air blown by the wind. In aerodynamics, the object in the flowing fluid has two forces exerted on it, drag force and lift force, which are in parallel and perpendicular to the relative wind direction respectively. Moreover, there are two other forces that must be considered, F_{Thrust} and F_r, which are important to the wind turbine engineer. F_{Thrust} is in the wind direction and is used in the design the turbine and tower to withstand the wind, whereas F_r is the force that causes torque to drive the turbine [2.4].
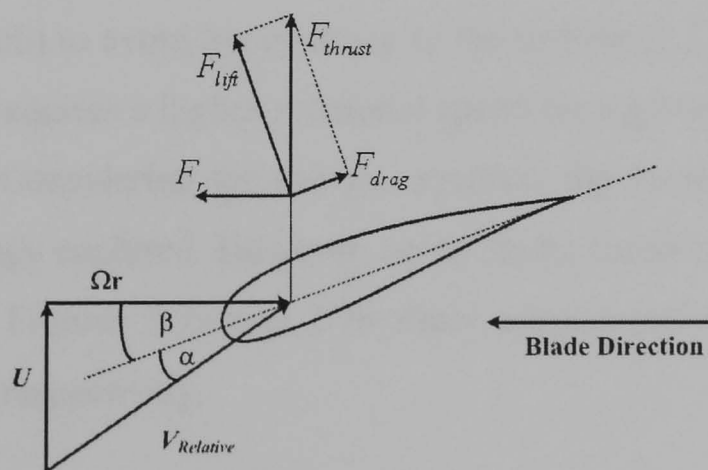
Figure 2.6 Schematic diagram of forces acting on an air-foil of the turbine's blade

From figure 2.6, **U** is wind speed, Ωr is rotational speed and $V_{Relative}$ is the relative wind speed. Moreover, other two necessary variables are angles α and β which are the angle of attack and blade pitch angle respectively.

VAWTs can be separated into drag types e.g. Savonius turbine and lift type e.g. Darrieus turbine. However, the vertical axis wind turbine has several disadvantages, as follows: lower wind speed caused by the turbine being near ground level, low efficiency, requires dismantling for bearing replacement and requires guy wires to hold the turbine up, as shown in figure 2.5a. For the HAWT, the main force that drives the wind turbine is lift force. The largest to-date (2007) wind turbine was manufactured by Enercon [2.17] named "Enercon E-126", having a capacity of 6 MW and is likely able to produce power up to 7MW. From this point, the word "wind turbine" refers to the HAWT. Wind turbines can be separated into upwind and downwind designs. Downwind towers are rarely used for large-scale wind turbines although they do not need an active yaw control. Downwind designs always have the problem of turbulence behind the blades and are used only for low power wind turbines.

i. Number of Blades

The number of blades can vary from one blade to multi blades [2.2, 2.3]. The more blades there are the slower the rotational speed required. All modern wind turbines are three-blade types [2.3]. This design is called the "Danish concept". Three blades have the particular advantage that the polar moment of inertia with respect to yawing is constant, and is independent of the azimuthal position of the rotor [2.2]. Two-bladed designs have the advantage of reduced blade cost, but have the problem of instability of the blades in high wind. They therefore require an adjustable axis for the hub (teetering hub) to avoid heavy shock to the turbine [2.3]. Moreover, the two-blade wind turbine requires a higher rotational speed for a given power which results in increased noise. Considering the energy captured, the more blades there are the smoother is the energy captured. However, more blades mean higher cost and higher moment of inertia. Figures 2.7a and 2.7b show commercial two-blade and three-blade wind turbines respectively.

(a)   (b)

Figure 2.7 Wind turbines classified by the number of blades

(a) 2 MW two-bladed wind turbine [2.18],

(b) GE 3.6 MW three-bladed wind turbine [2.19].

ii. Inside the Nacelle and Hub

The components in the nacelle of the wind turbine consist of both mechanical and electrical components. Figure 2.8a shows the nacelle and hub of a Vestas variable-speed wind turbine. In this nacelle, the front-end has the gear box with the low-speed side connected to the turbine rotor shaft and the high-speed side connected to the generator shaft via the brake. The generator used in this turbine is a doubly-fed induction generator. The power converters, transformer, controller and the yaw drive are also included in this nacelle. Figure 2.8b show the nacelle and hub of an Enercon [2.17] direct drive wind turbine. There is no gear box because the rotor is connected directly to a low speed generator, which in this turbine is a multi-pole wound rotor synchronous generator. The pitch actuators for both types of wind turbine are installed in the hub which is located in front of the nacelle as shown in figure 2.8.

Each blade has the necessary gears and pitch actuator, which can be either a hydraulic or electric motor.
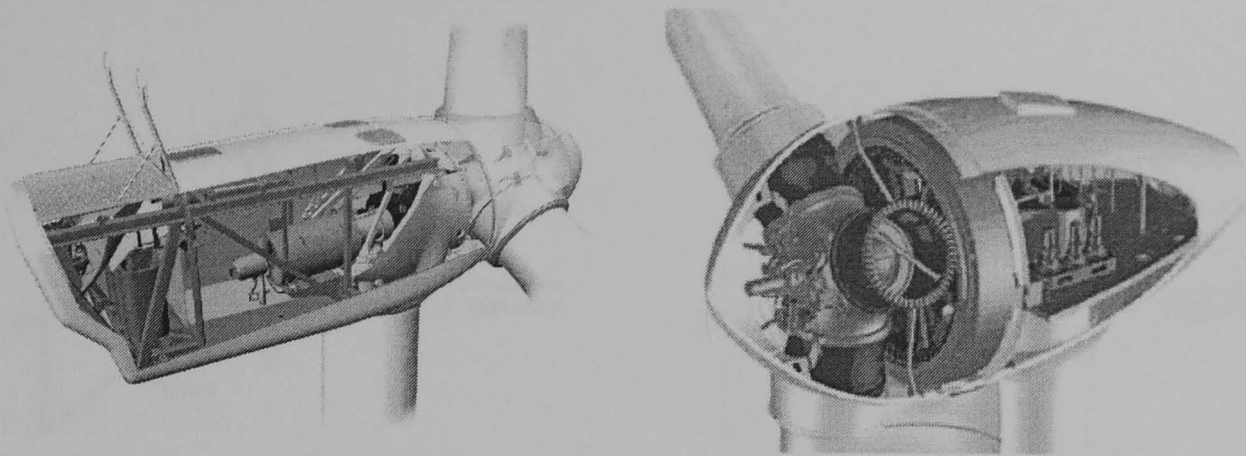
Figure 2.8 The drawing of the nacelle and hub of a wind turbine (a) the nacelle of the Vestas wind turbine [2.14] (b) the nacelle of the Enercon wind turbine [2.17]

2.3.2 Power Control of the Wind Turbines

Wind turbines can be broadly classified into two types – fixed speed and variable speed - which have different power control methods. Power control can be by control only of blade angle, by control only of generator or by control of both blade angle and generator [2.21].

i. Power Control by Aerodynamic Control

Blade angle control, also called "aerodynamic control", can be classified into three types - passive stall, active stall and pitch control. The main objective of aerodynamic control is to protect the generator, the turbine and other mechanical parts from overloading during high wind speed condition. With pitch angle control, optimised power capture throughout the entire operable wind speed can be achieved. The three types of aerodynamic control are shown in figure 2.9. The first method, "passive stall control", is generally applied to fixed-speed wind turbines. The blades are fixed to the hub at one angle. This control depends only on wind speed. According to the aerodynamics of the airfoil, as wind speed increases the relative wind speed also increases resulting in an increase of the angle of attack α. If α is still below its critical limit, the wind flowing above the blade is still a streamline. When the angle increases, this streamline turns to turbulence and becomes complete turbulence if α is above its critical limit. This phenomenon results in a decrease in lift force and an increase in drag force. Reference [2.3] noticed that the blade is

twisted slightly as observed moving along the blade's longitudinal axis. This is partly done to ensure that the rotor blade gradually stalls instead of abruptly stalls when the wind speed reaches its critical value.

(a)

(b)

(c)
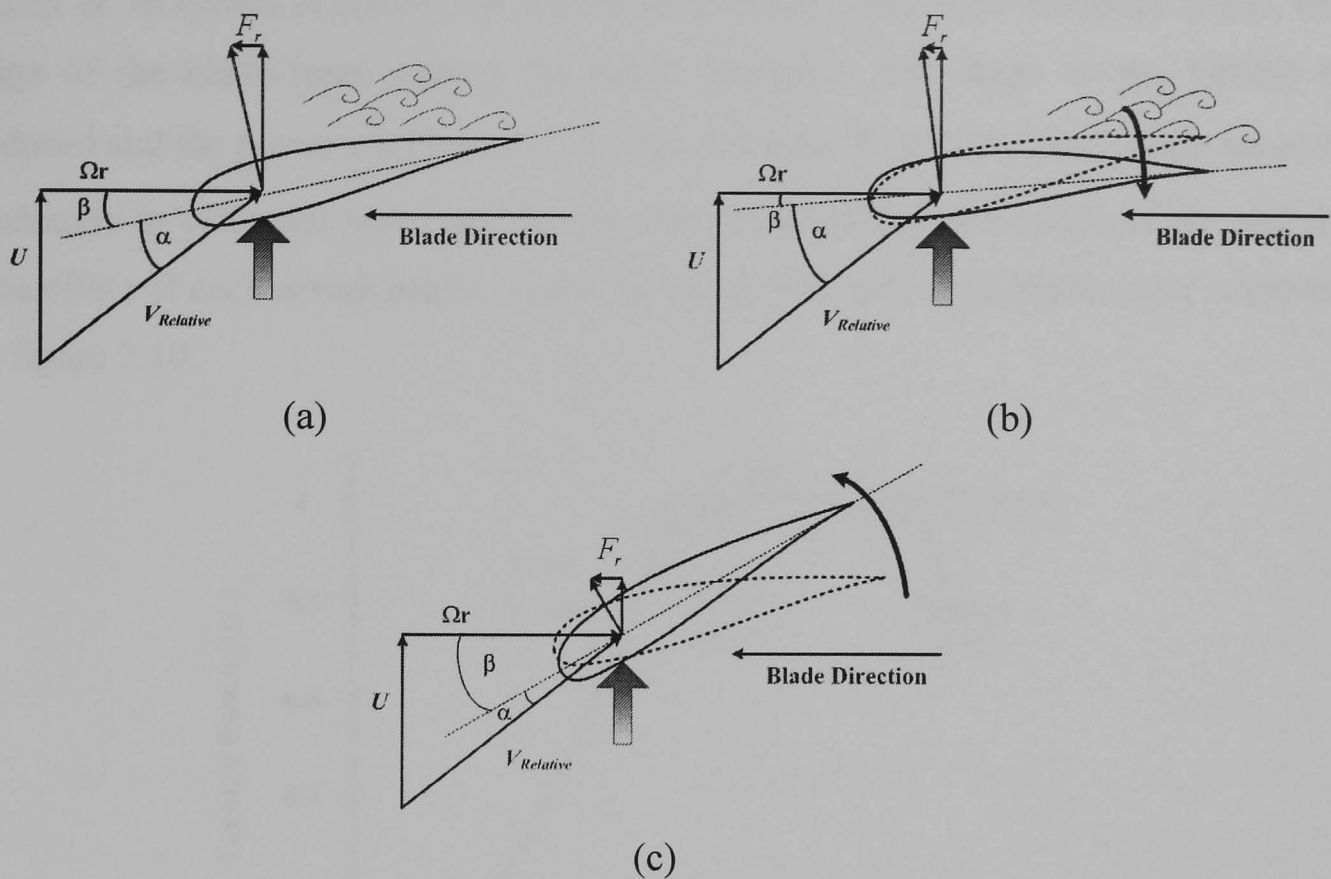
Figure 2.9 Schematics of blades for power control by aerodynamic control
(a) passive stall control, (b) active stall control and (c) pitch angle control

Active stall control is similar to passive stall control, but instead of having fixed blade angle there are mechanical rotational parts to turn the blade to increase the angle of attack α above its critical limit. This method helps avoid any overshoot of the rated power of the machine due the appearance of a wind gust [2.3] as shown in figure 2.10. This method is also applied to fixed-speed wind turbines which can operate only at one or two ideal wind speeds (generally two speeds). Therefore, under other wind speed conditions the power captured is not the maximum power that could be captured. The power output of each of these two types of wind turbine depends only on the wind speed. Under stall conditions, the wind turbine behaves like a wall as the flat side of the blade turns against the wind [2.11] resulting in high stress on the turbine structure.

With pitch control, over a range of wind speeds from cut-in wind speed to rated wind speed, the blade pitch angle β is adjusted to be zero or a small negative angle [2.21].

For wind speeds from rated wind speed to cut-off wind speed, the pitch angle β is steadily increased to reduce the aerodynamic force of the wind. The direction of increasing blade pitch angle β is opposite to the direction of increasing angle of attack α as shown in figure 2.9c, called feathering. Under fully feathered mode, the edge of the blade turns against the wind. Therefore, the stress on the turbine is reduced and the power coefficient c_p is also reduced. To achieve pitch angle control, hydraulic or electrical servo motors are used to adjust the pitch angle of the blades. The effect of each aerodynamic control on the turbine power characteristics is shown in figure 2.10.
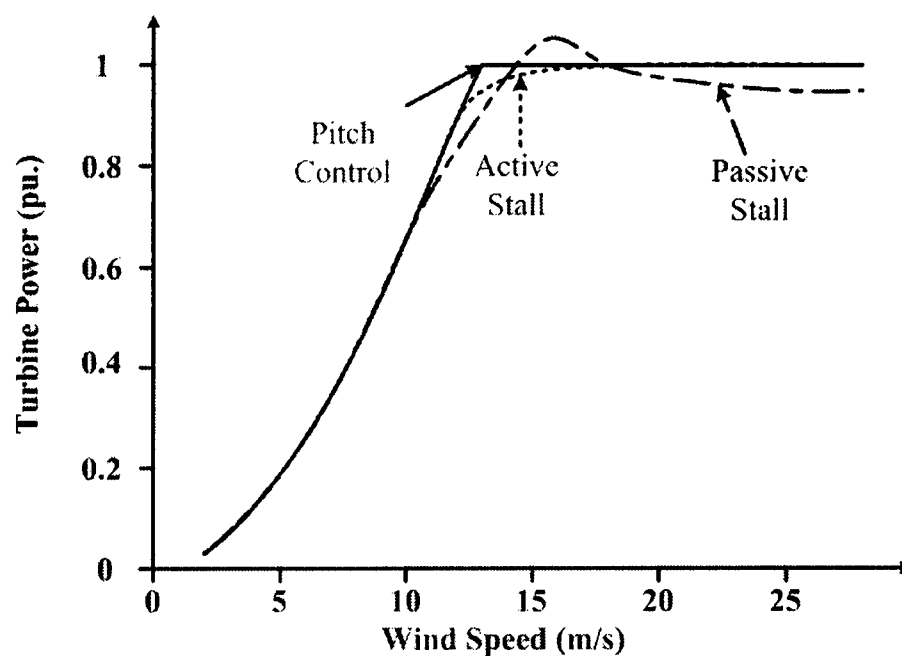
Figure 2.10 Characteristic of turbine power with different power control method

To date, pitch angle control is applied to variable-speed wind turbines with variable speed control of the generator to achieve maximum possible power at any wind speed.

ii. Power Control by a Variable-Speed Generator

The second system to control the power of the wind turbine is by using variable-speed generators. The aim of using a variable-speed generator is to optimally capture the power from the wind at any wind speed and to limit the power captured under maximum wind speed operation. Two methods for optimised operation have been proposed to achieve this task - constant tip speed ratio and maximum power tracking. The tip speed ratio λ is the ratio between blade tip speed and wind speed as follows

$$\lambda = \frac{\Omega r}{U},$$

(2.21)

where Ω is the angular velocity of the blades, r is the radius of the blade and U is the free stream wind speed.
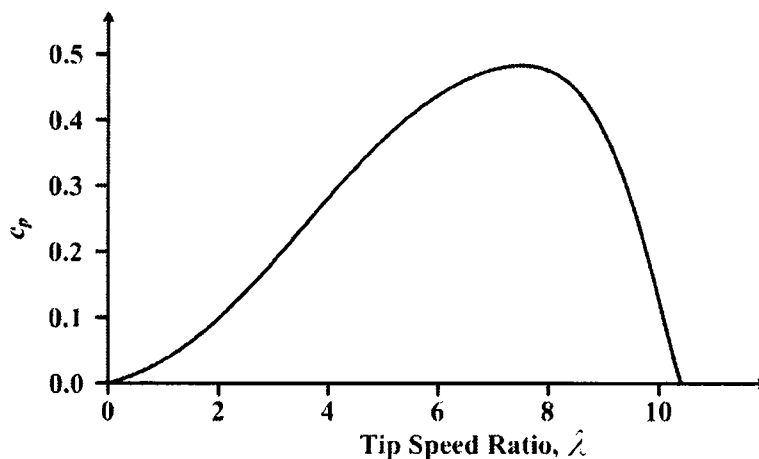
Figure 2.11 Rotor power coefficient vs. tip speed ratio curve

Considering figure 2.11, the constant tip speed ratio method is based on the fact that maximum power can be extracted from the wind at the tip speed ratio which provides the maximum c_p. This method requires a model of the wind turbine to calculate the reference $c_p - \lambda$ curve and store in the memory of the controller. The equation to calculate the $c_p - \lambda$ curve can be found in several references [2.21, 2.22]. The equation used in this thesis is the equation used in SimPowerSystem toolbox in MATLAB/SIMULINK [2.22] as follows,

$$c_p(\lambda,\beta) = 0.5176\left(\frac{116}{\lambda_i} - 0.4\beta - 5\right)e^{\left(\frac{-21}{\lambda_i}\right)} - 0.0068\lambda,$$

(2.22)

$$\lambda_i = \left(\frac{1}{\lambda + 0.08\beta} - \frac{0.035}{\beta^3 + 1}\right)^{-1}.$$

(2.23)

Continuous measurement of wind speed and rotor speed is required to calculate instantaneous λ and compare with the reference stored in the memory. The disadvantages of this method are inaccuracy of the measured wind speed due to the location of the measurement system, which is on the nacelle, and any dirt on the

blade surfaces which changes the characteristic of the wind turbine [2.21]. This method is used commercially in some present wind turbines and is also used in this research.

The second method, called maximum power point tracking (MPPT), is applied in cases where the model of the turbine is unknown. The idea of this method is to calculate the operating speed for which $\frac{dP}{d\omega} = 0$, which is the peak power point of the power-rotational speed curve. For this operation the generator power is continuously measured. If $\frac{dP}{d\omega} > 0$, the generator speed is increased but if $\frac{dP}{d\omega} < 0$ the generator speed is reduced. If $\frac{dP}{d\omega} \approx 0$, the speed is maintained constant and maximum power is being extracted from the wind. This method is insensitive to errors in wind speed measurement and is therefore better than tip speed ratio method. This method is also applied to modern wind turbine generators [2.21].

(a)   (b)
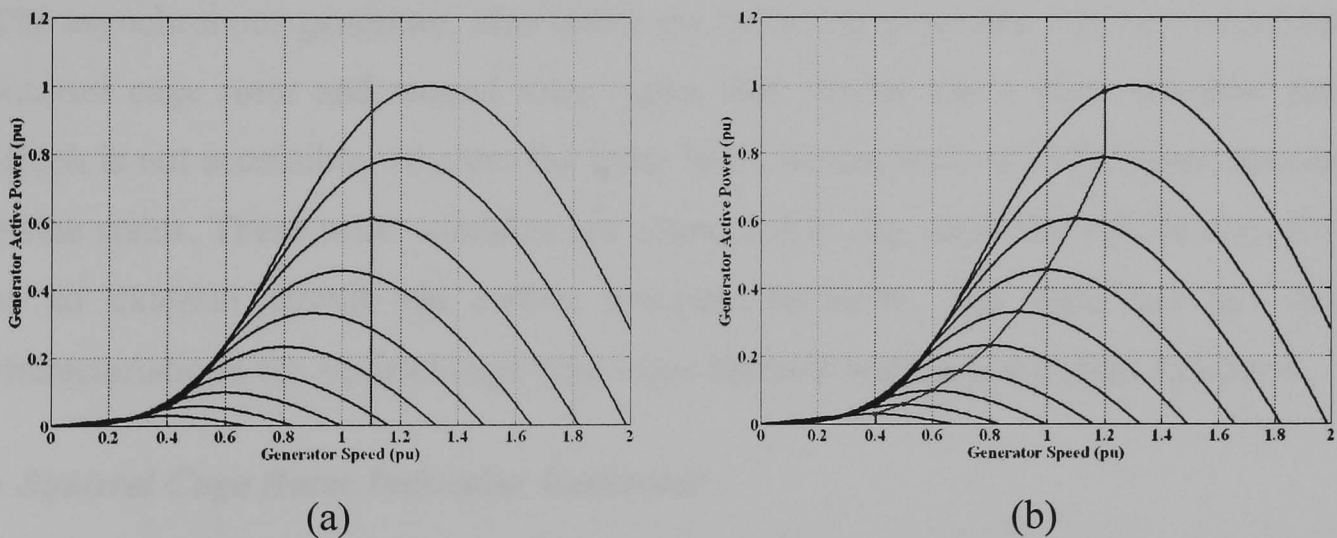
Figure 2.12 Operating points of different generators (a) fixed-speed wind turbine, (b) variable-speed wind turbine

Figure 2.12 compares the operating points between fixed-speed and variable-speed wind turbines. As shown in figure 2.12a, for the fixed-speed wind turbine, only one wind speed allows the turbine to extract the maximum power from the wind. In contrast, in figure 2.12b, the turbine is operating with a variable-speed generator and is under both pitch control and speed control to extract optimum power.

2.4 Energy Conversion Configurations

Different generator configurations have been proposed and used with wind turbines. The generators can be broadly classified into two types – synchronous and asynchronous. For the associated power electronic converters, several topologies have been used. The soft-starter is the usual configuration applied to fixed-speed wind turbines. The configurations that will be presented in this section are variable frequency converters for variable-speed wind turbines.

2.4.1 Detail Discussion of Different Configurations

This section describes energy conversion methods by the types of generator used and the power electronics circuits applied with such generators. Energy conversion configurations discussed in this sub-section are configurations that have been commercially used in many countries. Some special configurations that may be used in the future or may be under study are also briefly discussed.

i. Energy Conversion Systems Based on an Asynchronous Generator

The asynchronous generator, also called the induction generator, can be divided into squirrel cage rotor and wound rotor types. The former has a short circuited rotor which is not accessible, whereas the latter has a wound rotor with the same structure of the stator. These rotor windings are connected to slip rings and can be connected to an external circuit via carbon brushes. However, this type has the same characteristic as the squirrel cage type when its rotor windings are short-circuited.

• *Squirrel Cage Rotor Induction Generator*

The first configuration is a "Danish concept" which is used with a fixed-speed wind turbine together with stall control.
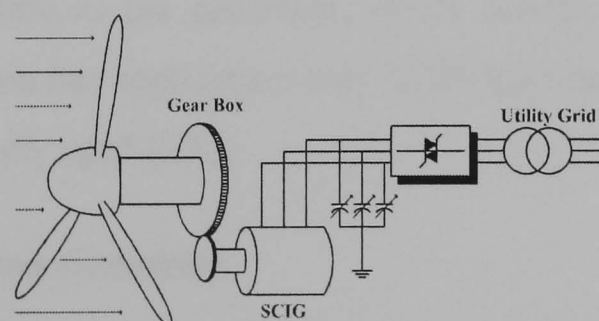
Figure 2.13 The first concept – fixed-speed wind turbine with a directly grid connected squirrel cage induction generator

This configuration, shown in figure 2.13, consists of a squirrel cage induction generator connected directly to the grid. It requires an auxiliary circuit to gradually increase the stator voltage to avoid inrush current during generator starting process and a capacitor bank for reactive power compensation. This configuration is optimal at only one or two wind speeds, depending on the design of the stator winding of the generator.

At other wind speeds it cannot acquire the maximum power from the wind [2.6, 2.7]. The power and power factor of this configuration are not controllable. The power depends only on the fixed blade pitch angle of the turbine. Moreover, if wind gusts occur, the power will fluctuate and can no longer be regulated [2.10].

The second configuration in this subclass is the variable-speed induction generator. Variable-speed operation is applied to this generator by connecting back-to-back voltage source converters between the generator and the grid to decouple the generator from the grid as shown in figure 2.14.
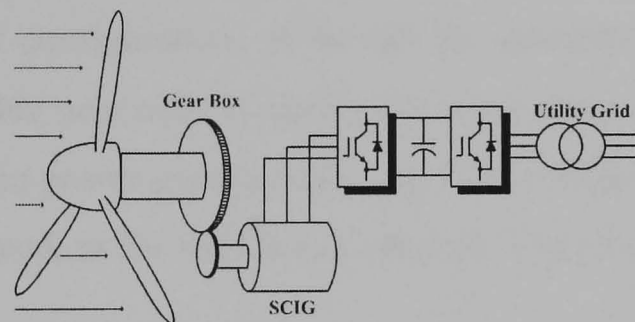
Figure 2.14 The second concept - variable-speed wind turbine with full rating back-to-back converters connected between a squirrel cage induction generator and the grid

This configuration provides the full control of the power factor and the grid-side converter can regulate the power supplied to the grid. However, the converter ratings must be at least the same as the generator, which results in an expensive system [2.10]. This configuration has application only in laboratories, and from the survey it has not been commercially used [2.8].

• *Wound Rotor Induction Generator*

The wound rotor induction machine is the most interesting machine used in many wind turbines. The first configuration is similar to the Danish concept except that the

rotor is connected to three-phase resistor bank paralleling with a diode bridge in parallel with a semiconductor switch [2.14, 2.21]. The schematic of this type is shown in figure 2.15.
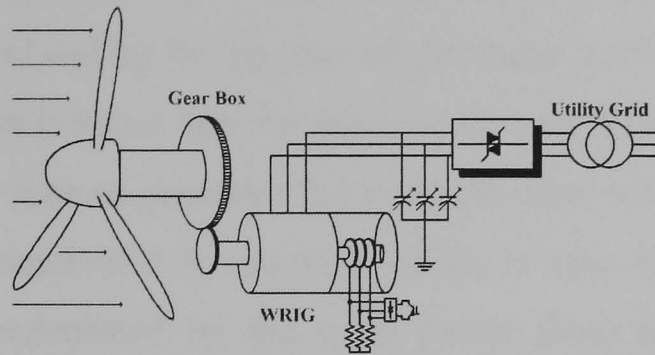
Figure 2.15 The third concept - variable-speed wind turbine with a wound rotor induction generator with variable resistor control

This concept is based on varying rotor resistance to control the speed of the generator. It was applied by Vestas [2.14, 2.21], the wind turbine manufacturer, under the name "OptiSlip". The Vestas V66-1.65MW is an example of a wind turbine that uses this configuration. Although the generator's stator is connected directly to the grid, this generator is used with wind turbines having pitch control which helps smooth the power generated [2.10]. This configuration can operate only above synchronous speed, as for the Danish concept. The rotor power is dissipated in the external resistor.

The next configuration, called the doubly-fed induction generator (DFIG), has been widely used. More than 70% [2.10] of the generators used in wind turbines are DFIGs. For this configuration, the stator is directly connected to the grid while the rotor is connected to the grid via back-to-back converters, as shown figure 2.16
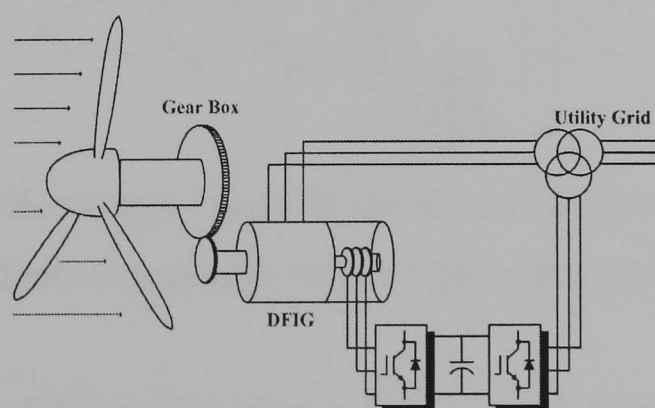
Figure 2.16 The fourth concept - variable-speed wind turbine with a doubly-fed induction generator

This generator can operate at sub-synchronous speed, synchronous speed and super-synchronous speed and can be controlled by controlling the rotor currents via the converters. Under super-synchronous speed generation, the generator sends power to the grid from both stator and rotor. Since the rotor power is a fraction of the stator power, as can be calculated by the product of the stator power and the slip, the VA rating of the converters is lower than the machine rating which can reduce the cost of the system. Since this type of generator has a wound rotor with slip rings and carbon brushes, periodic maintenance is required which is one drawback of this type. However, this is compensated by the extra power from the rotor and the cost reduction of the converters. Some research into brushless doubly-fed induction generators and brushless doubly-fed reluctance generators has been conducted [2.20]. These machines require no brushes or slip rings and are also applicable to low-speed operation. However, the technology in this area is not mature and only small-scale generators (less than 250 kW) have been built for test. The details of the theory and control of the DFIG will be discussed in the next chapter, as this configuration is the one used in this research.

Another possible configuration is shown in figure 2.17 [2.9]. This configuration is applicable to connection to a dc-transmission line and therefore no grid-side converter is required. Due to having a converter at both stator and rotor, this configuration has the flexibility to control the power from both stator and rotor.
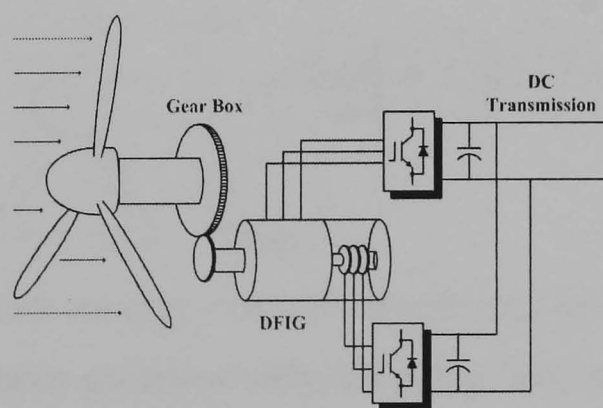
Figure 2.17 The fifth concept - variable-speed wind turbine using a doubly-fed induction generator with full generator control

ii. Energy Conversion Systems Based on a Synchronous Generator

Another generator type is the synchronous generator which can be divided into two subclasses - permanent magnet type and wound rotor type. The converters used with

this generator must have full rating because they are connected to the stator side of the generator.

• *Permanent Magnet Synchronous Generator*

The permanent magnet synchronous generator (PMSG) is the first configuration, shown in figure 2.18. It uses a diode bridge rectifier and boost converter for the machine-side converter [2.6, 2.9].
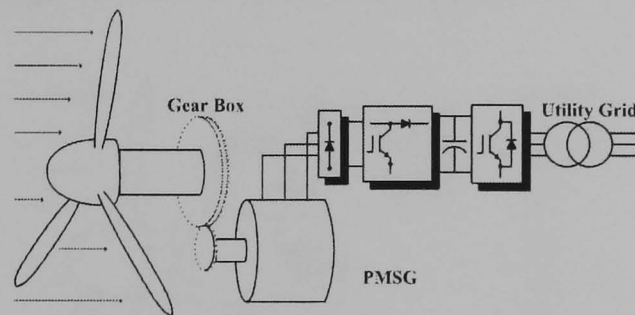
Figure 2.18 The sixth concept - variable-speed wind turbine with a permanent magnet synchronous generator and boost converter

The second configuration uses a PWM converter as the machine-side converter, which allows vector control of the generator. The grid-side converter is also a PWM converter, the same as that used in figure 2.14, to control the power and power factor to the grid.
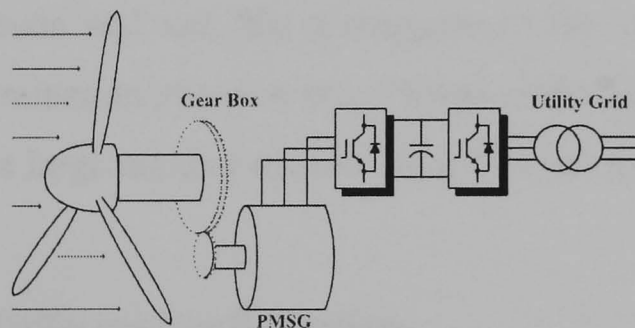
Figure 2.19 The seventh concept - variable-speed wind turbine with a permanent magnet synchronous generator with full-rating back-to-back converters

This configuration has been manufactured for both direct-drive systems, under the brand "Zepharos"[2.15], and geared systems by WinWind company [2.16]. The advantages of the permanent magnet generator are the ability to manufacture multi-pole designs and no rotor copper losses, because there is no rotor winding. However,

the cost of the generator is the main drawback, especially for the direct-drive configuration, because permanent magnets are so expensive [2.12].

• *Wound Rotor Synchronous Generator*

The third configuration uses the wound rotor synchronous generator (WRSG) connected to the shaft of the turbine. This configuration requires a converter to supply dc voltage to excite the generator field winding and the full converter rating for the stator side of the generator, as shown in figure 2.20.
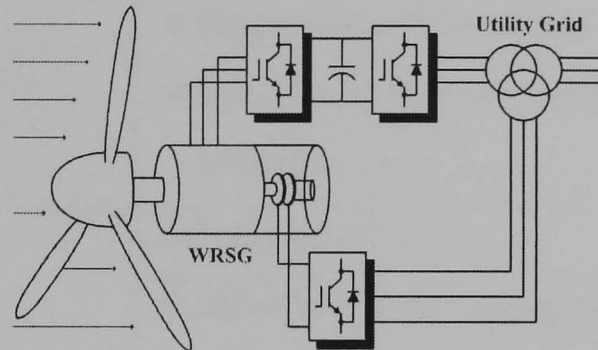
Figure 2.20 The eighth concept - variable-speed wind turbine using a wound rotor synchronous generator with full-rating back-to-back converters on the stator and a PWM rectifier on the rotor

Enercon [2.17] is the only manufacturer using this configuration commercially [2.12]. Moreover, at the time that this thesis is written the largest wind turbines are manufactured by Enercon and use this arrangement. The main advantage of this configuration is the elimination of a gear box. However the diameter of the generator is quite large because a large number of slots must be used for a multi-pole machine design.

2.4.2 Comparison of Different Configurations

As discussed in the previous section, each configuration has its advantages and disadvantages. These are summarised in table 2.1

Table 2.1: Advantages and disadvantages of different energy conversion configurations

Configuration	Advantages and Disadvantages
Concept 1	**Advantages**
	• squirrel cage induction generator is simple rugged and low maintenance
	Disadvantages
	• active and reactive power are not controllable
	• maintenance for gearbox
	• only one or two optimal operating points are available
Concept 2	**Advantages**
	• active and reactive power are controllable
	• squirrel cage induction generator is rugged and low maintenance
	Disadvantages
	• maintenance for gearbox
	• back-to-back converters having at least the same rating to the generator, expensive
Concept 3	**Advantages**
	• maximum power tracking is possible
	• low converter cost
	• simple control system
	Disadvantages
	• operating range is similar to the first concept
	• no rotor power fed to the grid
	• reactive power control is not possible
	• maintenance for the brushes, slip rings and
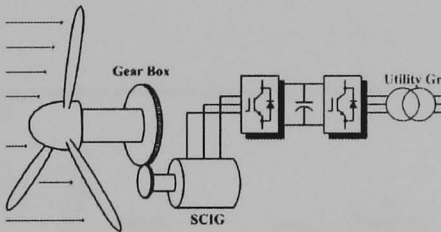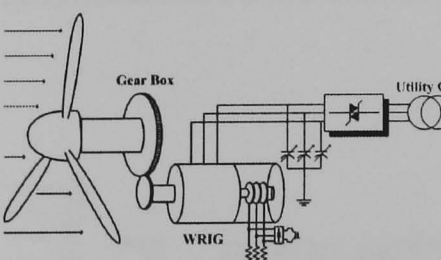
Table 2.1: Advantages and disadvantages of different energy conversion configurations (continued)

Configuration	Advantages and Disadvantages
  Concept 4	**Advantages**
	• small converter rating to control the generator for wide speed range • more power generated than stator-fed generator, at super-synchronous speed generation • low converter cost • full control of active and reactive power by lower converter rating
	Disadvantages
	• maintenance for the brushes, slip rings and gearbox
  Concept 5	**Advantages**
	• full control for both stator and rotor • no grid-side converter required
	Disadvantages
	• fully rating converter at stator side • maintenance for the brushes, slip rings and gearbox
  Concept 6	**Advantages**
	• fewer power semiconductor switches than back-to-back converters • no rotor winding loss and excitation is not required • active and reactive power are controllable • good for low wind speed sites
	Disadvantages
	• PMSG is expensive
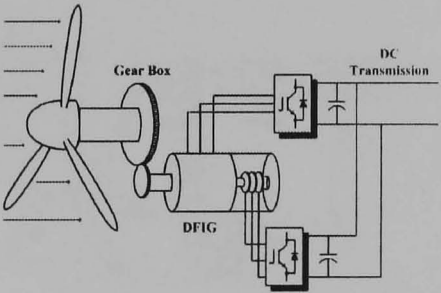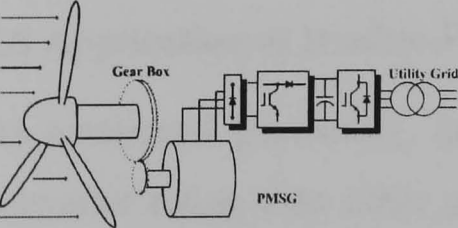
Table 2.1: Advantages and disadvantages of different energy conversion configurations (continued)

Configuration	Advantages and Disadvantages
Concept 7	**Advantages**
	• no rotor winding loss and excitation is not required
	• active and reactive power are controllable
	• no gearbox required for gearless system
	• good for low wind speed sites
	Disadvantages
	• PMSG is expensive
	• Fully rated converters at stator-side
	• expensive converters
Concept 8	**Advantages**
	• good for low wind speed sites
	• no gearbox required
	• active and reactive power are controllable
	Disadvantages
	• large diameter generator/heavy
	• fully rated converters at stator side
	• expensive converters
	• maintenance for brushes and slip-rings
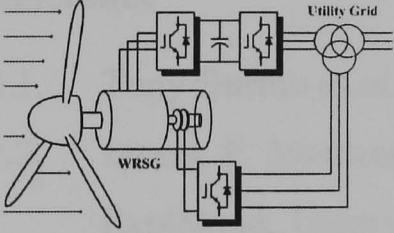
2.5 Application of Doubly-Fed Induction Generators to Wind Turbines

As mentioned previously, doubly-fed induction generators (DFIGs) require lower converter rating than other generator configurations. This is one of the benefits of using the DFIGs in wind power generation. As discussed in [2.12], the DFIG configurations use standard components which make this system relatively cheap compared to competitors, the wound rotor synchronous generators or permanent magnet synchronous generators.

2.6 Summary

As renewable energy becomes increasingly important, due to the fossil fuel and the pollution crises, wind energy becomes one of the effective and interesting energy sources since it is available almost everywhere and clean. Horizontal axis wind turbines have become the most well-known converters to extract wind energy and convert to electrical energy form. Several types of wind turbine have been designed and commercially used. Variable-speed wind turbines are widely used because they have the capability of extracting the maximum available power at any wind speed. Moreover, they also reduce the stress on the turbine tower. Several types of generator have been commercially used with variable-speed wind turbines, but only doubly-fed induction generators and wound rotor synchronous generators are commercially successful. However, comparing the two types, using the doubly-fed induction generator provides more benefit than using the wound rotor synchronous generator because the component used for this generator are standard ones and can be easily found in the market.

Reference

2.1. Tony Burton *et al.*, 'Wind Energy Handbook'. John Wiley & Sons Ltd, 2001

2.2. James. F. Manwell, Jon G. McGowan and Anthony L Rogers, 'Wind Energy Explained, Theory Design and Application'. John Wiley & Sons Ltd, 2002

2.3. http://www.windpower.org

2.4. G. L. Johnson, 'Wind Energy System'. Manhattan, KS, 2001

2.5. H. Polinder *et al.*, 'Basic Operation Principles and Electrical Conversion Systems of Wind Turbines'. EPE Journal, Vol.15 No.4, December 2005, pp. 43-50

2.6. L. H. Hansen *et al.*, 'Conceptual Survey of Generators and Power Electronics for Wind Turbines'. Report of Riso National Laboratory, Roskilde, Denmark, December 2001.

2.7. F. Blaabjerg *et al.*, 'Power Electronics and Control of Renewable Energy Systems'. Plenary Lectures in the 7th International Conference on Power Electronics and Drives Systems, 2007

2.8. J. M. Carrasco *et al.*, 'Power-Electronic Systems for the Grid Integration of Renewable Energy Sources: A Survey'. IEEE Trans. on Industrial Electronics, Vol. 53, No.4, August 2006, pp. 1002-1016.

2.9. J. Marques *et al.*, 'A Survey on Variable-Speed Wind Turbine System'. Congresso Brasileiro de Eletrˆonica de Potˆencia (COBEP), 2003, Fortaleza – CE.

2.10. S. Soter and R. Wegener, 'Development of Induction Machines in Wind Power Technology'. Proceeding of IEEE International Electric Machines & Drives Conference, 2007, pp. 1490-1495.

2.11. P. Mutschler and R. Hoffmann, 'Comparison of Wind Turbines Regarding their Energy Generation'. Proceeding of 33rd IEEE Annual Power Electronics Specialists Conference, 2002, pp. 6-11.

2.12. H. Polinder *et al.*, 'Comparison of Direct-Drive and Geared Generator Concepts for Wind Turbines'. IEEE Trans. on Energy Conversion, Vol. 21, No. 3, September 2006, pp. 725-733.

2.13. J. G. Slootweg and W. L. Kling, 'Is the Answer Blowing in the Wind'. IEEE Power & Energy Magazine, 2003, pp. 26-33.

2.14. http://www.vestas.com

2.15. http://www.peeraer.com/zephyros/

2.16. http://www.winwind.fi

2.17. http://www.enercon.de

2.18. http://www.windsofchange.dk

2.19. http://www.gepower.com

2.20. B. Hopfensperger and D. J. Atkinson, 'Doubly-Fed a.c. Machines: Classification and Comparison'. Proceeding of 9th European Conference on Power Electronics and Applications, EPE 2001, pp. P.1-P.17.

2.21. Z. Lubosny, 'Wind Turbine Operation in Electric Power Systems'. Springer-Verleg Berlin Heidelberg, 2003.

2.22. http://www.mathworks.com

2.23. http://www.esru.strath.ac.uk

Chapter Three

Doubly-Fed Induction Generators

This chapter covers the principle and control of a doubly-fed induction generator (DFIG) used with a wind turbine. Most of wind turbines to-date are built with DFIGs. The DFIG is a variable-speed generator which requires a converter having a rating which is a fraction of the generator rating. This is one of the advantages of the DFIG over other variable-speed generators which require full rating converters. The chapter begins with an introduction to the doubly-fed induction generator. A detailed mathematical model is then discussed to illustrate the physical behaviour of the DFIG. The chapter includes a review of the control methods for both machine-side and grid-side converters and a discussion of the control methods used in this thesis.

3.1 Introduction to the Doubly-Fed Induction Generator

A DFIG consists of a wound rotor induction machine (WRIM) having its stator directly connected to the grid and its rotor connected to the grid via back-to-back converters, a three-phase filter and usually a three-phase transformer. The connection diagram of the DFIG is shown in figure 3.1. The WRIM is controlled by the machine-side converter to operate as a variable speed constant frequency generator whereas the grid-side converter operates as the power conditioner to control the active and reactive power of the rotor.
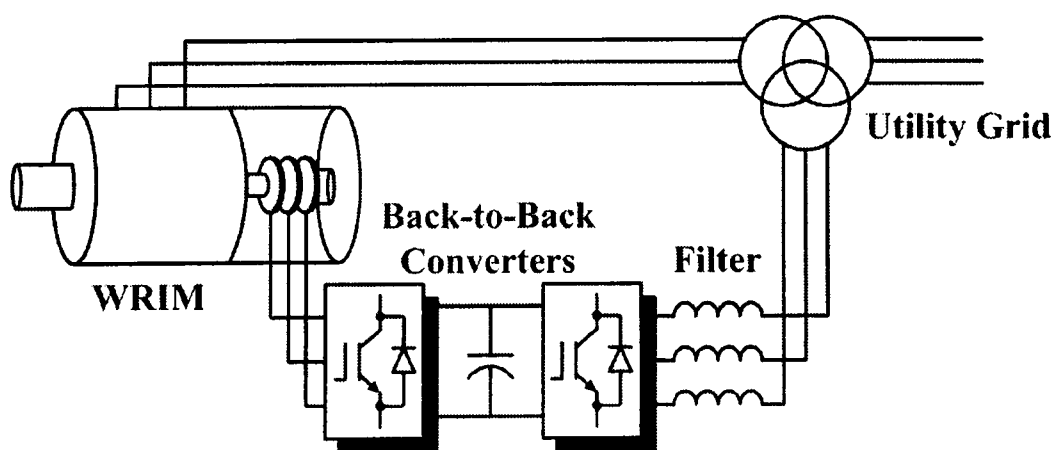
Figure 3.1 The connection diagram of a doubly-fed induction generator

As discussed in many textbooks on electrical machines, the rotor voltages as a function of the induction machine speed is still valid for the DFIG. Slip for the induction machine is defined as follows,

$$s = \frac{n_s - n_r}{n_s},$$

(3.1)

where n_s and n_r are the synchronous speed and rotor speed in rpm respectively. However, unlike the squirrel cage induction machine, the stator-rotor turns ratio must be taken into account for the WRIM. Therefore the rotor voltage u_r, stator voltage u_s and machine slip s are related as follows,

$$u_r = \frac{N_r}{N_s} su_s,$$

(3.2)

where N_s and N_r are the effective number of turns of the stator and rotor windings respectively, per phase.

Similar to a wound rotor synchronous generator, the DFIG is a rotor controlled generator. However, instead of controlling only stator power factor at synchronous speed, the DFIG can operate as a synchronous generator over a range of speeds depending on the rating of the rotor supply. Generally, for wind turbine applications the speed range is limited to approximately 33% [3.1] above and below synchronous speed. The generator can therefore operate at sub-synchronous speeds, synchronous speed and super-synchronous speeds. With the assumption that the system is lossless, for sub-synchronous speed generation, power is delivered from the stator but the rotor consumes power. For synchronous speed generation, the rotor frequency is zero; therefore, rotor currents are dc and the total rotor power is zero. The DFIG delivers power only from stator. For super-synchronous speed generation both stator and rotor deliver power to the grid. A wind turbine with a DFIG can use this benefit during high wind speed operation. This is one of the advantages of the DFIG over other variable speed generators [3.2]. The power flow diagram for these operations with the assumption that the system is lossless is presented in figure 3.2.

(a)

(b)

(c)
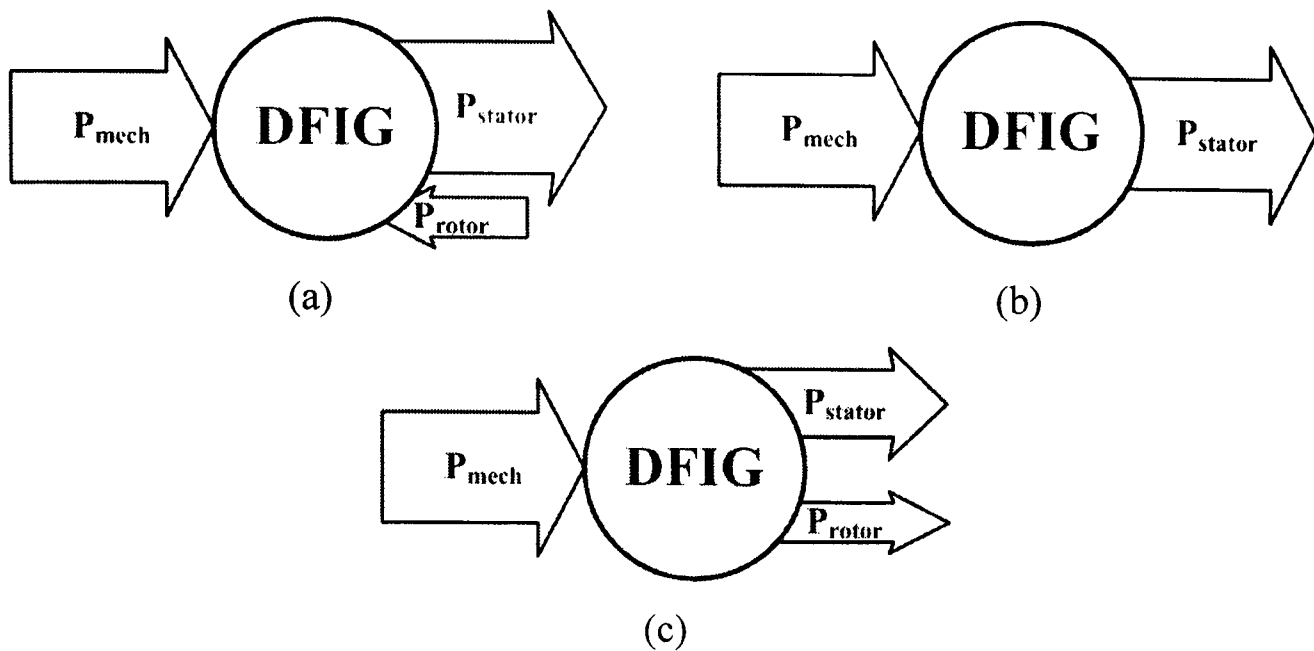
Figure 3.2 Power flow diagram of a doubly-fed induction generator under different operating region (a) sub-synchronous speed generation, (b) synchronous speed generation (c) super-synchronous speed generation

Assuming that the converter is lossless, the rotor power P_r is equal to converter power P_{conv}. As shown in figure 3.2, the total electrical power flowing to the grid is the sum of the power from the stator and the power from the rotor as follows,

$$P_{total} = P_s + P_{conv},$$ (3.3)

whereas the relationship between the stator power and the rotor power is

$$P_r = -sP_s,$$ (3.4)

where s is the per-unit slip.

This equation shows that the rotor power is a linear function of the generator slip. Due to the power-speed variation shown in figure 3.2, the DFIG has an advantage over the singly-fed induction generator. As explained, the DFIG operates above, below or at synchronous speed; therefore, the range of output power can be controlled by using converters having ratings of half of the power span dictated by the desired speed range [3.3] as shown in figure 3.3.
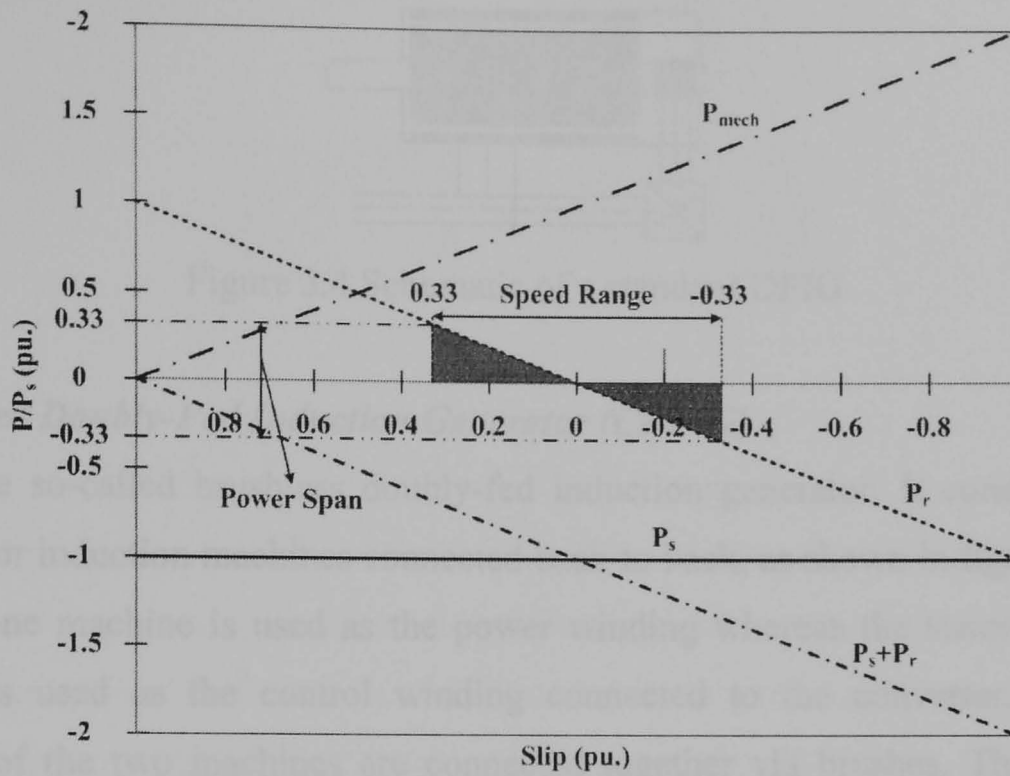
Figure 3.3 Power-speed relationship of a lossless DFIG under constant torque

This figure shows the advantage of the DFIG over the singly-fed induction generator with a fully rated converter. The converter used for the rotor can be any bi-directional converter e.g. matrix converter [3.4-3.7], cyclo-converter [3.8-3.11], current source converters [3.9, 3.10], or PWM voltage-source back-to-back converters. Only the latter are considered and used in this thesis.

3.1.1 Classification of Doubly-Fed Induction Generators

Doubly-fed induction generators can be classified into two groups - brushed type and brushless type. The brushless type can also be separated into different subgroups, depending on their construction [3.3].

i. Standard Doubly-Fed Induction Generator (SDFIG)

The standard DFIG is normally a wound rotor induction machine. This machine has a rotor winding wound like the stator and connected to slip rings. This winding can be connected in either star or delta depending on applications. The rotor is connected to the external circuit via carbon brushes on the slip rings. A schematic diagram of this generator is shown in figure 3.4. The main drawback of this type is the maintenance required for the brushes and slip rings. This is the type of generator that is used in this research.
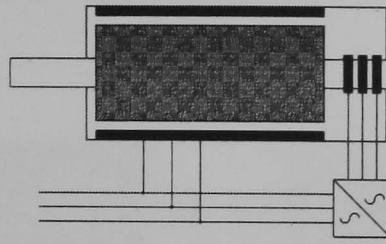
Figure 3.4 Schematic of a standard DFIG

ii. Cascaded Doubly-Fed Induction Generator (CDFIG)

This is the so-called brushless doubly-fed induction generator. It consists of two wound rotor induction machines connected back-to back, as shown in figure 3.5. The stator of one machine is used as the power winding whereas the stator of another machine is used as the control winding connected to the converter. The rotor windings of the two machines are connected together via brushes. The machines have both mechanical coupling and electrical coupling, as shown in figure 3.5. The connection of the rotor windings can be positive sequence or negative sequence, resulting in addition or subtraction of the torques of two machines. The positive phase sequence is made by connecting the same phases of each rotor winding together, whereas the negative phase sequence is achieved by swapping two phases. Positive phase sequence is the normal connection but negative phase sequence is applied for academic purposes. The synchronous speed of the cascaded DFIG can be calculated as follows [3.3],

$$n_r = \frac{60 \cdot \left(f_p + f_c\right)}{P_p + P_c}$$

(3.5)

where f_p and P_p are the frequency and number of pole pairs of the power machine and f_c and P_c are the frequency and the number of pole pairs of the control machine. Therefore, for zero frequency at the control winding, the generator operates with a cascaded synchronous speed as follows,

$$n_r = \frac{60 \cdot f_p}{P_p + P_c}.$$

(3.6)

This topology has greater losses than the standard DFIG because of losses in four windings.
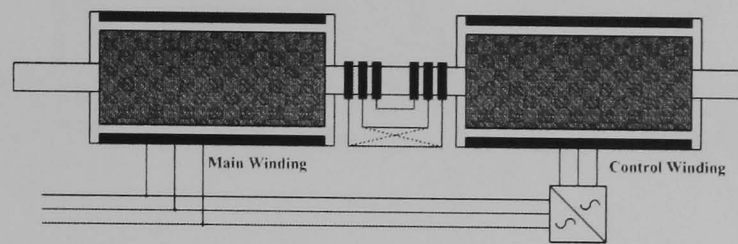
Figure 3.5 Schematic of a cascaded DFIG

iii. Single Frame Cascaded Doubly-Fed Induction Generator (SF-CDFIG)

Instead of having two separated machines, this generator is built in a single frame, which improves mechanical robustness. It has been used in Germany and it is manufactured up to 250 kW as a self-synchronous drive [3.3]. However, it suffers from the same loss problem as the cascaded DFIG. This generator is also called the twin stator generator [3.12]. A schematic of this generator is shown in figure 3.6.
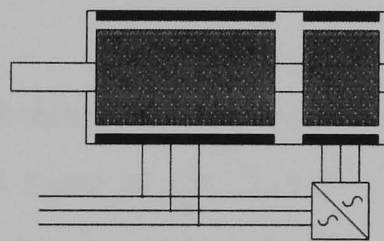
Figure 3.6 Schematic of a self-cascaded DFIG

iv. Brushless Doubly-Fed Induction Generator (BDFIG)

This type is a compact version of the brushless DFIG. The principle of operation is same as its ancestor, the CDFIG. However, the main winding and the control winding are placed in the same slots in the stator which makes the frame size bigger than a cage rotor machine with the same power rating. The rotor of this generator is a cage type with a special design. Different rotor structures have been designed and tested [3.13]. The main idea is to make the identical number of poles called nests as shown in figure 3.7. The number of rotor poles must be equal to the sum of the number of stator poles of both the stator windings, to couple the air-gap field from both [3.14]. The stator windings of this generator require different numbers of pole pairs to avoid direct transformer coupling and the difference in the number of pole pairs must be more than one to avoid magnetic pull on the rotor [3.3, 3.14].
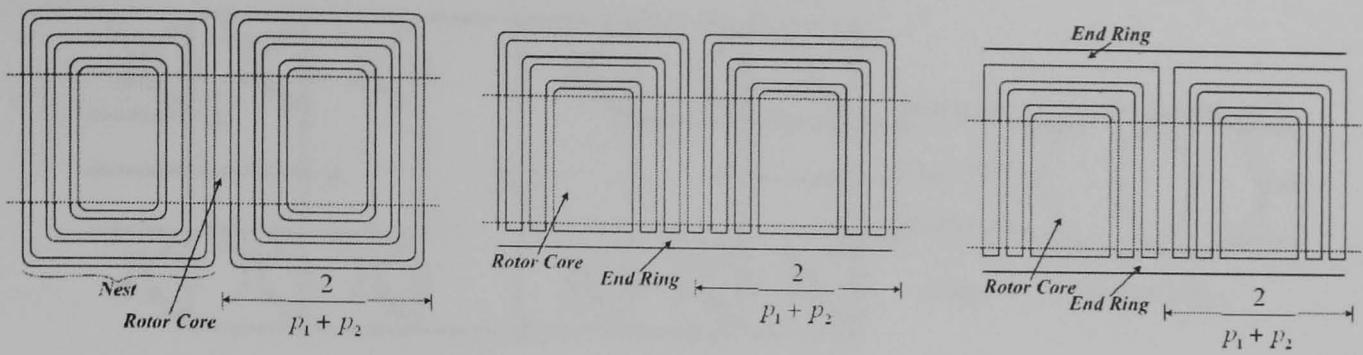
Figure 3.7 Variant nested loop rotor design for a BDFM [3.13]

A schematic of this generator is shown in figure 3.8.
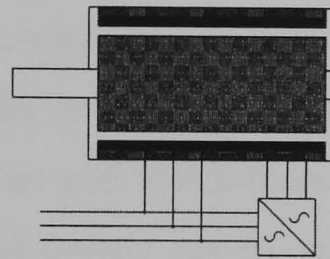
Figure 3.8 Schematic of a BDFIG

v. Brushless Doubly-Fed Reluctance Generator (BDFRG)

The schematic of this type is same as the BDFIG. It has the same stator winding configuration as the BDFIG, but instead of having a squirrel cage rotor, it has a reluctance rotor as shown in figure 3.9 [3.3]. The advantage of this type of generator is that the model and the control scheme are the same as the standard DFIG [3.3].
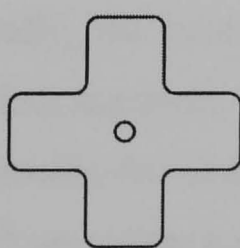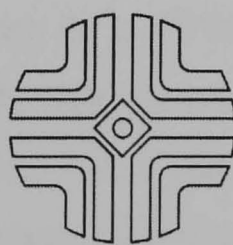
| Simple Salient | With Flux Barriers | Axially Laminated Anisotopic |
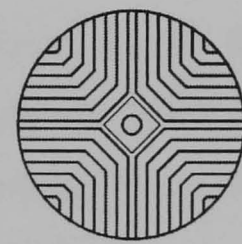
Figure 3.9 Schematic of cross-sectional view of several rotor designs of the BDFRG

3.1.2 Back-to-Back Converters, Three-Phase Filter and Transformer

The rotor converters consist of two PWM voltage source converters connected back-to-back with a dc-link capacitor, as shown in figure 3.10.
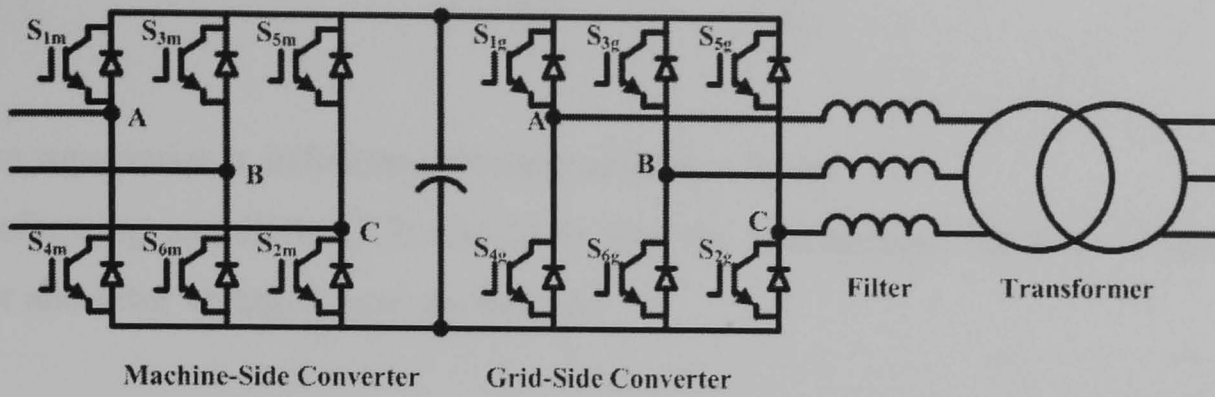
Figure 3.10 The back-to-back converters, three-phase choke and three-phase transformer

The machine-side converter is connected to the rotor of the DFIG and is controlled to achieve the optimised speed to capture the maximum power from the wind, and also to control the power factor of the generator. The grid-side converter is connected to the grid via the three-phase filter and transformer. This converter is controlled to regulate the dc-link voltage and control reactive power. The total reactive power required by the DFIG can be controlled by the combined action of the two converters. Their reactive powers can be controlled independently. The three-phase choke is used to filter the high frequency component from the current before delivering to the grid. The function of the three-phase transformer is to convert the grid voltage to suit the rotor and to limit the required VA rating of the converters in line with the working speed range.

3.2 Equations and Model of a Doubly-Fed Induction Generator

Generally, the model and equations for a DFIG are the same as for the familiar induction machine. This section illustrates the general model and the control model of a doubly-fed induction generator. For a more detailed analysis, the reader can consult any of the textbooks on electrical machines in the references.

3.2.1 General Model

In the stationary reference frame, the voltage equations of the stator and rotor are expressed in space vector form are as follows,

$$\bar{u}_s^s = R_s \bar{i}_s^s + \frac{d\bar{\lambda}_s^s}{dt},$$

$$(3.7)$$

$$\overline{u}_r^s = R_r \overline{i}_r^s + \frac{d\overline{\lambda}_r^s}{dt} - j\omega_r \overline{\lambda}_r^s, \tag{3.8}$$

where superscript *s* indicates stationary reference frame.

Transforming equations (3.7) and (3.8) into the synchronous reference frame, the stator and rotor voltage equations become

$$\overline{u}_s^e = R_s \overline{i}_s^e + \frac{d\overline{\lambda}_s^e}{dt} + j\omega_e \overline{\lambda}_s^e, \tag{3.9}$$

$$\overline{u}_r^e = R_r \overline{i}_r^e + \frac{d\overline{\lambda}_r^e}{dt} + j(\omega_e - \omega_r)\overline{\lambda}_r^e, \tag{3.10}$$

where superscript *e* indicates synchronous reference frame.

The stator and rotor flux linkage in equations (3.9) and (3.10) respectively can be expressed in terms of currents and inductances as follows,

$$\overline{\lambda}_s^e = L_s \overline{i}_s^e + L_m \overline{i}_r^e, \tag{3.11}$$

$$\overline{\lambda}_r^e = L_r \overline{i}_r^e + L_m \overline{i}_s^e, \tag{3.12}$$

where L_s, L_r and L_m are stator inductance, rotor inductance and magnetising inductance respectively.

The term $L_s \overline{i}_s^e$ and $L_m \overline{i}_s^e$ are stator flux linkage and mutual flux linkage produced by stator current, whereas the term $L_r \overline{i}_r^e$ and $L_m \overline{i}_r^e$ are the rotor flux linkage and mutual flux linkage produced by rotor current. The terms $L_s \overline{i}_s^e$ and $L_r \overline{i}_r^e$ can also be separated into leakage flux linkages $L_{sl} \overline{i}_s^e$ and $L_{rl} \overline{i}_r^e$ and magnetising flux linkages $L_m \overline{i}_s^e$ and $L_m \overline{i}_r^e$ respectively. The voltage equations in terms of inductances and currents can be derived from equations (3.9), (3.10), (3.11) and (3.12) as follows,

$$\overline{u}_s^e = R_s \overline{i}_s^e + \frac{d(L_s \overline{i}_s^e)}{dt} + \frac{d(L_m \overline{i}_r^e)}{dt} + j\omega_e(L_s \overline{i}_s^e + L_m \overline{i}_r^e), \tag{3.13}$$

$$\overline{u}_r^e = R_r \overline{i}_r^e + \frac{d(L_r \overline{i}_r^e)}{dt} + \frac{d(L_m \overline{i}_s^e)}{dt} + j(\omega_e - \omega_r)(L_r \overline{i}_r^e + L_m \overline{i}_s^e). \tag{3.14}$$

These space vector equations can be written in matrix form as follows,

$$\begin{bmatrix} \bar{u}_s^e \\ \bar{u}_r^e \end{bmatrix} = \begin{bmatrix} R_s & 0 \\ 0 & R_r \end{bmatrix}\begin{bmatrix} \bar{i}_s^e \\ \bar{i}_r^e \end{bmatrix} + \frac{d}{dt}\begin{bmatrix} L_s & L_m \\ L_m & L_r \end{bmatrix}\begin{bmatrix} \bar{i}_s^e \\ \bar{i}_r^e \end{bmatrix} + j\omega_e\begin{bmatrix} L_s & L_m \\ L_m & L_r \end{bmatrix}\begin{bmatrix} \bar{i}_s^e \\ \bar{i}_r^e \end{bmatrix}$$
$$- j\omega_r\begin{bmatrix} 0 & 0 \\ L_m & L_r \end{bmatrix}\begin{bmatrix} \bar{i}_s^e \\ \bar{i}_r^e \end{bmatrix}$$

(3.15)

This voltage equation consists of ohmic losses, transformer voltage, speed voltage due to rotation of the reference frame and the true speed voltage due to rotation of the rotor. Only the last term, $-j\omega_r\bar{\lambda}_r^e = -j\omega_r(L_r\bar{i}_r^e + L_m\bar{i}_s^e)$, contributes to the electro-mechanical energy conversion. The equivalent circuit for the space vector voltage equations is shown in figure 3.11.
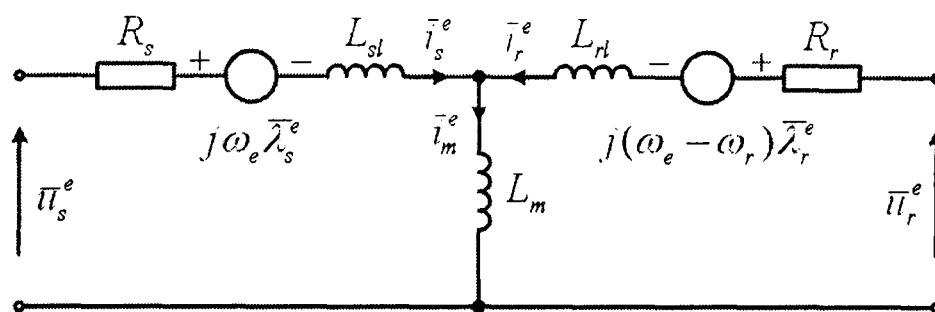
Figure 3.11 The dynamic equivalent circuit of the DFIG

Equation (3.15) can also be split into real and imaginary parts lying on direct-axis (d-axis) and quadrature-axis (q-axis). The equation can be written in matrix form for the sake of computer modelling as follows,

$$\begin{bmatrix} u_{sd} \\ u_{sq} \\ u_{rd} \\ u_{rq} \end{bmatrix} = \begin{bmatrix} R_s + pL_s & -\omega_e L_s & pL_m & -\omega_e L_s \\ \omega_e L_s & R_s + pL_s & -\omega_e L_s & pL_m \\ pL_m & -(\omega_e - \omega_r)L_m & R_r + pL_r & -(\omega_e - \omega_r)L_r \\ (\omega_e - \omega_r)L_m & pL_m & (\omega_e - \omega_r)L_r & R_r + pL_r \end{bmatrix}\begin{bmatrix} i_{sd} \\ i_{sq} \\ i_{rd} \\ i_{rq} \end{bmatrix}$$

(3.16)

From this point, words stator flux and rotor flux will be used to represent stator flux linkage and rotor flux linkage respectively for the sake of simplicity.

3.2.2 Control Model

Generally, the DFIG is controlled by stator-flux vector control or grid-flux vector control. This is similar to the case of rotor-flux vector control for the stator-fed

induction machine. Rotor-flux vector control is also possible, but its implementation is more complicated than stator-flux vector control due to the complexity of the rotor voltage equation. This is the same reason as with stator-flux vector control for the stator-fed induction machine [3.9, 3.10]

For grid-flux vector control, the virtual grid flux can be artificially calculated from

$$\overline{\lambda}_g^s = \frac{\overline{u}_s^s}{j\omega_g}, \tag{3.17}$$

where $\overline{\lambda}_g^s$ and ω_g are the grid flux vector and grid flux angular velocity respectively.

This method ignores stator resistance, and in large machines the voltage drop across the stator resistance is negligibly small compared with the stator voltage. This method can be adopted from the stator-flux vector control method.

In the case of stator-flux vector control, the reference frame used is fixed to stator flux, which can be estimated from

$$\overline{\lambda}_s^s = \int \left(\overline{u}_s^s - R_s \overline{i}_s^s \right) dt, \tag{3.18}$$

Considering the stator flux vector in a stationary reference frame, the stator flux vector can be expressed as

$$\overline{\lambda}_s^s = \lambda_{s\alpha} + j\lambda_{s\beta} = \left| \overline{\lambda}_s^s \right| e^{j\mu}, \tag{3.19}$$

where μ is the angle between stationary reference frame and the stator flux vector. The vector of the stator flux is aligned with the d-axis of the stator flux reference frame. This vector is rotating in space with velocity

$$\omega_{\lambda s} = \frac{d\mu}{dt}, \tag{3.20}$$

in the counter-clockwise direction. The stator flux vector in its own reference frame becomes

$$\overline{\lambda}_s^{\lambda s} = \overline{\lambda}_s^s e^{-j\mu} = \lambda_{sd} + j\lambda_{sq} .$$

(3.21)

When substituting equation (3.19) into equation (3.21), the stator flux becomes

$$\overline{\lambda}_s^{\lambda s} = \left|\overline{\lambda}_s^s\right| e^{j\mu} e^{-j\mu} = \lambda_{sd} + j0 = \left|\overline{\lambda}_s^s\right| .$$

(3.22)

This equation shows that in the stator flux reference frame, only the d-axis component of the stator flux exists, which is equal to the modulus of the stator flux space vector, as shown in figure 3.12.

Figure 3.12 The stator flux vector diagram

The stator flux can be written in terms of the three-phase magnetising inductance and the so-called stator magnetising current as follows,

$$\overline{i}_{ms}^{\lambda s} = \frac{L_s}{L_m}\overline{i}_s^{\lambda s} + \overline{i}_r^{\lambda s} .$$

(3.23)

From equation (3.23), $\dfrac{L_s}{L_m} = 1 + \sigma_s$, where σ_s is the stator leakage factor calculated

from $\sigma_s = \dfrac{L_{ls}}{L_m}$. Further detail on this concept is presented [3.8-3.10]. Therefore, the

stator magnetising current can be written as

$$\overline{i}_{ms}^{\lambda s} = \left(1 + \sigma_s\right)\overline{i}_s^{\lambda s} + \overline{i}_r^{\lambda s} .$$

(3.24)

43

Since only the d-axis component of the stator magnetising current exists, the stator current space vector in the stator flux reference frame can be calculated by equation (3.25),

$$\bar{i}_s^{\lambda s} = \frac{L_m}{L_s}\left(\left|\bar{i}_{ms}^{\lambda s}\right| - \bar{i}_r^{\lambda s}\right),$$

(3.25)

which can be split into d-axis and q-axis component as follows,

$$i_{sd} = \frac{L_m}{L_s}\left(\left|\bar{i}_{ms}^{\lambda s}\right| - i_{rd}\right),$$

(3.26)

$$i_{sq} = -\frac{L_m}{L_s}i_{rq}.$$

(3.27)

i. Voltage Equation of a DFIG

Referring to equation (3.13), the stator voltage equation in terms of the inductance and current in stator flux reference frame is

$$\bar{u}_s^{\lambda s} = R_s\bar{i}_s^{\lambda s} + L_s\frac{d\bar{i}_s^{\lambda s}}{dt} + L_m\frac{d\bar{i}_r^{\lambda s}}{dt} + j\omega_{\lambda s}L_s\bar{i}_s^{\lambda s} + j\omega_{\lambda s}L_m\bar{i}_r^{\lambda s}.$$

(3.28)

From the stator current calculated in equation (3.25) and substituting into equation (3.28), the stator voltage equation in the stator flux reference frame is

$$\bar{u}_s^{\lambda s} = \frac{R_s}{(1+\sigma_s)}\left(\left|\bar{i}_{ms}^{\lambda s}\right| - \bar{i}_r^{\lambda s}\right) + L_m\frac{d\left|\bar{i}_{ms}^{\lambda s}\right|}{dt} + j\omega_{\lambda s}L_m\left|\bar{i}_{ms}^{\lambda s}\right|.$$

(3.29)

Rewriting equation (3.29) in first-order differential equation form, the equation becomes

$$\tau_s\frac{d\left|\bar{i}_{ms}^{\lambda s}\right|}{dt} + \left|\bar{i}_{ms}^{\lambda s}\right|\left(1 + j\omega_{\lambda s}\tau_s\left|\bar{i}_{ms}^{\lambda s}\right|\right) = \frac{(1+\sigma_s)}{R_s}\bar{u}_s^{\lambda s} + \bar{i}_r^{\lambda s},$$

(3.30)

where $\tau_s = \frac{L_s}{R_s}$ is the stator time constant and σ_s is the stator leakage factor.

Since the stator flux amplitude is constant, separating equation (3.30) into d-axis and q-axis equation yields:

$$\tau_s \frac{d\left|\bar{i}_{ms}^{\lambda s}\right|}{dt} + \left|\bar{i}_{ms}^{\lambda s}\right| = \frac{(1+\sigma_s)}{R_s} u_{sd} + i_{rd},$$

(3.31)

$$\tau_s \omega_{\lambda s} \left|\bar{i}_{ms}^{\lambda s}\right| = \frac{(1+\sigma_s)}{R_s} u_{sq} + i_{rq}.$$

(3.32)

From equation (3.14), the rotor voltage equation of the DFIG in the stator flux reference frame is

$$\bar{u}_r^{\lambda s} = R_r \bar{i}_r^{\lambda s} + L_r \frac{d\bar{i}_r^{\lambda s}}{dt} + L_m \frac{d\bar{i}_s^{\lambda s}}{dt} + j(\omega_{\lambda s} - \omega_r)L_r \bar{i}_r^{\lambda s} + j(\omega_{\lambda s} - \omega_r)L_m \bar{i}_s^{\lambda s}.$$

(3.33)

The rotor voltage in terms of rotor current and stator magnetising current can be derived by substituting equation (3.25) into equation (3.33) resulting in

$$\bar{u}_r^{\lambda s} = R_r \bar{i}_r^{\lambda s} + \sigma L_r \frac{d\bar{i}_r^{\lambda s}}{dt} + L_r(1-\sigma)\frac{d\left|\bar{i}_{ms}^{\lambda s}\right|}{dt} + j\omega_{sl}\sigma L_r \bar{i}_r^{\lambda s} + j\omega_{sl}L_r(1-\sigma)\left|\bar{i}_{ms}^{\lambda s}\right|,$$

(3.34)

where σ is the total leakage factor calculated from $\sigma = 1 - \dfrac{L_m^2}{L_s L_r}$ and ω_{sl} is the slip

angular frequency.

Rewriting equation (3.34) in first-order differential form, the equation is

$$\sigma \tau_r \frac{d\bar{i}_r^{\lambda s}}{dt} + \bar{i}_r^{\lambda s} = \frac{\bar{u}_r^{\lambda s}}{R_r} - \tau_r(1-\sigma)\frac{d\left|\bar{i}_{ms}^{\lambda s}\right|}{dt} - j(1-\sigma)\tau_r\omega_{sl}\left|\bar{i}_{ms}^{\lambda s}\right| - j\sigma\tau_r\omega_{sl}\bar{i}_r^{\lambda s},$$

(3.35)

where $\tau_r = \dfrac{L_r}{R_r}$ is the rotor time constant.

Since the amplitude of stator magnetising current is constant, the derivative of $\left|\bar{i}_{ms}^{\lambda s}\right|$ is

zero. Equation (3.35) can be separated into d-axis and q-axis equations as follows,

$$\sigma\tau_r \frac{di_{rd}}{dt} + i_{rd} = \frac{u_{rd}}{R_r} + \sigma\tau_r\omega_{sl}i_{rq} \,, \tag{3.36}$$

$$\sigma\tau_r \frac{di_{rq}}{dt} + i_{rq} = \frac{u_{rq}}{R_r} - (1-\sigma)\tau_r\omega_{sl}\left|\overline{i}_{ms}^{\lambda s}\right| - \sigma\tau_r\omega_{sl}i_{rd} \,. \tag{3.37}$$

Following equations (3.36) and (3.37) and multiplying these equations by R_r, there are rotational cross coupling voltage between d-axis and q-axis which are $\sigma L_r\omega_{sl}i_{rq}$ and $-(1-\sigma)L_r\omega_{sl}\left|\overline{i}_{ms}^{\lambda s}\right| - \sigma L_r\omega_{sl}i_{rd}$. These terms can be compensated by adding the negative terms of these coupling voltages which are $-\sigma L_r\omega_{sl}i_{rq}$ and $(1-\sigma)L_r\omega_{sl}\left|\overline{i}_{ms}^{\lambda s}\right| + \sigma L_r\omega_{sl}i_{rd}$ into the outputs of the controller.

ii. Active Power, Reactive Power and Torque Equations of a DFIG

From the general power equation, the stator active and reactive power in stator flux-linkage reference frame can be calculated form dq-axis terminal voltages and currents as follows,

$$P_s = \frac{3}{2}\text{Re}\left(\overline{u}_s^{\lambda s}\overline{i}_s^{\lambda s*}\right) = \frac{3}{2}\left(u_{sd}i_{sd} + u_{sq}i_{sq}\right), \tag{3.38}$$

$$Q_s = \frac{3}{2}\text{Im}\left(\overline{u}_s^{\lambda s}\overline{i}_s^{\lambda s*}\right) = \frac{3}{2}\left(u_{sq}i_{sd} - u_{sd}i_{sq}\right). \tag{3.39}$$

For large machines, the voltage across the stator resistance is negligible, so the stator flux can be estimated from equation (3.17). In this case, the voltage vector is perpendicular to the flux linkage vector therefore, $u_{sd} = 0$ and $u_{sq} = \left|\overline{u}_s^{\lambda s}\right|$. Equations (3.38) and (3.39) become

$$P_s = \frac{3}{2}\left|\overline{u}_s^{\lambda s}\right|i_{sq} \,, \tag{3.40}$$

$$Q_s = \frac{3}{2}\left|\overline{u}_s^{\lambda s}\right|i_{sd} \,. \tag{3.41}$$

Under this assumption, the amplitude of stator voltage is equal to [3.9, 3.10],

$$\left|\bar{u}_s^{\lambda s}\right| = \omega_{\lambda s} L_m \left|\bar{i}_{ms}^{\lambda s}\right|, \tag{3.42}$$

therefore, substituting equations (3.27), (3.26) and (3.42) into (3.40) and (3.41), the stator active and reactive powers in terms of rotor current are

$$P_s = -\frac{3}{2}\omega_{\lambda s}\frac{L_m^2}{L_s}\left|\bar{i}_{ms}^{\lambda s}\right|i_{rq}, \tag{3.43}$$

$$Q_s = \frac{3}{2}\omega_{\lambda s}\frac{L_m^2}{L_s}\left(\left|\bar{i}_{ms}^{\lambda s}\right| - i_{rd}\right). \tag{3.44}$$

An electromagnetic torque equation can be derived from the torque equation in the stator flux reference frame presented in [3.9, 3.10] and the relationship between stator-torque producing current and rotor-torque producing current. The torque equation becomes

$$T_e = \frac{3}{2}P\lambda_{sd}i_{sq} = -\frac{3}{2}P\frac{L_m}{L_s}\lambda_{sd}i_{rq}, \tag{3.45}$$

where P is the number of pole pairs of the generator.

3.3 Equations and Model of the Grid-Side Converter

The equations and model of the grid-side converter depend on the reference frame and control method used for this converter. These can be classified into four types as presented in [3.15] - voltage vector control, direct power control based on voltage vector, virtual grid-flux vector control and direct power control based on virtual grid flux vector. Only voltage vector control is considered and used in this research.

(a)   (b)
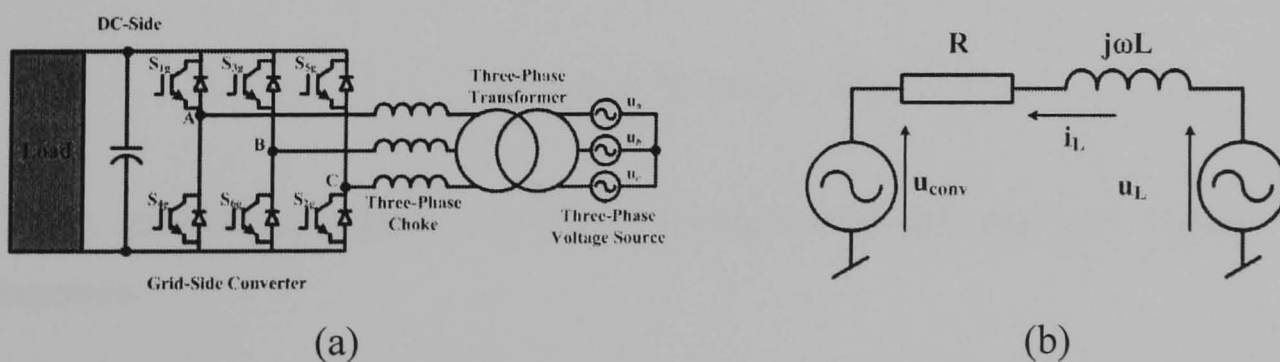
Figure 3.13 (a) The circuit diagram of the grid-side converter and (b) a simplified diagram of the grid-side converter

Referring to figure 3.13, the ac side of the converter is connected to the grid while the dc side is connected to a load or another converter.

3.3.1 Voltage Equation of the Grid-Side Converter

This converter can operate at unity power factor or at leading or lagging power factor. Moreover, this converter topology is capable of operating as a rectifier or an inverter. The voltage equation of the PWM rectifier can be written in vector form as follows,

$$\overline{u}_g^s = R_f \overline{i}_g^s + L_f \frac{d\overline{i}_g^s}{dt} + \overline{v}_{conv}^s . \tag{3.46}$$

Since this system is controlled by voltage vector control, the reference frame used is the reference frame fixed to grid voltage. Considering the grid voltage in stationary reference frame, the grid voltage vector can be expressed as

$$\overline{u}_g^s = u_{g\alpha} + ju_{g\beta} = \left|\overline{u}_g^s\right| e^{j\theta_g} , \tag{3.47}$$

where θ_g is the angle between stationary reference frame and the grid voltage vector. The vector of the grid voltage is aligned with the d-axis of the grid voltage reference frame which rotates at the speed

$$\omega_g = \frac{d\theta_g}{dt} , \tag{3.48}$$

in the counter-clockwise direction. The grid voltage vector in its reference frame becomes

$$\overline{u}_g^g = \overline{u}_g^s e^{-j\theta_g} = u_{gd} + ju_{gq} . \tag{3.49}$$

When substituting equation (3.47) into equation (3.49), the grid voltage vector becomes

$$\overline{u}_g^g = \left|\overline{u}_g^s\right| e^{j\theta_g} e^{-j\theta_g} = u_{gd} + j0 = \left|\overline{u}_g^s\right| . \tag{3.50}$$

This equation shows that only the d-axis component exists in its reference frame and is equal to the modulus of the grid-voltage vector as shown in figure 3.14. Referring to equation (3.46), transforming this equation into the grid voltage reference frame, the voltage equation of the PWM becomes

$$\overline{u}_g^g = R_f \overline{i}_g^g + L_f \frac{d\overline{i}_g^g}{dt} + j\omega_g L_f \overline{i}_g^g + \overline{v}_{conv}^g . \tag{3.51}$$

This equation can be written in the form of a first-order differential equation as follows,

$$\tau_f \frac{d\overline{i}_g^g}{dt} + \overline{i}_g^g = -\frac{\overline{v}_{conv}^g}{R_f} + \frac{\overline{u}_g^g}{R_f} - j\omega_g \tau_f \overline{i}_g^g , \tag{3.52}$$

where $\tau_f = \dfrac{L_f}{R_f}$ is the time constant of the three-phase choke of the PWM rectifier.

Since only the d-axis grid voltage exists in the control reference frame, the q-axis grid voltage will not appear in the equation. Splitting equation (3.52) into d-axis and q-axis components, it becomes

$$\tau_f \frac{di_{gd}}{dt} + i_{gd} = -\frac{v_{convd}}{R_f} + \frac{u_{gd}}{R_f} + \omega_g \tau_f i_{gq} , \tag{3.53}$$

$$\tau_f \frac{di_{gq}}{dt} + i_{gq} = -\frac{v_{convq}}{R_f} - \omega_g L_f i_{gd} . \tag{3.54}$$

As in the case of the machine-side converter control, the cross-coupling voltages between d-axis and q-axis which are $\dfrac{u_{gd}}{R_f} + \omega_g \tau_f i_{gq}$ and $-\omega_g L_f i_{gd}$ respectively must be added to the negative outputs of the controllers to compensate the cross-coupling terms.
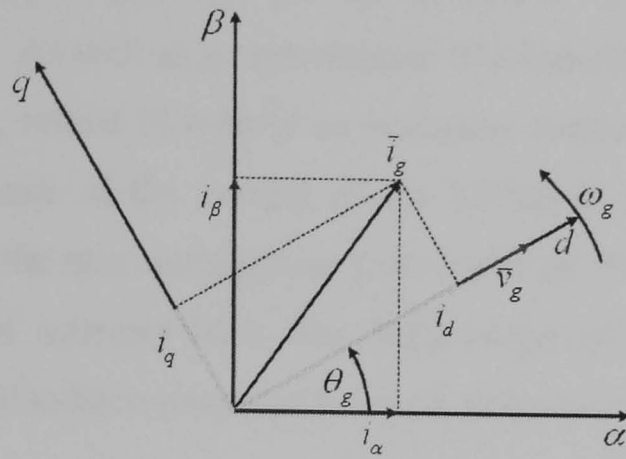
Figure 3.14 Voltage vector diagram for voltage vector control

3.3.2 Active and Reactive Power Equations of the Grid-Side Converter

From the general power equation, the grid-side converter power in grid voltage reference frame can be calculated as follows,

$$P_g = \frac{3}{2} \text{Re}\left(\bar{u}_g^g \bar{i}_g^{g*}\right) = \frac{3}{2}\left(u_{gd}i_{gd} + u_{gq}i_{gq}\right), \tag{3.55}$$

$$Q_g = \frac{3}{2} \text{Im}\left(\bar{u}_g^g \bar{i}_g^{g*}\right) = \frac{3}{2}\left(u_{gq}i_{gd} - u_{gd}i_{gq}\right). \tag{3.56}$$

Since only the d-axis component, which is equal to the modulus of the grid voltage vector, exists in this reference frame, the active and reactive power equations become

$$P_g = \frac{3}{2} u_{gd}i_{gd}, \tag{3.57}$$

$$Q_g = -\frac{3}{2} u_{gd}i_{gq}. \tag{3.58}$$

3.4 Control of an Induction Generator

This section describes the control of the machine-side converter which is used to control the wound rotor induction machine to operate as an induction generator for a wind turbine. Several control methods for each converter are first discussed and then followed by the method used in this research.

Generally, as discussed previously, the rotor currents are controlled by stator-flux vector control [3.8-3.10]. The reference frame used in this control method can be

either stator flux [3.16] or grid flux [3.17]. However, the grid voltage is also a possible choice [3.18]. As well as a conventional PI controller, several sophisticated methods, for example, robust PI control or nonlinear control, have been applied to improve the performance of the control of the DFIGs [3.19-3.21]. However, the objective is to extract the maximum power from the wind. Several direct power and reactive power control schemes have also been proposed [3.22-3.24]. Sensorless control schemes have also been proposed to avoid using rotational transducers [3.25-3.29].

Control of the DFIG is not the main objective of this research, but it is essential to allow the main objectives to be achieved. The next part discusses the process to achieve control of the machine-side converter to drive the wound rotor induction machine as a doubly-fed induction generator based on stator-flux vector control.

3.4.1 Stator Flux Estimation

The first task for this control is to acquire the stator flux vector for use as a reference frame. The stator flux can be estimated by integration of stator EMF in the stationary reference frame as shown in equation (3.18). However, direct integration is unpractical since there may be a dc-offset caused by the measurement offset error, resulting in the integral output saturation. Several alternative methods have been proposed. Pena and co-authors [3.16] used a digital band-pass filter with cut-off frequencies of 0.5Hz and 1Hz to eliminate dc-offset. Holtz [3.30] proposed a feedback low-pass filter to stabilise the integrator and prevent the integrator output from increasing indefinitely. This method requires the complement between the phase shift and the voltage drift level. Another estimator, proposed by Lascu and co-authors [3.31], used the combination of the current model and the voltage model for sensorless motor drive application. This estimator, with some modification, is used to estimate the stator flux for control of the DFIG. Since the rotor current is measurable, stator flux from the current model in a stationary reference frame can be simply calculated from

$$\overline{\lambda}_s^{si} = L_s \overline{i}_s^s + L_m \overline{i}_r^s,$$

(3.59)

where superscript *si* indicates current model in stationary reference frame.

The stator flux linkage in a stationary reference frame is calculated from the voltage model as follows

$$\overline{\lambda}_s^{sv} = \int\left(\overline{u}_s^s - R_s \overline{i}_s^s - \overline{u}_{comp}\right) dt = \int \overline{e}_{s\_comp} dt, \tag{3.60}$$

where and superscript *sv* indicates voltage model in stationary reference frame and $\overline{u}_{comp}$ is a compensation voltage calculated from the output of a PI controller having the difference between the stator flux from the voltage model and the stator flux from the current model.

This variable can be written in equation as follows,

$$\overline{u}_{comp} = K_p\left(\overline{\lambda}_s^{sv} - \overline{\lambda}_s^{si}\right) + K_i \int\left(\overline{\lambda}_s^{sv} - \overline{\lambda}_s^{si}\right) dt. \tag{3.61}$$

The proportional and integral gains can be simply calculated from [3.31]

$$K_p = \omega_1 + \omega_2, \quad K_i = \omega_1 \cdot \omega_2. \tag{3.62}$$

From [3.31], values of ω_1 = 2-5 rad/s and ω_2 = 20-30 rad/s are practical for a smooth transition between the two models. The flux speed can be estimated from [3.11] as follows,

$$\omega_{\lambda s} = \frac{\left(\lambda_{sd}^{sv} e_{s\_compq} - \lambda_{sq}^{sv} e_{s\_compd}\right)}{\left|\lambda_s^{sv}\right|^2}, \tag{3.63}$$

However, to improve the quality or the stator flux and angle, a three-phase phase-locked loop (PLL) is applied to stator-flux vector control. For PLL application, the q-axis stator flux component is fed to the PI controller and the controller output is used as the stator flux angular velocity $\omega_{\lambda s}$ and the integration of $\omega_{\lambda s}$ is the stator flux angle.

3.4.2 Control of the Machine-Side Converter

Once the stator flux in a stationary reference frame and its speed is estimated, the rotor current is oriented to the stator flux reference frame and controlled as shown in

figure 3.15. Referring to equation (3.34), since $\left|\bar{i}_{ms}^{\lambda s}\right|$ is constant this equation can be split into d-axis and q-axis components as follows,

$$u_{rd} = R_r i_{rd} + \sigma L_r \frac{di_{rd}}{dt} - \sigma L_r \omega_{sl} i_{rq},$$ (3.64)

$$u_{rq} = R_r i_{rq} + \sigma L_r \frac{di_{rq}}{dt} + \omega_{sl}\left((1-\sigma)L_r\left|\bar{i}_{ms}^{\lambda s}\right| + \sigma L_r i_{rd}\right).$$ (3.65)

From figure 3.15 and equations (3.64) and (3.65), the outputs of the PI controller of the inner loop of both dq currents v_{rd}' and v_{rq}' are

$$v_{rd}' = R_r i_{rd} + \sigma L_r \frac{di_{rd}}{dt},$$ (3.66)

$$v_{rq}' = R_r i_{rq} + \sigma L_r \frac{di_{rq}}{dt}.$$ (3.67)

As can be seen in equations (3.36) and (3.37), multiplying both equations by rotor resistance R_r, both equations have cross-coupling voltages $\sigma L_r \omega_{sl} i_{rq}$ and $-\omega_{sl}\left((1-\sigma)L_r\left|\bar{i}_{ms}^{\lambda s}\right| + \sigma L_r i_{rd}\right)$ respectively. As shown in figure 3.15, the cross-coupling compensation terms $-\sigma L_r \omega_{sl} i_{rq}$ and $\omega_{sl}\left((1-\sigma)L_r\left|\bar{i}_{ms}^{\lambda s}\right| + \sigma L_r i_{rd}\right)$ are added to equations (3.66) and (3.67) for the output voltage command before transforming to a stationary reference frame for the space vector modulation generator as follows,

$$v_{rd}^* = v_{rd}' - \sigma L_r \omega_{sl} i_{rq},$$ (3.68)

$$v_{rq}^* = v_{rq}' + \omega_{sl}\left((1-\sigma)L_r\left|\bar{i}_{ms}^{\lambda s}\right| + \sigma L_r i_{rd}\right).$$ (3.69)

Figure 3.15 Stator-flux vector control diagram of the machine-side converter

3.5 Control of the Grid-Side Converter

The main operating mode of the grid-side converter is the same as that of a PWM rectifier. Therefore, the equations and control method used for this converter are the same as for the PWM rectifier. Research on modelling and control are aimed at improving the control of the PWM rectifier to operate effectively and efficiently [3.32-3.35]. Several researchers have proposed novel methods and switching schemes to improve performance and simplify the control system [3.36-3.43]. Some strategies were about optimising or reducing the dc-link capacitor size [3.44 -3.46].

As indicated previously, control is not the main objective of this research but it is a necessary subject. This research deals with voltage vector control based on a simple PI controller. The diagram of the control of the grid-side converter is shown in figure 3.16.

Figure 3.16 Grid voltage vector control diagram of the grid-side converter

The voltage vector can be calculated from Clarke's transform $u_{g\alpha}$ and $u_{g\beta}$. These variables are then sent to the PLL to estimate the voltage angle and grid frequency. The equations for the control diagram shown in figure 3.16 can be derived as follows

$$u_{gd} = R_f i_{gd} + L_f \frac{di_{gd}}{dt} - \omega_g L_f i_{gq} + v^*_{convd}, \qquad (3.70)$$

$$u_{gq} = R_f i_{gq} + L_f \frac{di_{gq}}{dt} + \omega_g L_f i_{gd} + v^*_{convq}. \qquad (3.71)$$

The first two terms of these equations can be defined as v'_{gd} and v'_{gq}, thus

$$v'_{gd} = R_f i_{gd} + L_f \frac{di_{gd}}{dt}, \qquad (3.72)$$

$$v'_{gq} = R_f i_{gq} + L_f \frac{di_{gq}}{dt}. \qquad (3.73)$$

As shown in figure 3.15, the compensation voltage to decoupling the d and q axis voltage components, $\omega_g L_f i_{gq} + v_{gd}$ and $-\omega_g L_f i_{gd}$, must be added to the negative output of the PI controller. Therefore, the final voltage outputs of the controller become

$$v_{convd}^{*} = -v_{gd}^{'} + \left(\omega_{g}L_{f}i_{gq} + u_{gd}\right),$$
(3.74)

$$v_{convq}^{*} = -v_{gq}^{'} - \omega_{g}L_{f}i_{gd}.$$
(3.75)

The voltages in equations (3.74) and (3.75) are the command voltage for the switching function module which will be first transformed back to $\alpha - \beta$ form and fed to the switching function module.

3.6 Summary

DFIGs have been widely used in wind turbines as they require lower VA rating converters to control them. They are generally driven by the back-to-back converters connected between the rotor and the grid with direct connection of the stator to the grid. The converter size is half of the power span of the generator. The generator can be classified into brushed and brushless types. The brushes and slip rings are the main disadvantage of the brushed generator and therefore research on brushless DFIGs are ongoing. However, the technology in this field is not mature enough to use commercially. The usual method applied to control the DFIGs is stator-flux vector control, which is analogous to rotor-flux vector control for the stator-fed induction machine. This control can be achieved by the machine-side converter which is connected to the rotor of the generator. Another converter is used to control the power flowing between the rotor and the grid and also used to control the reactive power at the transformer at the grid side. The control method used in this research is voltage vector control. For this converter, it is usually controlled make the power factor at the grid side of the transformer be unity.

Reference

3.1.   S. Müller, M. Deicke, and Rik W. DE Doncker, 'Doubly-Fed Induction Generator Systems for Wind Turbines A Viable Alternative to Adjust Speed Over a Wide Range at Minimal Cost'. IEEE Industry Application Magazine, May/June 2002, pp. 26-33.

3.2.   R. Datta and V. T. Ranganathan, 'Variable-Speed Wind Power Generation Using Doubly Fed Wound Rotor Induction Machine-A Comparison with Alternative Schemes'. IEEE Trans. on Energy Conversion, Vol. 17, No.3, September 2002, pp. 414-421.

3.3.   B. Hopfensperger and D.J. Atkinson, 'Doubly-Fed a.c. Machines: Classification and Comparison'. Proceeding of 9th European Conference on Power Electronics and Applications, EPE 2001, pp. P.1-P.17.

3.4.   L. Zhang and C. Watthanasarn, 'A Matrix Converter Excited Doubly-Fed Induction Machine as a Wind Power Generator'. Proceeding of IEE Power Electronics and Variable Speed Drives, 1998, pp. 532-537.

3.5.   L. Zhang, C. Watthanasarn, and W. Shepherd, 'Application of a Matrix Converter for the Power Control of a Variable-Speed Wind-Turbine Driving a Doubly-Fed Induction Generator'. Proceeding of 23rd IEEE International Conference on Industrial Electronics, Control and Instrumentation, 1997. pp. 906-911.

3.6.   K. Ghdamsi, D. Aouzellag, and E. M. Berkouk, 'Application of Matrix Converter for Variable Speed Wind Turbine Driving a Doubly Fed Induction Generator'. Proceeding of IEEE International Symposium on Power Electronics, Electrical Drives, Automation and Motion, 2006, pp. S3-38 – S3-46.

3.7.   A. K. Dalal, P. Syam, and A. K. Chattopadhyay, 'Use of Matrix Converter as Slip Power Regulator in Doubly-Fed Induction Motor Drive for Improvement of Power Quality'. Proceeding of IEEE Power India Conference, 2006.

3.8.   W. Leonhard, 'Control of Electrical Drives'. Springer Verlag, 2001.

3.9.   P. Vas, 'Vector Control of AC Machines'. Oxford University Press, 1991.

3.10.   P. Vas, 'Sensorless Vector and Direct Torque Control'. Oxford University Press, 1998.

3.11.   B. K. Bose, 'Modern Power Electronics and AC Drives'. Prentice Hall PTR, 2001.

3.12.   J. Rickard, 'Get Ready to Connect (Getting Wind to the Grid)'. IET Power Engineer Journal, Vol. 18, September/October 2008, pp. 30-31.

3.13.   P. C. Roberts, 'A Study of Brushless Doubly-Fed (Induction) Machines'. Ph.D. Dissertation, University of Cambridge, 2004.

3.14.   M. S. Boger *et al.*, 'General Pole Number Model of the Brushless Doubly-Fed Machine'. IEEE Trans. on Energy Conversion, Vol. 31, No.5, September/October 1995, pp. 1022-1028.

3.15.   M. P. Kazmierkowski *et al.*, 'Control in Power Electronics, Selected Problems'. Academic Press, 2002.

3.16.   R. Pena, J. C. Clare, and G. M. Asher, 'Doubly-Fed Induction Generator Using Back-to-Back PWM Converters and Its Application to Variable Speed Wind-Energy Generation'. IEE Proceeding of Electric Power Applications, Vol. 143, No. 5, 1996, pp. 380-387.

3.17.   D. J. Atkinson, B. Hopfensperger, and R.A. Lakin, 'Field Oriented Control of a Doubly-Fed Induction Machine using Coupled Microcontrollers'. Proceeding of 8th European Conference on Power Electronics and Applications, 1999, pp. P.1-P.10.

3.18.   T. K. A. Brekken and Ned Mohan, 'Control of Doubly Fed Induction Wind Generator Under Unbalanced Grid Voltage Conditions'. IEEE Trans. on Energy Conversion, Vol. 22, No. 1, March 2007, pp. 129-135.

3.19.   Carles Batlle, Arnau Doria-Cerezo and Romeo Ortega 'A Robustly Stable PI Controller for the Doubly-Fed Induction Machine'. Proceeding of 32nd Annual Conference on IEEE Industrial Electronics, 2006, pp. 5113-5118.

3.20.   S. Drid, M. Tadjine, and M.-S. Naït-Saïd, 'Robust Backstepping Vector Control for the Doubly Fed Induction Motor'. Proceeding of IET Control Theory Application, 2007, pp. 861-868.

3.21.   N. P. Quang, A. Dittrich, and P. N. Lan, 'Doubly-Fed Induction Machines as Generator in Wind Power Plant: Nonlinear Control Algorithms with Direct Decoupling'. Proceeding of 11th European Conference on Power Electronics and Applications, 2005, pp. P.1-P.9.

3.22.   L. Xu and P. Cartwright, 'Direct Active and Reactive Power Control of DFIG for Wind Energy Generation'. IEEE Trans. on Energy Conversion, Vol.21, No.3, September 2006, pp. 750-758.

3.23. D. Zhi and L. Xu, 'Direct Power Control of DFIG with Constant Switching Frequency and Improved Transient Performance'. IEEE Trans. on Energy Conversion, Vol. 22, No. 1, March 2007, pp. 110-118.

3.24. M. Kayikci and J. V. Milanovic, 'Reactive Power Control Strategies for DFIG-Based Plants'. IEEE Trans. on Energy Conversion, Vol. 22, No. 2, June 2007, pp. 389-396.

3.25. R. Datta and V. T. Ranganathan, 'A Simple Position-Sensorless Algorithm for Rotor-Side Field Oriented Control of Wound-Rotor Induction Machine'. IEEE Trans. on Industrial Electronics, Vol. 48, No. 4, August 2001, pp. 786-793.

3.26. U. Rädel *et al.*, 'Sensorless Field-Oriented Control of a Slipring Induction Generator for a 2.5 MW Wind Power Plant from Nordex Energy GmbH'. Proceeding of 9th European Conference on Power Electronics and Applications, EPE 2001, pp. P.1-P.7.

3.27. S. Arnalte and J. L. Rodriguez-Amenedo, 'Sensorless Direct Power Control of a Doubloy-Fed Induction Generator for Variable Speed Wind Turbines'. Proceeding of 10th International Conference on Power Electronics and Motion Control, 2002, pp. P.1-P.6.

3.28. R. Ghosn *et al.*, 'A MRAS-Luenberger Sensorless Speed Control of Doubly Fed Induction Machine'. Proceeding of 10th European Conference on Power Electronics and Applications, 2003, pp. P.1-P.8.

3.29. S. Georges *et al.*, 'A Comparison of Sensorless Speed Estimation for a Doubly Fed Induction Machine'. Proceeding of 11th European Conference on Power Electronics and Applications, 2005, pp. P.1-P.9.

3.30. J. Holtz, 'Sensorless Control of Induction Motor Drives'. Proceeding of the IEEE, Vol. 90, No. 8, August 2002, pp. 1359-1394.

3.31. Cristian Lascu, Ion Boldea, and Frede Blaabjerg, 'A Modified Direct Torque Control for Induction Motor Sensorless Drive'. IEEE Trans. on Industry Application, Vol. 36, No. 1, January/February 2000, pp. 122-130.

3.32. H. Mao, D. Boroyevich, and Fred C. Y. Lee, 'Novel Reduced-Order Small-Signal Model of a Three-Phase PWM Rectifier and Its Application in Control Design System Analysis'. IEEE Trans. on Power Electronics, Vol. 13, No. 3, May 1998, pp. 511-521.

3.33. N. Hur, J. Jung, and K. Nam, 'A Fast Dynamic DC-Link Power-Balancing Scheme for a PWM Converter-Inverter System'. IEEE Trans. on Industrial Electronics, Vol.48, No.4, August 2001, pp. 794-803.

3.34. Y. Ye, M. Kazerani, and Victor H. Quintana, 'Modeling, Control and Implementation of Three-Phase PWM Converters'. IEEE Trans. on Power Electronics, Vol. 18, No.3, May 2003, pp. 857-864.

3.35. Jyoti Sastry, Olorunfemi Ojo, and Zhiqiao Wu, 'High-Performance Control of a Boost AC-DC PWM Rectifier/Induction Generator System'. IEEE Trans. on Industry Applications, Vol. 42, No.5, September/October 2006, pp. 1146-1154.

3.36. M. P. Kazmierkowski and L. Malesani, 'Current Control Techniques for Three-Phase Voltage-Source PWM Converters: A Survey'. IEEE Trans. on Industrial Electronics, Vol.45, No. 5, October 1998, pp. 691-703.

3.37. B. R. Lin and H. H. Lu, 'Three-Phase AC/DC/AC Converter with Random Pulse Position PWM'. Proceeding of 8th European Conference on Power Electronics and Applications, 1999.

3.38. M. P. Kazmierkowski, 'Control Strategies for PWM Rectifier/Inverter-Fed Induction Motors'. Proceedings of the IEEE International Symposium on Industrial Electronics, 2000, Vol. 1, pp. TU15-TU23.

3.39. R. Kennel and A. Linder, 'A Simplified Algorithm for Space Vector Modulation of Three-Phase Voltage Source PWM Rectifier'. Proceeding of 35th Annual IEEE Power Electronics Specialists Conference, 2004, pp. 3665-3670.

3.40. Mariusz Malinowski, Marek Jasin'ski, and Marian P. Kazmierkowski, 'Simple Direct Power Control of Three-Phase PWM Rectifier Using Space-Vector Modulation (DPC-SVM)'. IEEE Trans. on Industrial Electronics, Vol. 51, No. 2, April 2004, pp. 447-454.

3.41. M. Malinowski and M. P. Kazmierkowski, 'DSP Implementation of Adaptive Modulator for Three-Phase PWM Rectifier/Inverter'. Proceeding of 9th International Conference on Power Electronics and Motion Control, 2000, pp. 288-292.

3.42. Marek Jasinski, M. P. Kazmierkowski, and M. Zelechowski, 'Unified Scheme of Direct Power and Torque Control for Space Vector Modulated AC/DC/AC Converter/Fed Induction Motor'. Proceeding of 11th International Conference on Power Electronics and Motion Control 2004.

3.43. Liu Xiao-ming, Wen Ji-bin, and Wang Jian, 'Research for PWM Rectifier Based on Voltage Space-Vector Pulse-Width Modulation'. Proceeding of International Conference on Electrical Machines and Systems, 2007, pp. 133-136.

3.44. A. Carlsson, M. Alaküla, and L. Gertmar, 'On Output Capacitor Size in Boost-Type Power-Converters with Constant Power'. Proceeding of 8th European Conference on Power Electronics and Applications 1999, pp. P.1-P.10.

3.45. M. Winkelnkemper and S. Bernet, 'Design and Optimization of the DC-Link Capacitor of PWM Voltage Source Inverter with Active Front End for Low-Voltage Drives'. Proceeding of 10th European Conference on Power Electronics and Applications 2003, pp. P.1-P.9.

3.46. M. Jasinski, 'Direct Power and Torque Control for AC/DC/AC Converter with Reduced DC-Link Capacitor'. Proceeding of International Conference on Power Electronics and Intelligent Control for Energy Conversion 2005, pp. 1-7.

Chapter Four

System Design, Simulation and Implementation

This chapter describes the design and construction of the simulation and experimental systems for this research. The chapter begins with the design of the system in simulation based on MATLAB/SIMULINK [4.1]. The experimental system is then built to implement control of a doubly-fed induction generator (DFIG), converter fault detection and system reconfiguration, which will be presented in later chapters. The knowledge required for system implementation is discussed in this chapter.

4.1 Operation of a DFIG

This section concentrates on the design of the control systems for DFIG operation. The algorithms and methods presented here are applied to both simulation and experiment. In the simulation, most parts of the model are built using existing SIMULINK blocks, although some of them, especially the code for the space vector modulation (SVM), are written in an m-file s-function for ease of implementation and modification for the main part of this research.

4.1.1 Design of Machine Control

The design of the control system must satisfy the purpose of controlling the DFIG for application with a wind turbine. For machine control, two line-to-line stator voltages, two stator phase currents and two rotor phase currents are measured and then per-unitised by the base values shown appendix A. All measured variables are transformed to two-phase variables in their own reference frame by equation (4.1) for stator voltages and equation (4.2) for both stator and rotor currents, as follows,

$$
\begin{bmatrix} v_{s\alpha} \\ v_{s\beta} \end{bmatrix} = \frac{2}{3} \begin{bmatrix} 1 & \frac{1}{2} \\ 0 & \frac{\sqrt{3}}{2} \end{bmatrix} \begin{bmatrix} v_{sab} \\ v_{sbc} \end{bmatrix},
\tag{4.1}
$$

$$\begin{bmatrix} i_{s\alpha,r\alpha} \\ i_{s\beta,r\beta} \end{bmatrix} = \frac{2}{3} \begin{bmatrix} \dfrac{3}{2} & 0 \\ \dfrac{\sqrt{3}}{2} & \sqrt{3} \end{bmatrix} \begin{bmatrix} i_{sa,ra} \\ i_{sb,rb} \end{bmatrix}. \tag{4.2}$$

The factor $\dfrac{2}{3}$ appears in the transformation matrices due to the used of the non-power-invariant transformation in this research.

i. Stator Flux Estimation

Rotor currents are transformed to a stationary reference fixed to the stator, for the purpose of estimating the stator flux linkage, by inverse Park's transform as follows,

$$\begin{bmatrix} i_{r\alpha}^s \\ i_{r\beta}^s \end{bmatrix} = \begin{bmatrix} \cos\mu & -\sin\mu \\ \sin\mu & \cos\mu \end{bmatrix} \begin{bmatrix} i_{r\alpha} \\ i_{r\beta} \end{bmatrix}. \tag{4.3}$$

Since the system is to be implemented by a DSP, both simulation and experiment are implemented in discrete forms. According to equations (3.59)-(3.63), these equations are simulated and implemented in per-unit discrete forms. First, the stator fluxes calculated by using a current model are

$$\overline{\lambda}_{s\alpha}^{sl} = L_s i_{s\alpha}^s(k) + L_m i_{r\alpha}^s(k), \tag{4.4}$$

$$\overline{\lambda}_{s\beta}^{sl} = L_s i_{s\beta}^s(k) + L_m i_{r\beta}^s(k). \tag{4.5}$$

The stator fluxes in a voltage model are discretised by trapezoidal approximation [4.2] as follows,

$$\overline{\lambda}_{s\alpha}^{sv}(k) = \overline{\lambda}_{s\alpha}^{sv}(k-1) + \frac{T_s}{2}\left(e_{s\alpha}^s(k) + e_{s\alpha}^s(k-1)\right), \tag{4.6}$$

$$\overline{\lambda}_{s\beta}^{sv}(k) = \overline{\lambda}_{s\beta}^{sv}(k-1) + \frac{T_s}{2}\left(e_{s\beta}^s(k) + e_{s\beta}^s(k-1)\right), \tag{4.7}$$

where T_s is the sampling time and $e_{s\alpha}^s$ and $e_{s\beta}^s$ are the stator back emf which can be computed by

$$e^s_{scomp\_\alpha}(k) = u^s_{s\alpha}(k) - R_s i^s_{s\alpha}(k) - u^s_{scomp\_s\alpha}(k), \tag{4.8}$$

$$e^s_{scomp\_\beta}(k) = u^s_{s\beta}(k) - R_s i^s_{s\beta}(k) - u^s_{scomp\_s\beta}(k). \tag{4.9}$$

The compensation voltage $u^s_{scomp\_s\alpha}$ and $u^s_{scomp\_s\beta}$ are calculated by PI control discretised by trapezoidal approximation as follows,

$$u^s_{scomp\_s\alpha}(k) = K_p \left(\lambda^{sv}_{s\alpha}(k) - \lambda^{si}_{s\alpha}(k) \right) + u^s_{comp\_s\alpha i}(k-1), \tag{4.10}$$

$$u^s_{scomp\_s\beta}(k) = K_p \left(\lambda^{sv}_{s\beta}(k) - \lambda^{si}_{s\beta}(k) \right) + u^s_{comp\_s\beta i}(k-1), \tag{4.11}$$

where $u^s_{comp\_s\alpha i}$ and $u^s_{comp\_s\beta i}$ are the integral terms calculated from

$$u^s_{comp\_s\alpha i}(k) = u^s_{comp\_s\alpha i}(k-1) + K_\omega K_i \left(\lambda^{sv}_{s\alpha}(k) - \lambda^{si}_{s\alpha}(k) \right), \tag{4.12}$$

$$u^s_{comp\_s\beta i}(k) = u^s_{comp\_s\beta i}(k-1) + K_\omega K_i \left(\lambda^{sv}_{s\beta}(k) - \lambda^{si}_{s\beta}(k) \right), \tag{4.13}$$

where $K_\omega = \dfrac{1}{\omega_{base}}$. The value of K_p and K_i can be calculated from equation (3.62).

The stator flux angular frequency and its angle are estimated by using a three-phase phase-locked loop (PLL) as shown in figure 4.1.
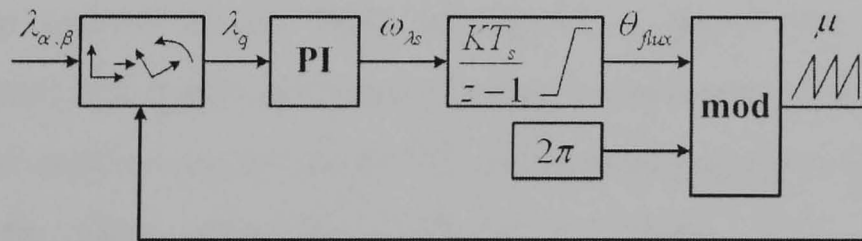
Figure 4.1 Diagram of the PLL applied to the stator flux linkage angular frequency and angle estimation

Generally, only the direct axis (d-axis) stator flux component exists in its own reference frame and no quadrature axis (q-axis) stator flux component exists. The existence of any q-axis stator flux component indicates that there is variation of the stator flux frequency. Therefore, the q-axis component is used as an input for the PLL. The q-axis component is fed to the PI controller, the output of which is the

stator flux angular frequency in pu. This output is then integrated to estimate the angle of the stator flux. The value of the angle is also in pu, where 1 pu is equivalent to 2π radian.

Transforming the stator flux into its own reference frame, only the d-axis component exists. Therefore, the stator magnetising current is

$$i_{ms}(k) = \frac{\lambda_{sd}(k)}{L_m}.$$

(4.14)

This current is used to calculate the compensating voltage which will be discussed in the next subsection.

ii. Loop Control for the Machine-Side Converter (MSC)

Loop control for the MSC can be separated into the inner loop, which is used to control the d-axis and q-axis currents, and the outer loop, which is used to control the speed of the generator. For inner-loop control, all variables are transformed to the stator flux reference frame by Park's transform as follows

$$\begin{bmatrix} i_{sd,rd} \\ i_{sq,rq} \end{bmatrix} = \begin{bmatrix} \cos\theta & \sin\theta \\ -\sin\theta & \cos\theta \end{bmatrix} \begin{bmatrix} i_{s\alpha,r\alpha} \\ i_{s\beta,r\beta} \end{bmatrix},$$

(4.15)

where θ is μ for stator variables and $\mu - \varepsilon$ for rotor variables as shown in figure 3.12.

The inner loop control of the MSC is control of the d-axis (flux-producing) component current and q-axis (torque-producing) component current. Generally the stator active and reactive power can be calculated from equations (3.38) and (3.39). By neglecting the stator resistance, as shown in chapter 3, the stator active and reactive power can be calculated by [4.3-4.5]

$$P_s = -\frac{3}{2}\omega_{\lambda s}\frac{L_m^2}{L_s}\left|\bar{i}_{ms}^{\lambda s}\right|i_{rq},$$

(4.16)

$$Q_s = \frac{3}{2}\omega_{\lambda s}\frac{L_m^2}{L_s}\left|\bar{i}_{ms}^{\lambda s}\right|\left(\left|\bar{i}_{ms}^{\lambda s}\right| - i_{rd}\right),$$

(4.17)

where $\omega_{\lambda s}$ is the angular frequency of the flux.

From equation (3.45), the electromagnetic torque of the generator can be derived from

$$T_e = -\frac{3}{2} P \frac{L_m^2}{L_s} \left| \bar{i}_{ms}^{\lambda s} \right| i_{rq},$$ (4.18)

where P is the number of pole pairs.

Due to implementation in per-unit, the factors of $\frac{3}{2}$ and P are not included. Therefore, the controlled torque, active and reactive powers are

$$T_e = -\frac{L_m^2}{L_s} \left| \bar{i}_{ms}^{\lambda s} \right| i_{rq},$$ (4.19)

$$P_s = -\omega_{\lambda s} \frac{L_m^2}{L_s} \left| \bar{i}_{ms}^{\lambda s} \right| i_{rq},$$ (4.20)

$$Q_s = \omega_{\lambda s} \frac{L_m^2}{L_s} \left| \bar{i}_{ms}^{\lambda s} \right| \left(\left| \bar{i}_{ms}^{\lambda s} \right| - i_{rd} \right).$$ (4.21)

However, equations (4.20) and (4.21) are for the machines having size larger than 10 kW [4.5, 4.6] which their stator resistance can be neglected. In this research, for the sake of simplicity, equation (4.21) is used in d-axis current control loop. During implementation, by assuming that $\left| \bar{i}_{ms}^{\lambda s} \right|$ is constant, the command to the change in reactive power is reduced to d-axis current command.

Two identical PI controllers are used for the d-axis and q-axis currents. The controller outputs are sent to the space vector modulation module. According to equations (3.68) and (3.69), the d-axis and q-axis voltages are

$$v_{rd}^* = \left(R_r i_{rd} + \sigma L_r \frac{di_{rd}}{dt} \right) + \left(-\sigma L_r \omega_{sl} i_{rq} \right),$$ (4.22)

$$v_{rq}^* = \left(R_r i_{rq} + \sigma L_r \frac{di_{rq}}{dt} \right) + \left(\omega_{sl} \left((1-\sigma) L_r \left| \bar{i}_{ms}^{\lambda s} \right| + \sigma L_r i_{rd} \right) \right).$$ (4.23)

The terms in the first parenthesis are the current controller outputs v'_{rd} and v'_{rq} before compensating for the cross coupling terms, as shown in equations (3.66) and (3.67) respectively. The terms in the second parenthesis are the compensation voltages that require to be added into the voltage equations for decoupling between d-axis and q-axis components. The transfer function of the system in the s-domain is

$$\frac{I_{rd}(s)}{U'_{rd}(s)} = \frac{I_{rq}(s)}{U'_{rq}(s)} = H_r(s) = \frac{\frac{K_r}{\tau'_r}}{s + (\frac{1}{\tau'_r})}, \qquad (4.24)$$

where $K_r = \dfrac{1}{R_r}$ and $\tau'_r = \dfrac{\sigma L_r}{R_r}$.

By using a zero-order hold, the discrete-time transfer function of the system in equation (4.24) is

$$H_r(z) = K_r \frac{1 - e^{\left(\frac{-T_s}{\tau'_r}\right)}}{z - e^{\left(\frac{-T_s}{\tau'_r}\right)}}. \qquad (4.25)$$

Likewise, the PI controller in the discrete form can be derived as

$$PI(z) = K_p(K_i T_s + 1)\frac{Z - \frac{1}{(K_i T_s + 1)}}{z - 1}. \qquad (4.26)$$

Referring to equations (4.22) and (4.23), the compensating voltages are added to the outputs of the PI controllers to yield the command voltages for the switching function module to drive the MSC. With knowledge of the plant's transfer function and the controller model, the inner loop control diagram of the MSC can be described as shown in figure 4.2.
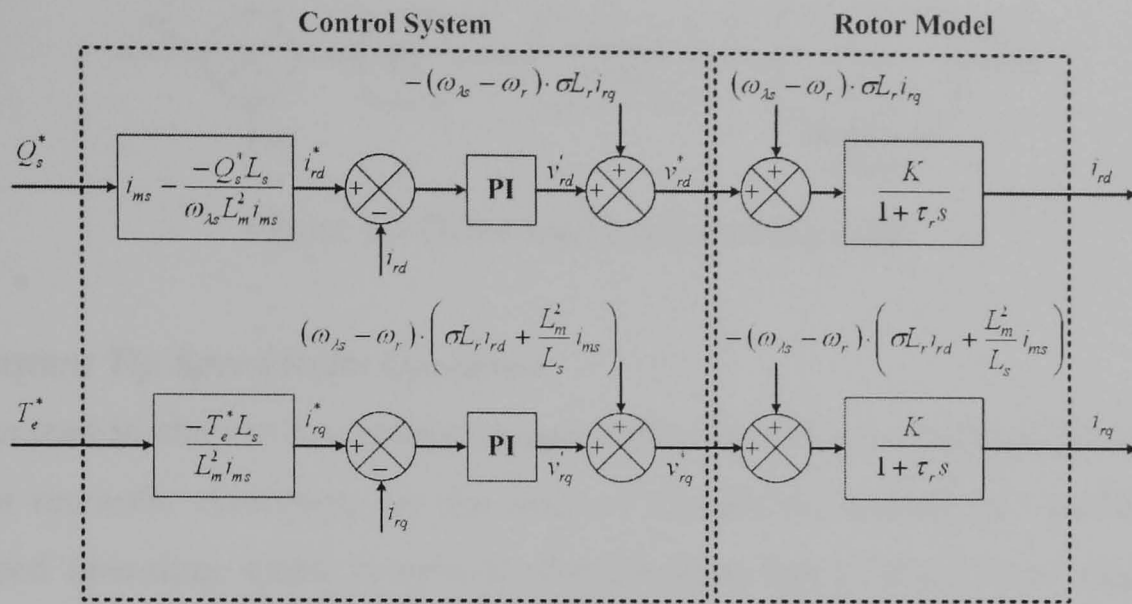
Figure 4.2 Inner-loop control of the MSC

Outer-loop control of the q-axis current is the speed loop control, used to control the speed of the DFIG to achieve maximum power from the particular wind speed. Assuming that the current loop is fast, then the dynamics of the inner loop can be neglected. The mechanical model of the machine is a first-order model which is in the same form as the inner loop. The same principle is applied to the speed loop having a transfer function as follows,

$$\frac{T_e(s)}{\omega(s)} = H_m = \frac{\frac{K_m}{\tau_m}}{s + (\frac{1}{\tau_m})} \cdot \frac{1 - e^{-T_s s}}{s}, \qquad (4.27)$$

where J is the moment of inertia of the DFIG-dc motor, B is the friction coefficient of the system, $K_m = \frac{1}{B}$ and $\tau_m = \frac{J}{B}$.

Discretising equation (4.27) by first-order hold, the transfer function in the z-domain is

$$H_m(z) = K_m \frac{1 - e^{\left(\frac{-T_s}{\tau_m}\right)}}{z - e^{\left(\frac{-T_s}{\tau_m}\right)}}. \qquad (4.28)$$

The diagram of the outer loop control for the MSC is shown in figure 4.3

68
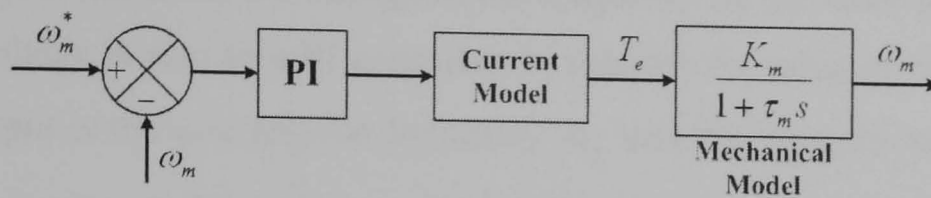
Figure 4.3 Outer-loop control of the MSC

iii. Constant Tip Speed Ratio Operation

As discussed in chapter 2, constant tip speed ratio operation is assumed for the DFIG for this research. However, for the sake of simplicity, instead of calculating the optimised operating speed command directly from the turbine power equation in chapter 2, the speed command is created from the linear relationship between wind speed in meters/second (m/s) and optimised generator speed required in pu, as follows,

$$\omega_r^* = a_0 + a_1 v_w .$$
(4.29)

This wind speed command is also used to calculate the torque command for the dc motor drive which represents the wind turbine which will be discussed in a later section.

4.1.2 Design of Grid-Side Converter Control

As discussed in chapter 3, the main function of this converter is to regulate the dc-link voltage and reactive power of the rotor converter.

i. Phase-Locked Loop (PLL)

A phase-locked loop is applied to the grid-side converter to determine the grid frequency and the angle of the grid voltage. Several techniques have been proposed to improve the performance of a PLL under distorted voltage condition [4.6-4.8]. The technique used here is the simple three-phase PLL that uses the assumption that the frequency does not vary too much. The PLL measures two line voltages or three phase voltages and then transforms these voltages into a voltage vector rotating reference frame. When the frequency of the estimated signal matches the frequency of the real voltage signal, voltages in their own reference frame have only d-axis components and the q-axis components are zero. Hence the existence of any q-axis

voltage indicates that there is a change in the frequency of the three-phase voltages. The q-axis voltage is sent to a PI controller to regulate its value to be zero. The PI controller output is the grid angular frequency ω_g and the integration of this output is the phase angle of the voltage vector. This phase angle is fed back to the transformation module. This procedure can be simply represented in figure 4.4.
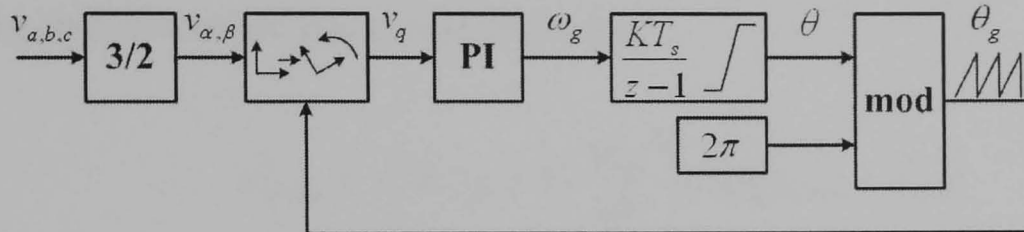
Figure 4.4 The diagram of the three-phase PLL

ii. Loop Control for the Grid-Side Converter (GSC)

The outputs of this PLL, ω_g and θ_g, are used for orientation and control of the GSC current. The grid current vector is oriented to the grid voltage reference frame by using equation (4.30).

$$\begin{bmatrix} i_{gd} \\ i_{gd} \end{bmatrix} = \begin{bmatrix} \cos\theta_g & \sin\theta_g \\ -\sin\theta_g & \cos\theta_g \end{bmatrix} \begin{bmatrix} i_{g\alpha} \\ i_{g\beta} \end{bmatrix}, \tag{4.30}$$

Similar to the MSC, the GSC control loop can also be separated into an inner loop, which is used to control currents, and an outer loop, which is used to control the dc-link voltage. Unlike the MSC, the d-axis current is used to control active power, whereas the q-axis current is used to control reactive power. As presented in chapter 3, the active power and reactive power equations in the grid voltage reference frame can be derived as shown in equation (4.31) and (4.32) respectively, in which due to implementation in the per-unit system, the factor of $\dfrac{3}{2}$ is again not included.

$$P_g = u_{gd} i_{gd}, \tag{4.31}$$

$$Q_s = -u_{gd} i_{gq}. \tag{4.32}$$

70

Generally, unity power factor operation is preferable for the GSC and therefore the reactive power command is set to zero. However, in this research, due to existence of three-phase transformer, the secondary side, which is connected to the GSC via three-phase choke, must be magnetised to make unity power factor of the primary side, which is connected to the grid. As in the case of the MSC, the outputs of the PI controllers are the voltage commands for the space vector modulation module. The d-axis and q-axis controlled voltage equations are

$$v^*_{convd} = -\left(R_f i_{gd} + L_f \frac{di_{gd}}{dt} \right) + \left(\omega_g L_f i_{gq} + u_{gd} \right), \qquad (4.33)$$

$$v^*_{convq} = -\left(R_f i_{gq} + L_f \frac{di_{gq}}{dt} \right) + \left(-\omega_g L_f i_{gd} \right). \qquad (4.34)$$

The terms in the first parenthesis are the output of the current controller u'_{gd} and u'_{gq}, whereas the terms in the second parenthesis are the compensation voltage that must be added to the negative outputs of the controllers. The transfer function of the system in the s-domain is

$$\frac{I_{gd}(s)}{U'_{gd}(s)} = \frac{I_{gq}(s)}{U'_{gd}(s)} = H_g(s) = \frac{\frac{K_f}{\tau_f}}{s + (\frac{1}{\tau_f})}, \qquad (4.35)$$

where $K_f = \frac{1}{R_f}$ and $\tau_f = \frac{L_f}{R_f}$. By using a zero-order hold, the discrete-time transfer function of the system in equation (4.35) is

$$H_g(z) = K_f \frac{1 - e^{\left(\frac{-T_s}{\tau_f} \right)}}{z - e^{\left(\frac{-T_s}{\tau_f} \right)}}. \qquad (4.36)$$

The same discrete-time PI controller structure as used in the MSC is used in the GSC. Following equations (4.33) and (4.34), the compensating voltages are added to the negative outputs of the PI controllers to generate the voltage command for the

switching function to drive the GSC. The inner-loop control of the GSC is shown in figure 4.5
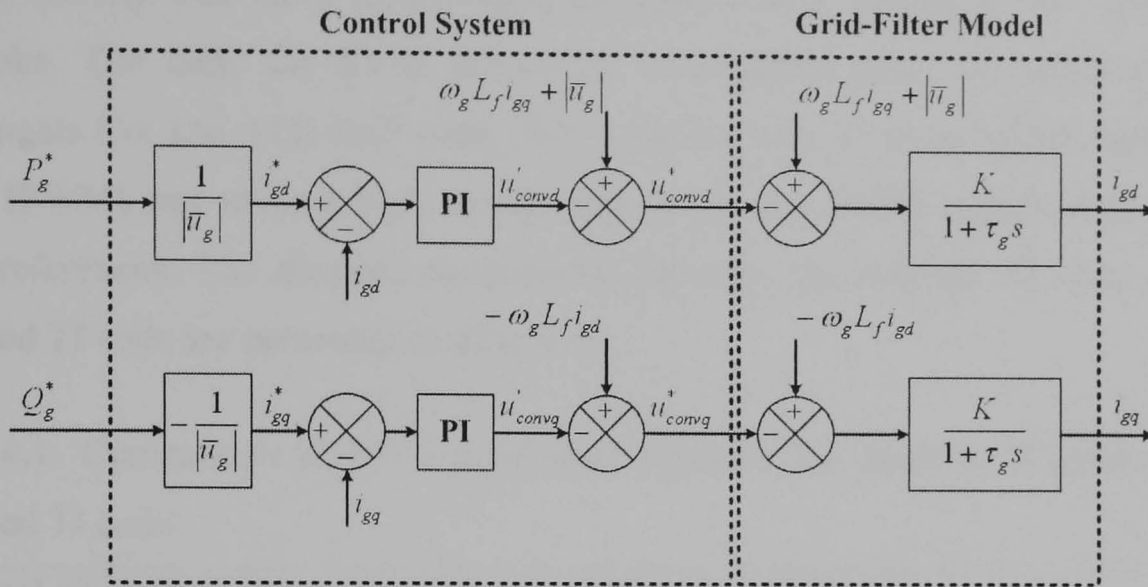
Figure 4.5 Inner-loop control of the GSC

The outer loop of the GSC is placed in the d-axis control loop to regulate the dc-link voltage. The transfer function of the outer-loop control is conveniently expressed in the integral form instead of the first order form. This transfer function in the s-domain can be derived as follows,

$$\frac{V_{dc}(s)}{I_{gd}(s)} = H_c(s) = \frac{1}{Cs}, \tag{4.37}$$

where C is the capacitance value of the dc-link capacitor.

The transfer function of the dc-link voltage control the in s-domain is

$$H_c(z) = \frac{1}{C}\left(\frac{z}{z-1}\right). \tag{4.38}$$

The diagram of the outer loop control is shown in figure 4.6.
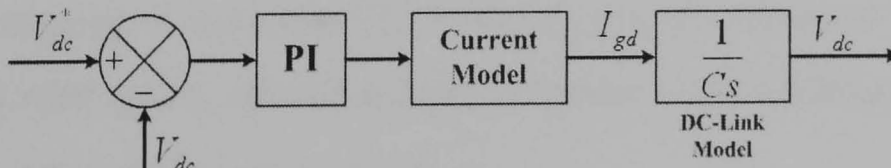
Figure 4.6 Outer-loop control of the GSC

4.1.3 Switching Command

The switching command for the converters is based on the space vector modulation method (SVM). For more information, the reader may consult power electronics textbooks. The code for SVM generation is modified from the original Texas Instruments Co. Ltd. (TI) DSP code [4.2, 4.10] because TI pulse width modulation signal (PWM) has reverse logic comparing to general PWM signals presented in many references. The detailed comparisons between the original TI code and the modified TI code are presented in table 4.1.

Table 4.1: Comparison of SVM generation between the original TI code and the modified TI code

Original TI code	Modified TI code
• uses position (positive or negative) of each phase command voltage to determine sector • require transformation • require two phase/three phase transformation • different reference axes are used when transforming the two phase signals to three phase signals	• use angle calculated from two-phase input signals to determine sector • no transformation required • the code follows several references • slightly longer code • provides same output as original TI code

4.2 Wind Turbine Representation

In this research, the wind turbine is represented by a dc motor controlled by a two-quadrant line commutated dc motor drive. As discussed in section 4.1.1.*iii*, the per-unit generator speed command is calculated as a function of wind speed in m/s. Likewise, the per-unit torque command for dc drive is also calculated as a function of wind speed. Referring to equations (2.22) and (2.23), the relationship between per-unit torque and wind speed, calculated from the power at the maximum c_p, is written in the form of a binomial function as follows,

$$T_m^* = b_0 + b_1 v_w + b_2 v_w^2 . \qquad (4.39)$$

Equations (2.22) and (2.23) are used to calculate the power-speed curve and the maximum power point for each wind speed, as shown in figure 4.7. In this research, the operating speed range is from 0.8 pu to 1.2 pu as shown in figure 4.7. The cut-in wind speed is 7 m/s. From this plot at 7m/s, the generator operates at 0.8 pu speed but as the wind speed increases over 8 m/s but below 12 m/s, the generator operates under an optimised operating speed command which can be written as follows,

$$\omega_r^* = 0.1 v_w , \qquad (4.40)$$

where ω_r^* is the rotor speed command for speed control loop in pu and v_w is the programmed wind speed command.

When the wind speed is over 12 m/s, the generator speed command is maintained at 1.2 pu as shown in figure 4.7. Due to the torque mismatch between the DFIG and the dc motor, the dc motor is not able to drive the DFIG at its rated torque.
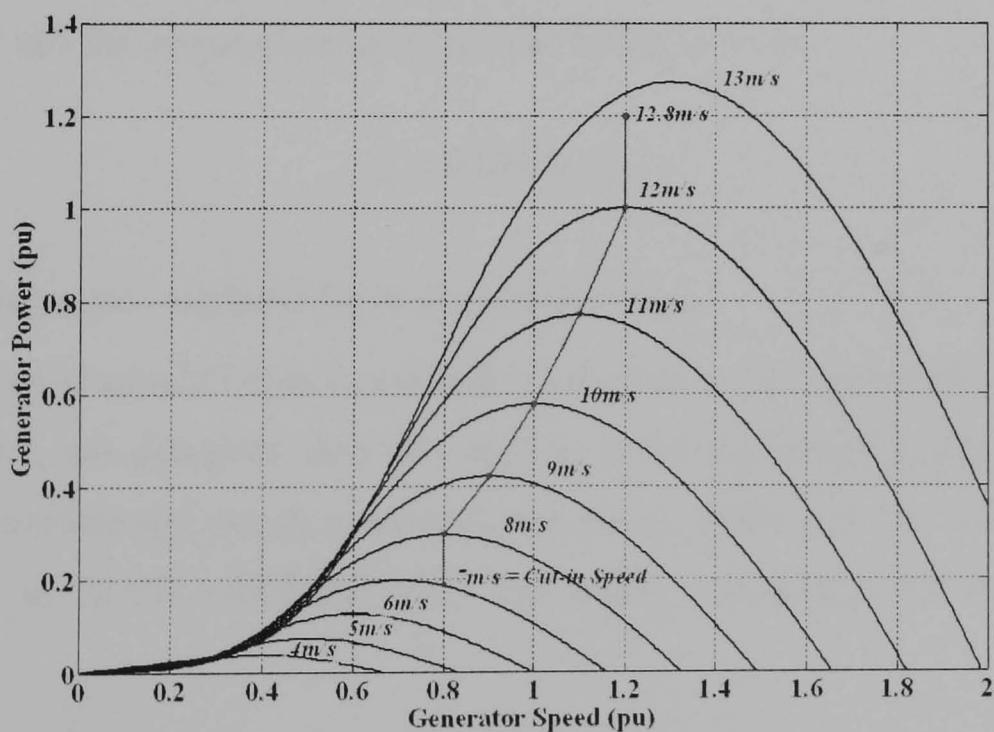
Figure 4.7 Power-speed curves with the maximum power points
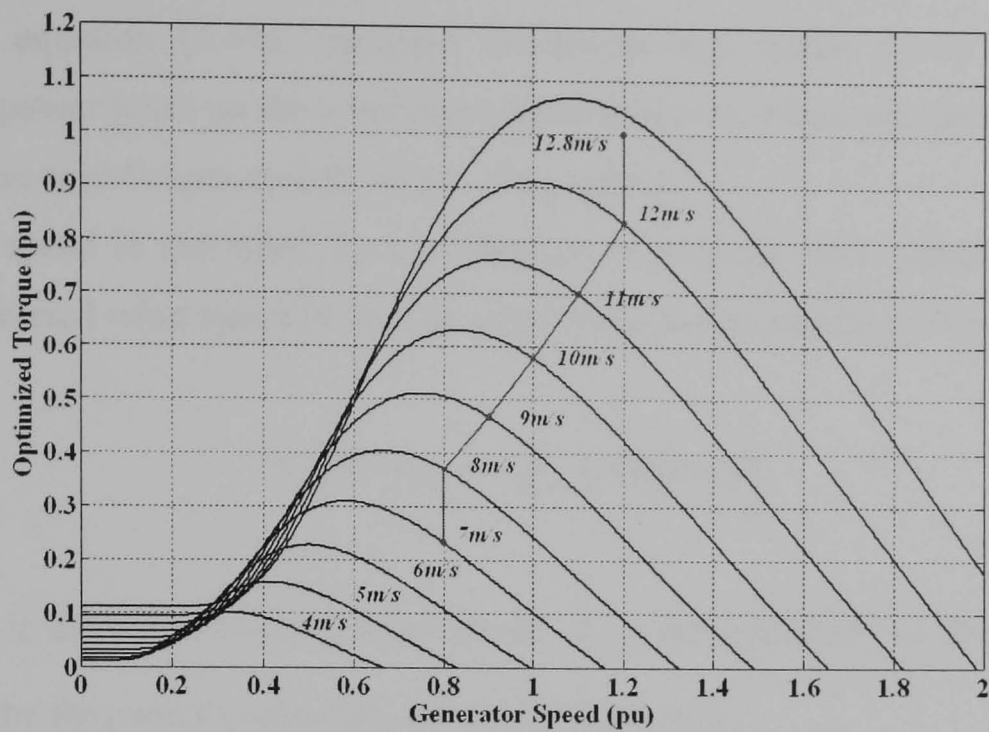
Figure 4.8 Torque-speed curve with the operating points that yield maximum power from the wind turbine curve shown in figure 4.7

The torque command for the dc motor is calculated from figure 4.7 and shown in figure 4.8. In system implementation, there are three equations which are used to command the dc drive to follow the curve in this plot. For wind speeds between 8 m/s and 12 m/s the torque equation in terms of wind speed is

$$T_m^* = 0.0057872v_w^2,$$ (4.41)

where T_m^* is torque command for dc motor drive in pu.

Under low wind speed (7-8 m/s) and high wind speed (>12 m/s) conditions, as shown in figure 4.7, the generator does not operate at the maximum power point of the turbine. Therefore the torque commands for the dc motor must be different. From calculation in MATLAB/SIMULINK, the torque commands can be derived as follows,

for $7 < v_w < 8$ m/s: $T_m^* = 0.13532v_w - 0.71857$, (4.42)

for $v_w > 12$ m/s: $T_m^* = 0.20533v_w - 1.63$. (4.43)

75

The speed command for the DFIG, equation (4.40), and the torque command for the dc motor, equation (4.41), represent the torque and speed which describe the maximum power point on the wind characteristic curves. These are not the equations of the torque-speed characteristic of the wind turbine.

The wind speed is modelled by combination of average wind speed, ramp wind speed and varied wind speed [4.9]. The wind speed model can be written as follows,

$$v_w(t) = v_{w0}\left(1 + \sum_k A_k \sin(\omega_k t)\right), \qquad (4.44)$$

where v_{w0} is the mean value of wind speed, A_k is the amplitude of the kth harmonic and ω_k is the frequency (pulsation) of the kth harmonic.

In this research, frequency varies between 0.01Hz and 1Hz and the value of k is set to 20. This wind speed equation is applied only to generate the torque command for dc motor, to introduce torque variations as would appear with real wind. The average wind speed is used for calculating the generator speed command (no harmonic components) because in reality the wind turbine has a high moment of inertia.

4.3 Simulation and Experimental Validation

This section presents the results of simulation and experimental testing for the purpose of confirming the theory found in many references and making the system ready for the main objective of this research. As mentioned previously, the algorithms presented are applied to both simulation and experimental system implementation. All variables and parameters are per-unitised by the base values listed in Appendix A. The switching frequencies and sampling frequencies of both MSC and GSC in simulation and experiment are 5 kHz.

4.3.1 Simulation Validation

In this research, the simulated system is generated in MATLAB/SIMULINK program. Since a built-in asynchronous machine model supports only a squirrel cage machine and 1:1 turn ratio for a wound rotor machine, therefore the modification to match the experimental machine is required.

76

Modification in this machine is made by changing the base voltage of the rotor and putting the gain to the rotor currents. The value of the ratio is acquired by measuring the rotor voltage while doing open–circuit test. For the current gain, the locked-rotor test is performed and the stator and rotor currents are measured. The gain is calculated from the ratio between one stator phase current and one rotor phase current. However, this gain is required to be adjusted to match the real currents during the experiments.

Due to the large size of the simulated system, some procedures used in the real system must be ignored to save memory. In simulation, the system is started by energising both stator and rotor at the same time by direct on-line start. The rotor winding are short circuited through the negative dc bus by turning on all bottom switches and turning off all top switches in the MSC, which is the same as operating the MSC in 000 vector state of SVM. This method provides no effect on the grid-side converter during building up the DC voltage.

Once the dc-link voltage, boosted by the GSC, is steady at the reference level and the torque input is at the set-point, the PWM signal changes from 000 vector state to SVM mode and follows the maximum tip speed ratio algorithm. The mechanical input of the generator is set to torque and the wind turbine data are simulated by equations (4.41)–(4.43). This section presents the simulation results which are necessary to prove that the DFIG system is operating successfully. The same operations will also be presented later in the experimental section. The schematic of the simulation system is shown in figure 4.9
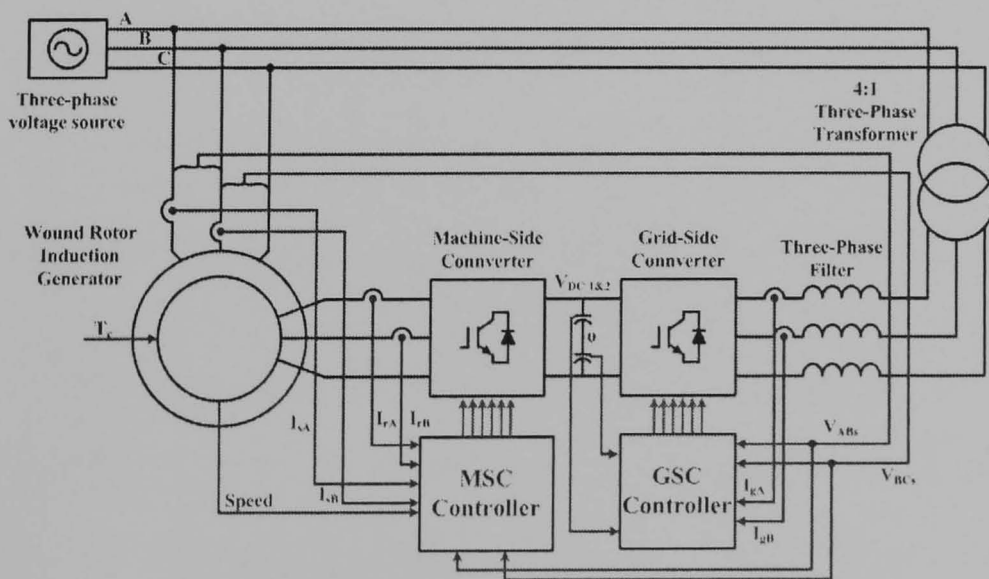
Figure 4.9 Schematic of the simulation system

i. Steady-State Operation

These results show the waveforms under steady-state operating conditions. Figure 4.10 shows the stator current and rotor current waveforms for sub-synchronous speed generation (0.8 pu speed, 1200 rpm). Under the same operating conditions, figure 4.11 shows the generator torque, stator active power, grid-side converter active power and total active power. The rotor current waveforms shown in figure 4.10 contain distortion at the peaks of the waveforms due to the effect of switching currents. This distortion is quite significant because the amplitude of the currents is quite low.
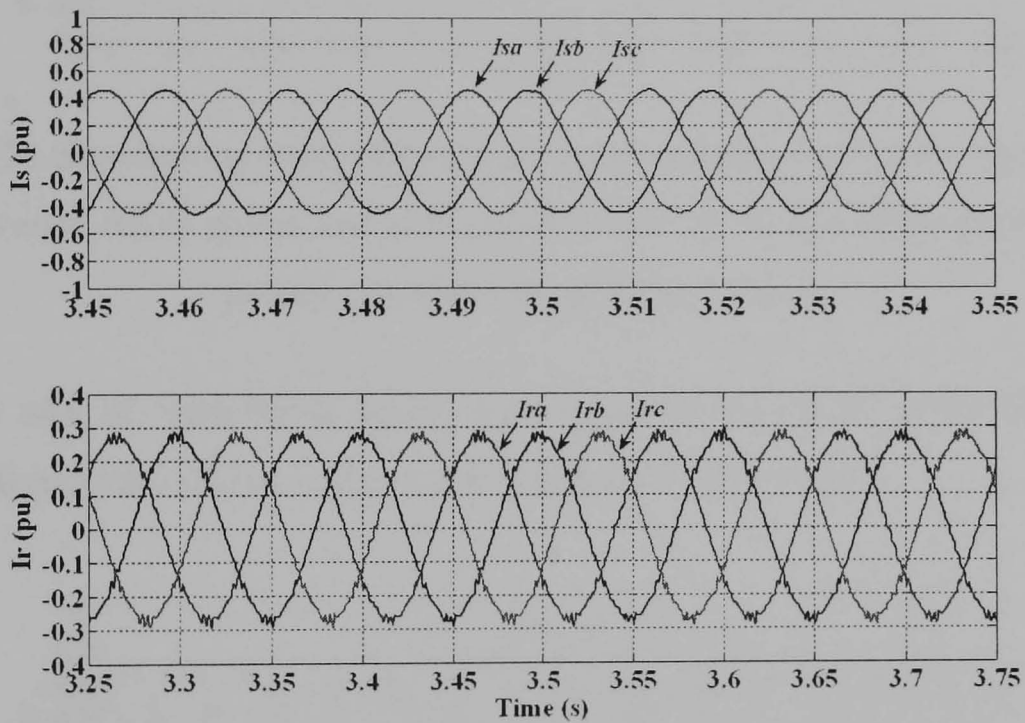
Figure 4.10 Simulation results showing stator and rotor current waveforms for steady-state operation at 0.8 pu sub-synchronous speed generation
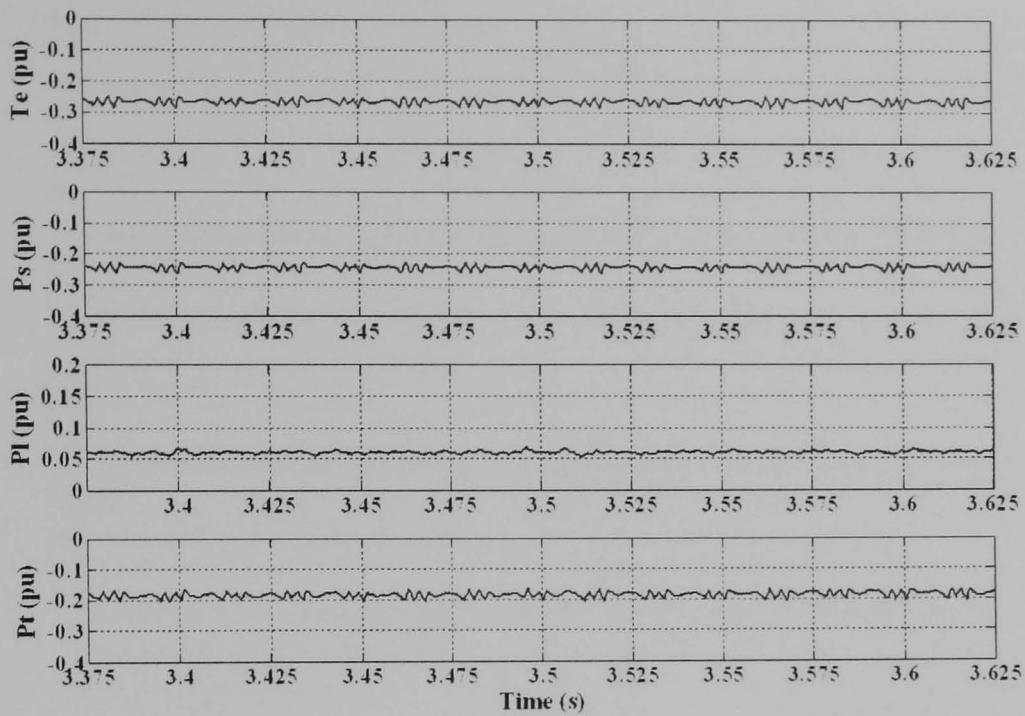
Figure 4.11 Simulation results showing generator torque, stator active power, grid-side converter active power and total active power for steady-state operation at 0.8 pu sub-synchronous speed generation

The same sets of waveforms under super-synchronous speed generation (1.2 pu speed 1800 rpm) are shown in figures 4.12 and 4.13 respectively.
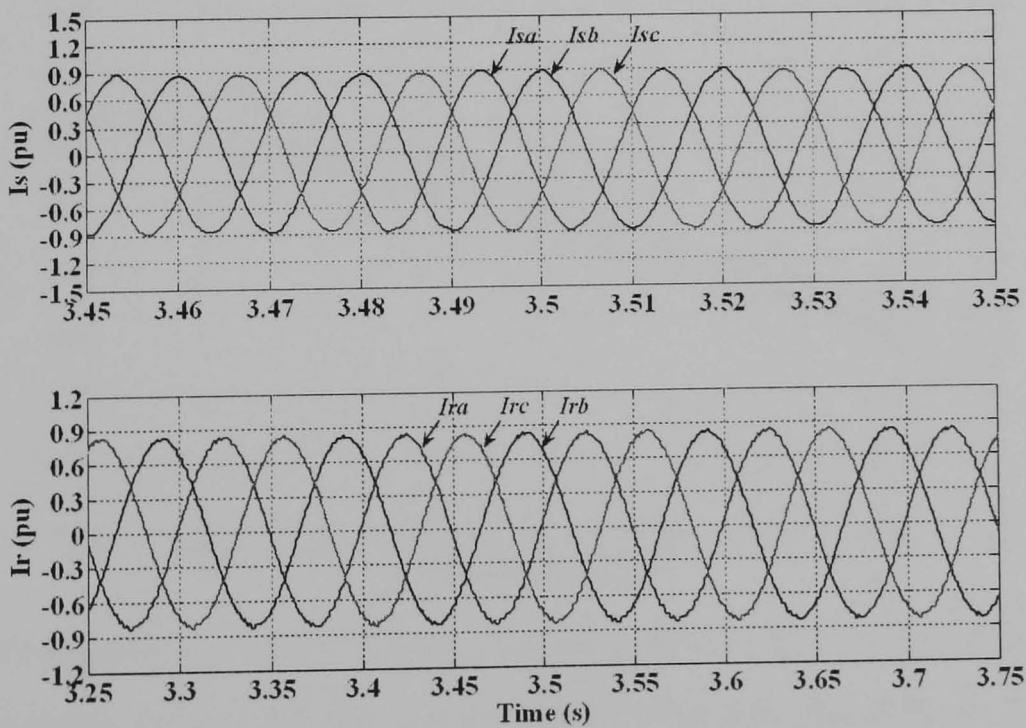
Figure 4.12 Simulation results showing stator and rotor current waveforms for steady-state operation at 1.2 pu super-synchronous speed generation
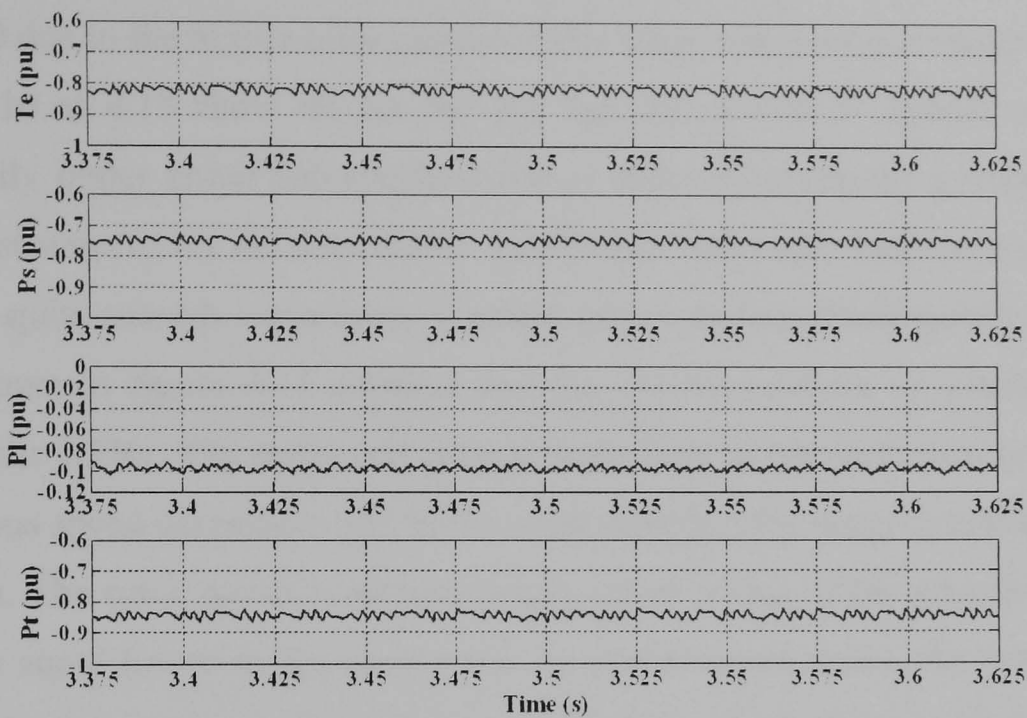
Figure 4.13 Simulation results showing generator torque, stator active power, grid-side converter active power and total active power for steady-state operation at 1.2 pu super-synchronous speed generation
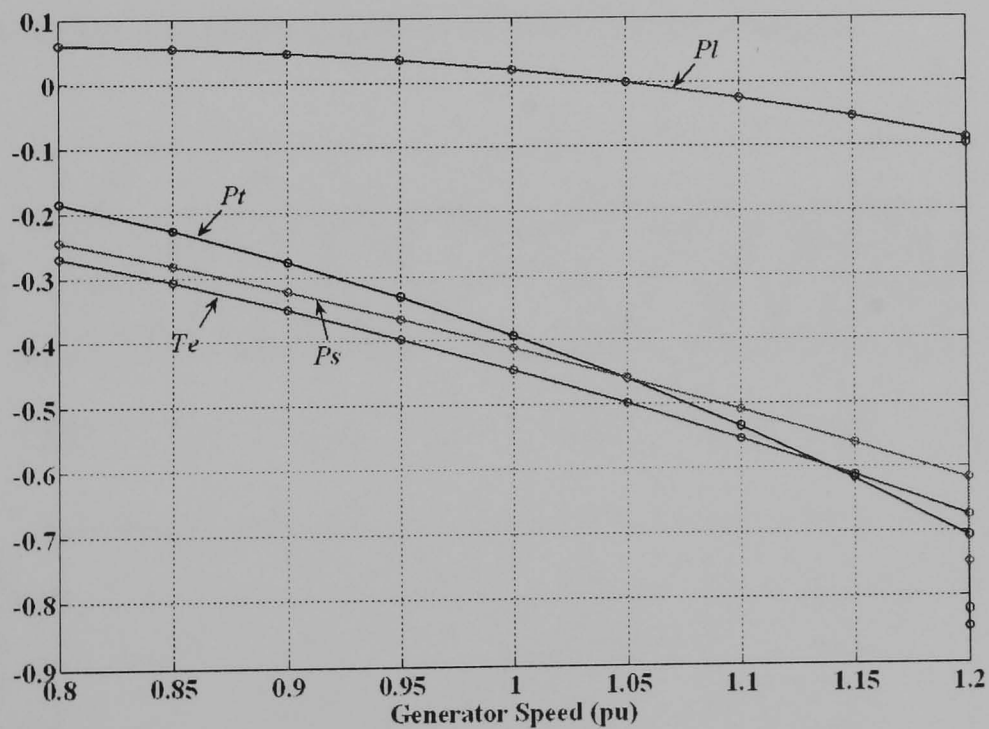
Figure 4.14 Simulation results showing average value of the electromagnetic torque (Te), total active power (Pt), stator active power (Ps) and grid-side converter active power (Pl) at different operating speed

The rotor current waveforms in figure 4.12 are smoother than the waveforms in figure 4.10 due to the higher rotor current under super-synchronous speed operation. Figures 4.10 to 4.13 show results proving that the system is capable of operating satisfactorily under either sub-synchronous or super-synchronous generation mode. The current waveforms do not contain significant high-order harmonic components leading to quite smooth waveforms of active power and electromagnetic torque. The results shown in figure 4.14 confirm that the system operates as explained in the theory of the DFIG. The stator and rotor powers flow in opposite directions for sub-synchronous speed generation and in the same direction for super-synchronous speed generation. The rotor power is approximately equal to that of the grid-side converter due to the small losses in the converters. At synchronous speed, the rotor power is not zero due to rotor copper and converter losses which are compensated by the power generated from the rotor at 1.05 pu speed.

ii. Operation through Synchronous Speed

This subsection presents the results under operation through synchronous speed. As shown in figure 4.15, when the speed changes from sub-synchronous region to super-synchronous region, the phase sequence of rotor current changes
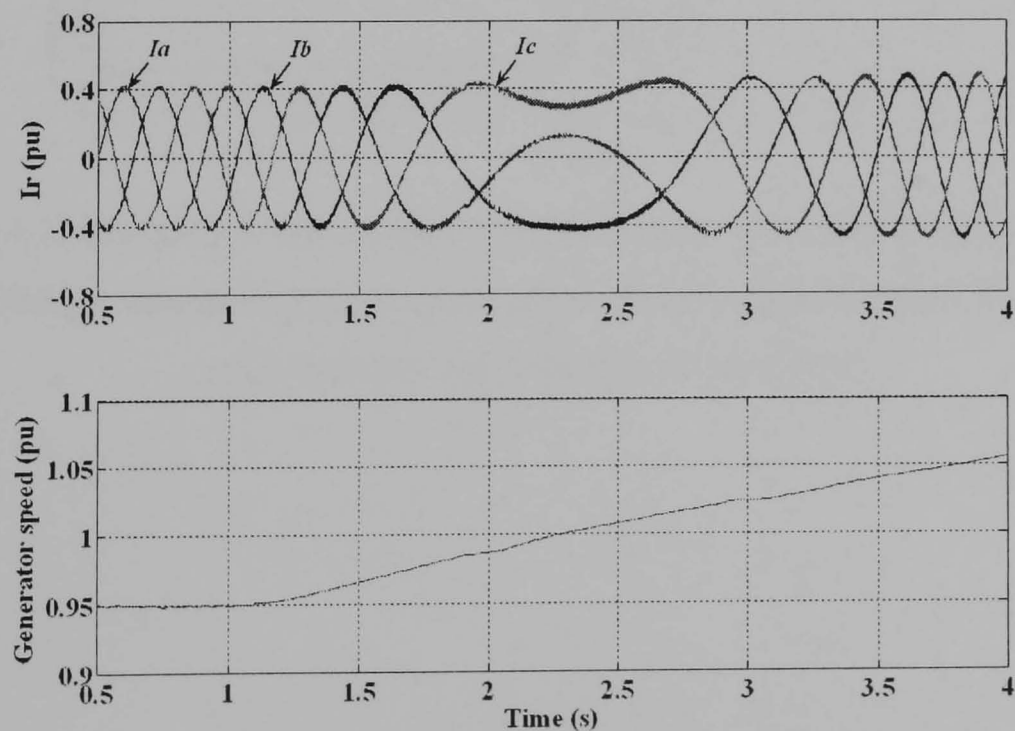
Figure 4.15 Simulation results showing operation through synchronous speed

This is because when induction machine operates above synchronous speed, the rotor speed is faster than the air-gap flux speed. Therefore, to maintain the rotor flux at synchronous speed the rotor phase sequence must change.

iii. Step Change in Stator Reactive Power

The response to a step change in stator reactive power command reveals the capability of controlling the stator reactive power by the d-axis rotor current. The results show response to a step change in stator reactive power by changing d-axis current command at sub-synchronous and super-synchronous speed. The simulation results for this subsection are shown in figures 4.16 and 4.17 respectively
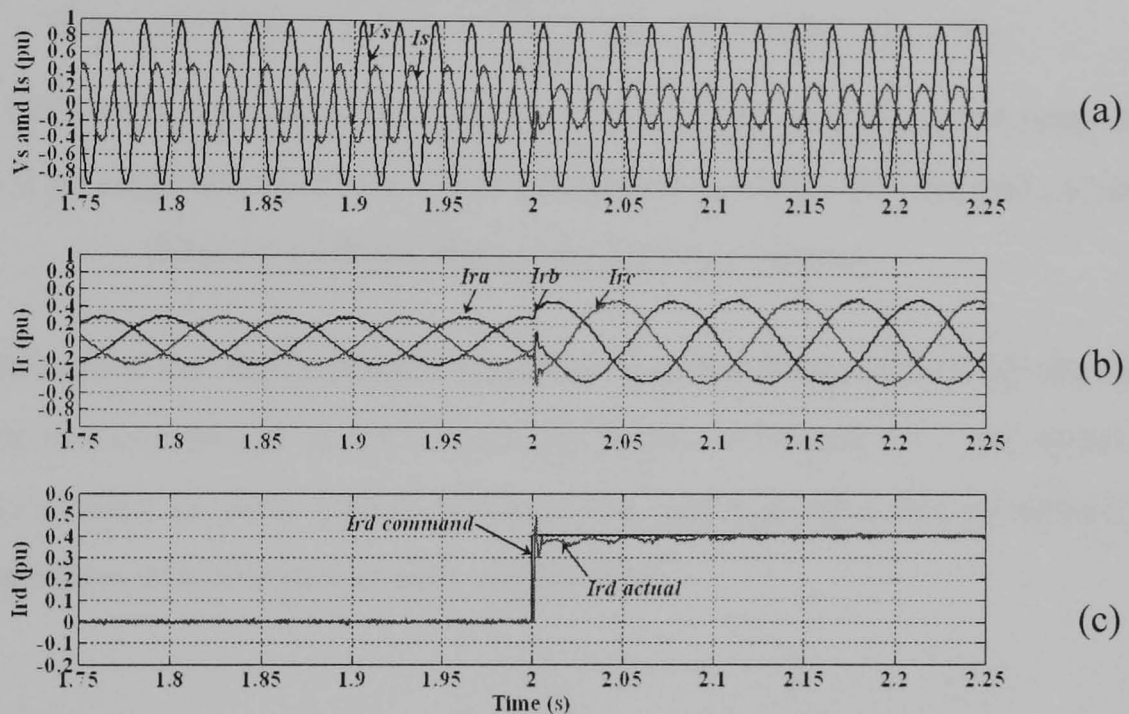
Figure 4.16 Simulation results showing the response to a step change in reactive power at 0.8 pu sub-synchronous speed generation (a) stator voltage and current, (b) rotor currents and (c) d-axis rotor current
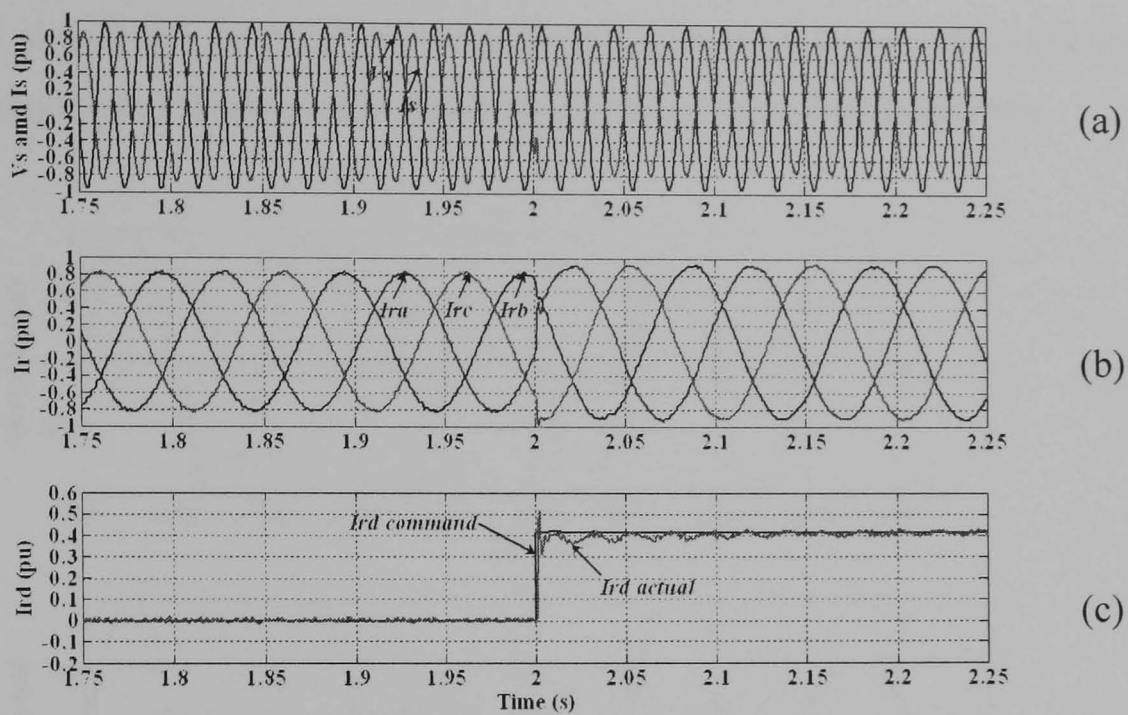
Figure 4.17 Simulation results showing the response to a step change in reactive power at 1.2 pu super-synchronous speed generation (a) stator voltage and current, (b) rotor currents and (c) d-axis rotor current

Under normal operation, the generator consumes reactive power only from the stator and the rotor reactive power is set to zero. In figures 4.16 and 4.17, the system is controlled to change to unity power factor at the stator. Under this condition, the generator consumes reactive power only via the rotor.

iv. Grid-Side Converter Operation

Figure 4.18 shows the operation of the grid-side converter under sub-synchronous (rectifying mode) and super-synchronous (inverting mode) speed generation.

(a)

(b)
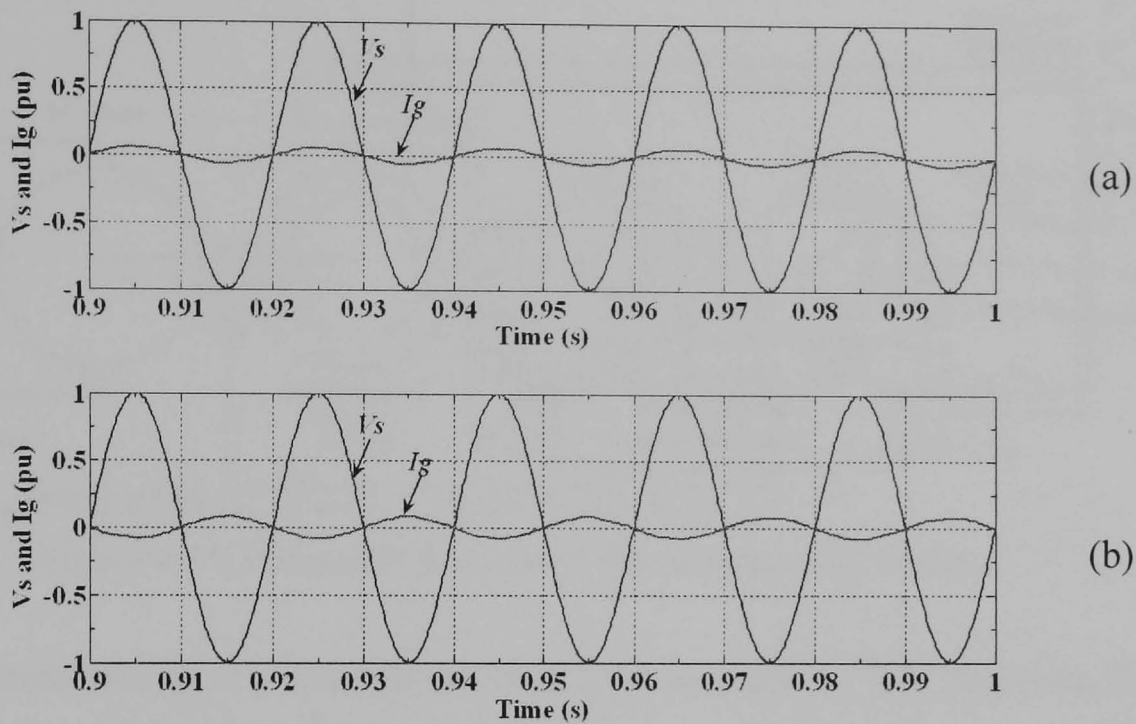
Figure 4.18 Simulation results showing the grid-side converter operation under
(a) rectifying mode (b) inverting mode

This figure shows the waveform of grid voltage and the primary-side (grid side) current of the three phase transformer. Generally, this converter operates at unity power factor. However, since there is a transformer in the system, to make the power factor on the grid side unity the converter has to be controlled to magnetise the transformer on the converter side.

4.3.2. System Implementation

A schematic diagram of the whole system is shown in figure 4.19 The DFIG is directly mechanically coupled to the dc motor operated as the wind turbine under torque control. The main apparatus used in this system are a wound rotor induction machine, a dc motor, an analogue dc drive, a three-phase variac, a three-phase transformer, three single-phase chokes, two dc-link capacitors, six single-leg IGBT modules and the TI DSP board eZdsp F2812 [4.12]. The ratings and specifications of these apparatus are listed in appendix A.
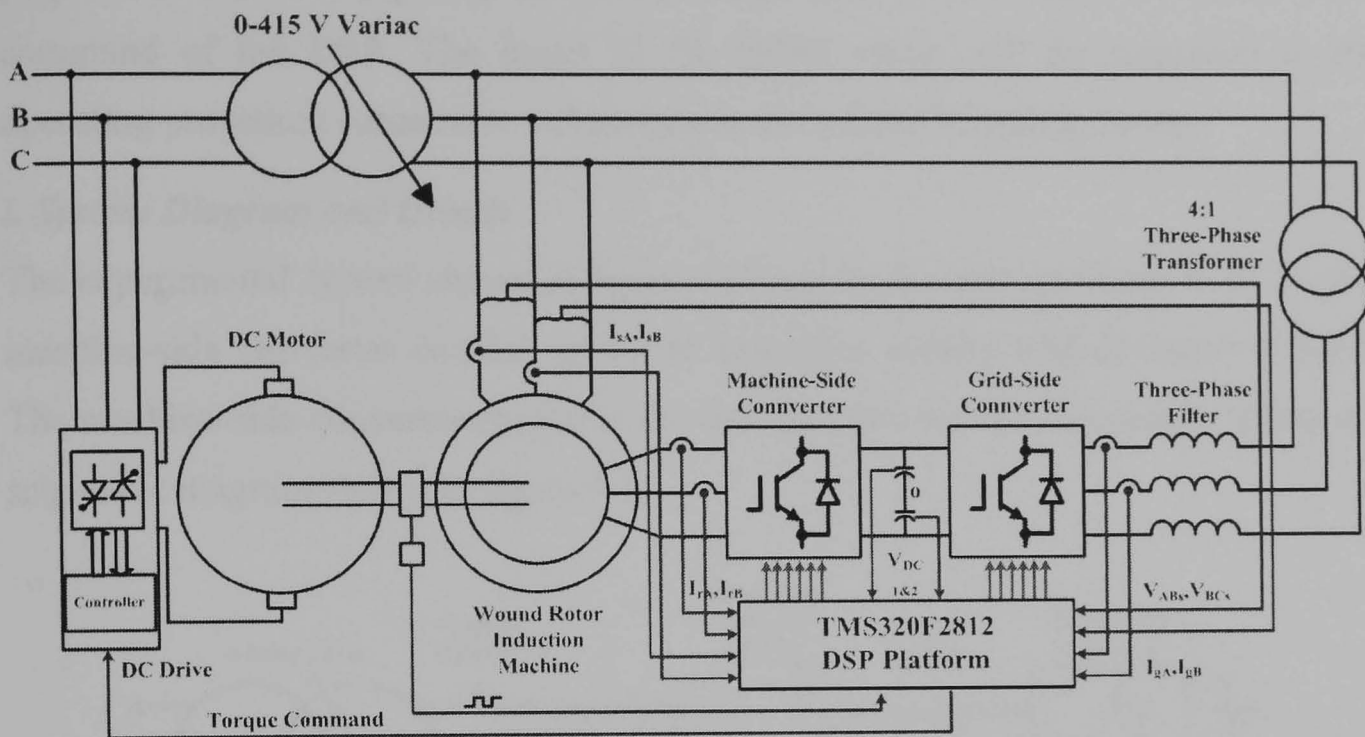
Figure 4.19 Schematic diagram of the experimental system

The converters used in this research are built from six 1200V, 75A single-leg IGBT modules type SKM75GB123D made by Semikron [4.15]. The experimental system is controlled by a TI digital signal processor (DSP) type TMS320F2812 [4.11] in the development platform eZdsp F2812 [4.12], shown in figure 4.20. The features of this DSP are listed in [4.11]. For more detailed information, consult the TI datasheet [4.11].
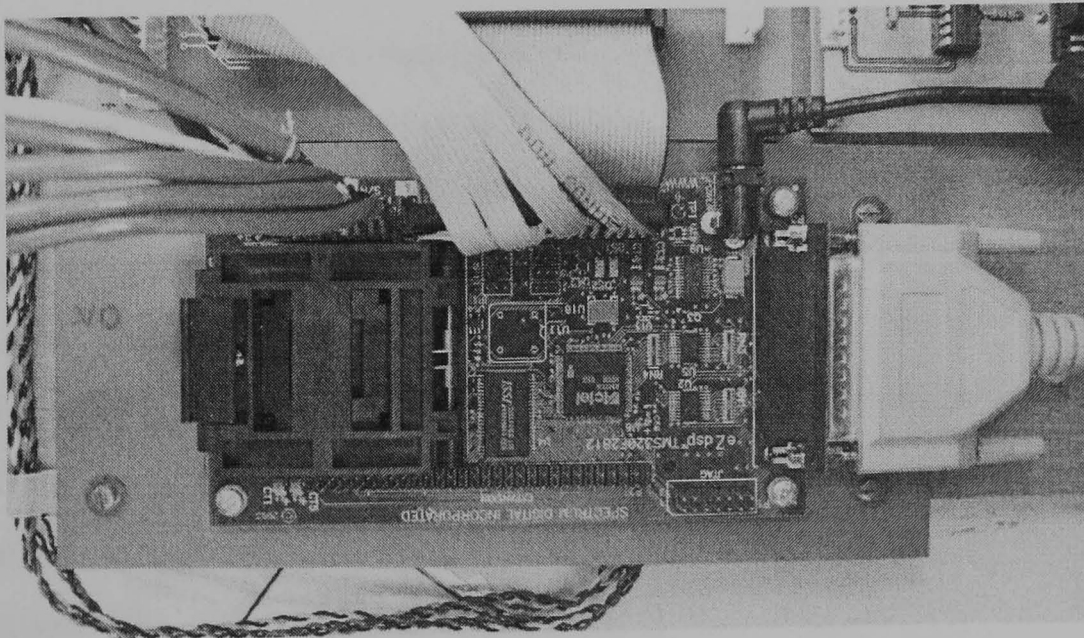
Figure 4.20 Photograph of the eZdsp F2812 board

This DSP can be programmed in C language. In this research, the program is stored in the flash memory which has higher capacity than the on-chip RAM. The general

purpose I/Os (GPIOs) [4.14] are used as indicators and as inputs for controls as command of the DSP. The detail of the GPIO usage will be presented in the operating procedure subsection. All programs are written in polling mode.

i. System Diagram and Details

The experimental system shown in figure 4.19 can be divided into three main parts – machine-side converter control, grid-side converter control and dc motor control. The machine-side converter control is the first part that will be discussed, having the schematic diagram shown in figure 4.21.
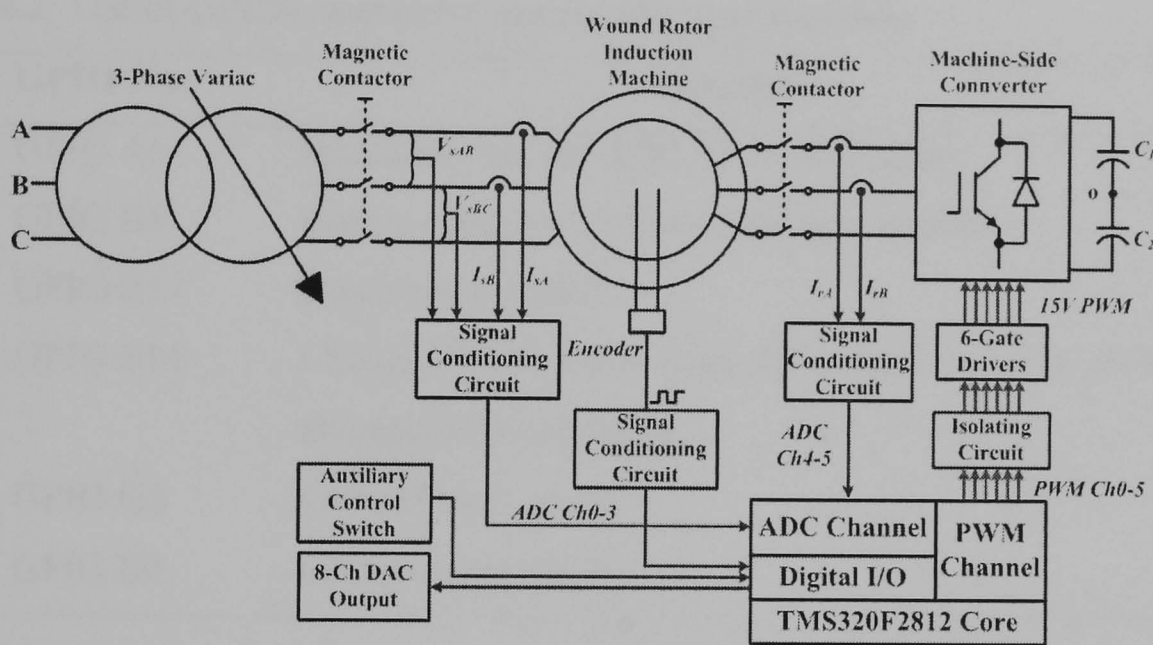
Figure 4.21 Detailed diagram of the machine-side converter implementation

There are six analogue signals required – two line voltages, two stator-phase currents and two rotor-phase currents, which are fed into ADC channels 0 to 5. The sampling method for ADC channel is simultaneous sampling, which can sample two channels at the same time. This has the benefit of no delay for the same types of signal being sampled. All signals are fed into a signal conditioning circuit to scale their amplitudes and limit the maximum amplitude to 3.0Vdc. The maximum values of all ac signals are set to 2 pu.

An incremental encoder with a resolution of 1000 pulses/revolution is used as the speed sensor. The output of the encoder consists of two continuous pulse trains shifted 90 degree from each other and an index pulse to indicate that the shaft has rotated 1 revolution. The outputs are fed to the signal conditioning circuit to remove noise and limit the maximum amplitude to 3.3Vdc. One of the requirements for

encoder installation is to isolate the encoder shaft from the machine shaft to avoid any electromagnetic interference (EMI) that can distort the encoder pulses. The code used to calculate the rotor angle is taken from TI code [4.10].

Six PWM channels (PWM Ch0-5) are used to drive the MSC. They are fed to isolating circuit to avoid damage to the DSP due to faults in the converter. The auxiliary control switches are connected to several GPIOs used for step commands and for indicating readiness of the system to start. The GPIOs used in the system are listed in table 4.2.

Table 4.2: List of GPIOs used in the system and their functions

GPIO No.	Functions
GPIO A6	Indicating that the ADC channel is ready
GPIO B8	Enable open-switch fault detection module
GPIO B12	Disable one switch
GPIO B11	Change PWM mode from 50% duty cycle to SVM and control wind speed
GPIO G5	Control wind speed
GPIO E0	Control wind speed

The schematic diagram for the control of the GSC is shown in figure 4.22.
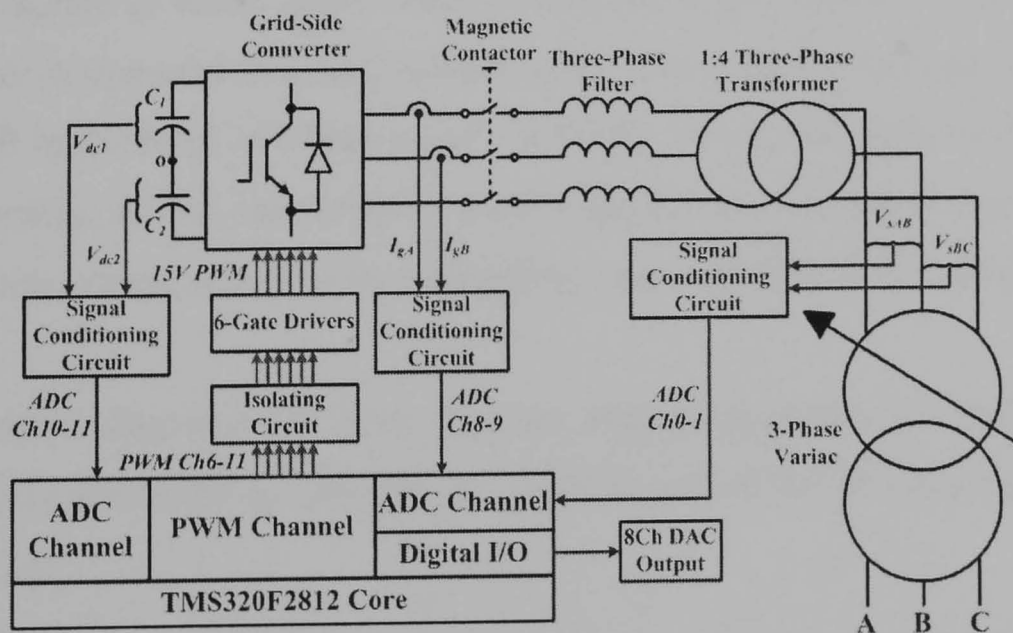
Figure 4.22 Detailed diagram of the grid-side converter implementation

For this converter, six analogue signals are required. The first two signals are two line voltages which are used in the machine-side converter control. Two grid-side converter currents and two dc-link voltage are fed into ADC channel 8-9 and 10-11 respectively. Six PWM channels (PWM Ch6-11) are used to drive this converter. Isolating circuits similar to those used in the control of the MSC are also used here.

The last main system which is the control of the dc motor as a wind turbine is shown figure 4.23
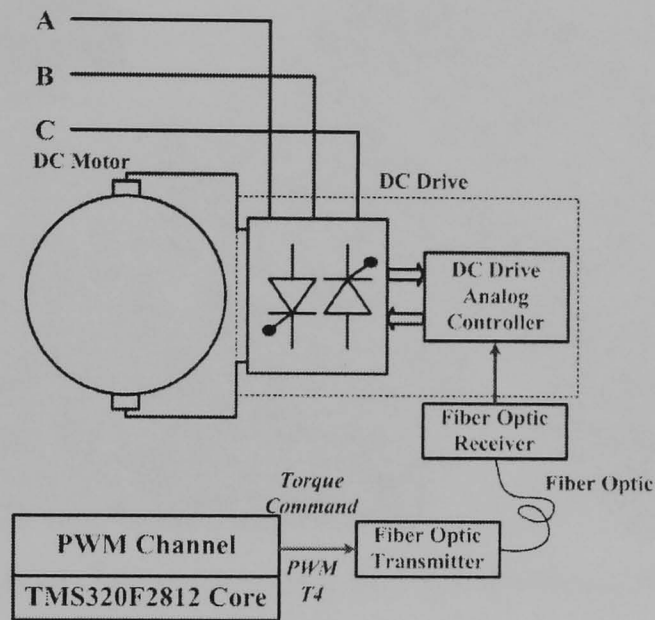
Figure 4.23 Detailed diagram of the dc motor control implementation

The dc motor is controlled by the commercial analogue dc motor drive circuit. This drive can operate in either speed control or torque control mode. For this research, the dc motor is operated in torque control mode. The torque command signal is sent from a DSP in the form of PWM signal via PWM T4 channel. Due to EMI radiated from the system, a fibre optic cable is used as the means of transmission. The output at the receiver is then amplified by a simple op-amp and filtered by a simple RC low-pass filter.

The schematic diagrams of some circuits and photographs of each necessary component are presented in appendix A. A photograph of the whole system is shown in figure 4.24.
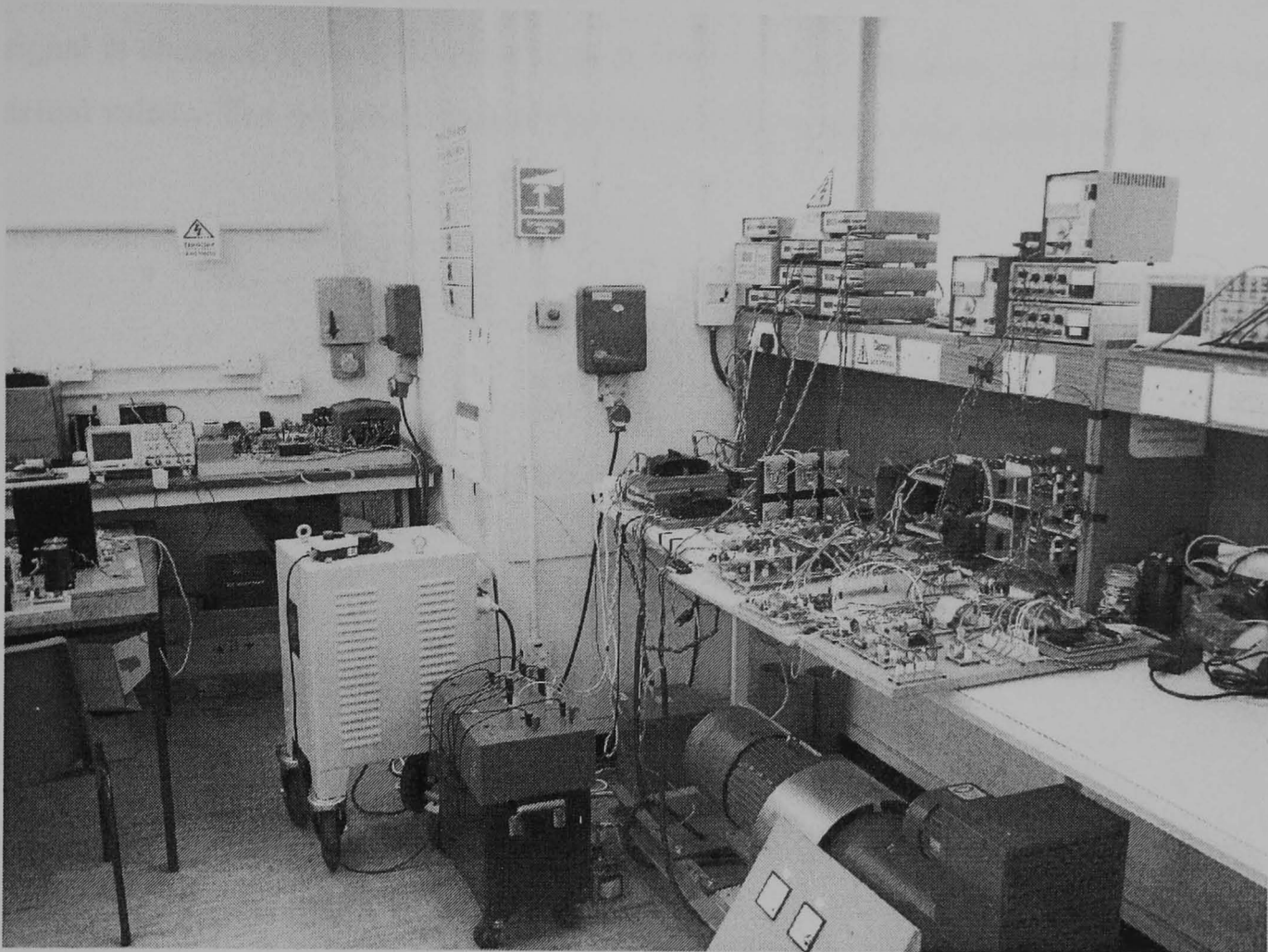
Figure 4.24 The photograph of the experimental system

ii. Operating Procedure

This subsection describes the operating procedure for the experimental system. The controller gains for both MSC and GSC were empirically tuned in simulation and readjusted while commissioning the system. All dc power supply must be started first and followed by the DSP. Due to errors in the ADC channels, all measured variables which should be zero must be averaged and then subtracted from their instantaneous values to set all channels to zero initially. The sequence of operations is shown in the flowchart in figure 4.25.

Instead of applying full voltage to the system, as in the simulation studies, the dc motor is first operated until its speed reach maximum speed with lowest torque command applied. The voltage for the DFIG system is gradually applied by the variable transformer until the voltage reaches rated voltage. During this process, the grid-side converter builds the dc-link voltage up to desired voltage and the generator is operating as a squirrel cage generator with rotor windings connected to the negative dc bus. During this process, the feedback signals of all controllers are set to

the reference value to generate zero errors. While operating at steady state, the PWM signal is changed from 000 vector state to SVM and the feedback signal is set to the actual values. The generator speed is brought down to minimum operating speed.
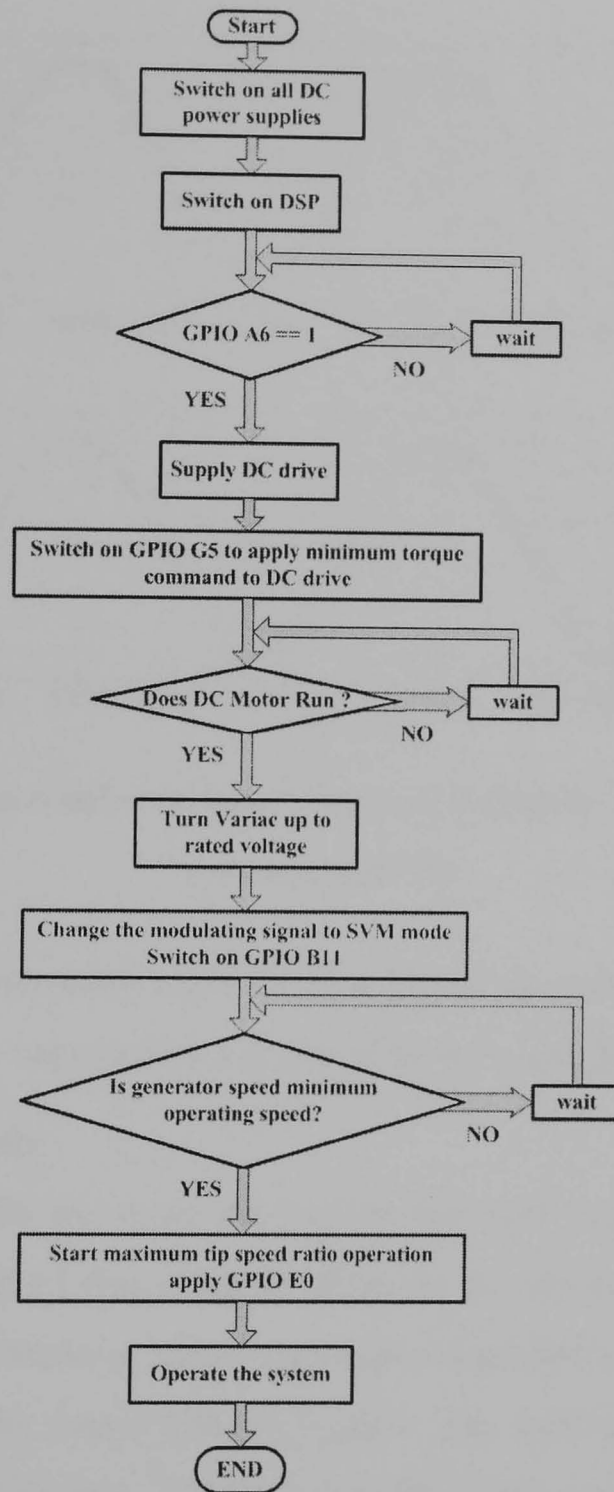
Figure 4.25 Flowchart of operating procedure

To tune the system to operate successfully, some internal variables are required and they can be measured from a digital-to-analogue converter (DAC). For this system, the McBSP is used in SPI mode [4.13] to transfer some variables to the 8-channel digital-to-analogue converter chip. For the sake of convenience, up to 8 measurable and immeasurable variables can be output via DAC channels. To prove that the

output from the DAC is usable, a DAC current signal was calibrated and compared with the output from a current probe. The comparison is shown in figure 4.26, indicating that the output from the DAC channels are satisfactory.
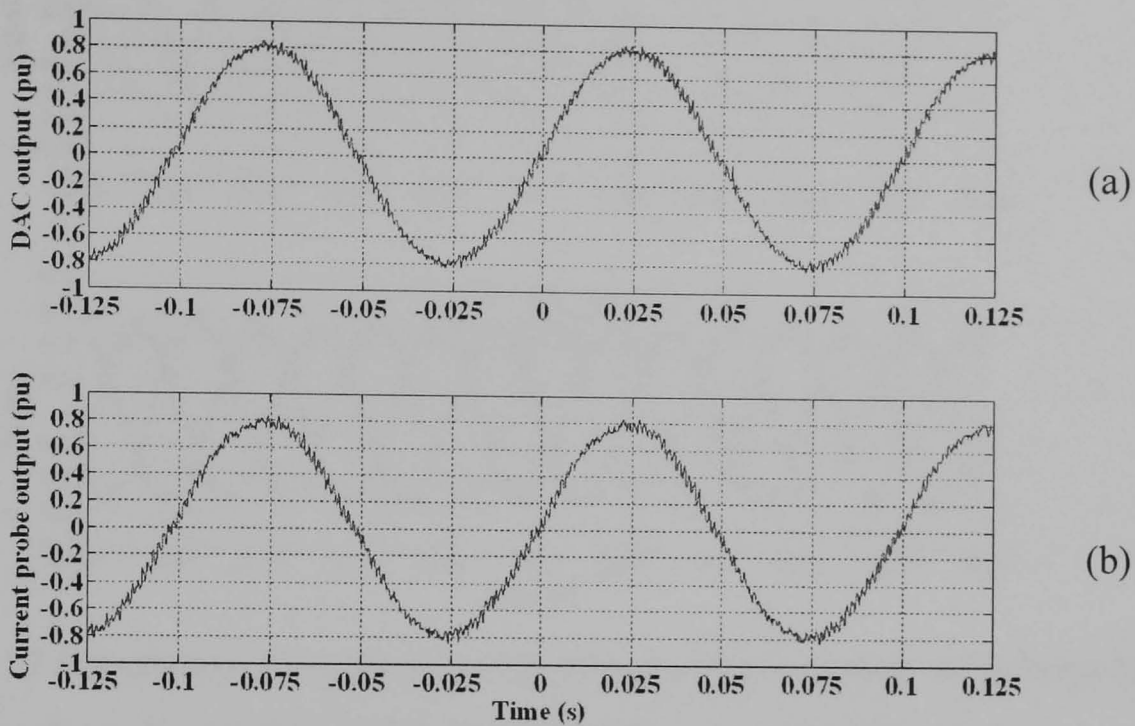
Figure 4.26 Comparison between signal from (a) digital-to-analogue converter and (b) current probe

The DAC signals are normally captured by a digital oscilloscope, but for long-term data the waveforms are captured by a National Instruments data acquisition card.

iii. Experimental Results

The experimental results shown in this section are used to prove that the system is ready for the main part of this research. First of all, the results under steady-state conditions at sub-synchronous speed and super-synchronous speed generation are presented. These results prove that the system can operate successfully over the range of operating conditions. The synchronous speed generation results are not presented here due to the difficulty in recording the results using an oscilloscope. However, operation at this speed will be presented in the long-term operation results which include the effects of wind fluctuation.

Figure 4.27 shows the stator current and rotor current waveforms for steady-state operation with sub-synchronous speed generation (0.8 pu speed 1200 rpm). Under the same operating conditions, figure 4.28 shows the generator torque, stator active power, grid-side converter active power and total active power. The equations used

for active and reactive power calculation of the generator are based on terminal voltages and currents as shown in equations (3.38) and (3.39).
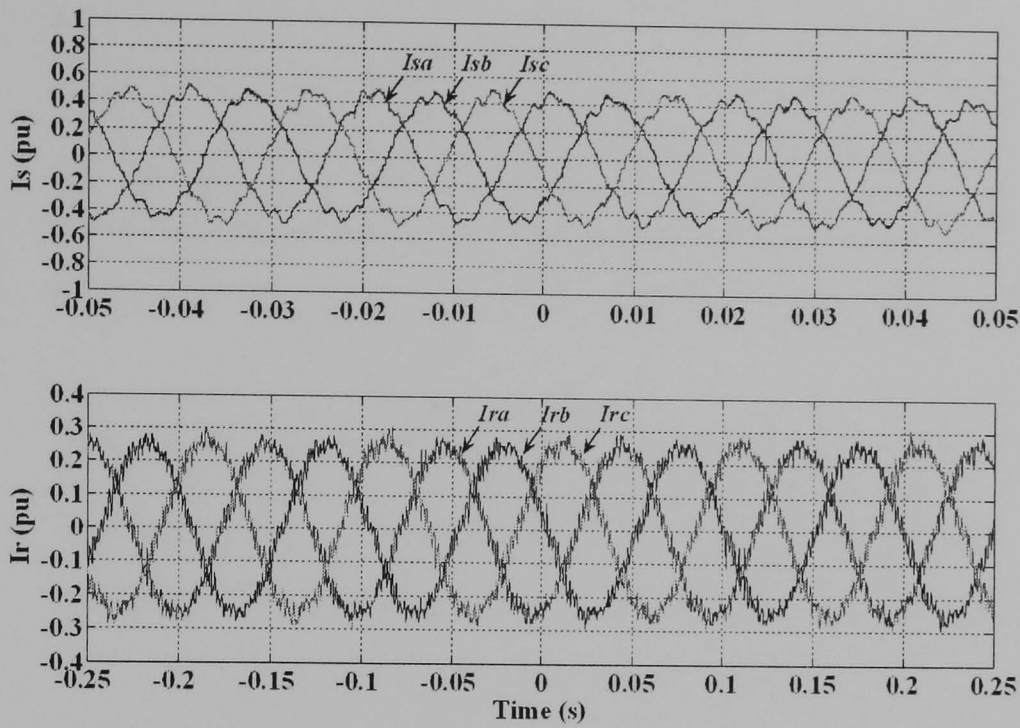
Figure 4.27 Experimental results showing stator and rotor current waveforms for steady-state operation at 0.8 pu sub-synchronous speed generation
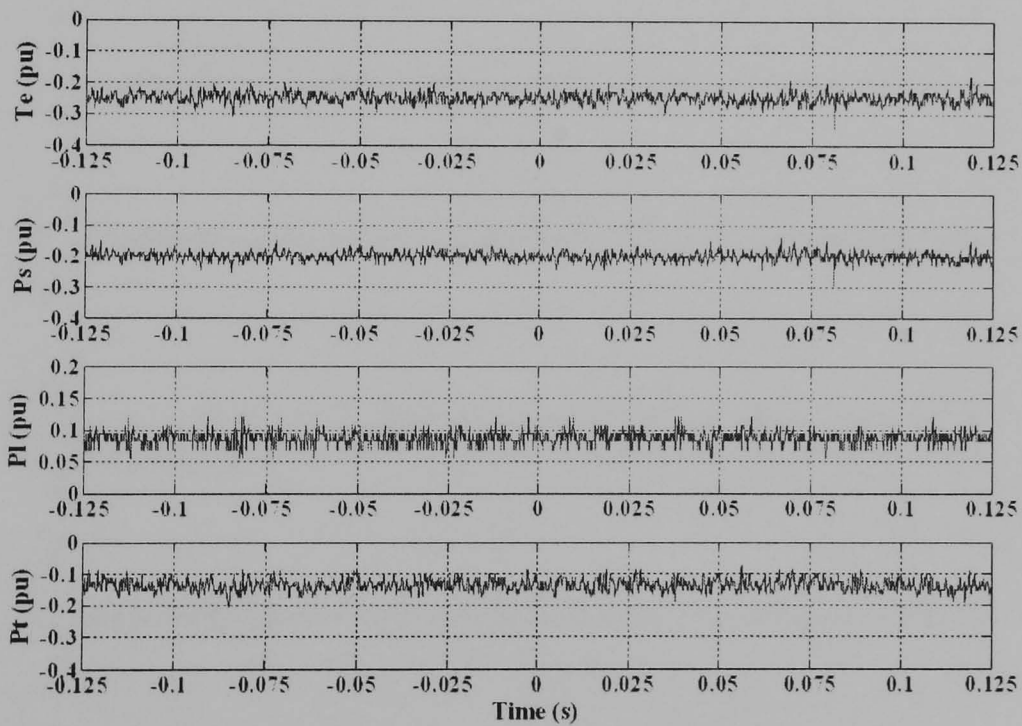
Figure 4.28 Experimental results showing generator torque, stator active power, grid-side converter active power and total active power for steady-state operation at 0.8 pu sub-synchronous speed generation

Figure 4.29 shows the stator current and rotor current waveforms for steady-state operation with super-synchronous speed generation. (1.2 pu speed 1800 rpm). Under

the same operating conditions, figure 4.30 shows the generator torque, total active power, stator active power and grid-side converter active power.
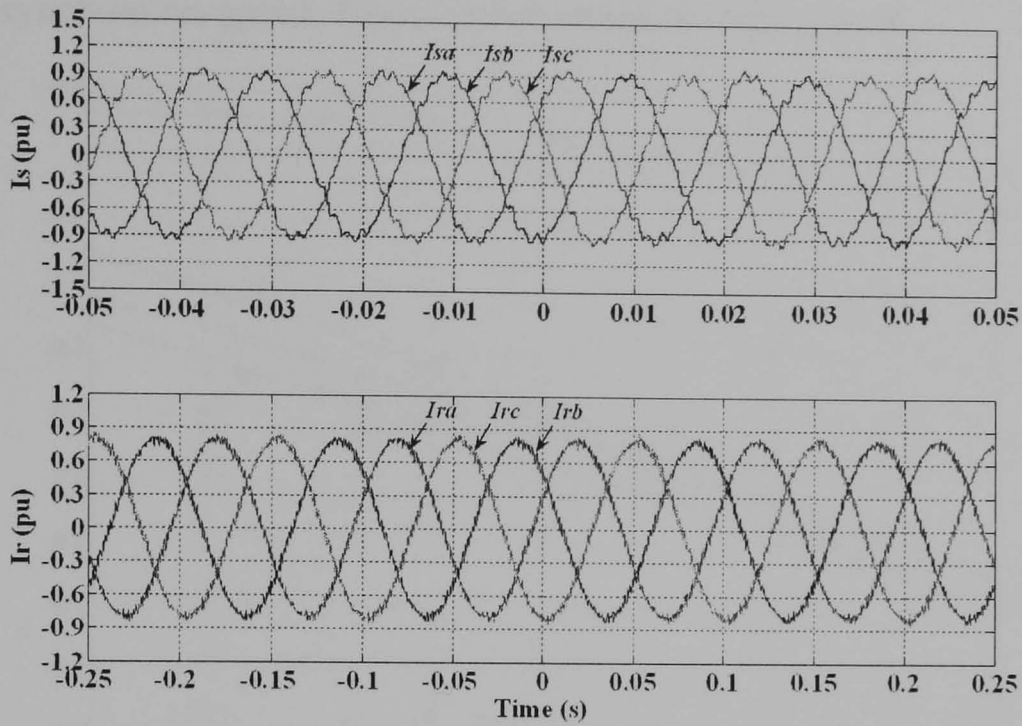
Figure 4.29 Experimental results showing stator and rotor current waveforms for steady-state operation at 1.2 pu super-synchronous speed generation
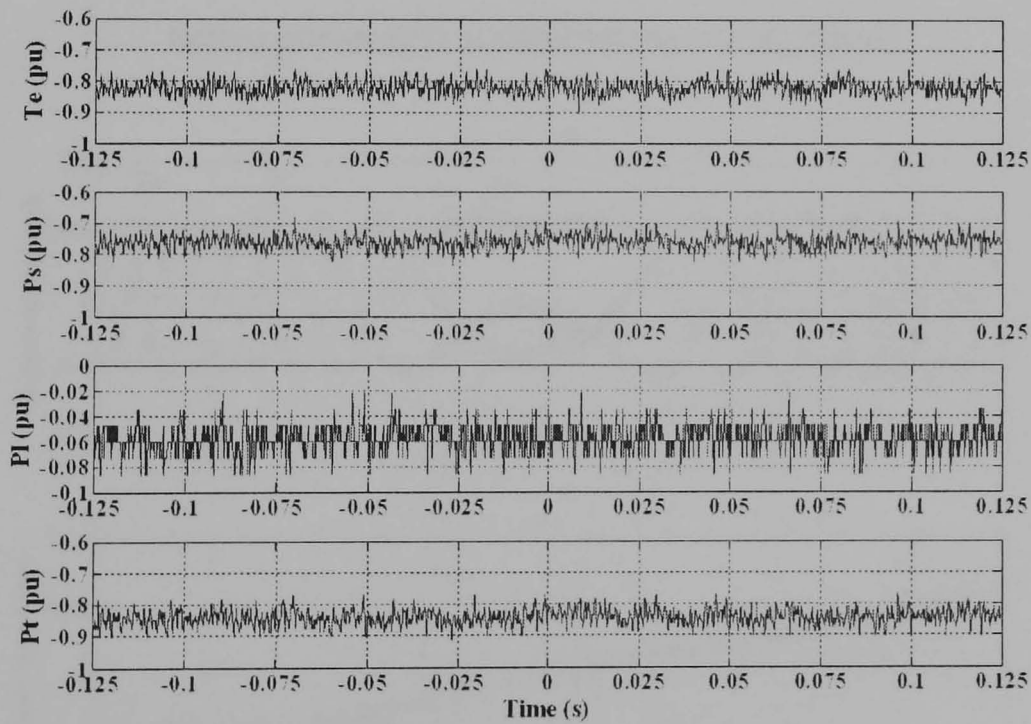
Figure 4.30 Experimental results showing generator torque, stator active power, grid-side converter active power and total active power for steady-state operation at 1.2 pu super-synchronous speed generation

Figure 4.31 shows the mean value of electromagnetic torque, stator active power, grid-side converter active power and total active power at different driven torque and

operating speed calculated from average wind speed. As shown in this figure, the grid-side converter active power is close to zero at approximately 1.065 pu speed instead of synchronous speed. This is due to losses in rotor circuit.
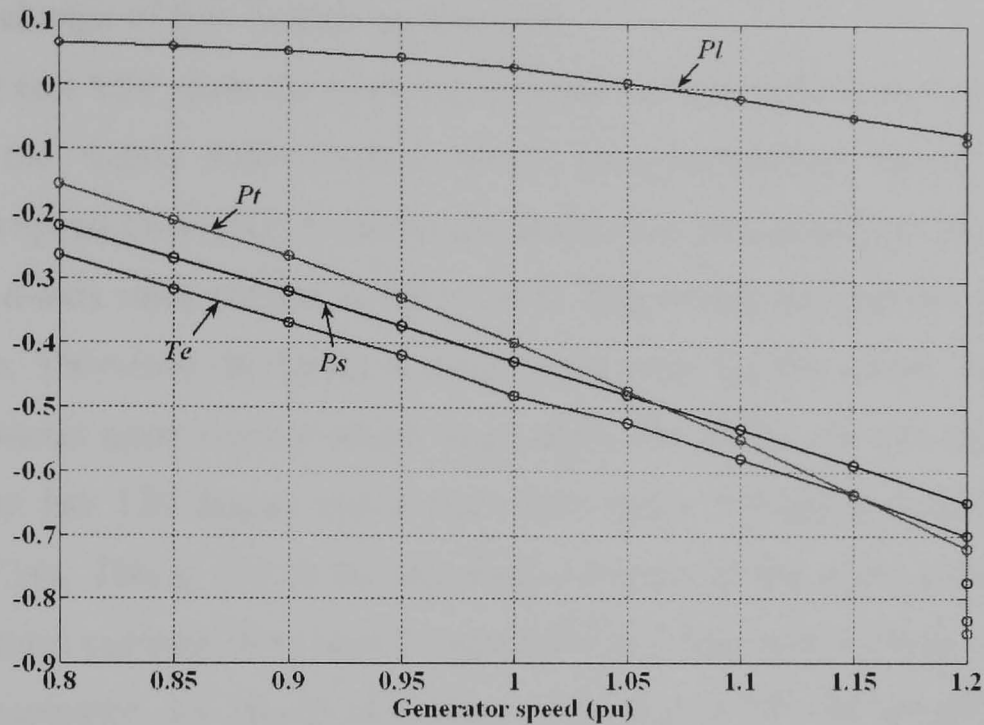
Figure 4.31 Experimental results showing average value of the electromagnetic torque (Te), total active power (Pt), stator active power (Ps) and grid-side converter active power (Pl) at different operating speed
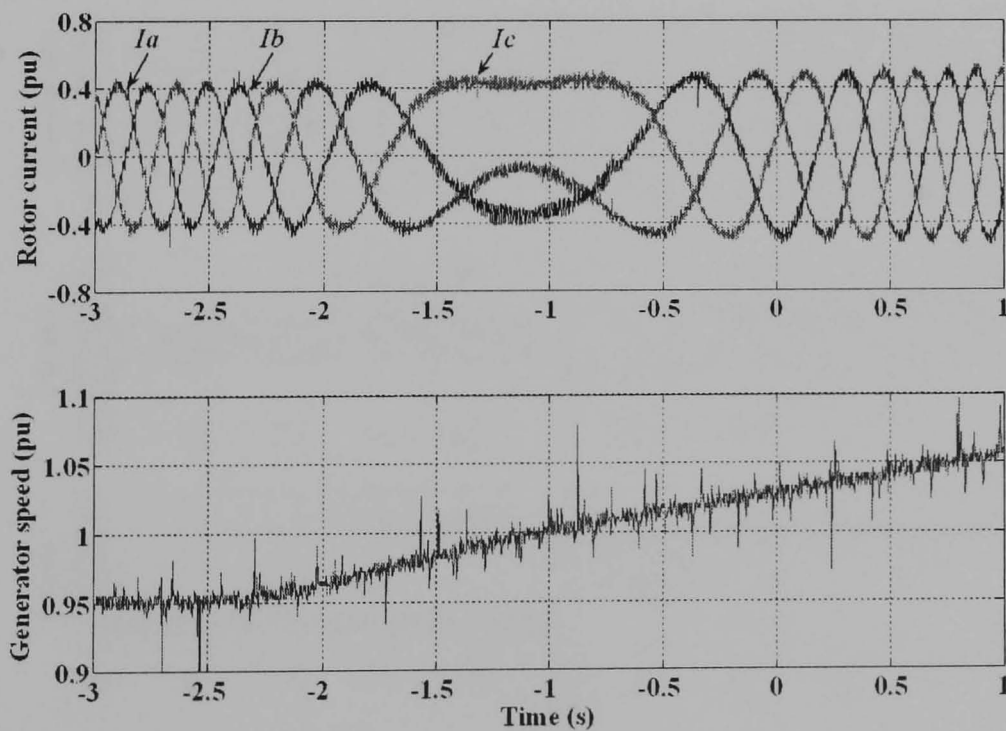
Figure 4.32 Experimental results showing operation through synchronous speed

Figure 4.32 shows rotor currents and generator speed for operation through synchronous speed. As shown by the rotor current waveform, the phase sequence is

changed from abc at sub-synchronous speed to acb at super-synchronous speed. As discussed for the simulation results of figure 4.15, the phase sequence of the generator rotor must be changed to produce counter-rotating rotor flux which opposes the change of flux linkage on the rotor.

Figures 4.33 and 4.34 show the response of stator current and rotor currents to a step change in the d-axis rotor current under sub-synchronous speed and super-synchronous speed generation respectively. Before the step change in the d-axis rotor current, the d-axis rotor current is set to zero. This means the reactive power at the rotor is zero. Therefore the DFIG is magnetised only via the stator. After the step change of d-axis rotor current which magnetises the DFIG via the rotor only, the stator current has 180 degree phase shift from stator voltage as shown in figures 4.33a and 4.34a. This is due to the reference direction of the stator current which is positive if stator currents flow into the generator and negative if stator currents flow out of the generator. As shown in figures 4.33b and 4.34b, the amplitude of rotor currents is increased because of magnetisation via the rotor. The rotor currents now consist of both torque producing current and flux producing current. Likewise, the amplitude of stator current is decreased, as shown in figures 4.33a and 4.34a.
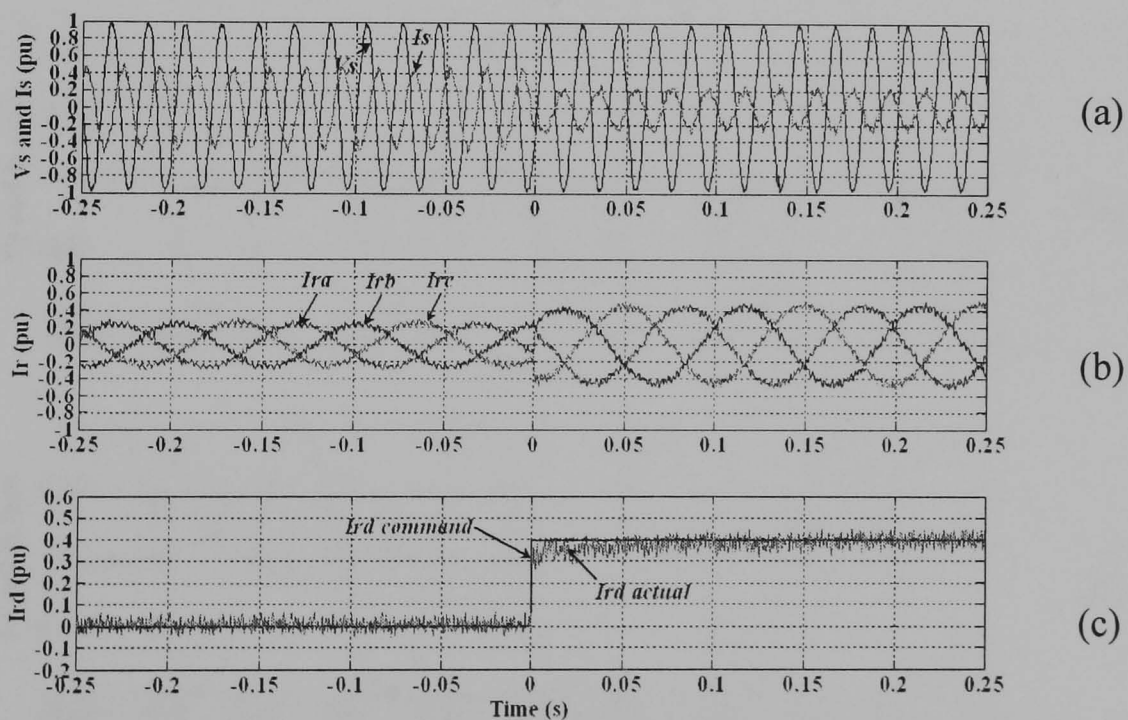
Figure 4.33 Experimental results showing the response to a step change in reactive power at 0.8 pu sub-synchronous speed generation (a) stator voltage and current, (b) rotor currents and (c) d-axis rotor current
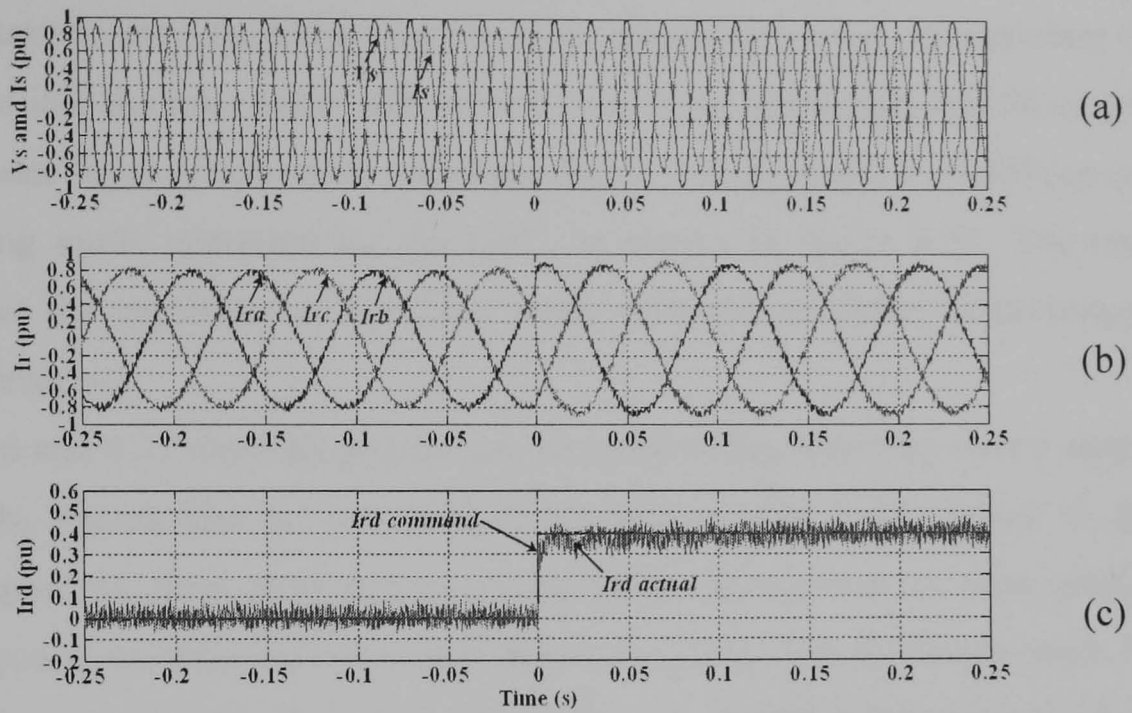
Figure 4.34 Experimental results showing the response to a step change in reactive power at 1.2 pu super-synchronous speed generation (a) stator voltage and current, (b) rotor currents and (c) d-axis rotor current

The waveforms in figure 4.35 are grid voltage and transformer primary (grid side) currents.
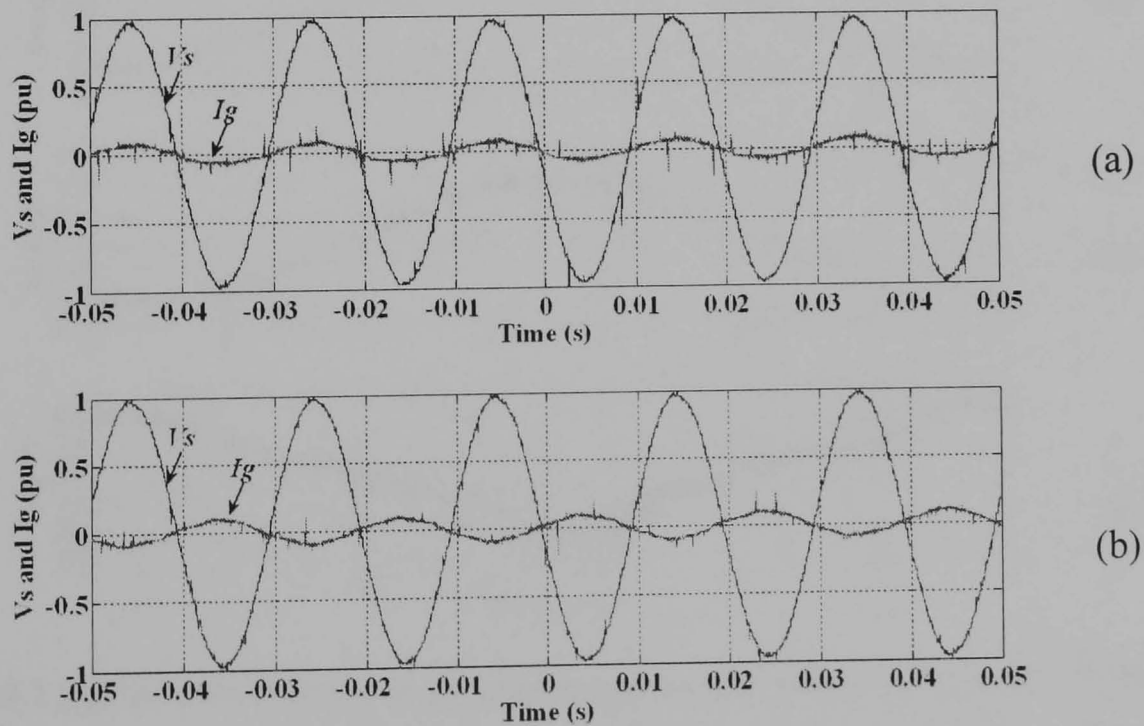
Figure 4.35 Experimental results showing grid-side converter operation under (a) rectifying mode and (b) inverting mode

As mentioned in the simulation results, to make the power factor unity on the grid side of the transformer, the transformer must be magnetised from the converter side. Power flows into the rotor under sub-synchronous speed generation and flows out of the rotor under super-synchronous speed generation which results in rectifying mode and inverting mode operation for the GSC, as shown in figure 4.35. The results shown prove the capability of operation under different condition as presented in several references.

Figures 4.36 and 4.37 show long-term data recorded while operating over a range of wind speeds. Theses data are presented as six relationships - wind speed vs. time, generator speed vs. time, generator torque vs. time, stator power vs. time, grid-side converter power vs. time and generator power vs. time. The operation starts from cut-in wind speed (7 m/s), then moves in steps to maximum wind speed (12.8 m/s) and then back to cut-in speed. A pseudo-random fluctuation in wind speed is included in the wind speed value for the torque command to introduce a realistic wind speed, but not for the speed command of DFIG. Due to high EMI in these measurements, all data are smoothed by moving average filters before plotting.
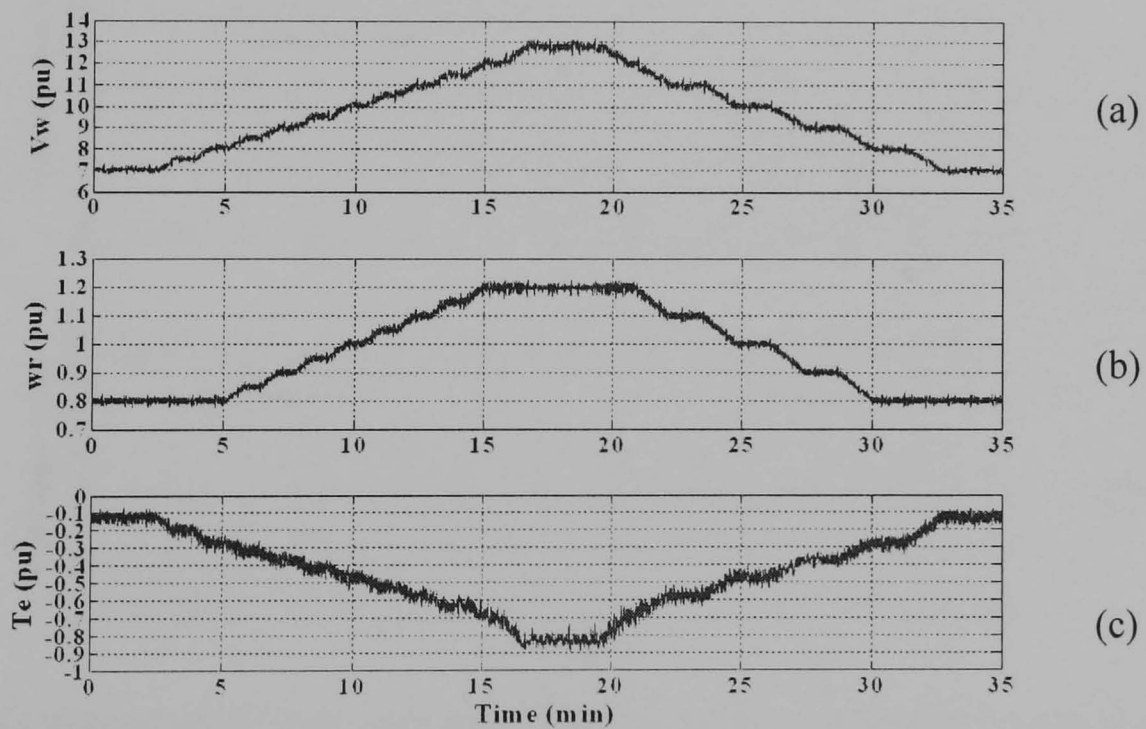
Figure 4.36 Experimental results of long-term operation of the DFIG under different wind speed (a) wind speed (b) generator speed and (c) electromagnetic torque
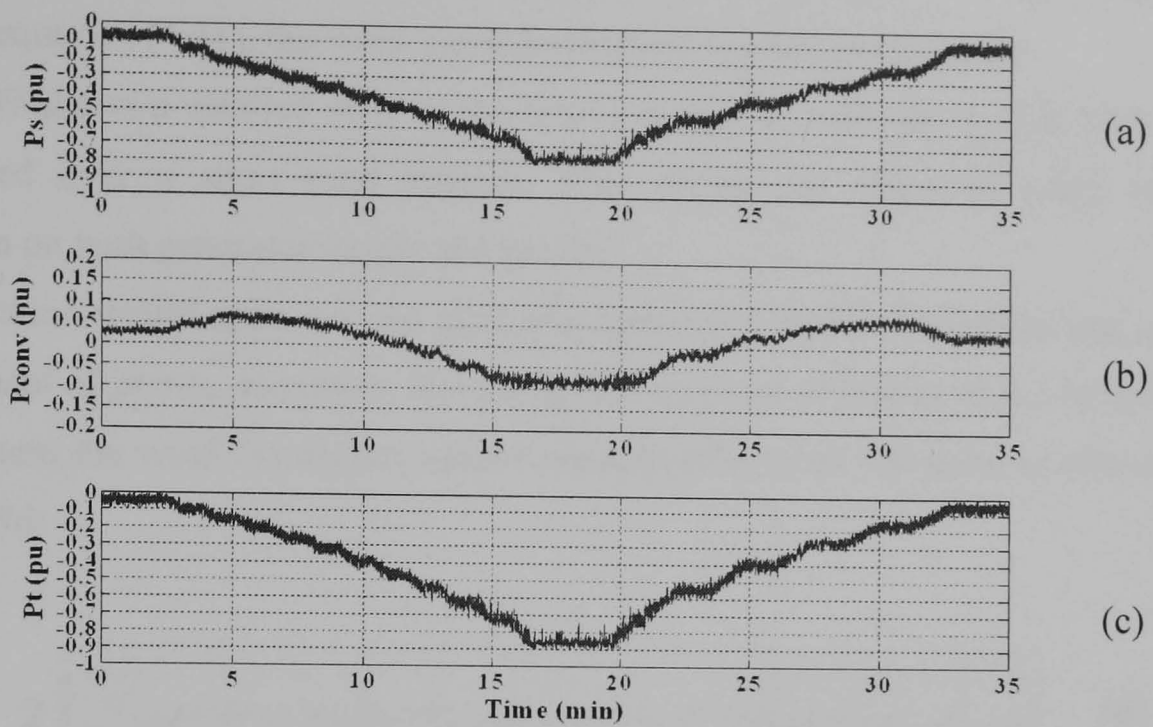
Figure 4.37 Experimental results of long-term operation of the DFIG under different wind speed (a) stator active power (b) grid-side converter active power and (c) total active power
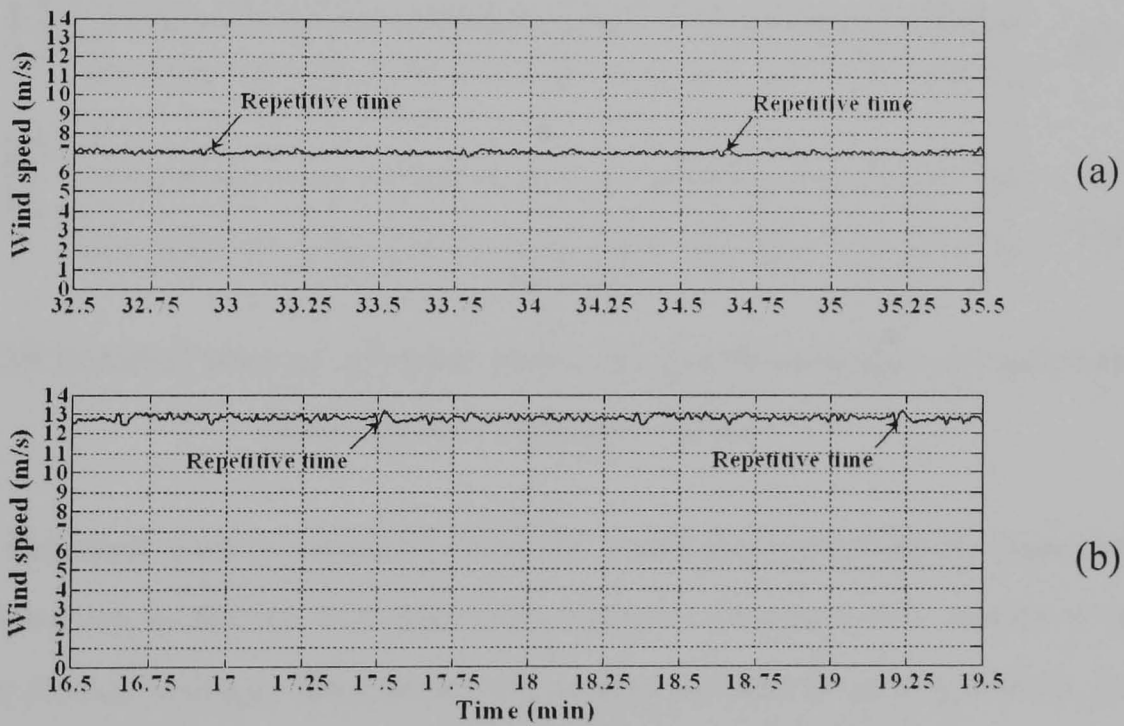
Figure 4.38 Comparison of two wind speed patterns (a) 8m/s wind speed and (b) 12.8 m/s wind speed

Figure 4.38 compares two wind speed patterns having different average values. As shown in equation (4.44), the fluctuation level is proportional to the average wind speed. Therefore, the wind fluctuation is higher at high wind speed and lower at low

98

wind speed. As the wind fluctuation is modelled by the summation of sine waves, as shown in equation (4.44), the wind speed fluctuation appears periodically.

Figure 4.39 shows a detailed view of the results in figures 4.36 and 4.37 at 12.8 m/s wind speed over a short time interval. This shows the effect of wind speed fluctuation on both generator torque and power.

Little variation would appear in the generator speed in a real wind turbine due to its high moment of inertia. However, due to the low moment of inertia of the dc motor-DFIG system the wind fluctuation causes considerable speed variation as shown in figure 4.39d.
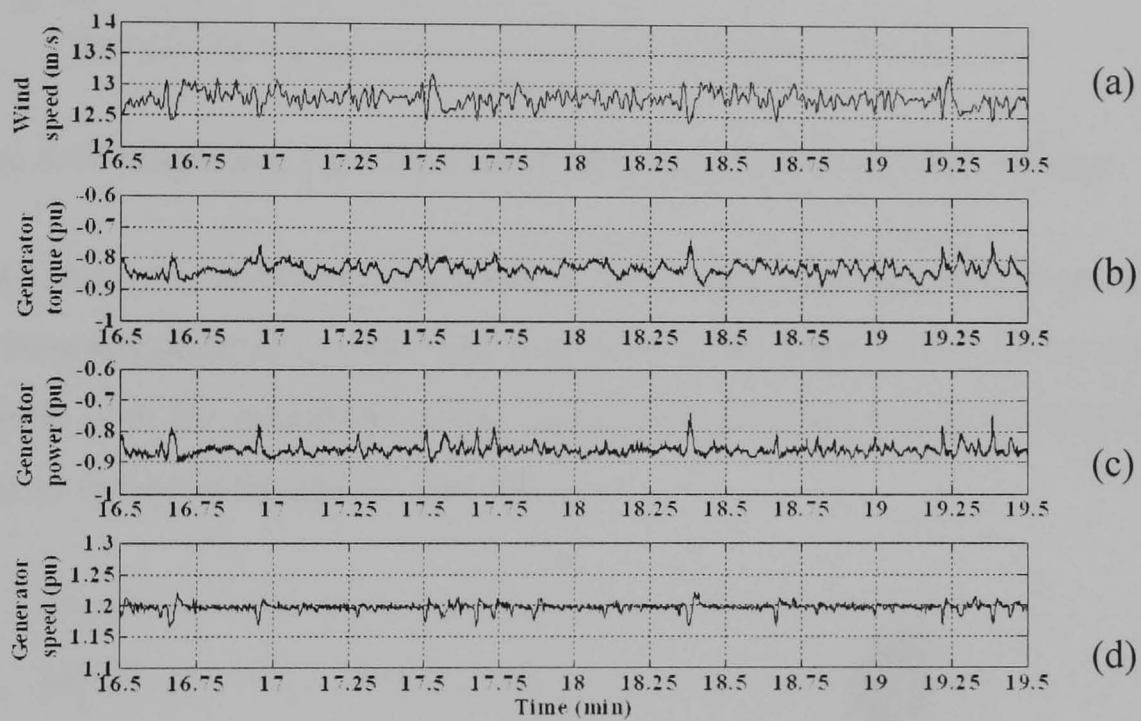
Figure 4.39 Detailed view of (a) wind speed, (b) generator torque, (c) generator power and (d) generator speed

The speed variation causes variation in rotor frequency resulting in rotor power variation. However, as shown in figure 4.40, variation in speed does not have much effect on the dc-link voltage. This means the dc-link voltage is well regulated, as can be seen from the detailed dc-link voltage variation, which is below 1%.
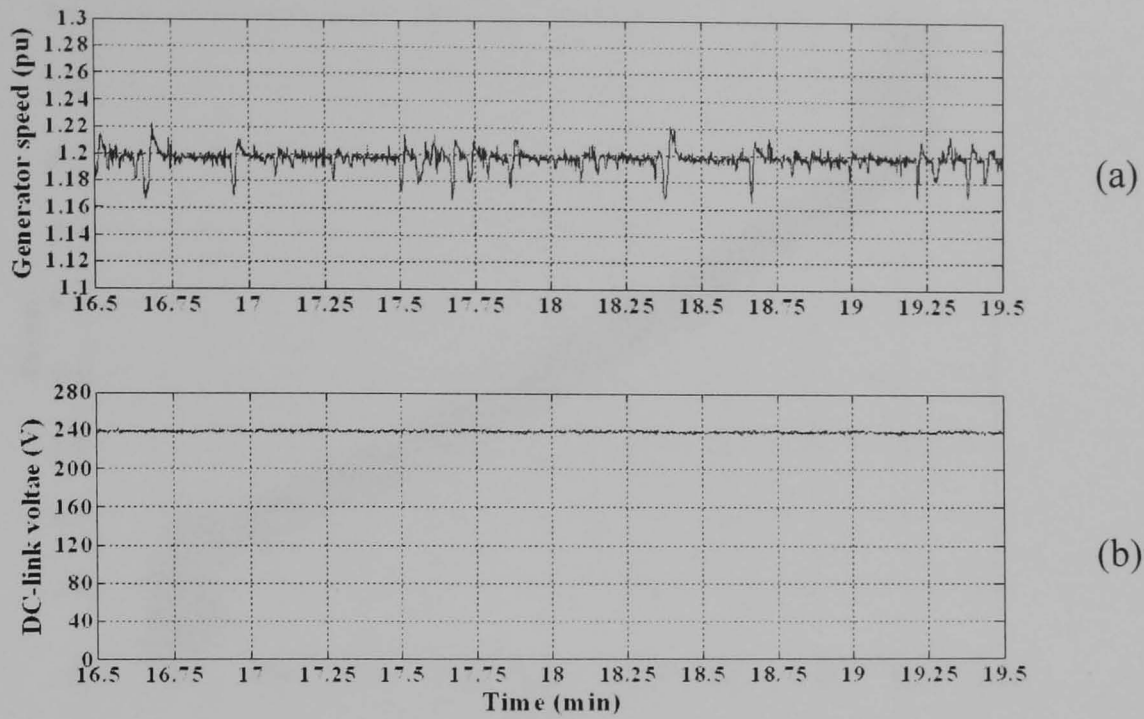
Figure 4.40 Magnified view of (a) generator speed and (b) dc-link voltage

Figures 4.41 and 4.42 show the relationship between generator torque and generator speed and between generator power and generator speed respectively. These results are compatible with the maximum power point and optimised torque for maximum power point as shown in figures 4.7 and 4.8.
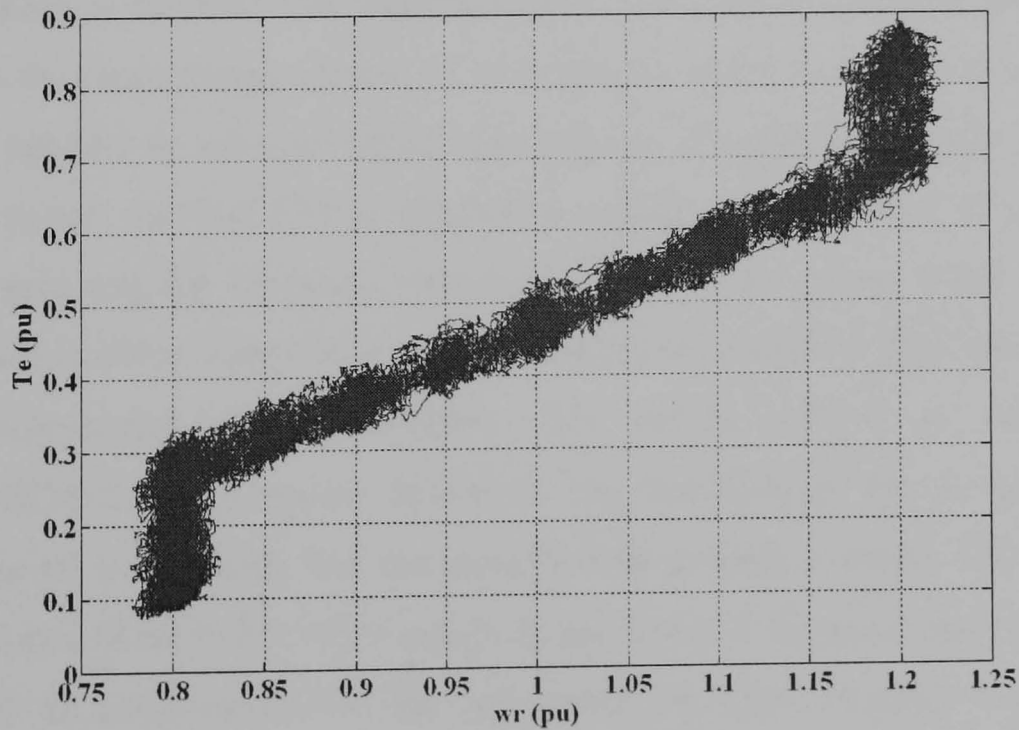
Figure 4.41 Electromagnetic torque vs. generator speed curve
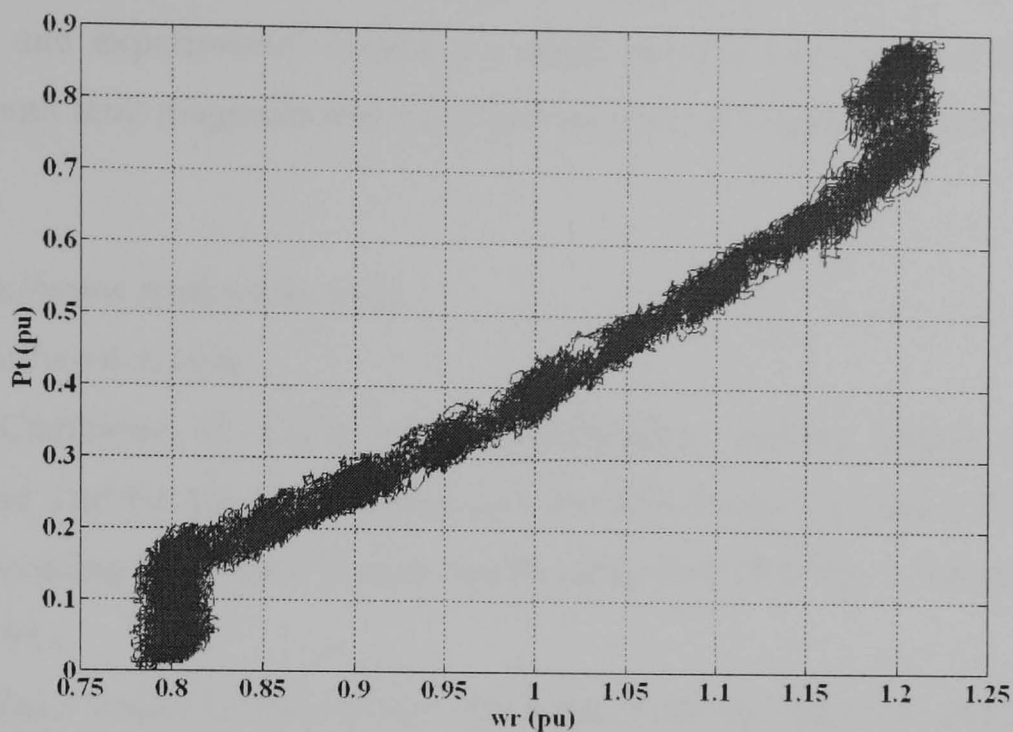
Figure 4.42 Generator power vs. generator speed curve

4.4 Summary

The necessary equations and methods required for simulation and experiment are summarised in this chapter. Both simulation and experimental systems are in discrete form, therefore, continuous model are discretised. For control of the MSC, the stator flux estimation is required and implemented by the method used for the sensorless application for direct torque control of an induction motor as discussed in chapter 3. A PLL is applied to estimate stator flux angular frequency and help smooth the frequency signal. Another PLL is applied to voltage vector control of the GSC for angle and grid angular frequency estimation. In the case of the wind turbine, the model of wind turbine acquired from MATLAB/SIMULINK as discussed in chapter 2 are implemented in this chapter. The whole system is simulated in MATLAB/SIMULINK program. However, the modification for an asynchronous machine model is required. For the experimental system, a single DSP is used to perform control of the MSC, GSC and dc motor. Up to 8 variables can be output and recorded by an oscilloscope for one experiment via DAC channel. For long-term operation, the results are captured by a National Instruments data acquisition card. The long-term operation results confirm that the experimental system can operate under fluctuated input torque and can operate for a long period of time without any

problems. Therefore, all simulation and experimental results confirm that, the simulation and experimental system are ready for the main part of this research which is about fault diagnosis and reconfiguration for the fault in power converters.

Reference

4.1. http://www.mathworks.com

4.2. http://www.ti.com

4.3. H. Camblong, G. Tapia, and M. Rodrı́guez, 'Robust Digital Control of a Wind Turbine for Rated-Speed and Variable-Power Operation Regime'. IEE Proceeding of Control Theory Application, Vol. 153, No. 1, January 2006, pp. 81–91.

4.4. P. Vas, 'Vector Control of AC Machines'. Oxford University Press, 1991.

4.5. P. Vas, 'Sensorless Vector and Direct Torque Control'. Oxford University Press, 1998.

4.6. V. Kaura and V. Blasko, 'Operation of a Phase Locked Loop System under Distorted Utility Conditions'. IEEE Trans. on Industry Applications, Vol. 33, No. 1, January/February 1997, pp. 58–63.

4.7. S. K. Chung, 'Phase Tracking System for Three Phase Utility Interface Inverters'. IEEE Trans. on Power Electronics, Vol. 15, No. 3, May 2000, pp. 431-438.

4.8. A. M. Salamah, S. J. Finney, and B. W. Williams, 'Three-phase phase-lock loop for distorted utilities'. IET Proceeding of Electric Power Applications, Vol. 1, No. 6, November 2007, pp. 937-945.

4.9. Z. Lubosny, 'Wind Turbine Operation in Electric Power Systems'. Springer-Verlag Berlin Heidelberg, 2003.

4.10. http://focus.ti.com/docs/toolsw/folders/print/sprc080.html

4.11. http://focus.ti.com/docs/prod/folders/print/tms320f2812.html

4.12. http://focus.ti.com/docs/toolsw/folders/print/tmdsezs2812.html

4.13. http://focus.ti.com/lit/ug/spru061c/spru061c.pdf

4.14. http://focus.ti.com/lit/ug/spru078e/spru078e.pdf

4.15. http://www.semikron.com

Chapter Five

Faults and Fault Diagnosis Methods in Electrical Drives

This chapter reviews the previous work on open-switch fault and short-circuit switch fault diagnosis in electrical drives. Basically, the diagnostic task can be classified into three steps - feature extraction or fault detection, fault identification and corrective action. The review starts with variable speed electrical drives and their protection [5.1] followed by the analysis of open-switch faults and their effects on the current and other variables of the drive. Other research on open-switch fault diagnosis is surveyed and classified into different approaches. The advantages and drawbacks of each method are also discussed. The analysis and effects of a short-circuit switch fault are then discussed. Previous work done on diagnosis of this fault is discussed and the advantages and drawbacks of each method are discussed.

5.1 Fault Protection Used in Conventional Inverter Drives

Inverter-fed drives are widely used in industry. In such applications, the reliability of the inverter system is highly important. An example of an inverter-fed drive is the open-loop volt/Hz control of an induction motor as shown in figure 5.1.
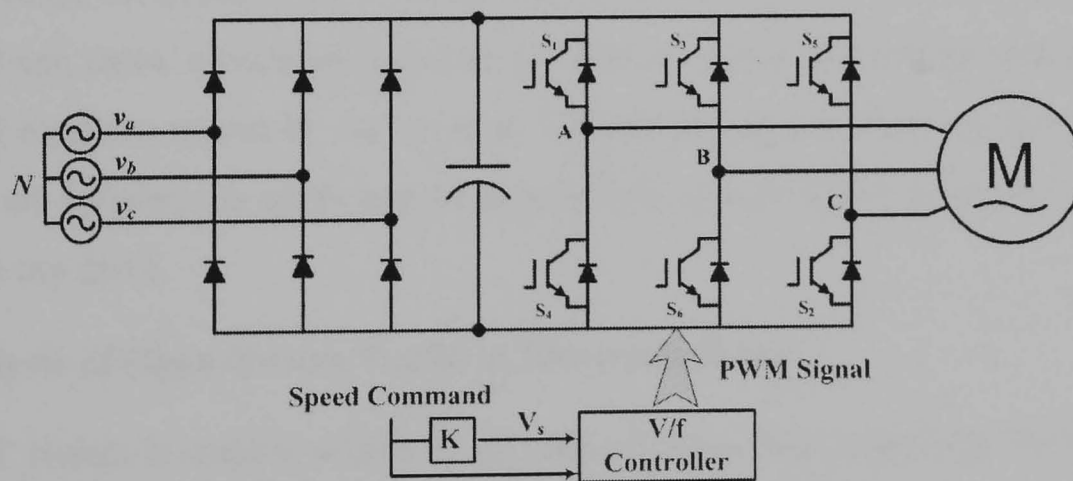
Figure 5.1 Voltage-fed AC drive based V/f control

This system consists of six-diodes on the rectifier side, a dc-link capacitor and six power semiconductor switches with six anti-parallel recovery diodes. Various possible fault modes have been reviewed by Kasha [5.1]. Such faults can be passively protected by the conventional protection system as shown in figure 5.2.

The input circuit breaker trips for steady state overcurrents whereas the metal oxide varistors protect the system against overvoltage. Input fuses will blow when a short circuit appears in the diode rectifier or dc-link capacitor. The fuse in the dc link protects the system from switch rupture caused by shoot-through faults in the voltage-fed inverter. Overtemperature conditions in the induction motor are protected by the circuit breaker activated by a thermal-relay. With this protection system, the components and motor are protected from severe damage such as explosive rupture, but the system shuts down which consequently causes down time.
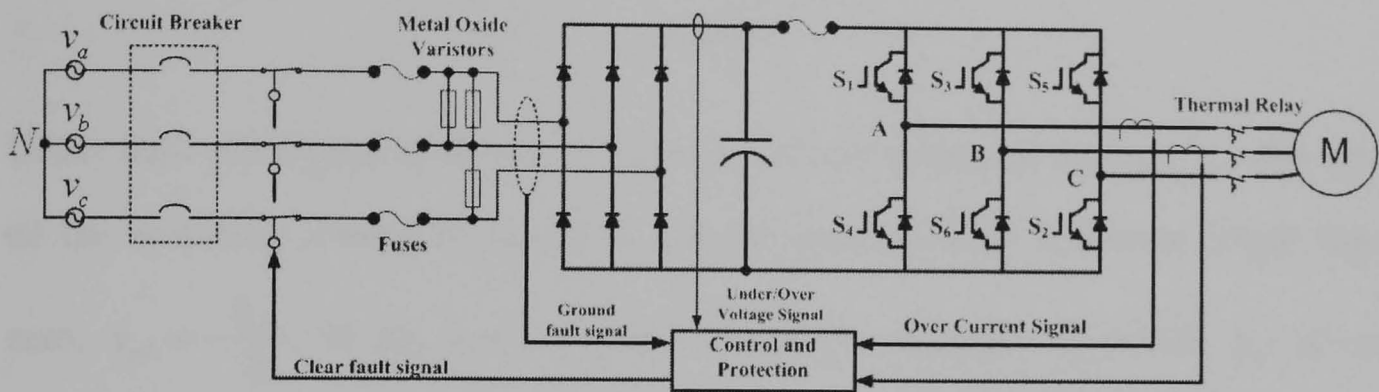
Figure 5.2 The structure of conventional drive system with protection

The protection system discussed above has no ability to determine whether the fault is critical or not. It operates when its protection variables exceed some threshold. For instance, if the machine is operating under light load conditions, an open-switch fault will not cause an overcurrent condition to activate protection devices. Nevertheless, this fault can cause catastrophic failure of other switches and mechanical parts of an electrical machine driven by the inverter. Understanding the effect of an open-switch fault on all variables is necessary to successfully detect it and to prevent a cascade failure in the drive.

5.2 Analysis of Open-Switch Faults in Electrical Drives

An IGBT switch is usually driven by an isolated gate drive amplifier. Malfunction of this unit can cause either an open-circuit switch or a short-circuit switch. An open-switch fault is usually caused by misfiring pulses from the gate drive unit. Once a switch in a converter leg becomes open circuit, only the anti-parallel diode is connected to either positive or negative dc bus, depending on which switch is faulty. The equivalent circuit of the faulty leg is shown in figure 5.3.
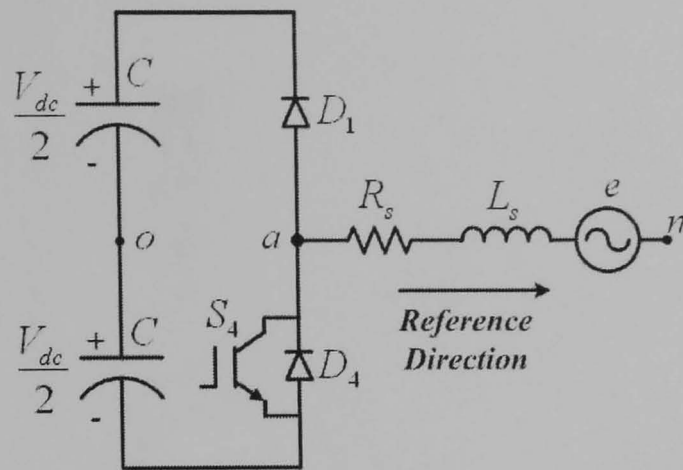
Figure 5.3 Circuit diagram of an inverter leg with an open-switch fault in the top switch

Under fault conditions, as shown in figure 5.3, the inverter pole voltage v_{a0} depends on the switching pattern of switch S_4. In the case of phase A current larger than zero, $v_{a0} = -\dfrac{V_{dc}}{2}$. In the case of phase A current negative, if switch S_4 is on $v_{a0} = -\dfrac{V_{dc}}{2}$ and if S_4 is off, $v_{a0} = \dfrac{V_{dc}}{2}$. A simulation model in MATLAB/SIMULINK for demonstrating an open-switch fault in the top switch of leg A of a conventional inverter-fed volt/Hz controlled induction motor is shown in figure 5.4

Figure 5.4 Simulation model for an open-switch fault in V/f system

5.2.1 Effects on Machine Currents

After the fault appears, phase A of the converter is connected to the positive dc bus via the diode. Under this condition, if the current in phase A is positive and switch S_1 is inoperative, i_a is connected to the negative bus via diode D_4 and consequently i_a decreases to zero. Under steady state conditions [5.2], since the purely inductive circuit in the electric machine cannot support any dc voltage, the current is biased either positive or negative for the whole cycle. Since the sum of the three-phase currents is zero, the healthy phase currents also have dc offsets with a sum equal to the dc offset of the faulty phase but of opposite sign. The current waveforms and torque-speed characteristic curve of the induction motor under open-switch fault conditions are shown in figures 5.5a and 5.5b respectively.
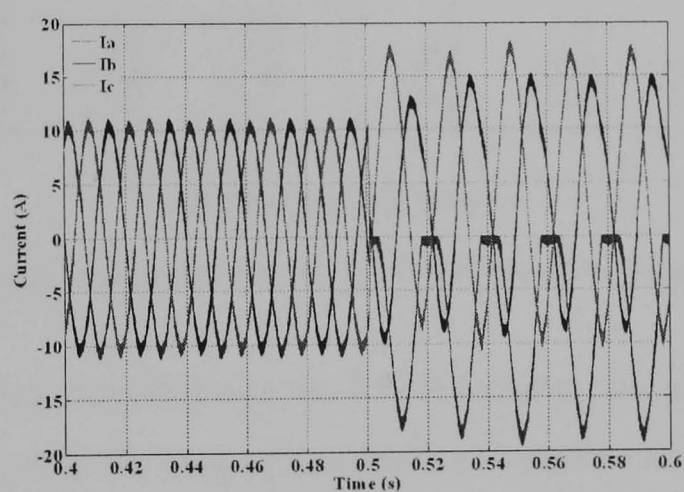
(a)
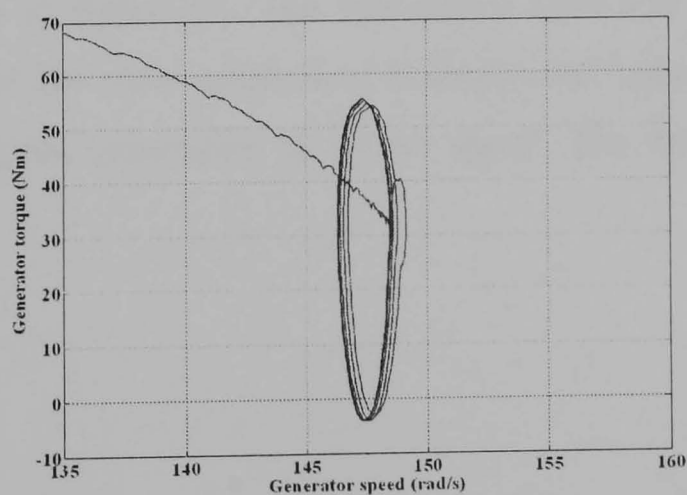
(b)

Figure 5.5 Simulation results showing (a) three-phase current waveforms and (b) torque-speed curve of the induction motor for an open-switch fault appearing at the top switch of phase A of the converter

i. Open-Switch Fault in a Closed-Loop PWM Rectifier

The PWM rectifier is generally used in a regenerative induction motor drive system. The ac side is connected to the grid and the dc side is connected to the dc-link capacitor, as shown in figure 5.6. This back-to-back topology is used to improve the quality of the grid interface including control of the grid power factor. In the PWM rectifier, the reference current direction is flowing to the converter, opposite to that for the inverter which is generally connected to an electrical machine in the drive system.
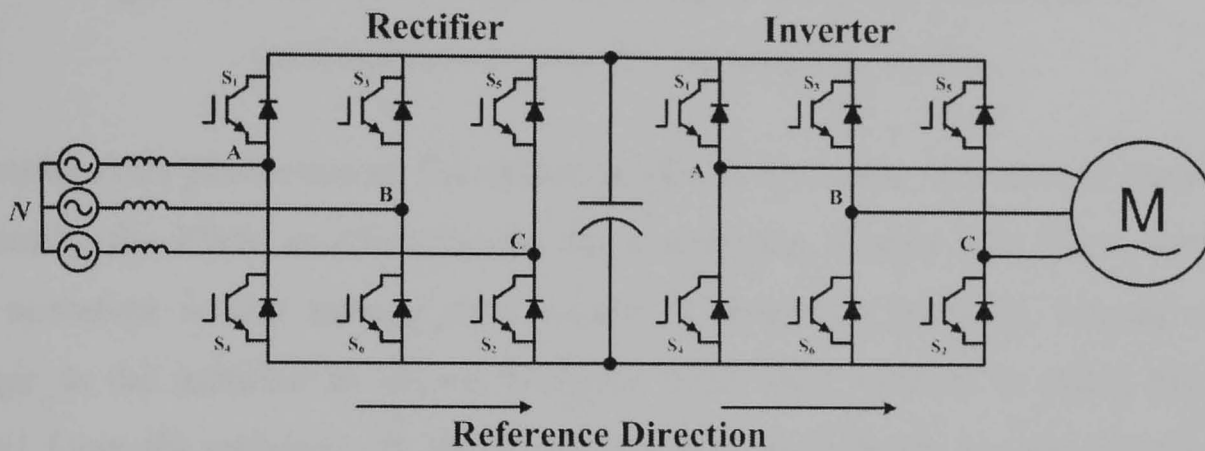
Figure 5.6 The induction motor drive with back-to-back converters

Under open-switch fault conditions in the PWM rectifier, the current in the faulty leg does not remain zero as in the case of the inverter. Current can flow through the anti-parallel diode associated with the faulty switch, allowing current to flow in the faulty half cycle, as shown in figure 5.7. The waveforms shown in figure 5.7 are the ac current waveforms of the rotor currents of a doubly-fed induction generator under super-synchronous speed generation at 1.2 pu speed. The fault appears in the top switch of phase A.

(a)   (b)
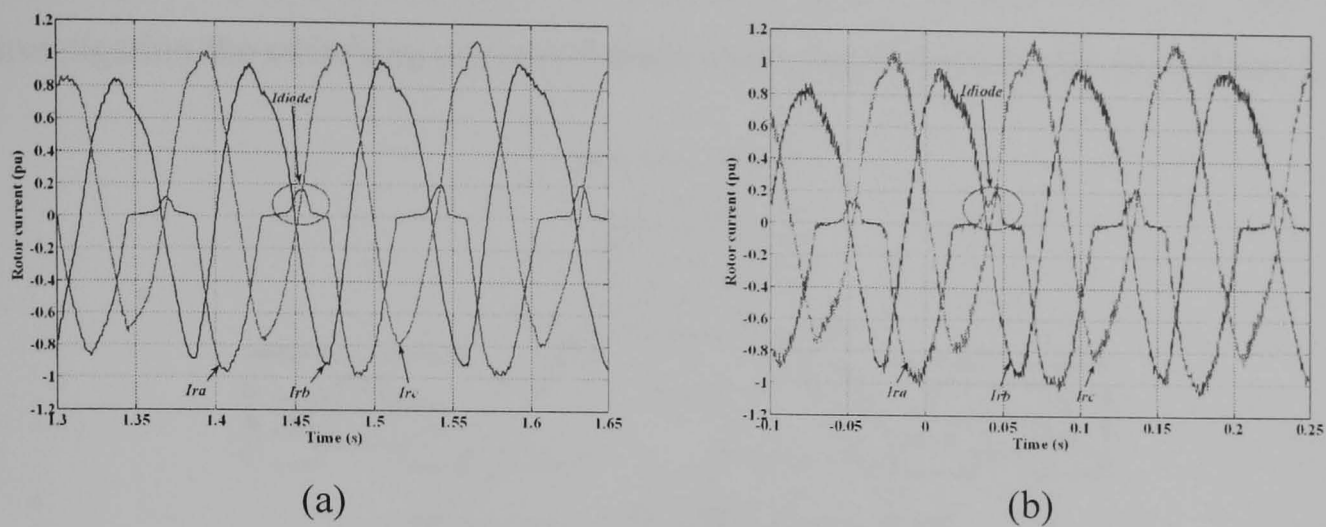
Figure 5.7 The diode current appearing in the faulty phase current

(a) simulation results (b) experimental results

To explain this phenomenon, the operation of a dc-dc boost converter is considered. Generally, the PWM rectifier has the same operating scheme as a boost converter. The operation is first turning on a switch to charge an inductor, causing energy storage in the inductor as shown in figure 5.8a. This duration is called the boost period. Once the switch is off, the energy stored in the inductor is released to the load through a diode, as in figure 5.8b.

(a)   (b)
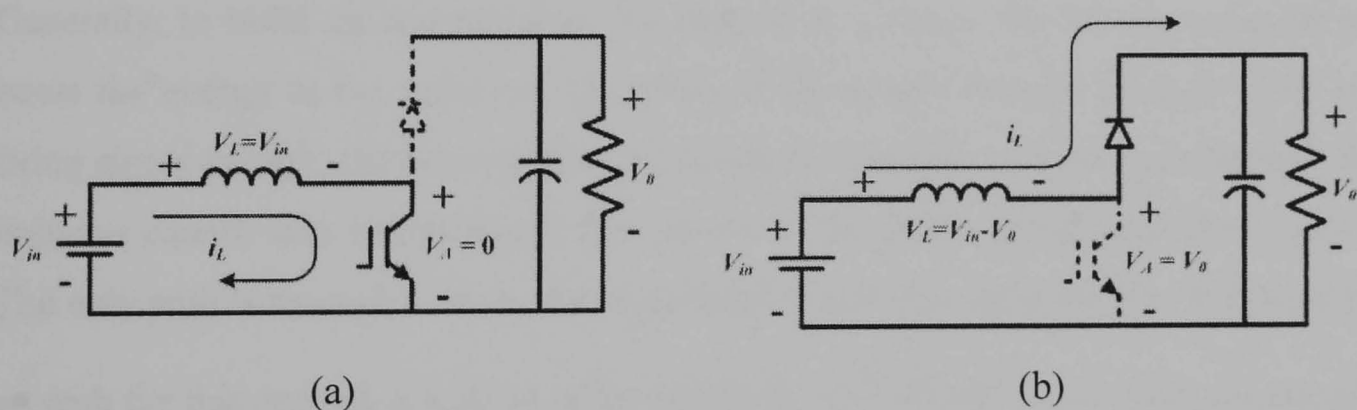
Figure 5.8 Boost converter operation mode (a) boost mode, (b) freewheeling mode

The semiconductor switch is thus responsible for boosting energy to the inductor, whereas the diode is responsible for freewheeling energy to the high voltage side. The same principle applies to a three-phase PWM rectifier. During the boost period of each phase for positive current, current from the ac source flows through the bottom IGBT and then via the diode of another phase, connected to the same negative dc bus. The same operation for negative current occurs with the top switch of the phase and the top diode of another phase.

Since space vector modulation is used to control the converter, for ease of investigation the switching pattern of space vector modulation is shown in figure 5.9
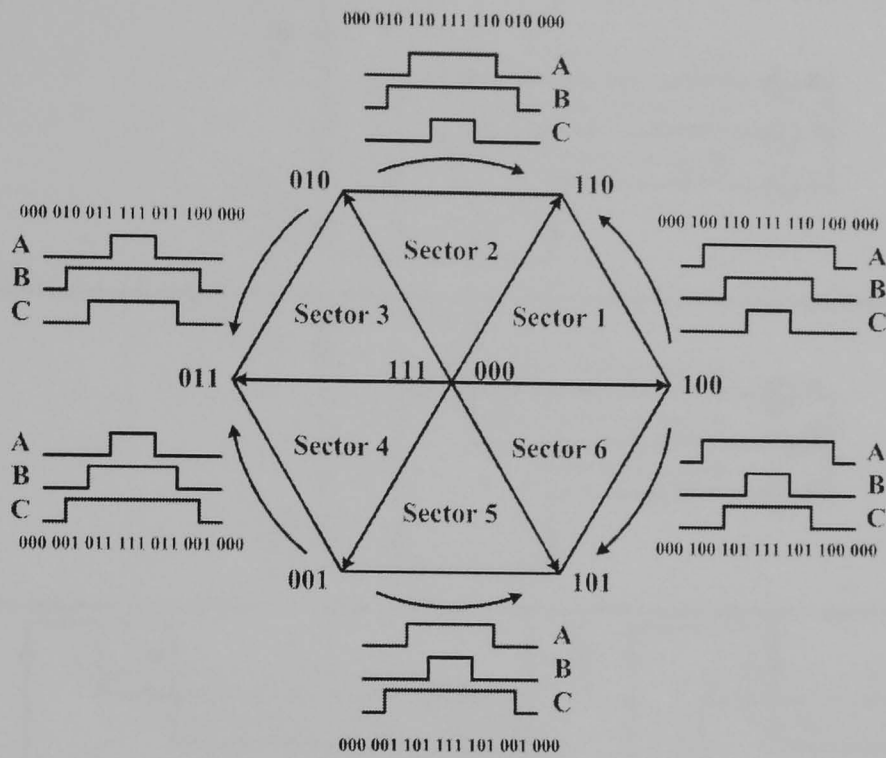
Figure 5.9 Switching pattern of the space vector modulation

To clearly explain the appearance of diode current, the example of an open-switch fault at the top switch of phase A of the grid-side converter is shown in figure 5.10. Generally, to build up and maintain the desired dc voltage, the switches require to boost the energy in the inductor. Therefore, if the switch is open (faulty) while its firing signal is high, the boost period is cancelled. Since the current flow through an inductor cannot stop immediately, the current of the faulty phase must find a path. The only path is through a diode that is associated with the faulty switch. If there was no path for this current, a voltage spike caused by $L\dfrac{di}{dt}$ would occur with consequent damage to the converter.

Signal	Healthy Condition	Faulty Condition
000		
010		
110		
111		
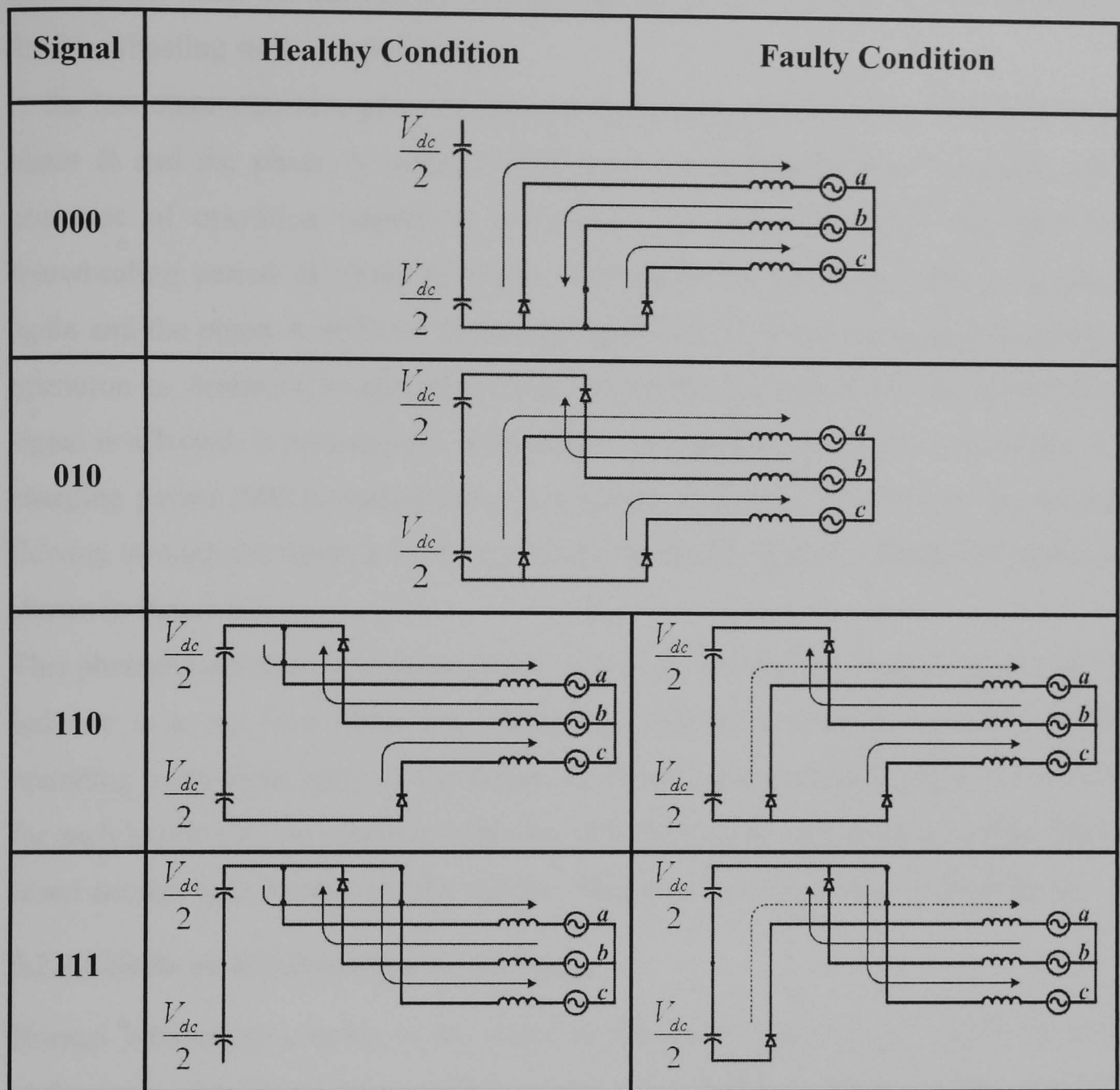
Figure 5.10 The current flow diagram of the faulty converter

The interpretation of this phenomenon is shown in figure 5.10. Beginning with the first command signal 000, phase B of the converter is in the boost state whereas the other phases are in the freewheeling state. As explained before, during the boost state the currents flowing through phase B switch will flow to other phases connected to the same dc bus. Therefore, the sum of the currents through the other phases is equal to the current in phase B inductor.

During the second command, 010, all three phases are in the freewheeling state. The current flowing in phase A is equal to $i_b - i_c$.

During command 110, phase A top switch should conduct current and phase A should be in boost state. However, because of the open-switch fault, the boost period

is cancelled. Since the current flowing through the inductor cannot stop immediately, the freewheeling state is maintained.

In the last command 111, phase C is in the boost state and its current flows through phase B and the phase A inductor discharges energy during this command. The sequence of operation returns to command 110 and 010, which maintain the freewheeling period of phase A. Under command 000, phase B becomes boosted again and the phase A inductor is charged again. Since the software for closed-loop operation is designed to minimise error, under faulty conditions the modulating signal is affected. It prolongs the sector that is occupied by the faulty switch and the charging period (000 command) becomes longer than usual. Therefore, the current flowing through the diode is built up until the diode continuously conducts current as shown in figure 5.7.

This phenomenon does not appear in the case of an inverter because the main task of inductor is to act as a filter. The operation is similar to a buck converter. While operating away from unity power factor, the diode peak current is reduced because, for each half cycle, the converter operates in both inverter and rectifier modes. There is not enough time for the rectifier mode to maintain current to flow through diode.

5.2.2 Effects on Electromagnetic Torque

Normal three-phase current in the stator of the motor generates an MMF wave in each phase. Their vectorial sum becomes the resultant MMF having constant magnitude rotating at synchronous speed, $\omega_s = \dfrac{2\pi f}{P}$ where f is the supply frequency and P is the number of pole pairs. This results in smooth electromagnetic torque. However, if an open-switch fault appears in the inverter supplying the stator of the motor, dc components appear in the phase currents and the fundamental component of the faulty phase current is reduced as shown in figure 5.11.

(a)   (b)
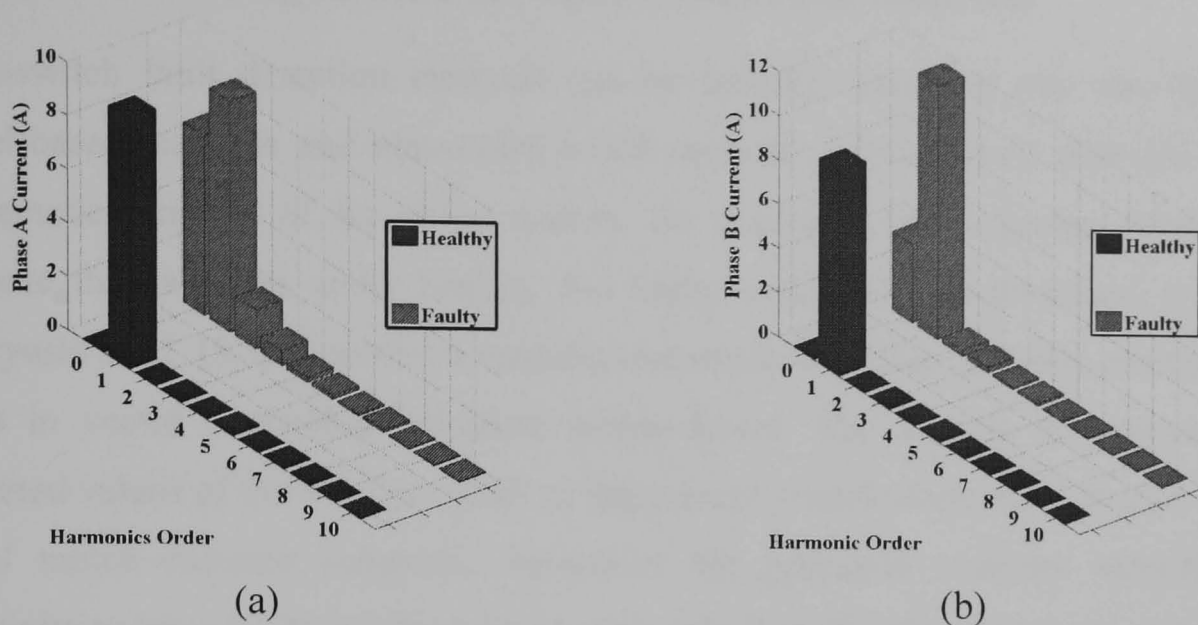
Figure 5.11 Current spectrum of phase A and phase B current during healthy conditions and with an open-switch fault on switch S1 (a) phase A current and (b) phase B current

This unbalanced three-phase current adversely affects the resultant MMF wave. The new MMF wave has a dc component as well as a fundamental component. The dc component is a stationary MMF, its position depending on which phase is faulty, whereas the fundamental component generates a rotating MMF wave. Therefore the strength of the MMF wave becomes unbalanced in the air-gap. The electromagnetic torque will oscillate at line frequency as shown in figure 5.12.
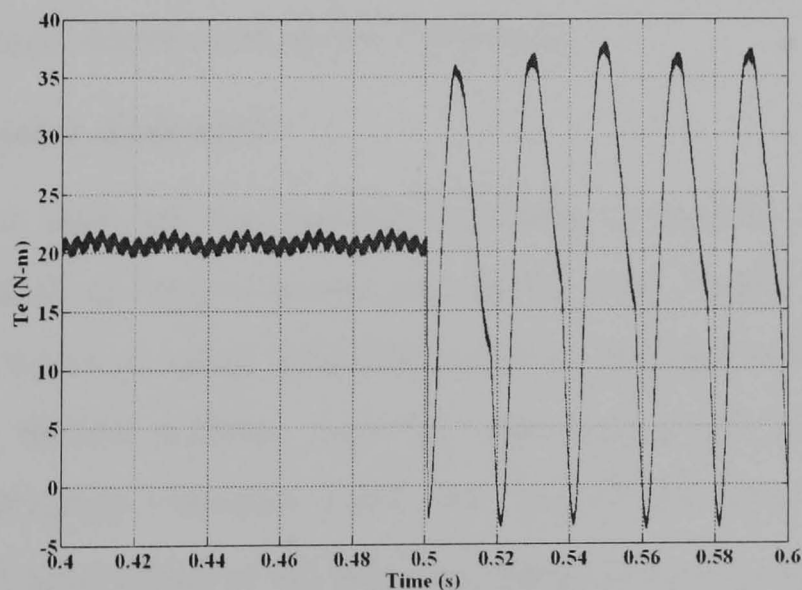
Figure 5.12 Simulation results showing electromagnetic torque of an inverter fed induction motor when an open-switch fault appears in the top switch of phase A of the converter

113

5.3 Review of Existing Methods for Open-Switch Fault Detection

Open-switch fault detection methods can be broadly classified into two types - model-based methods and non-model-based methods. Model-based methods use a mathematical model of the drive system, for example, the redundant model, to compare the variables under healthy and faulty conditions, as presented in [5.2]. Sleszynski *et al.* [5.3] proposed a model-based method applied to detect open-switch faults in vector controlled induction motor drives. The idea is to compare the predicted values of the voltage model or the current model of the drive system to the actual motor currents measured. However, the principal problem identified is sensitivity to error in the machine parameters, which makes the system unreliable. To solve this problem, an online parameter estimation routine is required, but this increases the complexity of the system and also requires a sophisticated mathematical model for this routine.

Non-model-based methods require knowledge of diagnostic variables under faulty conditions. Such knowledge is required to extract the fault signature from the diagnostic variable and is also used to identify and localise the fault. The advantage of non-model-based methods is that they are independent of system parameters and can be applied to highly non-linear systems. Several variables can be used for open-switch fault diagnosis. The best-known variables are three-phase current signals which have been modified, by various methods, to fulfil diagnostic tasks. In this work only non-model-based methods are considered.

5.3.1 Current Vector Approach

The space vector approach has become dominant in modern electrical machine analysis and control, as well as power electronics. The concept is to consider the variables to be a vector in space. This first requires a transformation, called Clarke's transform, from normal n-phase variables into orthogonal two-phase variables $(\alpha - \beta)$ in a stationary reference frame and having the same frequency as the original signals. These variables are then transformed to dc components $(d - q)$ in the chosen reference frame rotating at a specific speed.

In this approach, the current vectors are considered as diagnostic variables. Clarke's transform of three-phase currents is shown in (5.1),

$$i_\alpha = \frac{2}{3}i_a - \frac{1}{3}(i_b + i_c), \qquad (5.1a)$$

$$i_\beta = \frac{1}{\sqrt{3}}(i_b - i_c). \qquad (5.1b)$$

$$i_0 = \frac{1}{3}(i_a + i_b + i_c). \qquad (5.1c)$$

Assuming a three-wire system, $i_a + i_b + i_c = 0$, and so

$$i_\alpha = i_a, \qquad (5.2a)$$

$$i_\beta = \frac{1}{\sqrt{3}}i_a + \frac{2}{\sqrt{3}}i_b, \qquad (5.2b)$$

$$i_0 = 0. \qquad (5.2c)$$

The reverse transformation from two-phase to three-phase can be performed by

$$i_a = i_\alpha, \qquad (5.3a)$$

$$i_b = -\frac{1}{2}i_\alpha + \frac{\sqrt{3}}{2}i_\beta, \qquad (5.3b)$$

$$i_c = -\frac{1}{2}i_\alpha - \frac{\sqrt{3}}{2}i_\beta. \qquad (5.3c)$$

These α and β components in a stationary reference frame can be transformed into a rotating reference frame, displaced by angle θ, using Park's transformation

$$i_d = i_\alpha \cos\theta + i_\beta \sin\theta, \qquad (5.4a)$$

$$i_q = -i_\alpha \sin\theta + i_\beta \cos\theta. \qquad (5.4b)$$

The reverse transformation to $\alpha - \beta$ is by

$$i_\alpha = i_d \cos\theta - i_q \sin\theta, \tag{5.5a}$$

$$i_\beta = i_d \sin\theta + i_q \cos\theta. \tag{5.5b}$$

A graphical relationship among three-phase current, $\alpha - \beta$ current and d-q current is shown in figure 5.13.
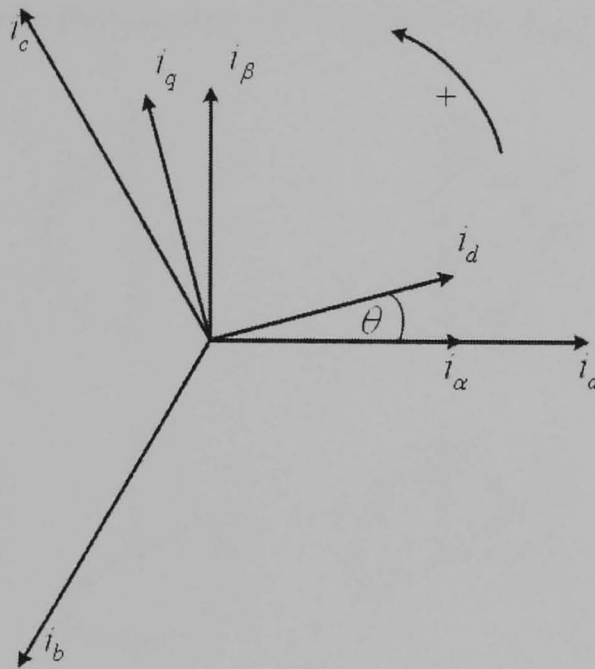
Figure 5.13 The current vectors of i_a, i_b, i_c, i_α, i_β and i_d, i_q

The first diagnostic method using this approach is the slope method proposed by Peuget *et al.* [5.4, 5.5]. In this method the trajectory of the $\alpha - \beta$ current components is used to detect the fault. The trajectory of the $\alpha - \beta$ currents is a circle under healthy conditions and becomes a semi-circle under open-switch fault conditions. In addition, the linear part of the semi-circle has different angles depending on which switch is faulty, as shown in figure 5.14. Under the feature extraction process, with the assumption that $i_a + i_b + i_c = 0$, the equations used for calculating the $\alpha - \beta$ currents are

$$i_\alpha = i_a, \tag{5.6a}$$

$$i_\beta = \frac{1}{\sqrt{3}}(i_a + 2i_b). \tag{5.6b}$$

The currents are sampled periodically with a variable sampling rate depending on the fundamental component of the currents. Subsequently, the slope σ of the linear portion of the current trajectory can be calculated from

$$\sigma = \frac{i_{\alpha(k)} - i_{\alpha(k-1)}}{i_{\beta(k)} - i_{\beta(k-1)}},$$ (5.7)

where k and $k-1$ refer to the present and the previous samples respectively.
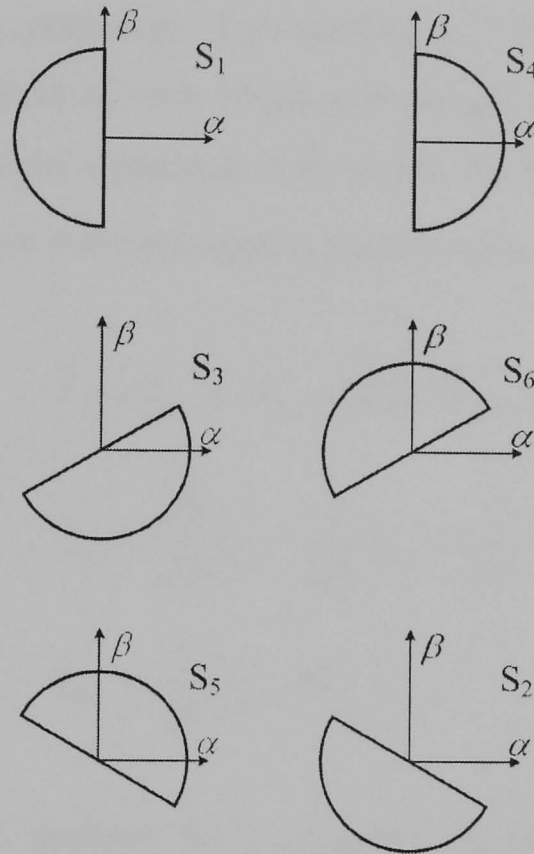
Figure 5.14 Current trajectory of the $\alpha - \beta$ current under open-switch fault

The results from (5.7) vary depending on the faulty phase, as shown in table 5.1.

Table 5.1: Localisation of an open-switch fault with the Slope Method

Faulty Phase	A	B	C
σ	0	$\sqrt{3}$	$-\sqrt{3}$

The fault identification step can be done by using a hysteresis band to check the missing half cycle of the faulty phase current. This process can identify and localise the faulty switch in the inverter. This method has some problems as discussed by

Rothenhagen and Fuchs [5.12, 5.13]. The method showed poor performance by taking a long time to detect a fault. Moreover, it is also difficult to detect the fault by this method because the angle calculated during normal operation is not very different from that of the faulty state [5.13]. Another problem is the tuning effort required for this method due to the threshold needed for the hysteresis band to localise the fault [5.12]. In the case of varying load a fixed threshold will not work properly and can cause either false alarms or fail to detect the fault.

Another method, proposed by Mendes and Cardoso [5.6, 5.7], also used $\alpha - \beta$ currents in the diagnostic procedure. This method calculates the average value (dc component) over one period of each phase current and then converts them to the $\alpha - \beta$ plane as presented in equations (5.8)-(5.10). Under healthy conditions, the average value of each phase current is approximately zero.

$$\bar{I}_{av} = I_{\alpha_{av}} + jI_{\beta_{av}} = \left|\bar{I}_{av}\right| \angle \theta_{av}, \tag{5.8}$$

$$I_{\alpha_{av}} = \frac{\sqrt{2}}{\sqrt{3}} I_{a_{av}} - \frac{1}{\sqrt{6}} I_{b_{av}} - \frac{1}{\sqrt{6}} I_{c_{av}}, \tag{5.9}$$

$$I_{\beta_{av}} = \frac{1}{\sqrt{2}}\left(I_{c_{av}} - I_{b_{av}}\right), \tag{5.10}$$

The equations needed to perform fault diagnosis by this method are shown in equations (5.11)-(5.15). The hypothesis is that under faulty conditions of the three wire system, the average value of the faulty phase current becomes significant and has the opposite sign from the averages of the other healthy phase currents. Therefore, this can be used to detect the fault, and localise the faulty switch, by introducing a threshold for the dc component. Once a fault occurs, the average value will exceed the threshold.

$$I_{v_{av}} = \frac{1}{N} \sum_{k=1}^{N} I_{v}(k\tau), \tag{5.11}$$

$$\left|\bar{I}\right| = \sqrt{\left(I_{\alpha}^{2} + I_{\beta}^{2}\right)}, \tag{5.12}$$

$$\theta_{av} = \arctan\left(\frac{I_{\beta_{av}}}{I_{\alpha_{av}}}\right),$$ (5.13)

$$\frac{1}{f_{mains}} = N\tau,$$ (5.14)

$$v \in [\alpha, \beta].$$ (5.15)

The localisation process is by calculating the angle θ_{av} as shown in equation (5.13). The angle varies depending on the type of fault and the location of the faulty switch. The list of the angles referring to switch arrangement shown in figure 5.1 is shown in table 5.2 [5.6, 5.7].

Table 5.2: Localisation of the Park's Vector Method

IGBT	Range of the θ_{av}
S1	$150° < \theta_{av} < 210°$
S2	$210° < \theta_{av} < 270°$
S3	$270° < \theta_{av} < 330°$
S4	$330° < \theta_{av} < 30°$
S5	$30° < \theta_{av} < 90°$
S6	$90° < \theta_{av} < 150°$

However, when this method is applied to a PWM rectifier the angles must be shifted by 180 degrees.

Like the Slope Method, this method also has a problem with varying load. A threshold value set for one load current will not be suitable for another load current, and consequently there will be false alarm problems and failure to detect.

5.3.2 Control Deviation Approach

This approach uses the feedback signal in the current control loop of the field oriented control of an induction motor to detect and localise an open-switch fault in the inverter [5.8]. Normally, the command and feedback variables in the flux producing current, i_{dref} and i_d, and torque producing current, i_{qref} and i_q, have only

119

dc components. Under normal operating conditions, the error signal is almost zero, but under fault conditions or transient conditions, the current loop is in a transient state and there is an error. This error not only has a dc component but also other harmonic components, the most significant of which is the fundamental component. To detect a fault, the ratio of the fundamental component of the error to the dc component of the error is calculated and its absolute value compared with a threshold of 0.5. The equations used in this method are as follows,

$$\Delta i_s = i_{sref} - i_{sact} = \sqrt{\left(i^2_{d,ref} - i^2_{d,act}\right)^2 + \left(i^2_{q,ref} - i^2_{q,act}\right)^2} \,, \qquad (5.16)$$

$$C^m = \frac{1}{N} \sum_{k=0}^{N-1} |\Delta i_{s,k}| e^{\frac{j2\pi mk}{N}} \,, \qquad (5.17)$$

$$f_{fault} = \frac{C^1}{C^0} \begin{cases} if |f_{fault}| > 0.5, fault \\ if |f_{fault}| < 0.5, no\ fault \end{cases}, \qquad (5.18)$$

$$\theta_{f_{fault}} = \arctan\left[\frac{Re\{f_{fault}\}}{Im\{f_{fault}\}}\right], \qquad (5.19)$$

where N is the total number of points per period and k is $0, 1, 2 ... N - 1$.

The fault localising step is completed by calculating the angle by equation (5.19). The list of angles for this approach is shown in table 5.3 [5.8]. In the case of a PWM rectifier, the angles presented here must be shifted by 180 degrees.

Table 5.3: Location of faulty switch by the Control Deviation Method

IGBT	Threshold	Range of $\theta_{f_{fault}}$
S1		$\left|\theta_{f_{fault}}\right| < 30°$
S2		$30° < \theta_{f_{fault}} < 90°$
S3	> 0.5	$-150° < \theta_{f_{fault}} < -90°$
S4		$\left|\theta_{f_{fault}}\right| > 150°$
S5		$90° < \theta_{f_{fault}} < 150°$
S6		$-90° < \theta_{f_{fault}} < -30°$

Although this method is reliable and easy to implement, it requires modification of a DSP control software which may be costly for the system end user. Moreover, a DFT calculation is required which uses considerable computational time of the DSP.

5.3.3 Voltage Detection Approach

An alternative method proposed by Ribeiro *et al.* [5.9] uses the inverter pole voltages via several voltage measurements. The principle of this method is based on the following assumptions: for example, in the case of an open-switch fault occurring at phase A top switch, these if...then routines are performed as follows:

if $i_{sa} > 0$ then

$$v_{a0} = -\frac{V_{dc}}{2}$$

else if $i_{sa} < 0$ and $s_1 = 1$ then

(s_1 = pulse state of IGBT phase A top switch)

(1 = on, 0 = off)

$$v_{a0} = -\frac{V_{dc}}{2}$$

else if $i_{sa} < 0$ and $s_1 = 0$ then

$$v_{a0} = \frac{V_{dc}}{2}$$

End if.

There are four different techniques proposed:

- inverter pole voltage measurement $v_{\varphi 0}$,

- machine phase voltage measurement v_{φ},

- system line voltage measurement v_{ll},

- machine neutral voltage measurement v_{no}.

The equation relevant to this method is the symmetrical component equation:

$$
\begin{bmatrix} v_{an} \\ v_{bn} \\ v_{cn} \end{bmatrix} = \begin{bmatrix} \dfrac{2}{3} & -\dfrac{1}{3} & -\dfrac{1}{3} \\ -\dfrac{1}{3} & \dfrac{2}{3} & \dfrac{-1}{3} \\ -\dfrac{1}{3} & -\dfrac{1}{3} & \dfrac{2}{3} \end{bmatrix} \begin{bmatrix} v_{10} \\ v_{20} \\ v_{30} \end{bmatrix}
\tag{5.20}
$$

Under an open-switch fault condition in the top switch of phase A, the inverter pole voltage error is, $\pm \Delta v_{a0}$. Such an error can cause deviation in the other voltages as shown in the following equations,

- Phase voltage v_{an}'

$$
\begin{bmatrix} v_{an}' \\ v_{bn}' \\ v_{cn}' \end{bmatrix} = \begin{bmatrix} \dfrac{2}{3} & -\dfrac{1}{3} & -\dfrac{1}{3} \\ -\dfrac{1}{3} & \dfrac{2}{3} & -\dfrac{1}{3} \\ -\dfrac{1}{3} & -\dfrac{1}{3} & \dfrac{2}{3} \end{bmatrix} \begin{bmatrix} v_{10} - \Delta v_{10} \\ v_{20} \\ v_{30} \end{bmatrix},
\tag{5.21}
$$

- Neutral voltage v_{no}'

$$
v_{n0}' = \frac{1}{3}\left[(v_{10} - \Delta v_{10}) + v_{20} + v_{30}\right],
\tag{5.22}
$$

- Line voltage v_{ll}'

$$
\begin{bmatrix} v_{ab}' \\ v_{bc}' \\ v_{ca}' \end{bmatrix} = \begin{bmatrix} 1 & -1 & 0 \\ 0 & 1 & -1 \\ -1 & 0 & 1 \end{bmatrix} \begin{bmatrix} v_{10} - \Delta v_{10} \\ v_{20} \\ v_{30} \end{bmatrix}.
\tag{5.23}
$$

To implement this method, extra voltage transducers are required in the system, as shown in figure 5.15. Of the four voltage measurement techniques, only the neutral voltage measurement technique needs just one voltage transducer whereas the others need three voltage transducers.

Figure 5.15 Locations of the voltage sensors for the voltage detection method [5.9]

Simulation results and experimental results show the good performance of this method, with detection times less than 1 cycle [5.9]. Although this method provides good performance, its drawbacks can be summarised according to the choice of voltage measurements:

- inverter pole voltage measurement (referring to dc-link midpoint):
    - requires dc-link midpoint,
    - requires three-extra voltage transducers,
- line voltage measurement:
    - requires three-extra voltage transducers,
- phase voltage measurement:
    - requires three-extra voltage transducers,
    - dependent on balance of machine winding,
    - requires neutral accessibility,
- neutral voltage measurement:
    - dependent on balance of machine winding,
    - requires neutral accessibility and a voltage transducer.

5.3.4 DC Component of Phase Current Approach

This approach was first proposed by Abramik *et al.* [5.10]. Several methods exist to detect an open-switch fault based on the dc component of the current: for instance, the average Park's current vector method, which suffers fast transient and load variation problems. Using a fixed threshold leads to false alarm problems and failure to detect problems. To solve such problems, an adaptive threshold is required. However, to avoid this complication, Abramik *et al.* [5.10] proposed the Normalised DC Current Method. The dc component of each phase current is normalised with reference to the fundamental component of each phase. A variable frequency sampling technique was proposed in this work [5.10]. The number of sampling points of the signal in each cycle is fixed but the sampling period varies with the command frequency. Therefore, the samples occur at fixed angles of the sampled signal. A graphical interpretation of this sampling scheme is shown in figure 5.16.
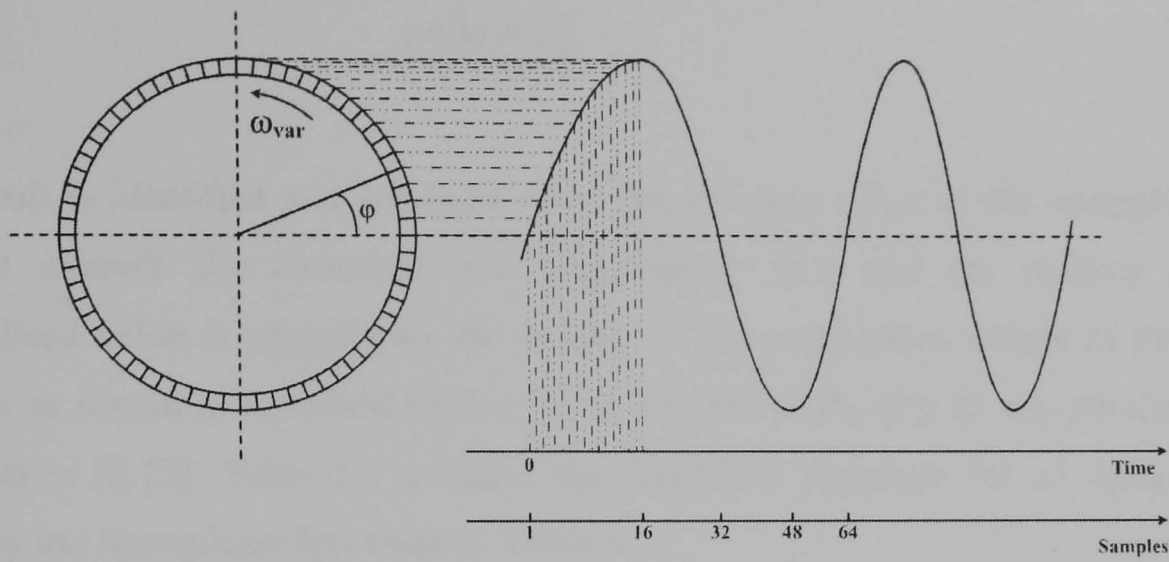
Figure.5.16 The variable period sampling scheme (Reproduced from [5.10])

To reduce computational effort, the recursive DFT algorithm used in this method is implemented with the help of a circular buffer. The equations to calculate the variables for this method are shown as follows,

$$\mu_v = \frac{1}{N} \sum_{k=1}^{N} I_v(k\tau), \tag{5.24}$$

$$I_{1,v} = a_{1,v} \cos\left(\frac{2\pi}{T} k\tau\right) + b_{1,v} \sin\left(\frac{2\pi}{T} k\tau\right), \tag{5.25}$$

$$\gamma_v = \frac{\mu_v}{I_{1,v}}, \tag{5.26}$$

$$a_{1,v} = \frac{2}{N} \sum_{k=1}^{N} I_v(k\tau) \cos\left(\frac{2\pi k}{N}\right), \tag{5.27}$$

$$b_{1,v} = \frac{2}{N} \sum_{k=1}^{N} I_v(k\tau) \sin\left(\frac{2\pi k}{N}\right), \tag{5.28}$$

$$d_{1,v} = \begin{cases} 1 : \gamma_v > 0 \\ 0 : \gamma_v \le 0 \end{cases}, \tag{5.29}$$

$$d_{2,v} = \begin{cases} 1 : |\gamma_v| > 0.45 \\ 0 : |\gamma_v| \le 0.45 \end{cases}, \tag{5.30}$$

$$v \in [a,b,c].$$

(5.31)

The fault is identified and localised when the absolute value of the normalised dc current exceeds the detection ratio (equation (5.30)) and the polarity of the normalised value is opposite to the polarity of the normalised values of the other phases, as shown in equations (5.29)-(5.31). The threshold of 0.45 was derived from experience [5.12]. Table 5.4 contains the diagnostic signature for an open-switch fault by the Normalised DC Current Method.

Table 5.4: The diagnosis signature for open IGBT faults using the Normalised DC Current Method

IGBT	$d_{1,a}$	d_{2a}	$d_{1,b}$	$d_{2,b}$	$d_{1,c}$	$d_{2,c}$
S1	0	1	1	0	1	0
S2	0	0	0	0	1	1
S3	1	0	0	1	1	0
S4	1	1	0	0	0	0
S5	1	0	1	0	0	1
S6	0	0	1	1	0	0

Rothengen and Fuchs [5.12, 5.13] compared all these current based methods when applied to a rectifier and the inverter-fed stator of a PMSM. The comparison shows that the Modified Normalised DC Current Method is the best, as presented in [5.12, 5.13]. This method has the same algorithm as the Normalised DC Current Method, but uses a less restrictive way to localise the faulty switch, as displayed in table 5.5. The modified method reduced the conditions to detect the fault by ignoring cases of multiple values exceeding the normalised dc threshold value. Only the largest normalised dc value was considered to be the faulty case.

An alternative method, called the Simple Direct Current Method, was also proposed [5.12, 5.13]. This method used only the direct current component of each phase, as calculated in equation (5.24), and compared it with the threshold value δ to localise the faulty switch as shown in table 5.6. If more than one direct current exceeded the

threshold, the largest absolute value is taken. The advantage of this method is simplicity in calculation, but it still suffers detection errors under load variation and fast transient conditions though using a fixed detection threshold.

Table 5.5: The diagnosis signature for open IGBT faults using the Modified Normalised DC Current Method

IGBT	$d_{1,a}$	d_{2a}	$d_{1,b}$	$d_{2,b}$	$d_{1,c}$	$d_{2,c}$
S1	0	1				
S2					1	1
S3			0	1		
S4	1	1				
S5					0	1
S6			1	1		

Table 5.6: The diagnosis signature for open IGBT faults using the Simple Direct Current Method

IGBT	$> \mu_a$	$> \mu_b$	$> \mu_c$
S1	$< -\delta$		
S2			$> \delta$
S3		$< -\delta$	
S4	$> \delta$		
S5			$< -\delta$
S6		$> \delta$	

The advantages and drawbacks of these methods are discussed in [5.12, 5.13]. The most significant problem identified was false alarms, and this was partially resolved by introducing a fixed dead time for each method [5.12]. However, this was not able to prevent false alarms under every operating condition.

5.3.5 Artificial-Intelligent-Based Methods

Simulation programs, for example MATLAB/SIMULINK, have been developed to support simulation of faults in electrical drives and help the user analyse fault behaviour without dealing with complicated mathematical models. The simulation results are necessary to select the most appropriate diagnostic variables for fault identification. The results can also be used as information for a knowledge-based system or neural network training. Therefore the artificial intelligent (AI)-based approach is possible in fault identification. There are many AI-techniques proposed [5.14]: fuzzy logic, neural networks and other statistical methods. AI-techniques can be classified into two main groups - knowledge-based systems and non-linear function approximation. Fuzzy logic is in the knowledge-based methods which require knowledge or experience to make the rules representing the physical model. Neural networks and other statistical methods are considered as non-linear function approximations which use the relationships between inputs and outputs (supervised learning) or only input relationships (unsupervised learning).

Several methods based on AI techniques have been proposed for condition monitoring and fault diagnosis for induction machines and other electric machines [5.14]. Several internal machine faults are proposed for diagnosis; for instance, stator faults, rotor broken bars and bearing faults, based on AI-techniques [5.15]. However, little research is concerned with faults in the inverter drive system based on AI-techniques.

One example of an AI-based method is proposed by Scot and co-authors [5.16]. This paper reported the use of time domain analysis to detect intermittent misfiring with a pattern recognition algorithm. This method showed improved performance over frequency domain analysis in detection speed and its response to intermittent faults.

Khanniche and Mamat-Ibrahim [5.17, 5.18] proposed a method based on a combination of the discrete wavelet transform (DWT) and a fuzzy-logic based control system to detect an open-switch or intermittent misfiring fault in a voltage-fed inverter. In the fault detection stage, the three-phase current signals are fed to the DWT to calculate the wavelet coefficient. A change is detected if the wavelet coefficient falls outside a given band. Then the fault identifier stage will be processed by the fuzzy logic system by calculating the dc offset of the three-phase

current. A permanent open-switch fault and intermittent misfiring fault will then be extracted by checking the dc offset in the current after few cycles.

The pattern recognition approach applied to Park's current vector is used to diagnose open-switch faults with improved robustness of the diagnostic system [5.19]. The radial basis function neural network is used to distinguish abnormal conditions from normal conditions by generating the boundary of the operating area. However, this work shows that the Park's current vector is not reliable under light load conditions.

5.4 Analysis of Short-Circuit Switch Faults in Electrical Drives

The most common fault is the short-circuit switch fault, which can be caused by excessive current stress or voltage stress [5.1]. Such a fault appearing at the top switch of phase A, as shown in figure 5.17, is the examples for this case.
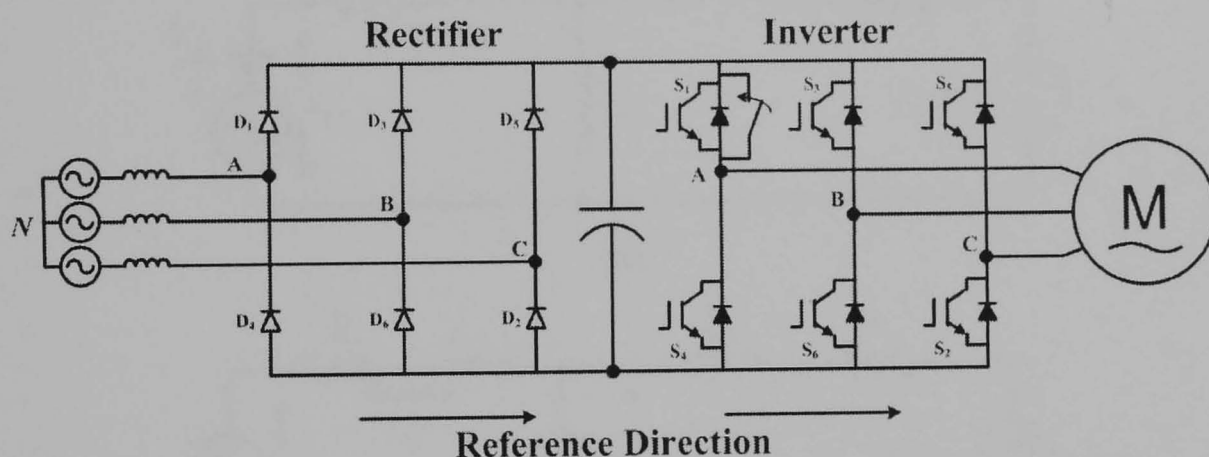
Figure 5.17 A voltage-fed inverter with a short-circuit switch fault at phase A

During the fault, phase A is permanently connected to the positive dc bus. Under this condition, using a three-wire system, the stator voltage of each phase becomes

$$v_{as} = V_{dc}, \tag{5.32}$$

$$v_{bs} = \frac{1}{2}V_{dc} + \hat{v}_{bs}, \tag{5.33}$$

$$v_{cs} = \frac{1}{2}V_{dc} + \hat{v}_{cs}. \tag{5.34}$$

Phase A voltage becomes a dc voltage whereas the other two phases, are ac voltages with dc offset. Transforming equations (5.32)-(5.34) into two phase form in a stationary reference frame fixed to the stator, the d-axis and q-axis equations become

$$v_{s\alpha} = \frac{1}{3}V_{dc} - \frac{1}{3}(\hat{v}_{bs} + \hat{v}_{cs}),$$

(5.35)

$$v_{s\beta} = \frac{1}{\sqrt{3}}(\hat{v}_{bs} - \hat{v}_{cs}).$$

(5.36)

The α-axis and β-axis equivalent circuit of an induction motor under a short circuit switch fault of phase A top switch are shown in figure 5.18

(a)

(b)
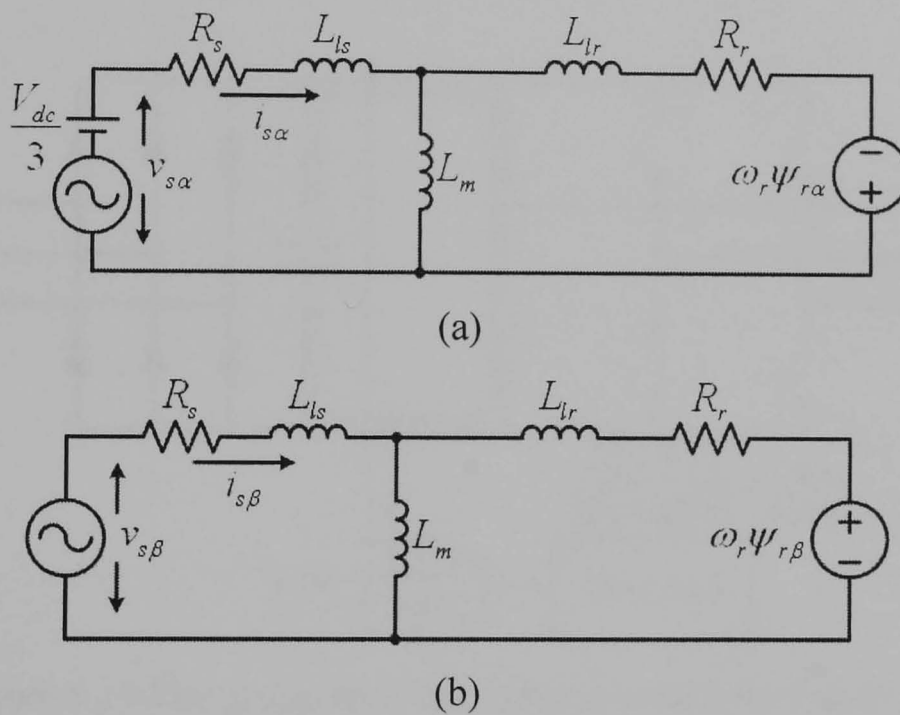
Figure 5.18 α - β equivalent circuit in stationary reference frame

This consequently results in a symmetrical three-phase short circuit. A counter emf will be generated causing dynamic braking until the stator flux decays to zero [5.1]. However, this case is not the general case since the fault can occur anytime under one switching cycle. If the fault occurs while the complementary switch is on, this fault will end up at shoot-through fault across the dc bus which will damage the healthy switch in the same leg.

5.5 Review of Existing Short-Circuit Switch Fault Detection and General Protection Methods

Several methods to detect a short-circuit switch fault and to protect the converter system from damage have been proposed. The detection methods can be broadly classified into two types by the location of the sensors – the global type, which requires placing the sensors somewhere in the converter circuit [5.20-5.24] and the local type, which requires placing the sensors at each switch in the converter bridge or at the gate driver circuit of each switch [5.25].

For the global type, current sensors are generally placed in the dc bus, because during a shoot-through fault, a high current discharges from the capacitor through the faulty leg in the converter [5.20] as shown in figure 5.19.
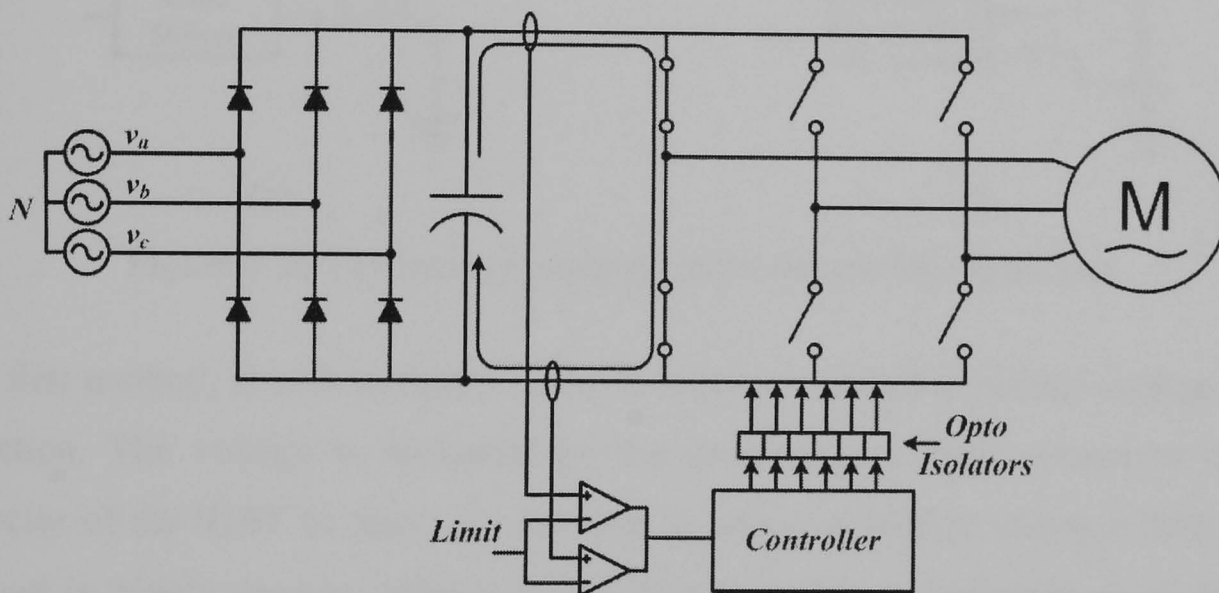
Figure 5.19 The global type short-circuit switch fault detection

As shown, the signal from the transducer is compared with a threshold and the comparator output signal is sent to the controller to disable all switches via opto-isolator circuits [5.20]. Blaabjerg *et al.* [5.21-5.24] proposed a low cost method which can detect a short-circuit switch fault by using only one current transducer. However, this method required a longer path for the dc link which increases the stray inductance in dc path. The detection and protection circuits using current sensors in the dc path have high cost when compared with the cost of the inverter for small HP drives. Therefore, many IGBT manufacturers have designed a switch having short-circuit switch detection capability in a single IC [5.20].

The local type can be summarised into four main methods, as shown in figure 5.20 [5.25].

(a)

(b)

(c)

(d)
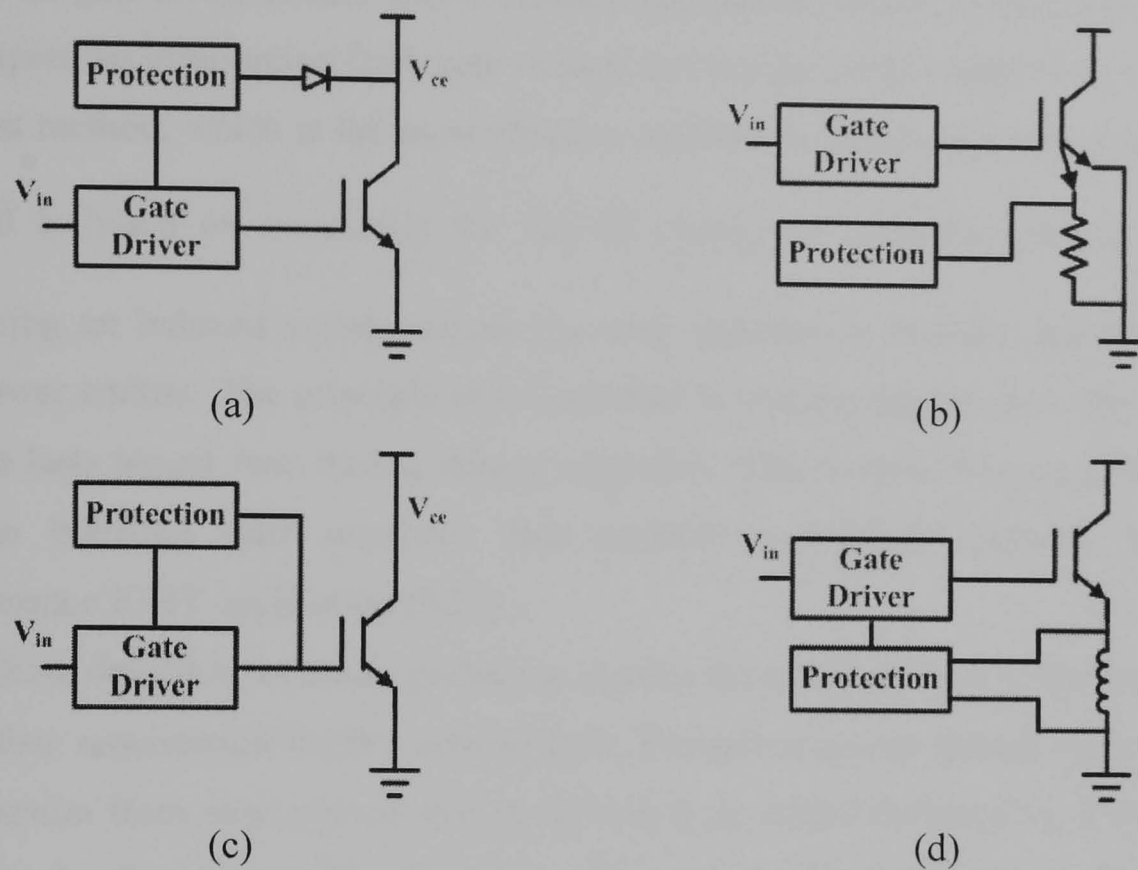
Figure 5.20 The local type short-circuit switch fault detection

The first method, shown in figure 5.20a, is based on collector-emitter voltage (V_{ce}) detection. The voltage is measured by the de-saturation diode connected to the collector of the IGBT to detect the increase in collector voltage during a fault. This method is widely used in industry [5.20]. However, due to switching noise in V_{ce}, this method requires a blanking time for noise reduction [5.25]. This blanking requires approximately 1-5 μs which is not fast enough for high performance applications.

The second method, shown in figure 5.20b, is based on collector current (I_c) detection. For this method, a second IGBT is integrated in the main IGBT for the purpose of carrying a scaled down current (mirror current) [5.25]. This current is measured by the voltage drop across a known resistor. This method requires special designs of semiconductors resulting in increased cost of the IGBTs.

The third method, shown in figure 5.20c, is based on measuring the change in gate voltage V_{ge} reflected by the change of V_{ce}. This phenomenon occurs because during a fault the large current through the collector-gate capacitor (Miller capacitance) is

imposed on the gate resistance resulting in change in gate voltage. This is the simplest of all the methods because there is no need to deal with the high voltage side of the gate driver circuit. However, the complicated protection circuit is required to interpret the information from gate voltage and protect IGBTs effectively [5.25].

The last method, which is the most effective method, is shown in figure 5.20d. This method is based on measuring the rate of change of collector current, $\frac{di}{dt}$, by measuring an induced voltage across the stray inductance between Kelvin emitter and power emitter. The principle of this method is that during the fault, the induced voltage lasts longer than during normal operation. This method has no noise issues and no blanking time required. This method is therefore suitable for high performance IGBT application [5.25].

Apart from detection methods, protection against the consequences of the fault is the immediate requirement for this type of fault. Protection can be treated on two levels – protection from case rupture and protection from IGBT destruction. The method used for the first case is based on fuses. Several high speed fuses can be used to protect IGBTs or inverter modules from rupture but they cannot protect IGBT switches or converters from destruction because of the time to isolate the fault [5.26-5.29].

The second protection level can protect against both destruction and rupture. The idea is to immediately disable both switches in the faulty leg of the converter. Several methods have been proposed [5.20]. As discussed previously in detection methods, the best known protection method is based on detection of V_{ce} while the device turns on. During the fault, the voltage exceeds the specified limit and the associated gate signals are turned off to prevent the IGBTs from destruction [5.20].

5.6 Summary

The diagnostic process can be divided into three main steps: feature extraction, fault identification and corrective action. Feature extraction is the process of distinguishing the signal under faulty conditions from the signal under healthy conditions; for example, Park's vector, normalised dc current and voltage measurement. The next process is to identify and locate the fault; for example, the angle of the Park's vector, slope detection and the threshold and sign of the

threshold. The aim of corrective action is to clear the fault from the system and make a decision either to operate under derated conditions or shutdown. Corrective action will be discussed in the system reconfiguration chapter. Fault detection for an open-switch fault can be divided into non-AI-based methods and AI-based methods. The non-AI based methods, such as the several methods from section 5.3.1-5.3.5, are normally performed by "if-then" rules which is "hard computing" whereas the AI-based methods are "soft computing", performed using fuzzy-logic and other nonlinear function approximations. Some AI-based methods, for example neural networks, require knowledge of the relationship between input and output to train the neural which requires complicated and high performance tools to implement.

For a short-circuit switch fault, the detection methods can be divided into two main types by the location of the currents sensors. The first is by placing the current sensors at dc busses to detect the discharge of the capacitor. The second is by placing a sensor at each switch or its gate driver circuit, and four methods are reviewed here. For this type of fault, immediate protection is required. There are two protection types for the IGBT. The first is by fuses, which can protect IGBTs from explosion but cannot protect them from destruction. The second type is to shut down the gate signal once the fault has been detected.

Reference

5.1.   D. Kastha and B. K. Bose, 'Investigation of Fault Mode of Voltage-Fed Inverter System for Induction Motor Drive", IEEE Trans. on Industry Application, Vol.30, No. 4, August 1994, pp. 1028–1038.

5.2.   P. J. Chrzan and R. Szczesny, 'Fault Diagnosis of Voltage-Fed Inverter for Induction Motor Drive'. Proceedings of the IEEE International Symposium on Industrial Electronics 1996, Vol. 2, pp. 1011-1016.

5.3.   Wojciech Sleszynski, Janusz Nieznanski, and Artur Cichowski, 'Real-Time Fault Detection and Localization in Vector-Controlled Induction Motor Drives'. Proceedings of the EPE 12th European Conference on Power Electronics and Applications, 2005, pp. P.1-P.7.

5.4.   R. Peuget, S. Courtine, and J. P. Rognon, 'Two Knowledge-Based Approaches to Fault Detection and Isolation on a PWM Inverter'. Proceedings of the 1997 IEEE International Conference on Control Applications, pp. 565-570.

5.5.   R. Peuget, S. Courtine, and J. P. Rognon, 'Fault Detection and Isolation on a PWM Inverter by Knowledge-Based Model'. IEEE Trans. on Industry Applications, Vol. 34, No. 6, November/December 1998, pp. 1318-1326.

5.6.   A. M. S. Mendes and A. J. Marques Cardoso, 'Voltage Source Inverter Fault Diagnosis in Variable Speed AC Drives, by the Average Current Park's Vector Approach'. Proceedings of International Conference Machine and Drives, 1999 pp. 704-706.

5.7.   A. M. S. Mendes and A. J. Marques Cardoso, 'Fault Diagnosis in a Rectifier-Inverter System Used in Variable Speed AC Drive, by the Average Park's Vector Approach'. Proceedings of the 1999 EPE 8th European Conference on Power Electronics and Applications, pp. P.1-P.9.

5.8.   C. Kral and K. Kafka, 'Power Electronics Monitoring for a Controlled Voltage Source Inverter'. Proceedings of IEEE Power Electronics Specialists Conference, 2000, Vol.1, pp. 213-217.

5.9.   R. L. D. A. Ribeiro *et al.*, 'Fault Detection of Open-Switch Damage in Voltage-Fed PWM Motor Drive Systems'. IEEE Trans. on Power Electronics, Vol. 18, No.2, March 2003, pp. 587-593.

5.10.   S. Abramik *et al.*, 'A Diagnostic Method for On-line Fault Detection and Localization in VSI-Fed AC Drive'. Proceedings of the 2003 EPE 10th European Conference on Power Electronics and Applications, pp. P.1-P.8.

5.11.   F. W. Fuchs, 'Some Diagnosis Methods for Voltage Source Inverters in Variable Speed Drives with Induction Machines a Survey'. Proceedings of the 29th Annual Conference of the IEEE Industrial Electronics Society, 2003, Vol. 2, November 2003, pp. 1378-1385.

5.12.   K. Rothenhagen and F. W. Fuchs, 'Performance of Diagnosis Methods for IGBT Open Circuit Faults in Voltage Source Active Rectifiers'. Proceedings of the 2004 IEEE 35th Power Electronics Specialists Conference, pp. 4348-4354.

5.13.   K. Rothenhagen and F. W. Fuchs, 'Performance of Diagnosis Methods for IGBT Open Circuit Faults in Three Phase Voltage Source Inverters for AC Variable Speed Drives'. Proceedings of the 2005 EPE 12th European Conference on Power Electronics and Applications, pp. P.1-P.7.

5.14.   F. Filippetti *et al.*, 'AI Technique in Induction Machines Diagnosis Including the Speed Ripple Effect'. IEEE Trans. on Industry Application, Vol. 34, No.1, January/February 1998, pp. 98-108.

5.15.   Subhasis Nandi, Hamid A. Toliyat, and Xiaodong Li, 'Condition Monitoring and Fault Diagnosis of Electrical Motors—A Review'. IEEE Trans. on Energy Conversion, Vol. 20, No.4, December 2005, pp. 719-729.

5.16.   Kenneth Scot Smith, Li Ran, and Jim Penman, 'Real-Time Detection of Intermittent Misfiring in a Voltage-Fed PWM Inverter Induction-Motor Drive'. IEEE Trans. on Industrial Electronics, Vol. 44, No. 4, August 1997, pp. 468-476.

5.17.   M. S. Khanniche and M.R. Mamat-Ibrahim, 'Wavelet-Fuzzy-Based Algorithm for Condition Monitoring of Voltage Source Inverter'. Electronics Letters Vol. 40, Issue 4, February 2004, pp. 267–268.

5.18.   M. Rozailan Mamat, M. Rizon, and M. S. Khanniche, 'Fault Detection of 3-Phase VSI using Wavelet-Fuzzy Algorithm'. American Journal of Applied Sciences 3(1), 2006, pp. 1642-1648.

5.19.   D. Diallo *et al.*, 'Fault Detection and Diagnosis in an Induction Machine Drive: A Pattern Recognition Approach Based on Concordia Stator Mean Current Vector'. IEEE Trans. on Energy Conversion, Vol. 20, No. 3, September 2005, pp. 512-519.

5.20.   T. Takahashhi, 'IGBT Protection in AC or BLDC Motor Drives'. International Rectifier Technical Paper, pp. 1-9.

5.21.   F. Blaabjerg *et al.*, 'Single Current Sensor Technique in the DC-Link of Three-Phase PWM-VS Inverter A Review and the Ultimate Solution'. Proceeding of 31st Industry Applications Annual Meeting Conference, 1996, pp. 1192-1202.

5.22.   F. Blaabjerg *et al.*, 'Single Current Sensor Technique in the DC Link of Three-Phase PWM-VS Inverters: A Review and a Novel Solution'. IEEE Trans. on Industry Applications, Vol. 33, No. 5, September/October, 1997, pp. 1241–1253.

5.23.   F. Blaabjerg and J. K. Pedersen, 'A New Low-Cost, Fully Fault-Protected PWM-VSI Inverter with True Phase-Current Information'. IEEE Trans. on Power Electronics, Vol. 12, No. 1, January 1997, pp. 187–197.

5.24.   F. Blaabjerg *et al.*, 'Reconstruction of Output Currents and Fault Detection in a B4-Inverter with Only One Current Sensor'. Proceeding of 33rd Industry Applications Annual Meeting Conference, 1998, pp. 759–766.

5.25.   F. Huang and F. Flett, 'IGBT Fault Protection Based on di/dt Feedback Control'. Proceeding of IEEE Power Electronics Specialists Conference, 2007, pp. 1478-1484.

5.26.   F. Abrahamsen *et al.*, 'Fuse Protection of IGBT's against Rupture'. Proceeding of NORPIE 2000 Conference, pp. 64-68.

5.27.   Florin Iov, Frede Blaabjerg, and Karsten Ries "Prediction of Harmonic Power Losses in Fuses Located in DC-Link Circuit of an Inverter'. IEEE Trans. on Industry Applications, Vol. 39, No. 1, January/February 2003, pp. 2–10.

5.28.   Frede Blaabjerg, Florin Iov, and Karsten Ries, 'Fuse Protection of IGBT Modules against Explosions'. Proceeding of ICPE 2001 Conference, Korea, pp. 703-707.

5.29.   http://www.iet.aau.dk/~fi/LIFP/papers/Low_Inductance_IGBT_Fuse_Projec t.PDF

Chapter Six

Fault Diagnosis for a Doubly-Fed Induction Generator

This chapter focuses on fault diagnosis for a doubly-fed induction generator (DFIG) used in a wind turbine. The faults considered are open-switch faults and short-circuit switch faults in the back-to-back converters. The faults are first analysed by mathematical models to explain the physical behaviour and the effects of these faults on the DFIG. This analysis results in a diagnosis scheme which can be separated into open-switch fault and short-circuit switch fault diagnosis. In the case of open-switch fault diagnosis, some existing diagnostic methods are discussed. Problems appeared when applying the existing methods to the experimental system are discussed and investigated by simulation and experiment. This chapter proposes an alternative method to solve the problem and improve the reliability of the diagnostic system. Another method is also proposed to improve detection speed which can be applied to all voltage-fed inverter drive systems. The next section discusses short-circuit switch fault diagnosis and possible methods to detect the fault are proposed. Finally, all the proposed methods are proved by simulation and validated by experiment showing the effectiveness of the proposed methods.

6.1 Fault Analysis for a Doubly-Fed Induction Generator

As discussed in a chapter 3, the DFIG uses back-to-back converters, so when a switch fault appears in one converter it also affects the other converter. Such faults also affect other components in the system. This section aims to investigate the behaviour of the system and discuss the effects of converter faults on both the converters and the generator.

6.1.1 Effects on Converter System

Each converter is controlled by vector control but orientated to different reference frames. Moreover, the reference direction of the current flowing through each converter is different. Generally, one converter is an inverter whereas the other converter is a rectifier. The inverter and rectifier have different current reference

directions because of their operating mode; therefore, when a fault occurs in a switch having the same location the result may be different.

For ease of analysis, knowledge of the reference direction is necessary. The reference frame, the reference direction and the conducting devices for each fundamental half cycle are shown in Table 6.1.

Table 6.1: The conducting devices of each converter for current flowing in the reference direction and the reverse direction

Converter and (Reference Frame)	Current Direction	Switching Command	Conducting Devices
Machine-Side (**Stator flux**)	AC — DC (+ ←)	1	Top Switch
		0	Bottom Diode
	AC — DC (→ -)	1	Top Diode
		0	Bottom Switch
Grid-Side (**Grid Voltage**)	DC — AC (+ ←)	1	Top Diode
		0	Bottom Switch
	DC — AC (→ -)	1	Top Switch
		0	Bottom Diode
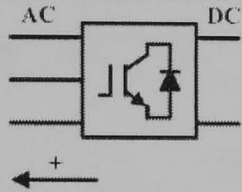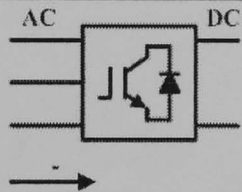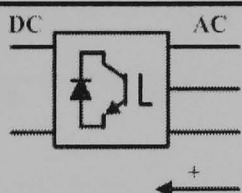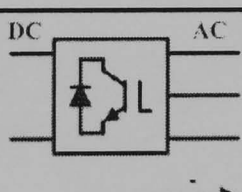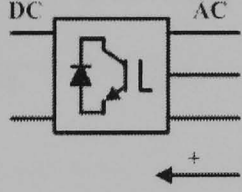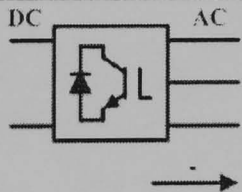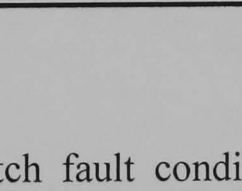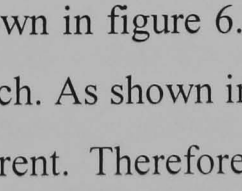
i. Open-Switch Fault

Normally, under open-switch fault conditions, the converter faulty phase current loses one half cycle, as shown in figure 6.1. This figure shows an open-switch fault appears in phase A top switch. As shown in table 6.1, the reference current directions of the converters are different. Therefore, the missing half cycle of each case is different. Depending on which switch is conducting, at synchronous speed generation, this fault will not be visible if current is not conducted by the faulty switch. If the DFIG remains operating at synchronous speed, the fault will never appear on the faulty phase current.

(a)

(b)
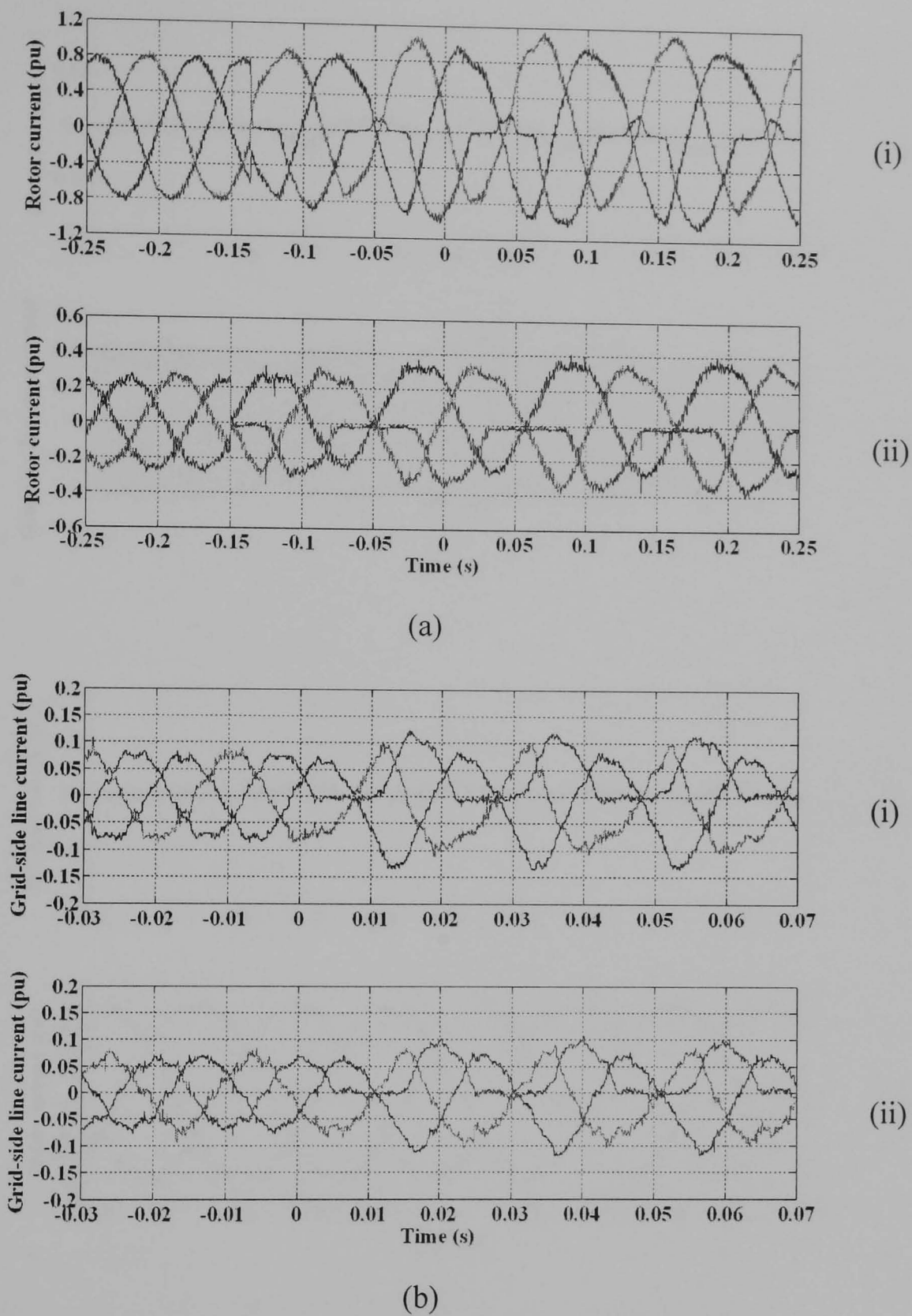
Figure 6.1 Rotor current waveforms under open-switch fault condition at phase A top switch in (a) the machine-side converter under super-synchronous speed generation (i) and sub-synchronous speed generation (ii) and grid-side converter currents under open-switch fault condition at phase A top switch in (b) the grid-side converter under super-synchronous speed generation (inverter mode) (i) sub-synchronous generation (rectifier mode) (ii)

(a)

(b)
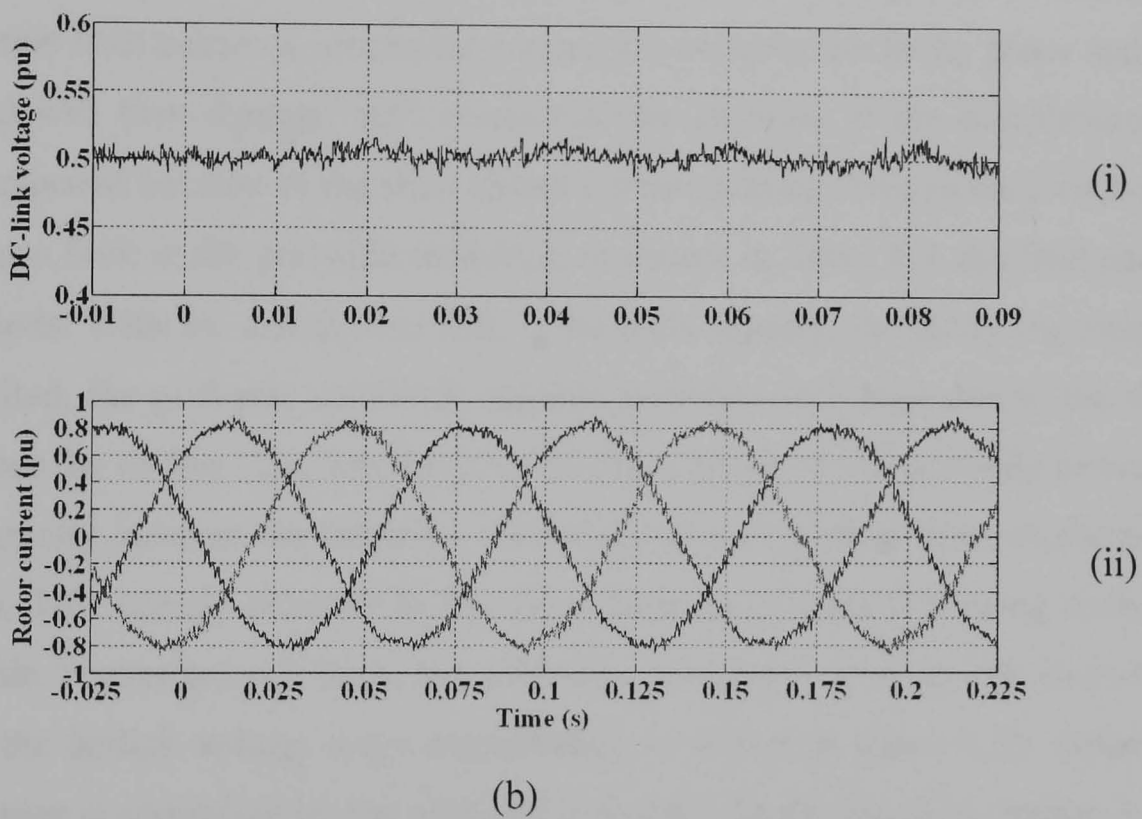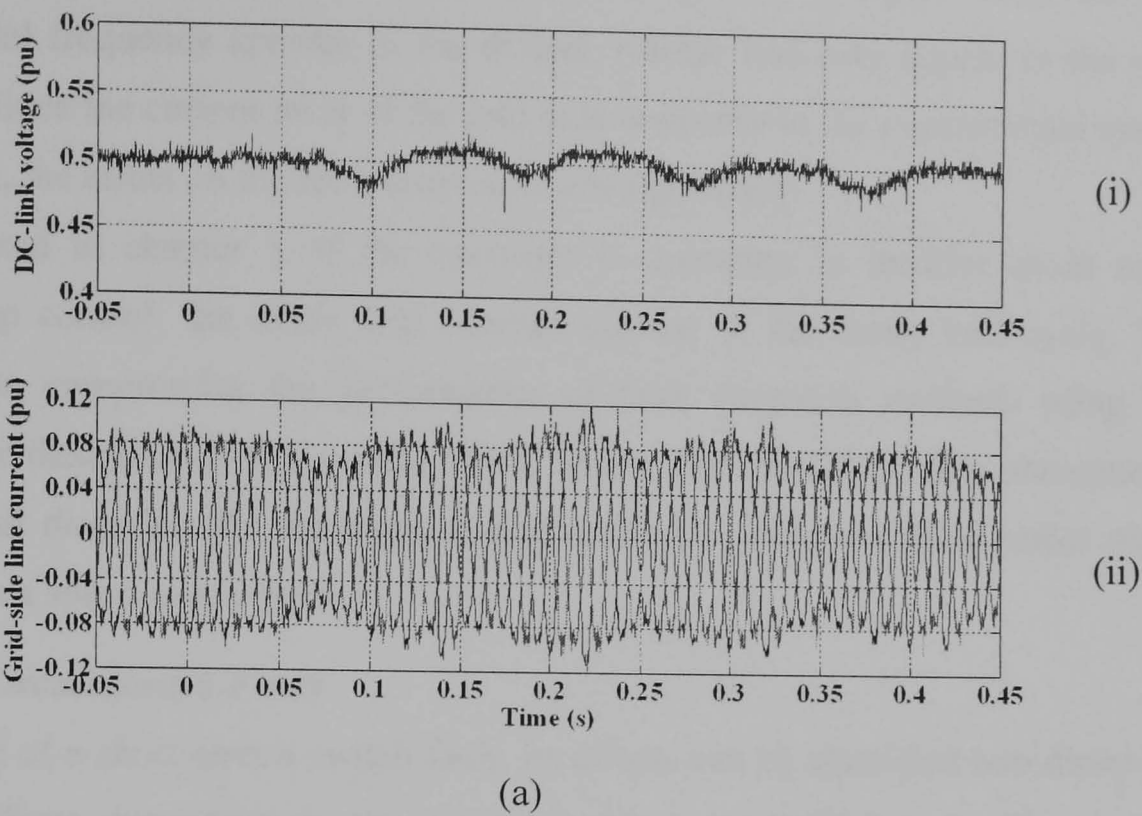
Figure 6.2 Experimental results showing effects of an open-switch fault in (a) the machine-side converter on (i) dc-link voltage and (ii) grid-side converter current and (b) the grid-side converter on (i) dc-link voltage and (ii) rotor current at 1.2 pu super-synchronous speed generation

An open-switch fault in the machine-side converter, as shown in figure 6.2a, will cause rotor frequency oscillations in the dc-link voltage and the grid-side converter current, which distorts the power flowing to the grid via the transformer. Likewise, if

the fault appears in the grid-side converter, as shown in figure 6.2b, the grid fundamental frequency appears in the dc-link voltage and may appear in the rotor currents. Since the current level of the grid-side converter in the experimental system is so small, the effect on the rotor currents is not significant.

As discussed in chapter 5, if the converter is operating in rectifier mode under closed-loop control, the diode will conduct current in the faulty half cycle. This current can compromise the performance of fault diagnosis methods using line currents or their derivative as a diagnostic index. For the DFIG, this phenomenon affects fault diagnosis for the machine-side converter while operating under super-synchronous speed generation.

ii. Short-Circuit Switch Fault

In the case of a short-circuit switch fault, its effects can be classified into direct and indirect effects depending on the converter that become faulty. As discussed in chapter 5, this fault causes a permanent connection between the faulty phase and the dc bus and will then damage both semiconductor switches if the complementary switch is activated because of the short circuit current passing through the switches.

Considering a fault in the grid-side converter, as shown in figure 6.3, the fault occurs at 1.2 seconds. With the assumption that, if the fault appears, the faulty leg remains short circuited, the grid-side converter currents becomes very high due to the short circuit across the dc bus. The amplitude of dc-link current of the grid-side converter increases greatly because the capacitor discharges in a very short time, as shown in figure 6.3a. This current recovers to low level because of current flowing from the machine-side converter, not from the grid-side converter. Due to the short-time discharge, the dc-link voltage drops immediately as shown in figure 6.3b. Since the dc-link voltage is controlled by the grid-side converter, as discussed in chapter 3 and 4, losing dc-link voltage increases the error of the dc voltage loop control. Since this short circuit is persistent, the dc-voltage controller output, which is the command for the d-axis current control loop, becomes saturated. This results in failure to control the current and finally results in very high line currents compared with normal current, as shown in figure 6.3c. Since this fault makes the dc bus voltage zero, the rotor of the DFIG becomes short circuited via the faulty leg of the grid-side

converter. As shown in figure 6.3d, machine-side dc-link current becomes high for the same short time that the rotor currents overshoot, as shown in figure 6.3e.

(a)

(b)

(c)

(d)

(e)
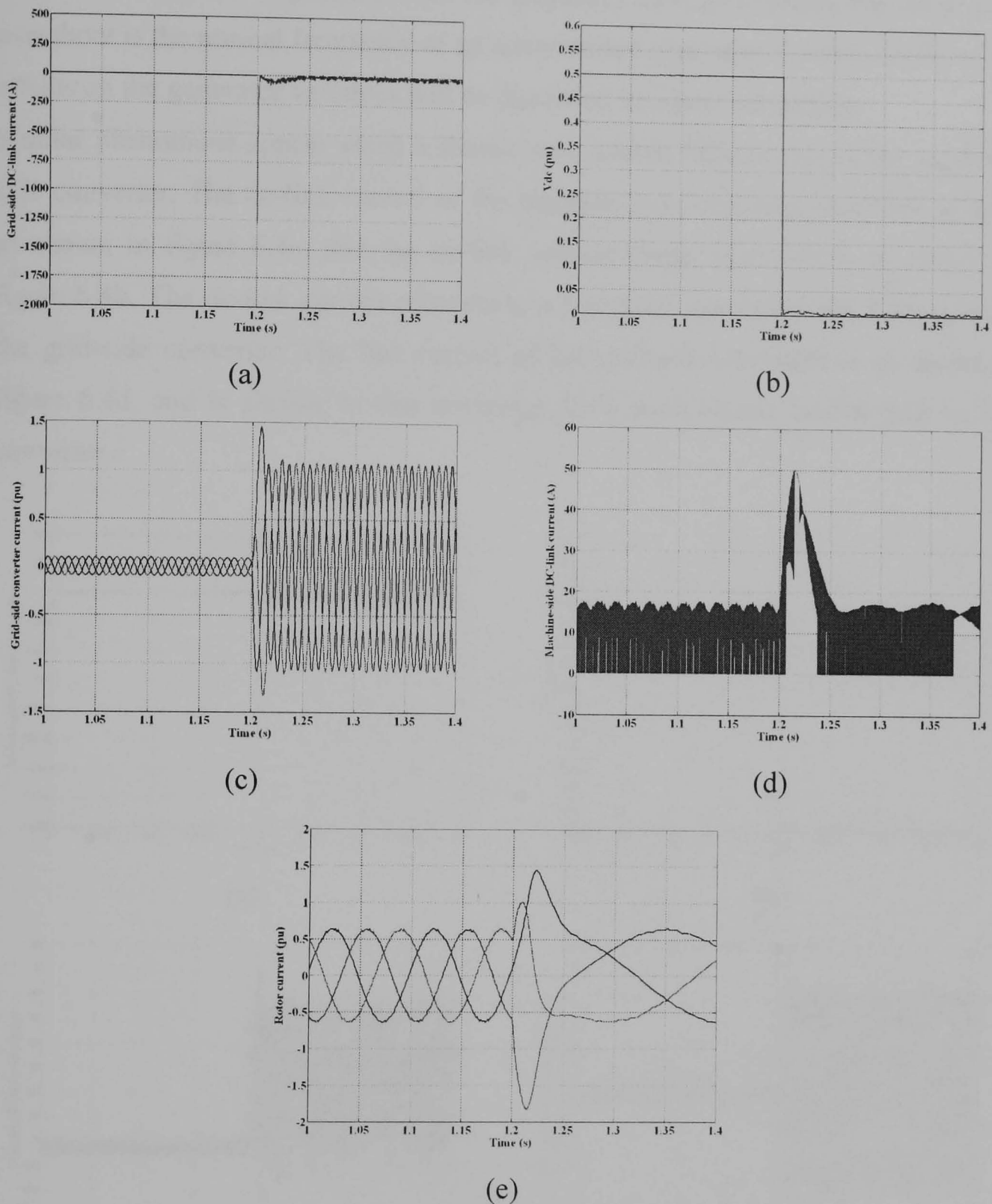
Figure 6.3 Simulation results showing effects of a short-circuit switch fault in the grid-side converter, phase A, top switch on (a) grid-side dc-link current, (b) dc-link voltage, (c) grid-side converter line currents, (d) machine-side dc-link current and (e) rotor currents

This peak current is due to transient rotor currents caused by the short circuit in the grid-side converter and as shown in figure 6.3d, the dc-link current after the transient

is from the machine-side converter. Due to loss of dc-link voltage, control of the DFIG by the machine-side converter becomes impossible. The DFIG becomes an uncontrolled induction generator and the frequency of rotor currents appearing after overshoot is the normal frequency of an uncontrolled generator. Further details of the effects on the generator variables will be discussed in a later subsection.

Similar phenomena appear when a short-circuit switch fault occurs in the machine-side converter. The dc-link current of the machine–side converter increases greatly, as shown in figure 6.4a, and the dc-link voltage drops immediately as shown in figure 6.4b. The dc-link current recovers to a low level due to current flowing from the grid-side converter. The line current of the grid-side converter is as shown in figure 6.4d, and is similar to that occurring for a short-circuit switch fault in this converter.
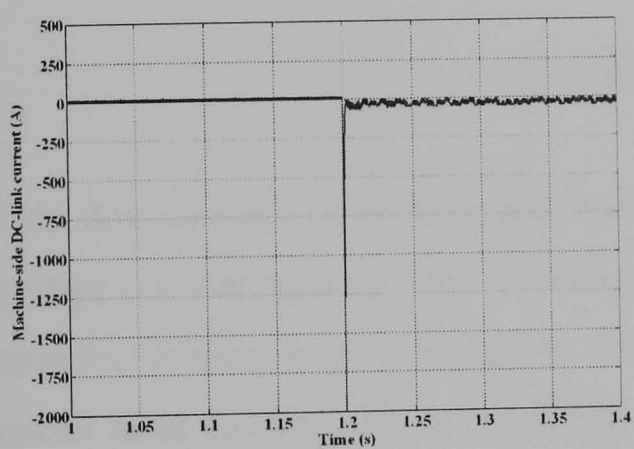
(a)
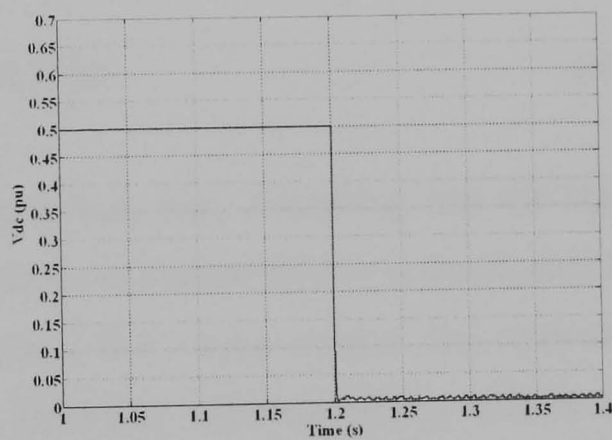
(b)
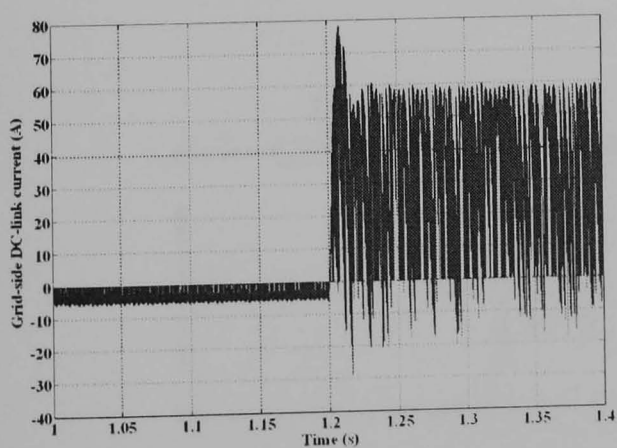
(c)
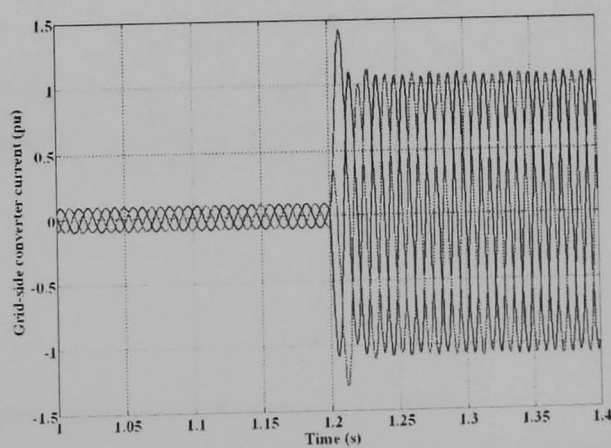
(d)

Figure 6.4 Simulation results showing effects of a short-circuit switch fault in the machine-side converter, phase A, top switch on (a) machine-side dc-link current, (b) dc-link voltage, (c) grid-side dc-link current and (d) grid-side converter line currents

143

6.1.2 Effects on Generator Variables

This section focuses on the effects of faults on generator variables. The effects of an open-switch fault will be first considered and then followed by the effects of a short-circuit switch fault.

i. Open-Switch Fault

In this case, only a fault in the machine-side converter will be considered because such a fault on the grid-side converter has little effect on the rotor currents as discussed in the previous section. Considering first the rotor current, this fault causes the faulty phase rotor current to lose one half cycle and also generates a dc offset in each phase current. To investigate the effect of the fault on the stator side, the stator flux and stator currents are first taken into consideration. The stator flux can be calculated from,

$$\overline{\lambda}_s^s = \int \left(\overline{v}_s^s - R_s \overline{i}_s^s \right) dt .$$
(6.1)

This flux consists of leakage part and magnetising part. Assuming that the stator voltage is unchanged and that the stator resistance of typical DFIGs is small, then the resistive voltage drop is negligible. Under stator-flux vector control, the equivalent circuit used for analysis of the DFIG in a stationary reference frame will be that shown in figure 6.5 [6.1]
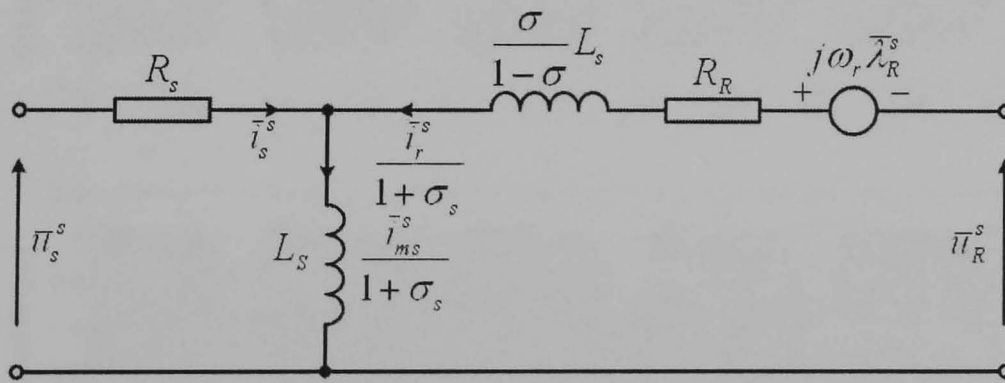
Figure 6.5 The T representation of a doubly-fed induction generator for stator-flux vector control

The definitions and parameters for this equivalent circuit are described in appendix B. As shown in figure 6.5, the stator flux linkage is mainly dominated by stator voltage. Therefore, if the stator voltage is fixed, stator flux linkage is constant. As

shown in figure 6.5, the stator magnetising current in a stationary reference frame can be represented as follows,

$$\bar{i}_{ms}^{s} = \left(1 + \sigma_s\right)\bar{i}_{s}^{s} + \bar{i}_{r}^{s}. \tag{6.2}$$

Since the stator flux linkage is constant, its magnetising current is also constant. Therefore, the effect of an open-switch fault on the rotor current will be transferred to the stator current. The stator currents can be synthesised by first transforming $\bar{i}_{ms}$ and $\bar{i}_r$ into a stationary reference frame fixed to stator. Then, stator current vector can be calculated from

$$\bar{i}_{s}^{s} = \frac{1}{\left(1 + \sigma_s\right)}\left(\bar{i}_{ms}^{s} + \bar{i}_{r}^{s}\right). \tag{6.3}$$

The synthesised stator currents are then transformed back to the stator three-phase reference frame. The results of a simulation with an open-switch fault on the machine-side converter are shown in figure 6.6, where figure 6.6a shows the synthesised stator currents and figure 6.6b shows the actual stator currents.
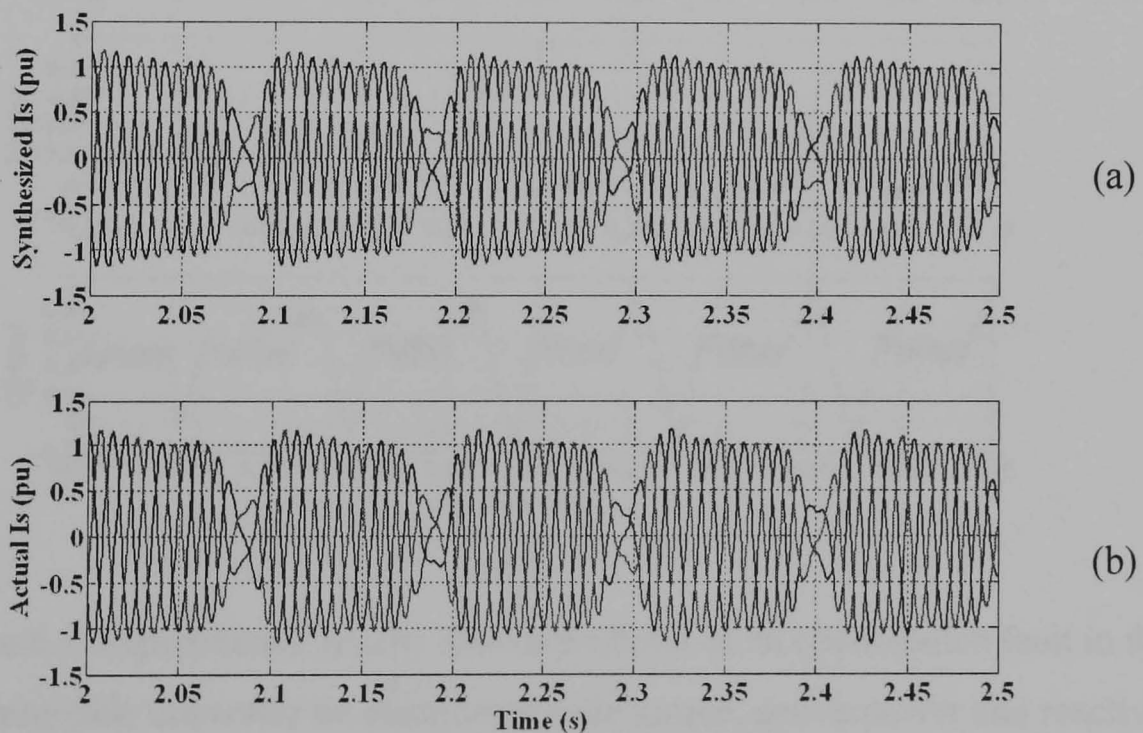
Figure 6.6 Comparison of the simulated stator currents between (a) synthesised stator currents and (b) actual stator currents

As shown in figure 6.6, there is an excellent match between the synthesised stator current waveform and the actual stator current waveforms.
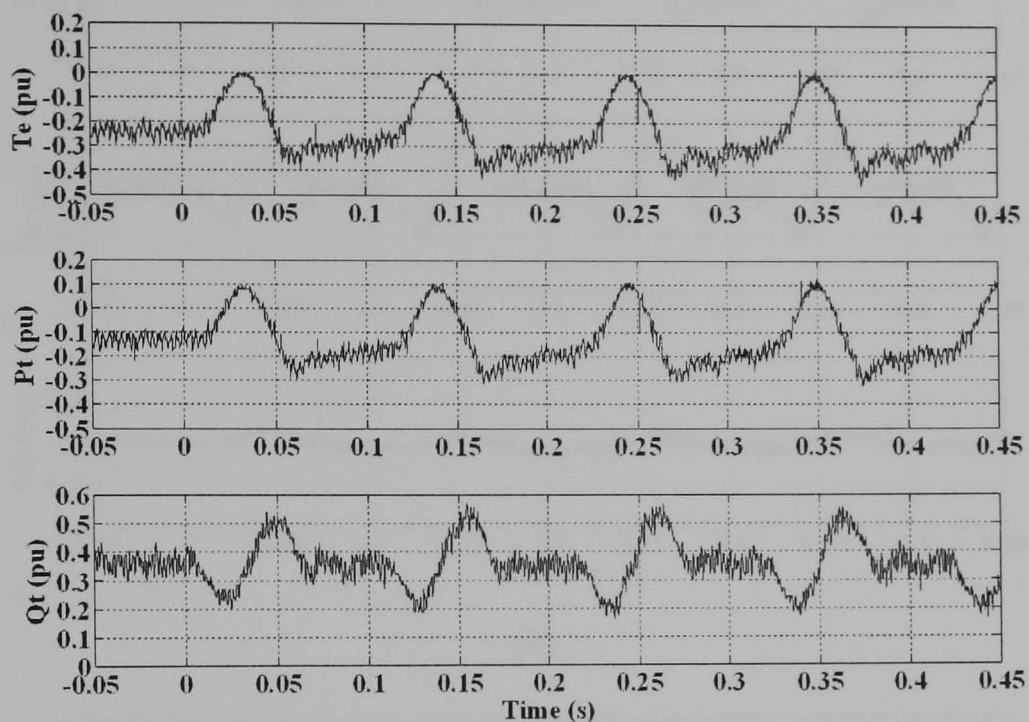
(a)
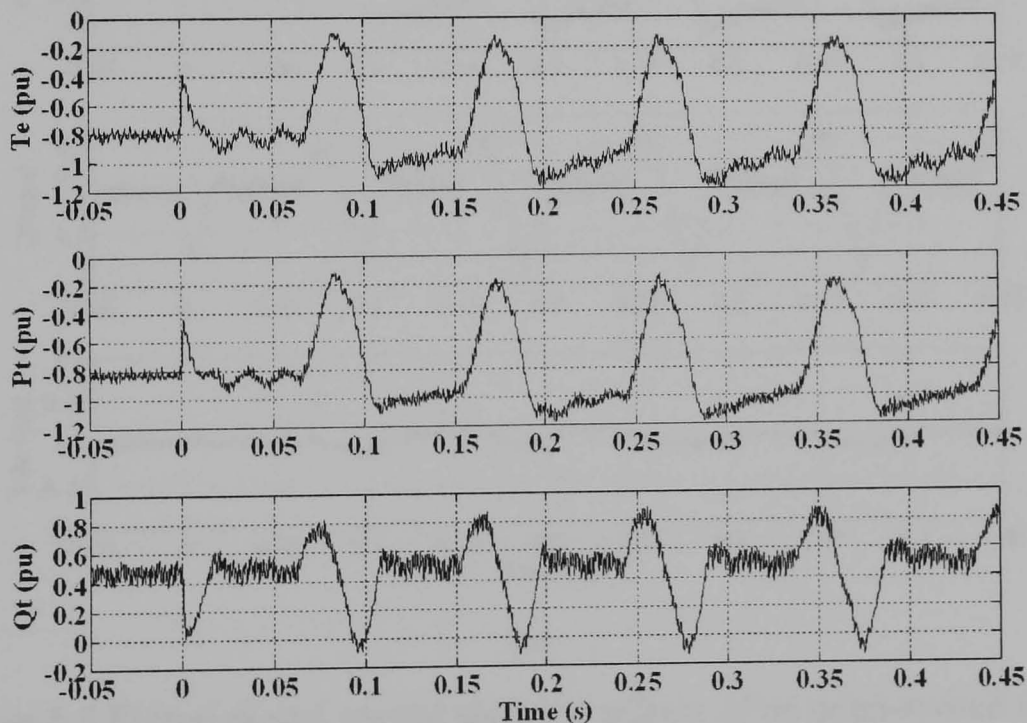
(b)

Figure 6.7 Experimental results showing effects of an open-switch fault in the machine-side converter on electromagnetic torque, active power and reactive power for (a) sub-synchronous speed generation and (b) super-synchronous speed generation
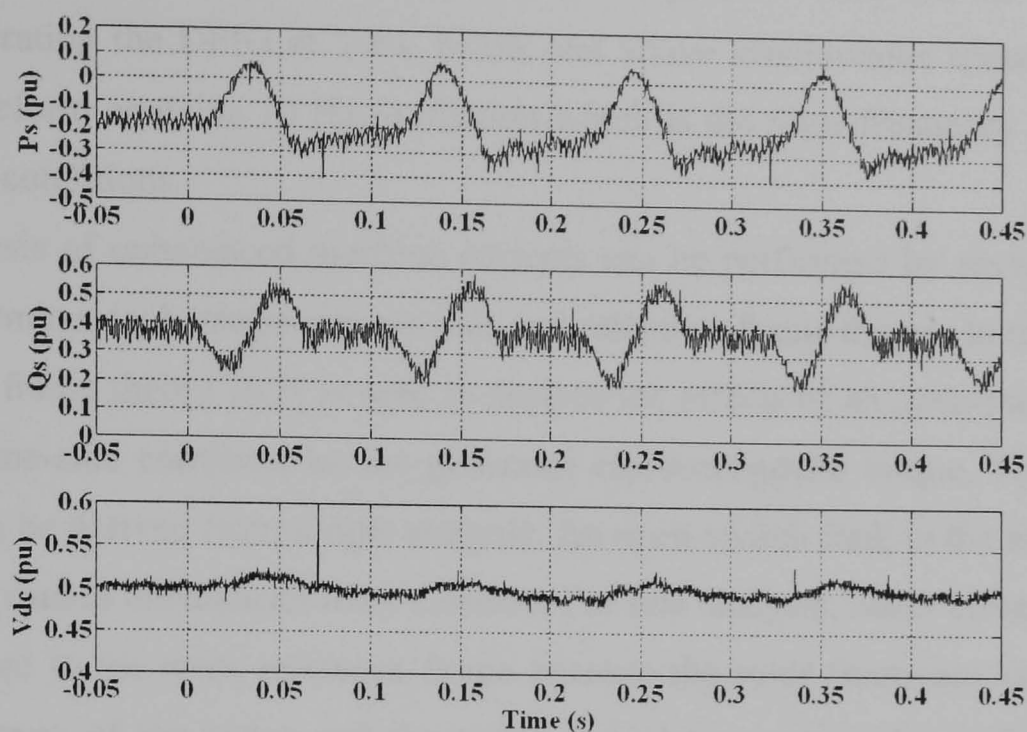
(a)
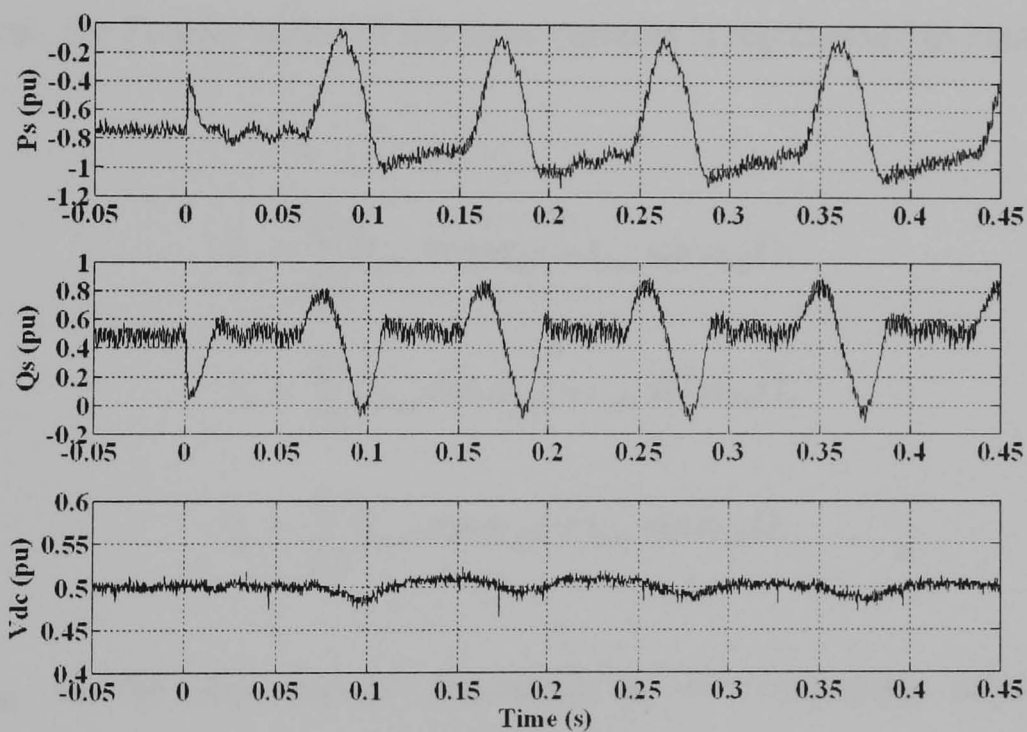
(b)

Figure 6.8 Experimental results showing effects of an open-switch fault in the machine-side converter on stator active power, stator reactive power and dc-link voltage for (a) sub-synchronous speed generation and (b) super-synchronous speed generation

An open-switch fault in the machine-side converter causes torque pulsations and oscillation in the generator active and reactive powers, as shown in figure 6.7. Likewise, the stator active power, stator reactive power and dc-link voltage are also

147

affected by this fault, as shown in figure 6.8. In figures 6.7 and 6.8, the fault occurs while operating the DFIG at 20% below and above synchronous speed. Therefore each waveform contains 10 Hz oscillation which is the rotor frequency under these operating conditions.

The analysis of unbalanced machine currents can be performed by several methods such as symmetrical component analysis and reference frame theory. In this research, reference frame theory [6.2] is used to analyse the effects of an open-switch fault in the machine-side converter on the generator electromagnetic torque. The generator power can be derived from torque analysis. An open-switch fault in the machine-side converter causes unbalanced rotor currents. For this analysis, stator currents must be transformed to the rotor reference frame because the rotor frequency is lower than the frequency of the stator and the torque calculation cannot be performed using variables in different reference frames. Assuming that the stator of the generator is symmetrical, the Fourier series of the rotor currents is represented in equations (6.4)-(6.6).

$$i_{ar} = \sum_{k=0}^{\infty} \left(i_{arkc} \cos \omega_{slk} t + i_{arks} \sin \omega_{slk} t \right), \tag{6.4}$$

$$i_{br} = \sum_{k=0}^{\infty} \left(i_{brkc} \cos \omega_{slk} t + i_{brks} \sin \omega_{slk} t \right), \tag{6.5}$$

$$i_{cr} = \sum_{k=0}^{\infty} \left(i_{crkc} \cos \omega_{slk} t + i_{crks} \sin \omega_{slk} t \right). \tag{6.6}$$

where ω_{slk} is the slip angular frequency at k^{th} harmonic, calculated from $\omega_{ek} - \omega_r$ and ω_{ek} is the synchronous frequency at k^{th} harmonic.

Transforming the three-phase variables into a synchronous reference frame for each rotor harmonic, by equation (6.7),

$$\mathbf{A} = \frac{2}{3} \begin{bmatrix} \cos \beta & \cos\left(\beta - \frac{2\pi}{3}\right) & \cos\left(\beta + \frac{2\pi}{3}\right) \\ -\sin\beta & -\sin\left(\beta - \frac{2\pi}{3}\right) & -\sin\left(\beta + \frac{2\pi}{3}\right) \\ \frac{1}{2} & \frac{1}{2} & \frac{1}{2} \end{bmatrix}, \qquad \begin{array}{l} \beta = \theta - \theta_r \\ \\ \theta_r = \omega_r t. \end{array} \tag{6.7}$$

Then the rotor currents in a synchronous reference frame become,

$$i_{dr} = \sum_{k=0}^{\infty} \{ i_{drkA} \cos[(\omega_{slk} + \omega_r)t - \theta] + i_{drkB} \sin[(\omega_{slk} + \omega_r)t - \theta] \}$$
$$+ \sum_{k=0}^{\infty} \{ i_{drkC} \cos[(\omega_{slk} - \omega_r)t + \theta] + i_{drkD} \sin[(\omega_{slk} - \omega_r)t + \theta] \} \qquad (6.8)$$

$$i_{qr} = \sum_{k=0}^{\infty} \{ i_{qrkA} \cos[(\omega_{slk} + \omega_r)t - \theta] + i_{qrkB} \sin[(\omega_{slk} + \omega_r)t - \theta] \}$$
$$+ \sum_{k=0}^{\infty} \{ i_{qrkC} \cos[(\omega_{slk} - \omega_r)t + \theta] + i_{qrkD} \sin[(\omega_{slk} - \omega_r)t + \theta] \} \qquad (6.9)$$

$$i_{0r} = \frac{1}{3} \sum_{k=0}^{\infty} [(i_{arkc} + i_{brkc} + i_{crkc}) \cos \omega_{slk} t + (i_{arks} + i_{brks} + i_{crks}) \sin \omega_{slk} t]$$
$$= \sum_{k=0}^{\infty} i_{0rk} \qquad (6.10)$$

where i_{drkA}, i_{qrkA}, i_{drkB}, i_{qrkB}, i_{drkC}, i_{qrkC}, i_{drkD} and i_{qrkD} are balanced components of rotor currents and can be derived as follows,

$$i_{drkA} = \frac{1}{3} \left[i_{ark\alpha} - \frac{1}{2} i_{brk\alpha} - \frac{1}{2} i_{crk\alpha} + \frac{\sqrt{3}}{2} (i_{brk\beta} - i_{crk\beta}) \right], \qquad (6.11)$$

$$i_{drkB} = \frac{1}{3} \left[i_{ark\beta} - \frac{1}{2} i_{brk\beta} - \frac{1}{2} i_{crk\beta} - \frac{\sqrt{3}}{2} (i_{brk\alpha} - i_{crk\alpha}) \right], \qquad (6.12)$$

$$i_{drkC} = \frac{1}{3} \left[i_{ark\alpha} - \frac{1}{2} i_{brk\alpha} - \frac{1}{2} i_{crk\alpha} - \frac{\sqrt{3}}{2} (i_{brk\beta} - i_{crk\beta}) \right], \qquad (6.13)$$

$$i_{drkD} = \frac{1}{3} \left[i_{ark\beta} - \frac{1}{2} i_{brk\beta} - \frac{1}{2} i_{crk\beta} + \frac{\sqrt{3}}{2} (i_{brk\alpha} - i_{crk\alpha}) \right], \qquad (6.14)$$

$$i_{qrkA} = -\frac{1}{3} \left[i_{ark\beta} - \frac{1}{2} i_{brk\beta} - \frac{1}{2} i_{crk\beta} - \frac{\sqrt{3}}{2} (i_{brk\alpha} - i_{crk\alpha}) \right], \qquad (6.15)$$
$$= -i_{drkB}$$

$$i_{qrkB} = \frac{1}{3} \left[i_{ark\alpha} - \frac{1}{2} i_{brk\alpha} - \frac{1}{2} i_{crk\alpha} + \frac{\sqrt{3}}{2} (i_{brk\beta} - i_{crk\beta}) \right], \qquad (6.16)$$
$$= i_{drkA}$$

$$i_{qrkC} = \frac{1}{3}\left[i_{ark\beta} - \frac{1}{2}i_{brk\beta} - \frac{1}{2}i_{crk\beta} + \frac{\sqrt{3}}{2}\left(i_{brk\alpha} - i_{crk\alpha} \right) \right],$$

$$= i_{drkD}$$

(6.17)

$$i_{qrkD} = -\frac{1}{3}\left[i_{ark\alpha} - \frac{1}{2}i_{brk\alpha} - \frac{1}{2}i_{crk\alpha} - \frac{\sqrt{3}}{2}\left(i_{brk\beta} - i_{crk\beta} \right) \right].$$

$$= -i_{drkC}$$

(6.18)

As shown in equations (6.8) and (6.9), there are two arguments in these equations - $\left(\omega_{slk} + \omega_r \right)t - \theta$ and $\left(\omega_{slk} - \omega_r \right)t + \theta$ respectively. In the case of $k=1$, terms $\omega_{slk} + \omega_r = \omega_e$ and $\omega_{slk} - \omega_r = \omega_e - 2\omega_r$. For the sake of simplicity, by setting $\theta = 0$ in equations (6.8) and (6.9), the terms with argument $\left(\omega_{slk} + \omega_r \right)t - \theta$ generate an air-gap MMF which rotates positively at ω_e relative to the stationary reference frame and positive to the rotor windings if $\omega_r < \omega_e$ and negative to the rotor windings if $\omega_r > \omega_e$. The terms with argument $\left(\omega_{slk} - \omega_r \right)t + \theta$ generate an air-gap MMF which rotates negatively if $2\omega_r < \omega_e$ and positively if $2\omega_r > \omega_e$ relative to the stationary reference frame. The rotational direction is the reverse of a positive balanced set referred to the rotor windings. There are four balanced sets appearing after transformation. Subscripts A and B are associated with the positively rotating balanced sets whereas C and D are associated with the negatively rotating balanced sets. Generally, unbalanced rotor conditions cause air-gap MMFs rotating at $\omega_r + \omega_{slk}$ and $\omega_r - \omega_{slk}$ relative to the stationary reference frame [6.2] In this research, only harmonic components up to the 9th are considered. In this analysis the 10 Hz component is considered to be the fundamental rotor frequency component as it is the frequency of the rotor while operating at 0.8 pu or 1.2 pu speed.

To calculate electromagnetic torque from stator and rotor variables, both variables must be in the same reference frame. Therefore, for this analysis, the stator currents must be transformed to a stationary reference frame fixed to the rotor. This can be done by transforming the stator currents in the synchronous reference frame to the rotor reference frame by the inverse Park's transform. Then, transforming these variables into the three-phase rotor reference frame by the inverse Clarke's transform, resulting in the stator currents having rotor frequency in the rotor

reference frame. After transformation, the stator current components are then calculated by using equations (6.4)-(6.18). The electromagnetic torque calculated from stator and rotor balanced components are as follows

$$
T_e = \left(\frac{3}{2}\right) P L_m
$$

$$
\sum_{k=0}^{\infty} \sum_{K=0}^{\infty} \begin{bmatrix} \left(i_{drkA} i_{dsKA} - i_{drkA} i_{dsKB} + i_{drkC} i_{dsKD} - i_{drkD} i_{dsKC} \right) \cos\left(\omega_{slk} - \omega_{slK}\right)t \\ + \left(-i_{drkA} i_{dsKA} - i_{drkB} i_{dsKB} + i_{drkC} i_{dsKC} + i_{drkD} i_{dsKD} \right) \sin\left(\omega_{slk} - \omega_{slK}\right)t \\ + \left(i_{drkA} i_{dsKD} - i_{drkD} i_{dsKA} + i_{drkB} i_{dsKC} - i_{drkC} i_{dsKB} \right) \cos\left(\omega_{slk} + \omega_{slK}\right)t \\ + \left(-i_{drkA} i_{dsKC} + i_{drkC} i_{dsKA} + i_{drkB} i_{dsKD} - i_{drkD} i_{dsKB} \right) \sin\left(\omega_{slk} + \omega_{slK}\right)t \end{bmatrix} \quad (6.19)
$$

From this equation, under unbalanced condition and taking only the fundamental frequency component present in the rotor current, the terms with the argument $\left(\omega_{slk} + \omega_{slK}\right)$ cause a steady pulsating torque having two times the slip frequency of $2\left(\omega_e - \omega_r\right)$. This is the interaction between the air-gap MMF rotating at ω_e generated by the positive rotating balanced set and the air-gap MMF rotating at $2\omega_r - \omega_e$ generated by negatively rotating balanced set. This phenomenon is revealed by the simulation results shown in figure 6.9.

As shown in figure 6.9a, the torque generated by the fundamental components of both stator and rotor currents during an open-switch fault in the machine-side converter has a two-times rotor frequency pulsating torque riding on the average torque, as discussed previously. Figure 6.9b is a comparison between the actual torque and the torque synthesised from all nine harmonic components. As the moment of inertia of the simulated system is quite low the synthesised torque does not exactly match the actual torque due to speed variation.
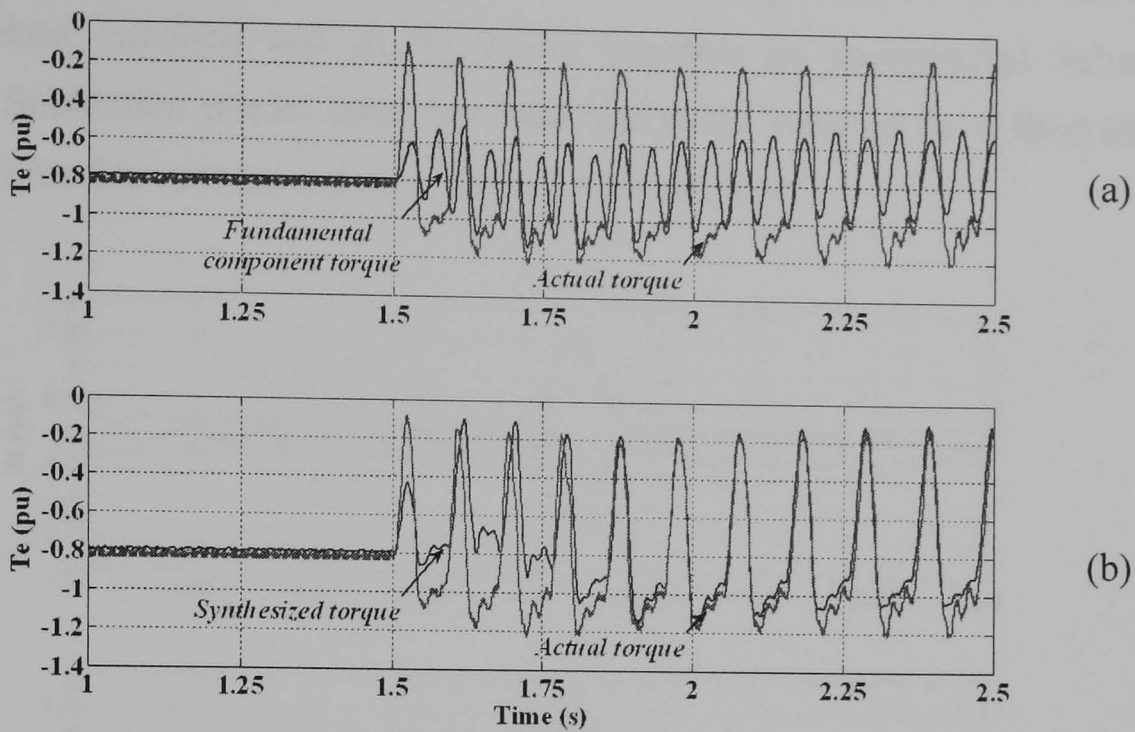
Figure 6.9 Comparison between actual torque and torque generated by (a) only fundamental component of stator and rotor currents and (b) all balanced set components

ii. Short-Circuit Switch Fault

A short-circuit switch fault in the back-to-back converters of the DFIG causes different phenomena from a short-circuit switch fault in the back-to-back converters of a stator-fed induction machine. If a short-circuit switch fault occurs in the latter case, the system is stopped and has to be isolated from the grid. Generally, when a short-circuit switch fault occurs, the fault detection circuit sends a command to the controller to disable all gate signals to stop the converter. However, this is not true for the DFIG because the stator of the generator is still connected to the grid even if its rotor is short circuited via the faulty leg. Under these circumstances the DFIG becomes an uncontrolled induction generator.

Assuming that there is no such short-circuit switch fault protection circuit, there can be two consequences of this type of fault – the faulty leg remains short circuited or the faulty leg becomes open circuited. This latter case can occur if the faulty switches explode and end up as open circuits in the faulty phase. In this event, the DFIG must be stopped for maintenance.

The former is likely if the switch case does not rupture as the latter case but the complementary switch is also likely to become a short circuit. Therefore the

converter will lose all dc-link voltage as the dc bus voltage becomes zero. The rotor becomes short circuited and so the DFIG becomes an uncontrolled induction generator. Simulation results show the rotor and stator currents for a short-circuit switch fault for this case are shown in figures 6.10 and 6.11.
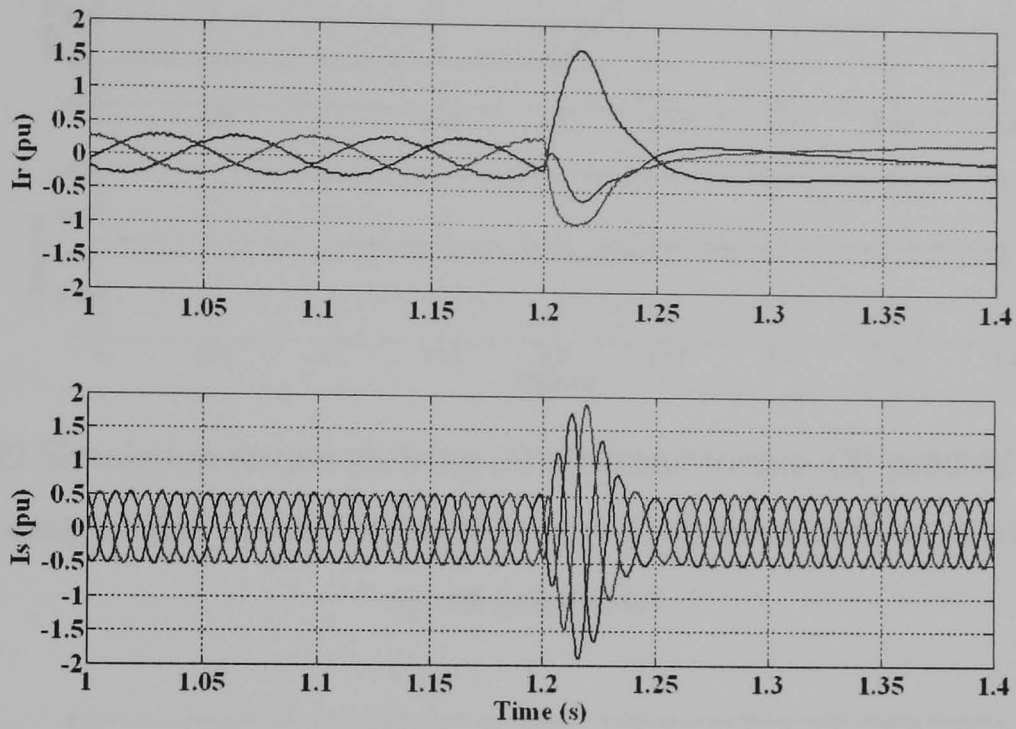
Figure 6.10 Rotor currents and stator currents during a short-circuit switch fault for sub-synchronous speed generation
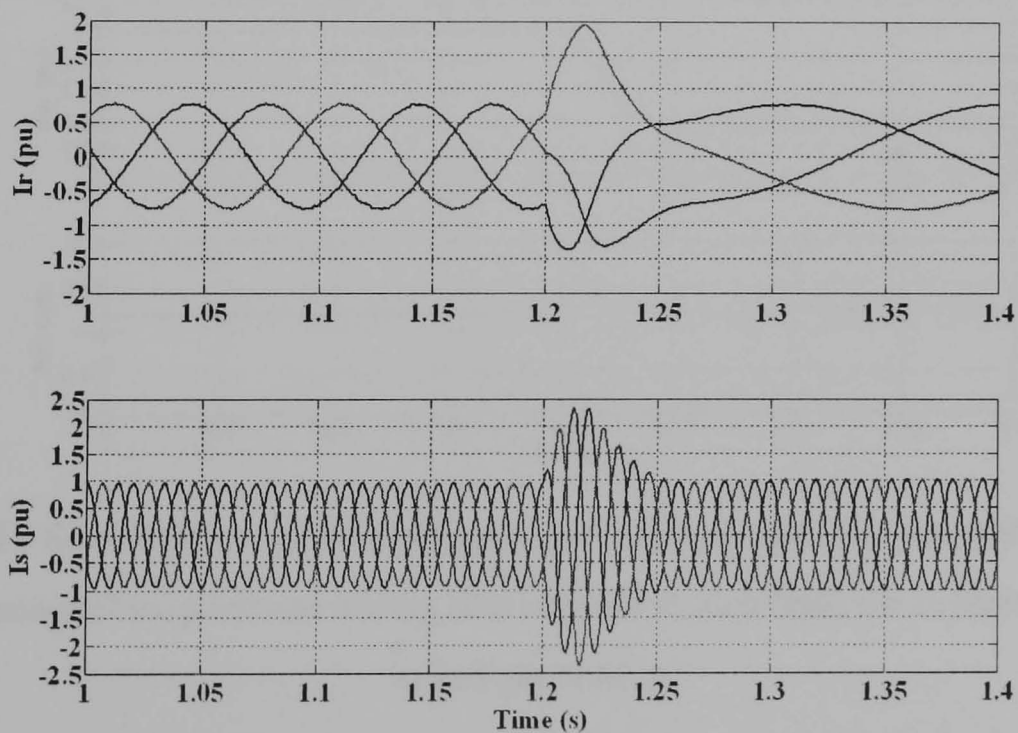
Figure 6.11 Rotor currents and stator currents during a short-circuit switch fault for super-synchronous speed generation

153
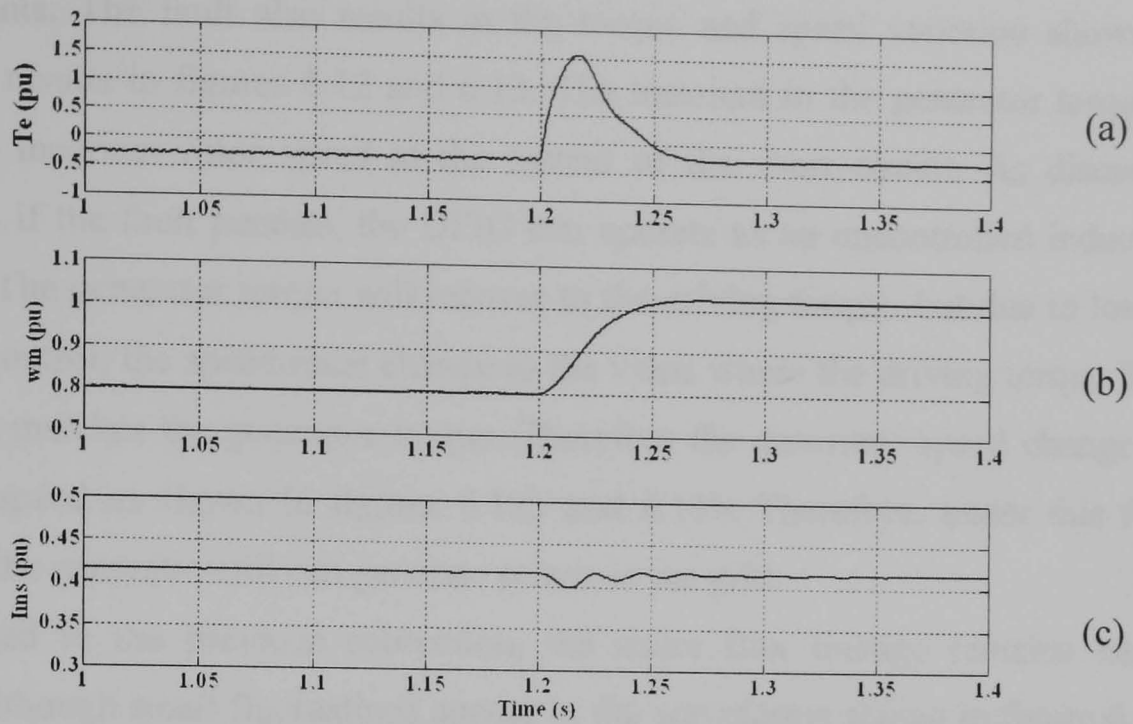
Figure 6.12 Simulation results showing (a) generator torque, (b) generator speed and (c) stator magnetising current during short-circuit switch fault for sub-synchronous speed generation
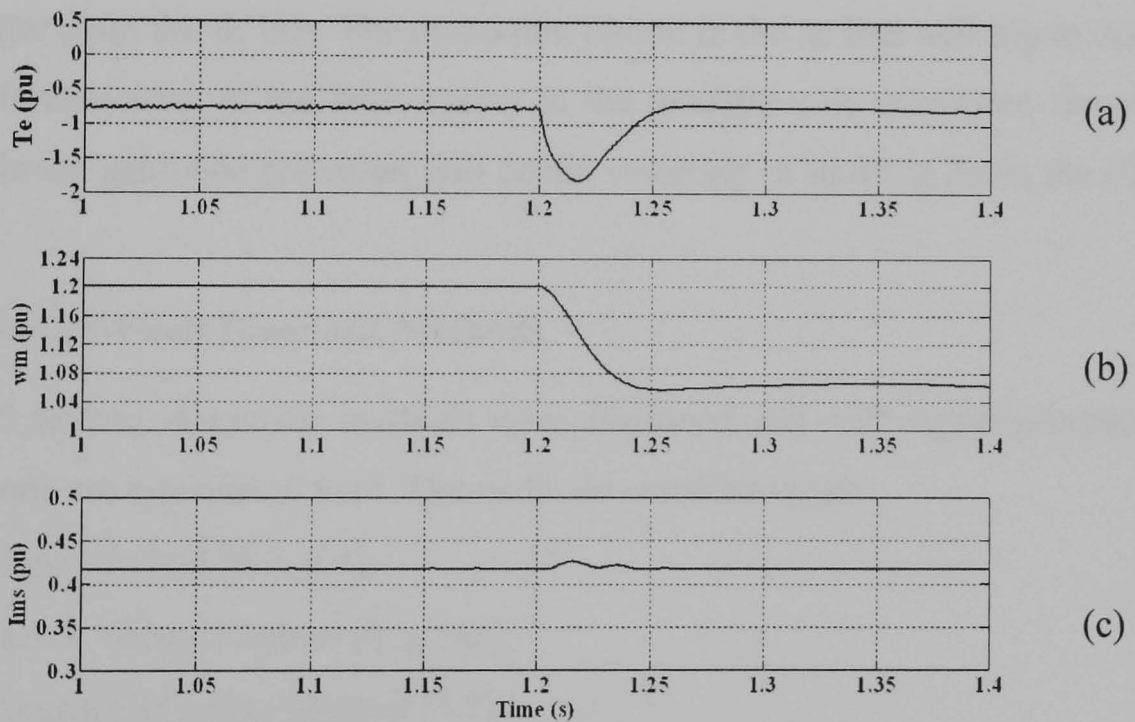
Figure 6.13 Simulation results showing (a) generator torque, (b) generator speed and (c) stator magnetising current during short-circuit switch fault for super-synchronous speed generation

As shown in figures 6.10 and 6.11, the fault appears at 1.2 second. During the fault the rotor currents increase for one and a half cycles due to the abrupt short circuit in the converter and the stator currents increase as a consequence of the increase in

rotor currents. The fault also results in the torque and speed variation shown in simulation results in figures 6.12 and 6.13. The transient in the generator torque is due to the incorrect rotor speed at the instant of the short circuit. As discussed previously, if the fault persists, the DFIG can operate as an uncontrolled induction generator. The generator torque will recover to the driving torque, but due to loss of converter control, the speed must change to the value where the driving torque from the turbine matches the generator torque. Therefore the generator speed changes to the stable speed as shown in figures 6.12b and 6.13b. Therefore, under this fault condition, the generator still can generate power to the grid

As discussed in the previous subsection, the stator flux linkage remains nearly constant, although small fluctuations appear in the waveforms shown in figure 6.12c and 6.13c. This fluctuation would be insignificant for a practical DFIG due to negligible voltage drop across the stator resistance.

In commercial wind turbines, it is likely that when a shoot-through fault occurs in the grid-side converter, the fuse in the dc link will blow resulting in isolation of the grid-side converter from the dc bus. The protection circuit in the ac line will trip to isolate the grid-side converter. If the fault occurs in the machine-side converter, the same process as in the grid-side converter will occur, resulting in shutting down the DFIG system.

6.2 Open-Switch Fault Diagnosis Methods

In chapter 5 several diagnostic methods were discussed, but only signal processing-based methods are considered here. The methods considered are:

- Slope Method [6.3, 6.4],
- Park's Vector Method [6.5, 6.6],
- Control Deviation Method [6.7],
- Normalised DC Current Method [6.8],
- Modified Normalised DC Current Method [6.10, 6.11],
- Simple DC Current Method [6.10, 6.11].

The advantages and drawbacks of these methods are discussed in [6.10, 6.11]. The most significant problem identified was false alarms, and this was partially resolved by introducing a fixed dead time for each method [6.10]. However, this was not able

to prevent false alarms under every operating condition. A fixed dead time could be used in the grid-side converter but cannot be used in the machine-side converter which has variable fundamental frequency. This is one of the weaknesses of the existing fault detection methods.

With the exception of the Slope Method, each method is based on a calculation of the dc component and/or fundamental component of either the space vector of the three-phase currents or of all three phase currents, and this is used as a diagnostic index. A recursive moving average technique is employed to achieve the calculation of these indices. However, in case of the machine-side converter, the frequency of the currents varies through zero frequency. Under this condition, when the speed of the generator passes synchronous speed, only the Slope Method and Control Deviation Method do not show false alarms. The Park's Vector Method, Normalised DC Current Method, Modified Normalised DC Current Method and Simple DC Current Method show false alarms under this condition, because of the nature of their moving average calculation. This requires the previous instantaneous data for the present moving average value. In case of N samples per cycle, the present average value needs the present value and $N-1$ previous values for calculation. When the machine passes synchronous speed the current becomes dc. Depending on the rate of change of speed the fundamental component of the current is zero or almost zero for a certain time. This causes the average and normalised average values to become very high after the speed passes synchronous speed.

The Control Deviation Method does not suffer from false alarms under these conditions because there is no fundamental component in the command current, but it has false alarms under transient conditions and under low current conditions. Moreover, the fault detection algorithm must be integrated into the control algorithm. The Slope Method did not perform well for fault detection as described in [6.10, 6.11]. It has a longer detection time compared with other methods because, under healthy conditions, the Slope Method has some values in the tolerance range of faulty states [6.10]. As illustrated in [6.10, 6.11], the Modified Normalised DC Current Method is the most effective of the existing methods. It was first proposed by Abramik *et al.* [6.8] and was later modified by Rothenhagen and Fuchs [6.10, 6.11]. This method uses the moving average value of the line current as a diagnostic

variable. To make this variable independent of load, the moving average value is normalised by the fundamental component of the line current by means of the Discrete Fourier Transform (DFT), as shown in the equations below,

$$\mu_v = \frac{1}{N}\sum_{k=1}^{N} I_v(k\tau),$$

(6.20)

$$I_{1,v} = a_{1,v}\cos\left(\frac{2\pi}{T}k\tau\right) + b_{1,v}\sin\left(\frac{2\pi}{T}k\tau\right),$$

(6.21)

$$\gamma_v = \frac{\mu_v}{I_{1,v}},$$

(6.22)

$$a_{1,v} = \frac{2}{N}\sum_{k=1}^{N} I_v(k\tau)\cos\left(\frac{2\pi k}{N}\right),$$

(6.23)

$$b_{1,v} = \frac{2}{N}\sum_{k=1}^{N} I_v(k\tau)\sin\left(\frac{2\pi k}{N}\right),$$

(6.24)

$$v \in [a,b,c],$$

(6.25)

$$\frac{1}{f} = N\tau,$$

(6.26)

where k is 1, 2, 3...64, N is 64, and γ_v is a diagnostic variable for the Modified Normalised DC Current Method of each phase.

Under healthy conditions, the value of γ_v is always within the threshold of 0.45 [6.10, 6.11], but under faulty conditions, the value of γ_v of the faulty phase exceeds the threshold. In the case where the value of γ_v exceeds the threshold in more than one phase, the phase with the highest absolute of γ_v is the faulty phase.

6.2.1 Problem Issues for Application to the DFIG

The Modified Normalised DC Current Method seems to work well for any frequency except when the frequency of the current signal is close to zero or passes zero. When applied to the detection of an open switch fault in the machine-side converter of the DFIG, if the rotor speed passes synchronous speed the normalised dc current value exceeds the threshold of 0.45 as shown in figure 6.14. Figures 6.14a (i) and 6.14b (i)

show the simulated and experimental rotor current waveforms respectively passing synchronous speed from the sub-synchronous speed region to the super-synchronous speed region. In this case, the Modified Normalised DC Current Method had a delay of one half cycle introduced, but the method still shows a false alarm.
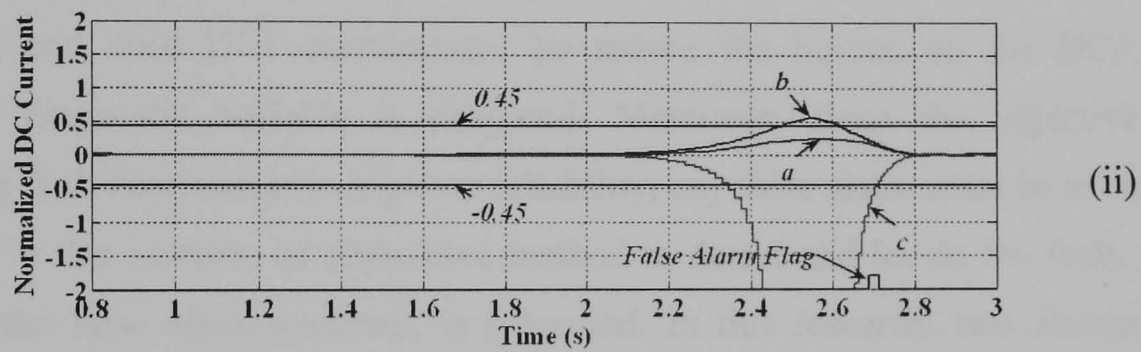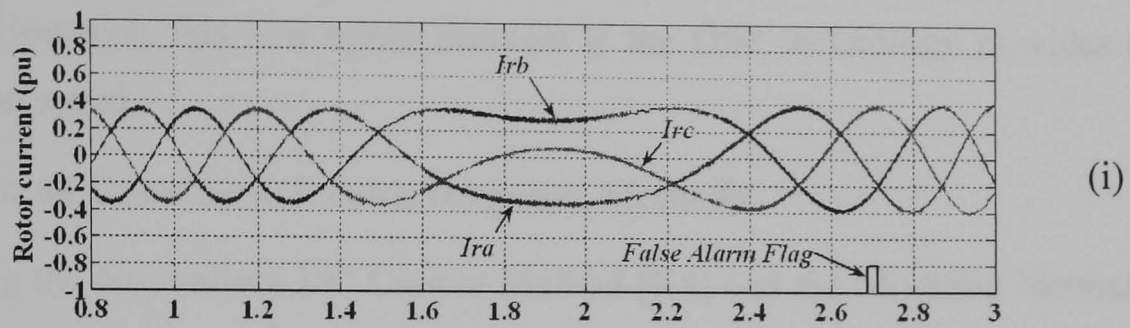
(a)
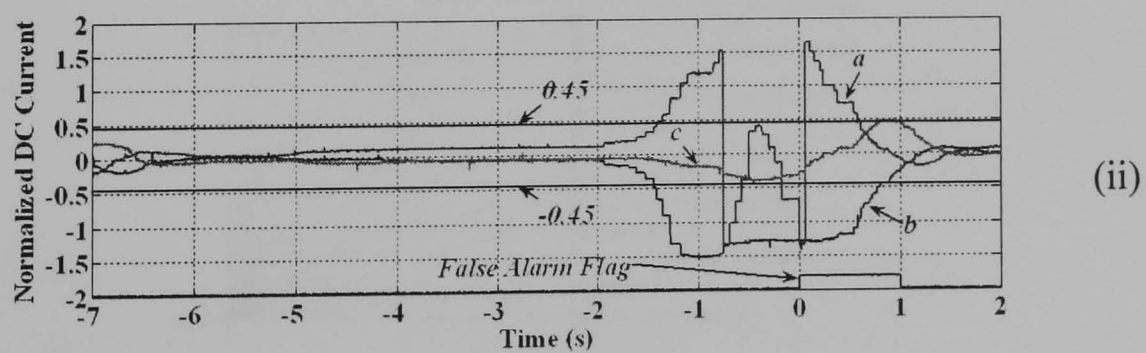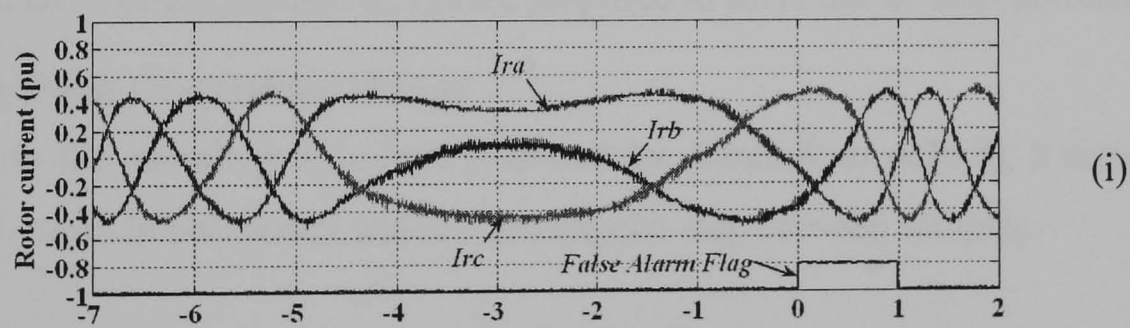
(b)

Figure 6.14 (a) Simulation results and (b) experimental results showing a false alarm during operating through synchronous speed while using the Modified Normalised DC Current Method as the fault detection method

A longer delay time might overcome this problem but the wind speed can cause the DFIG run continuously at speeds around synchronous speed and hence cause unavoidable false alarms. Moreover, a long delay time will increase the time to detect an open switch fault at other frequencies. This method also has a relatively long computational time because of the sinusoidal calculations and multiplications of the DFT. However, this is a minor problem if the DSP technology provides high computation speed.

6.2.2 Proposed Open-Switch Fault Diagnosis Methods

Considering the Normalised DC Current Method [6.8] and the Modified Normalised DC Current Method [6.10, 6.11], as explained earlier, these methods are time consuming and need DFT calculations. To reduce the burden on the DSP, an alternative diagnostic variable is proposed. Moreover, since the objective of introducing fault detection is to improve reliability, any false alarm must be avoided. Therefore, in this section, an alternative method to detect and locate the fault, and overcome the false alarm problem, is presented. In this research, two alternative methods named the Sampling Point Comparison Method and the Absolute Normalised DC Current Method [6.12] are proposed to solve one or both problems.

i. Sampling Point Comparison Method

According to the sampling technique proposed by Abramik *et al.*[6.8], a signal is sampled N times in one period with a fixed angular step between samples.
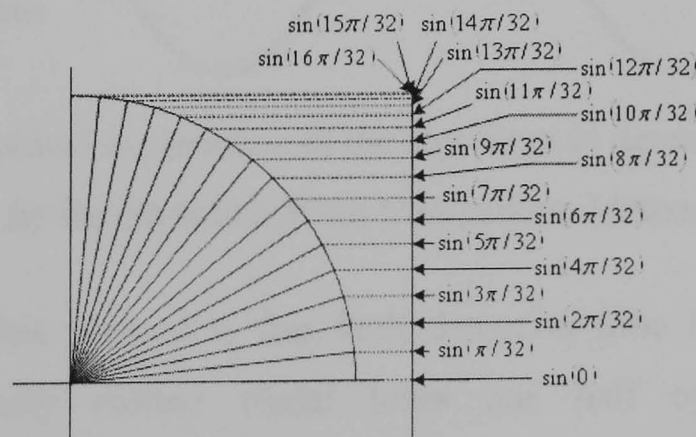
Figure 6.15 The first sector of a unit circle used for calculation of the faulty band for current during a faulty half cycle

Dividing a unit circle into 4 sectors, and considering only the first sector as shown in figure 6.15, each sector contains 16 samples with the value of $\sin(2m\pi / N)$, where m is 1, 2, 3,..., 16 and N is 1, 2, 3,..., 64.

The idea of this method is to check the number of samples lying in a "faulty band" and also in the positive and negative half cycles of the signal during faulty conditions. The faulty band ranges between the positive and negative product of the moving average value of the peak current vector and the sine value of the unit circle. The peak current can be obtained from the amplitude of the $\alpha - \beta$ components of the three-phase current vector. The value of $\sin\left(3\left(\frac{2\pi}{N}\right)\right)$ was found from both simulation and experiment to be a suitable multiplier to set the faulty band range.

The number of samples lying in the faulty band is included in the number of samples in both positive and negative half cycles. The number of samples is stored in a fault accumulator, a positive accumulator and a negative accumulator respectively. Once a fault appears in the converter, if the fault accumulator and either the positive or negative accumulator exceed the fault threshold, the faulty phase is detected. Then the sign of the moving average value of the faulty phase is checked to locate the faulty switch. This method can be graphically explained in figure 6.16.
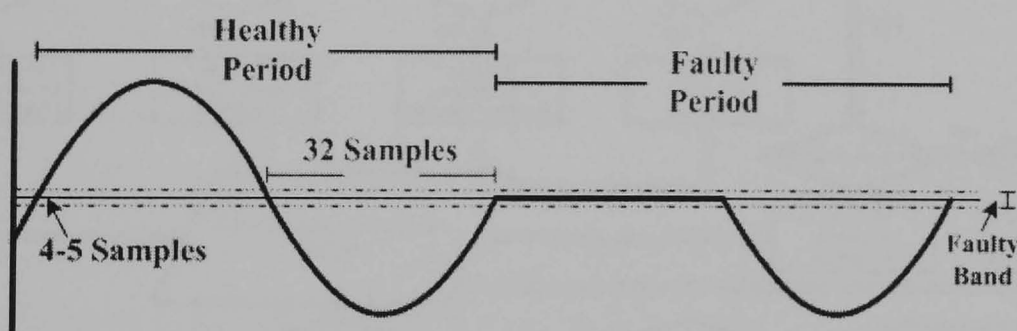
Figure 6.16 The graphical explanation of the algorithm to detect an open-switch fault by the Sampling Point Comparison Method

The advantage of this method is fast fault detection time because, under faulty conditions, the faulty current signal loses one half cycle. Moreover, the computational time required is much lower than that of the Modified Normalised DC Current Method because this method requires only moving average value calculation and if-else condition.

During a fault condition, the number of samples within the faulty band will exceed the limit (4 or 5 samples). If the threshold for the fault accumulator is set to a value

close to the limit e.g. 8 counts, and the threshold for both positive and negative accumulators is set to $N/2 + 8$ counts, the minimum detection time is approximately 1/8 cycle. This is much faster than the Modified Normalised DC Current Method which relies on the time that the value γ_v exceeds the threshold. Another advantage is that it can be used to detect two open switch faults in the same pole. Under two-open-switch fault condition, the faulty phase current become zero which means that the faulty current always stays within the faulty band. Therefore, the fault can be detected within 1 cycle. From experiments, if the number of samples in the fault accumulator exceeds 20 and the number of samples in the positive or negative accumulator exceeds 48, then a fault is recognised. These threshold values were determined by extensive tests at different speeds and torques. The algorithm used for the Sampling Point Comparison Method is represented in a flowchart, as shown in figure 6.17
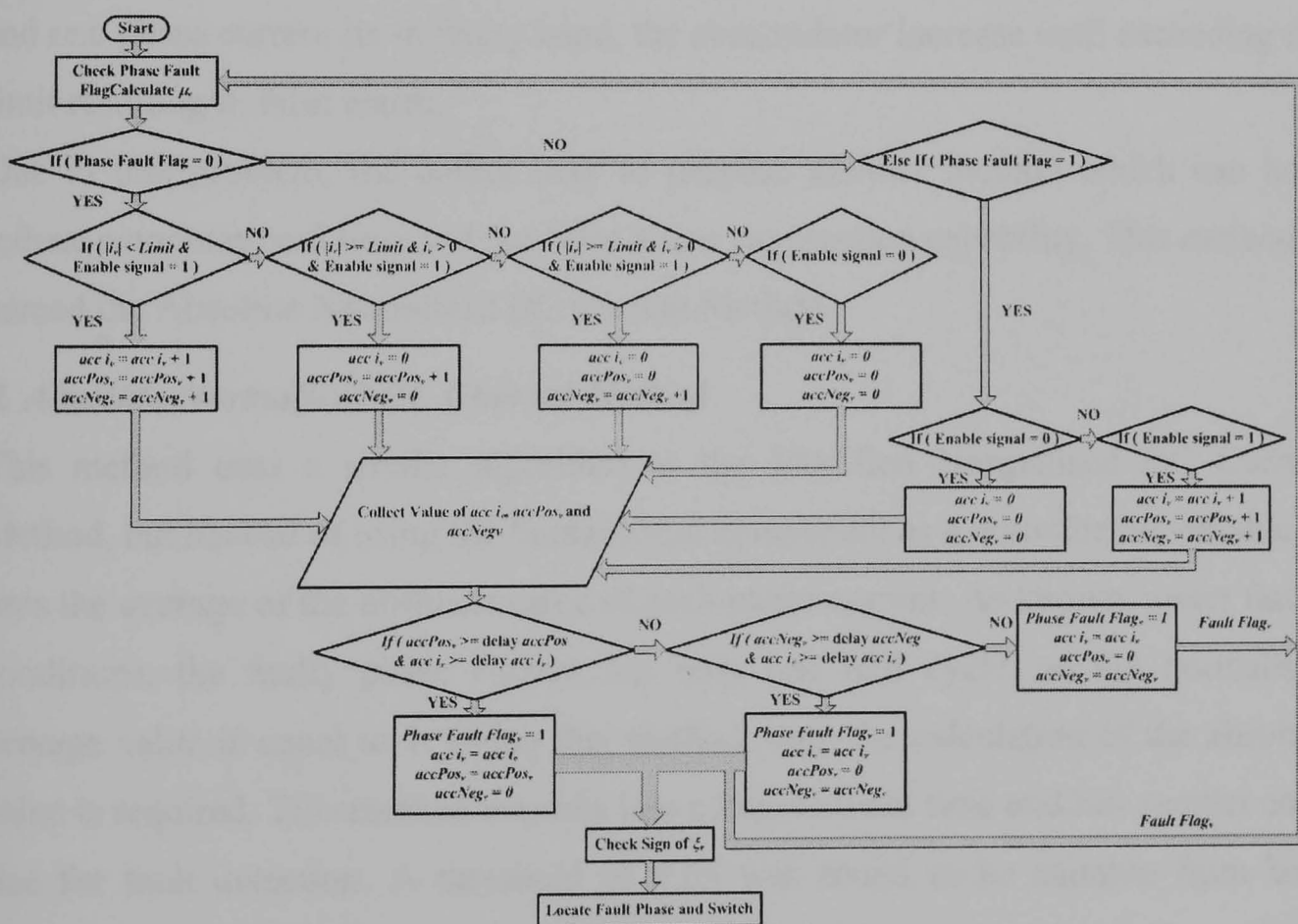
Figure 6.17 The flowchart representing the algorithm used for the Sampling Point Comparison Method

Although this method provides fast detection time and uses less computational time than the Modified Normalised DC Current Method, it may introduce false alarms

while operating around synchronous speed. This problem may arise at synchronous speed when one phase current stays within the faulty band. This can be explained by the equation applied to the code to enable circular buffer to update its array as follows,

$$if\left(rem\left(\frac{\theta}{\left(\frac{2\pi}{64}\right)} \right) \leq 2\pi f_1 T_s \right),$$
(6.27)

where θ is the sampled angle of the current signals, $rem\left(\frac{\theta}{\left(\frac{2\pi}{64}\right)} \right)$ is the remainder of $\frac{\theta}{\left(\frac{2\pi}{64}\right)}$, f_1 is the frequency of the current signals and T_s is the sampling period.

If equation (6.27) is true, the buffer in circular buffer is updated. Hence at synchronous speed, if small variation appears at f_1 causing equation (6.27) to be true and one phase current lie in faulty band, the accumulator increase until exceeding the limit resulting in false alarm.

Due to this problem, the author tries to propose another method which can both reduce computational time and has false alarm suppression capability. This method is named the Absolute Normalised DC Current Method.

ii. Absolute Normalised DC Current Method

This method uses a similar algorithm to the Modified Normalised DC Current Method, but instead of using the fundamental component as a normalising variable, it uses the average of the absolute value of each phase current. As known, under faulty conditions, the faulty phase current has only one half cycle, so the normalised average value is equal to 1. Using this method, only the calculation of the absolute value is required. This method requires less computational time and has smaller code size for fault detection. A threshold of 0.65 was found to be suitable from both simulation and experiment. The equations used to calculate the diagnostic variable for this method are the average value of the current as shown in equation (6.20) and the following equations,

$$\lambda_v = \frac{1}{N} \sum_{k=1}^{N} \left| I_v(k\tau) \right|,$$ (6.28)

$$\xi_v = \frac{\mu_v}{\lambda_v},$$ (6.29)

where ξ_v is the diagnostic variable for the Absolute Normalised DC Current Method of each phase.

As shown in figure 6.18a, phase A top switch is open and therefore it loses positive half cycles. The values of ξ_v after an open-switch fault in the machine-side converter are shown in figure 6.18b. The value of ξ_v of phase A exceeds the threshold and saturates at ± 1 whereas the value of ξ_v of phase B and C still lie within the threshold. This figure proves that ξ_v can be used as a diagnostic variable in the same way as γ_v.
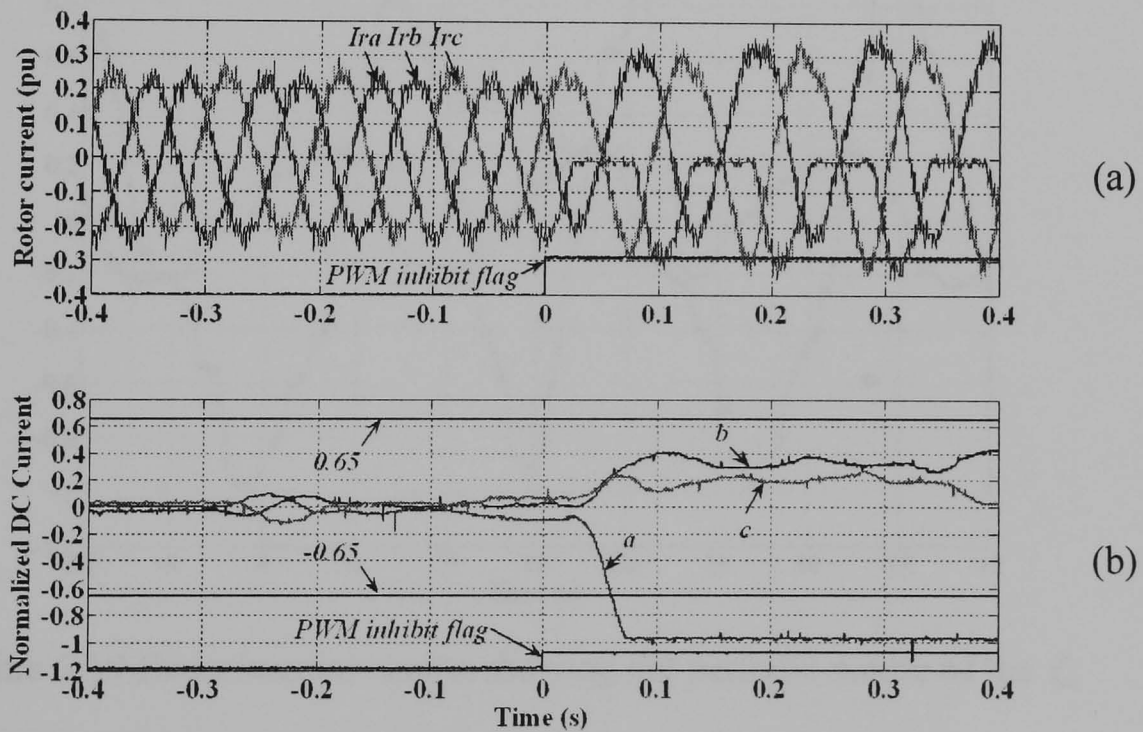
Figure 6.18 Experimental results showing (a) rotor currents and (b) the value of the diagnostic variables of the Absolute Normalised DC Current Method under an open-switch fault in the machine-side converter

The alternative normalising variable proposed helps reduce computational time for the fault detection module which is a minor problem when using the Modified

Normalised DC Current Method, and also has almost equal fault detection performance to that method. However, the major problem of false alarm still exists. This problem can be solved by proposing a false alarm suppression algorithm.

Due to the periodic nature of ξ_v, as shown in figure 6.19, if the DFIG operates at or around synchronous speed the value of ξ_v may exceed the threshold for at least 1/3 cycle. This periodic nature can be used in a false alarm suppression algorithm. To avoid false alarms, a delay of one half cycle ($\frac{N}{2}$ points) is introduced. During this delay, if the ξ_v of one of the other phases also exceeds the threshold, all phase fault flags are set to zero. Therefore, no false alarms appear although the speed of the generator swings slightly around synchronous speed. With this algorithm, the problem of operating the DFIG around synchronous speed or passing through synchronous speed is completely solved.
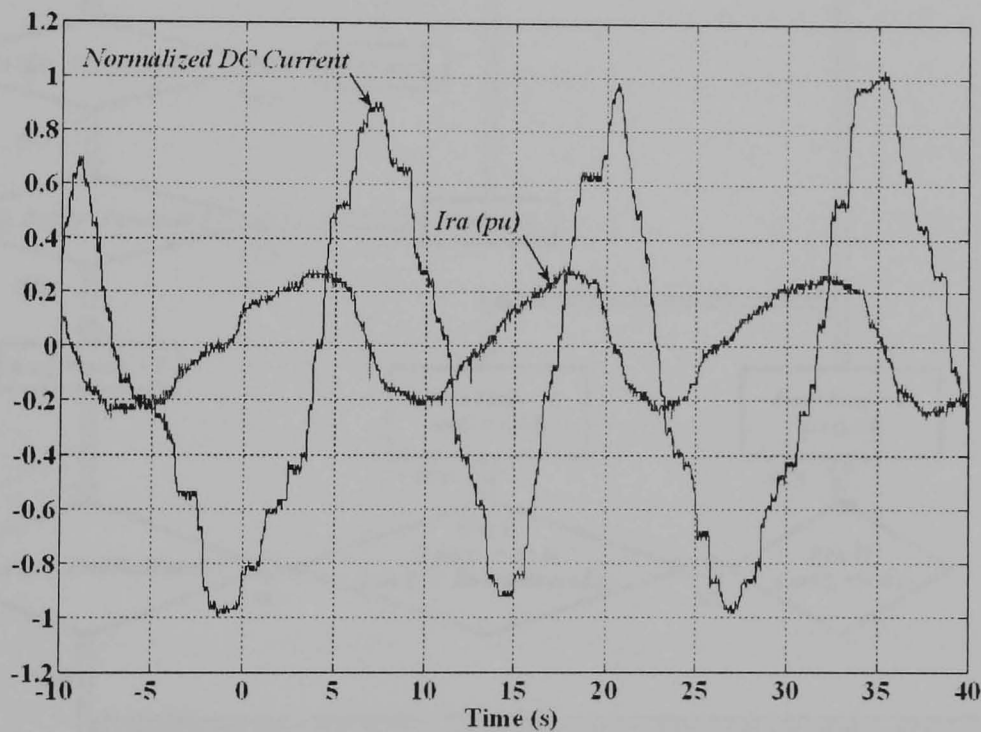
Figure 6.19 Experimental results showing the periodic nature of the ξ_v

This false alarm suppression algorithm may be applied to the Normalised DC Current Method but it requires more total computational time than the Absolute Normalised DC Current Method. Therefore, the Absolute Normalised DC Current Method is superior to the Modified Normalised DC Current Method.

The algorithm can be represented in a flowchart as shown in figure 6.20. The output of this method will be used for system reconfiguration, presented in the next chapter.

If both the Sampling Point Comparison Method and the Absolute Normalised DC Current Method are combined together, the combined method can detect one and two open-switch faults and has false alarm suppression capability. Furthermore, this method can also be applied to four quadrant electrical motor drives where the motor changes direction [6.12]. This method may also be applied to the Sampling Point Comparison Method to suppress false alarm but it will reduce efficiency of the Sampling Point Comparison Method.
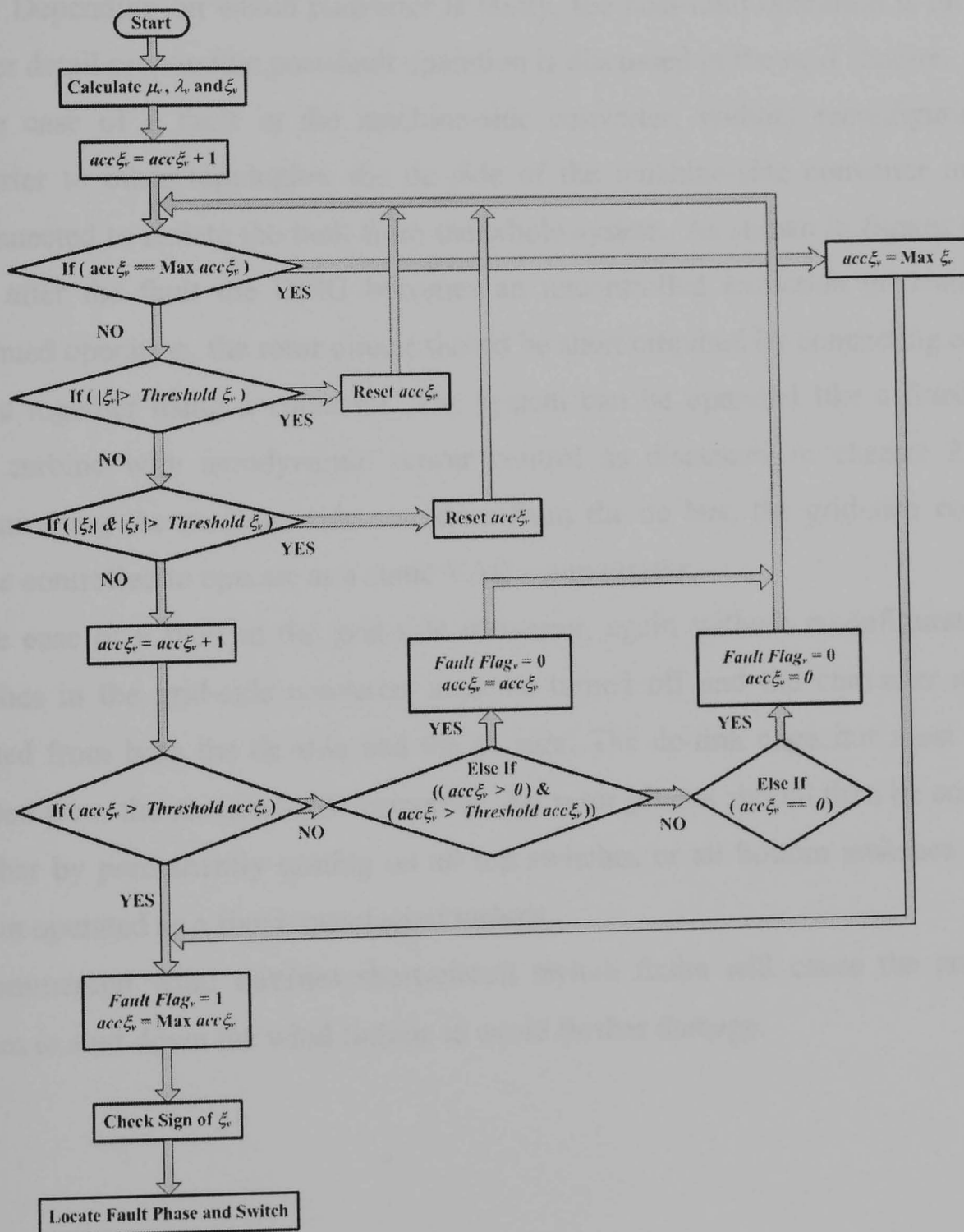
Figure 6.20 The flowchart representing the algorithm used for the Absolute Normalised DC Current Method

6.3 Short-Circuit Switch Fault Diagnosis Methods

As discussed in chapter 5, several methods to detect short-circuit switch faults have been discussed. Two main types of detection, depending on the location of sensors, were classified. The methods used for short-circuit switch fault diagnosis are applicable for the DFIG. However, the action taken after a fault is different from the case of the stator-fed machine. As discussed previously, a short-circuit switch fault in the DFIG does not require shutdown because the generator is still energised at its stator. Depending on which converter is faulty, the post-fault operation is different. Further detail on possible post-fault operation is discussed in the next chapter.

In the case of a fault in the machine-side converter, without reconfiguring the converter to other topologies, the dc side of the machine-side converter must be disconnected to isolate the fault from the whole system. As shown in figures 6.10 to 6.13, after the fault the DFIG becomes an uncontrolled induction generator. For continued operation, the rotor circuit should be short circuited by connecting all three phases together using a contactor. The system can be operated like a fixed-speed wind turbine with aerodynamic power control as discussed in chapter 2. After disconnecting the machine-side converter from the dc bus, the grid-side converter can be controlled to operate as a static VAR compensator.

In the case of a fault in the grid-side converter, again without reconfiguration, all switches in the grid-side converter must be turned off and the converter must be isolated from both the dc side and the ac side. The dc-link capacitor must also be isolated from the machine-side converter. All rotor phases should then be connected together by permanently turning on all top switches or all bottom switches and the system operated as a fixed-speed wind turbine.

In commercial wind turbines short-circuit switch faults will cause the protection system to shut down the wind turbine to avoid further damage.

6.4 Simulation Results
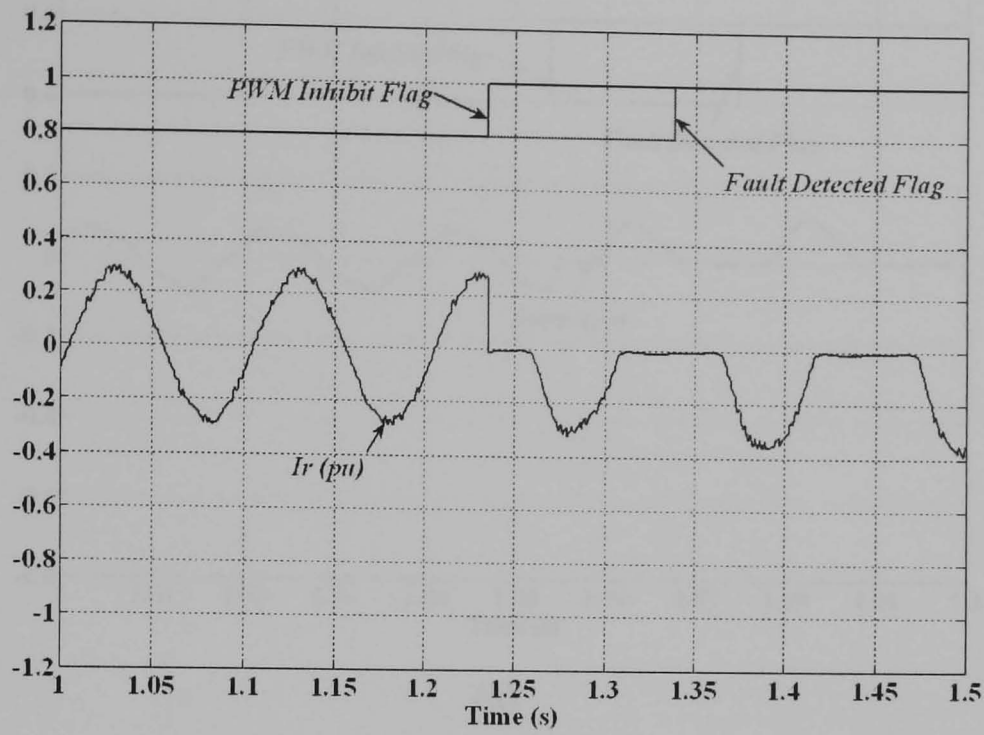
(a)
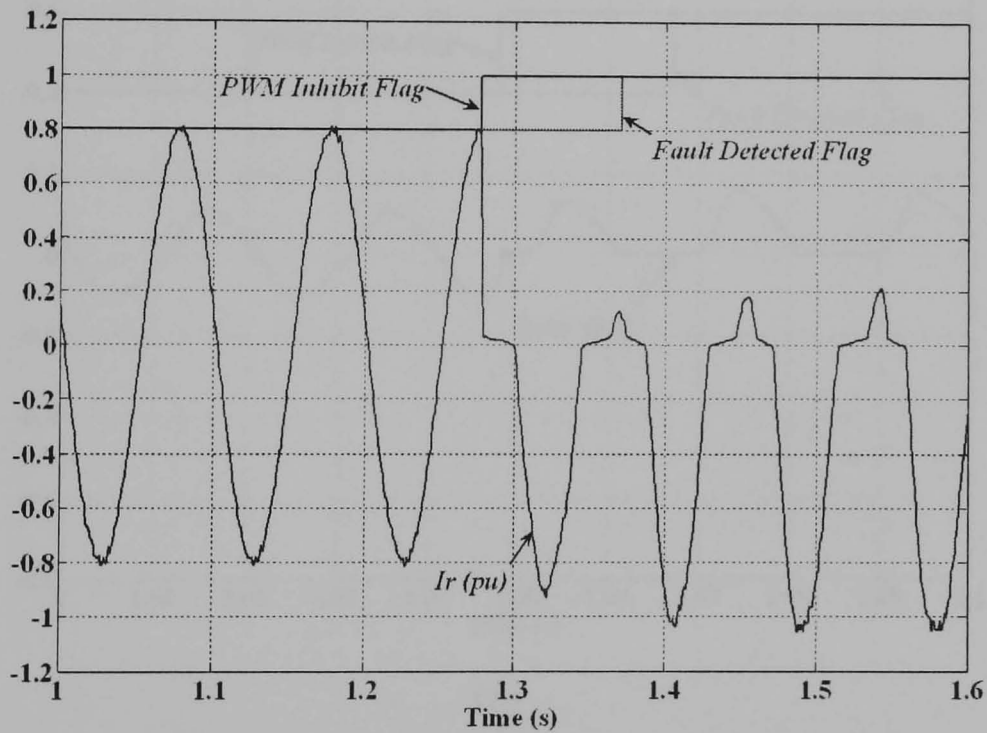
(b)

Figure 6.21 Simulation results for the Sampling Point Comparison Method to detect an open-switch fault in the machine-side converter for (a) sub-synchronous speed generation and (b) super-synchronous speed generation
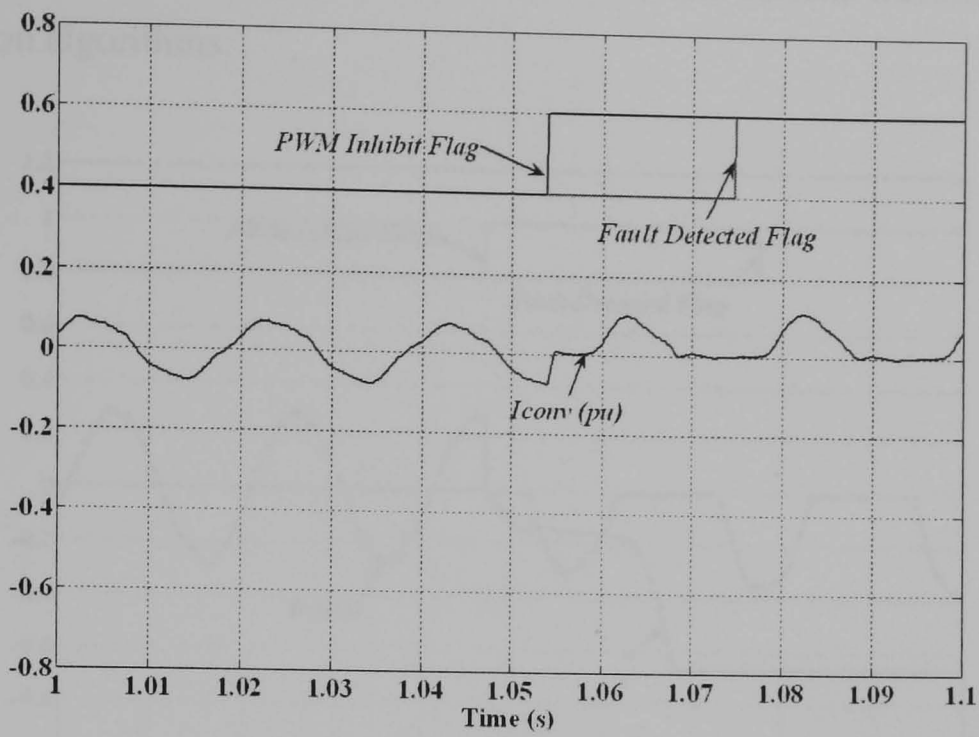
(a)
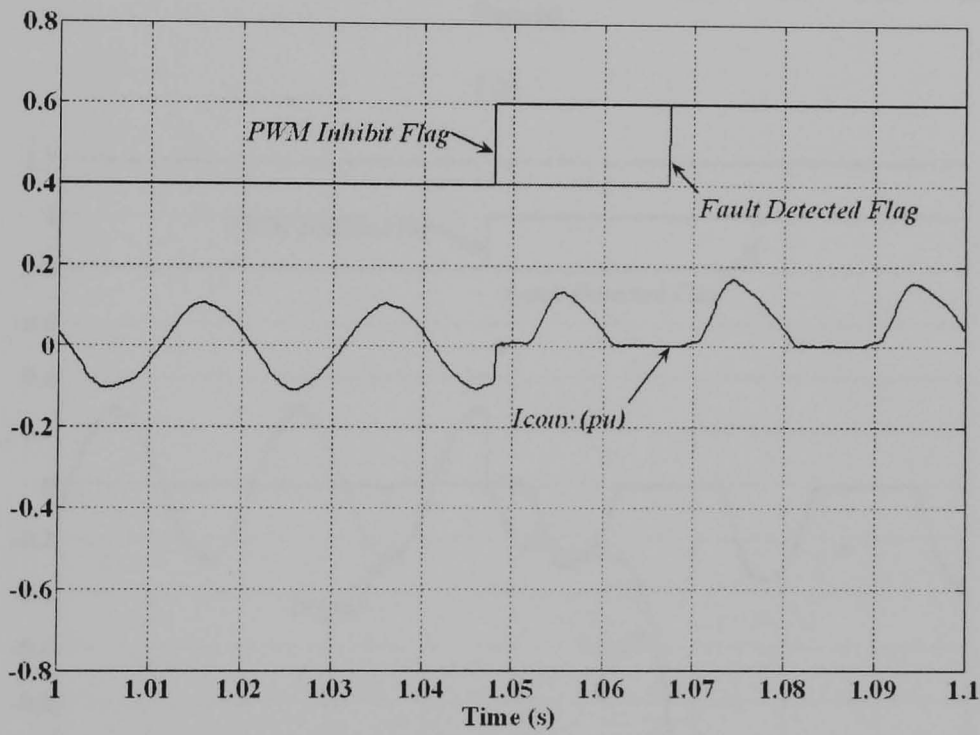
(b)

Figure 6.22 Simulation results for the Sampling Point Comparison Method to detect
an open-switch fault in the grid-side converter for (a) sub-synchronous speed
generation and (b) super-synchronous speed generation

The simulation results in figures 6.21 and 6.22 show that the time required to detect
the fault in each case is approximately 1 cycle. From these figures, the fault appears
approximately in the middle of the cycle conducted by the faulty switch. Creating the
fault at this point is to investigate the maximum time required for each fault detection

algorithm. The fault is applied at the same point on the current waveform for other fault detection algorithms.
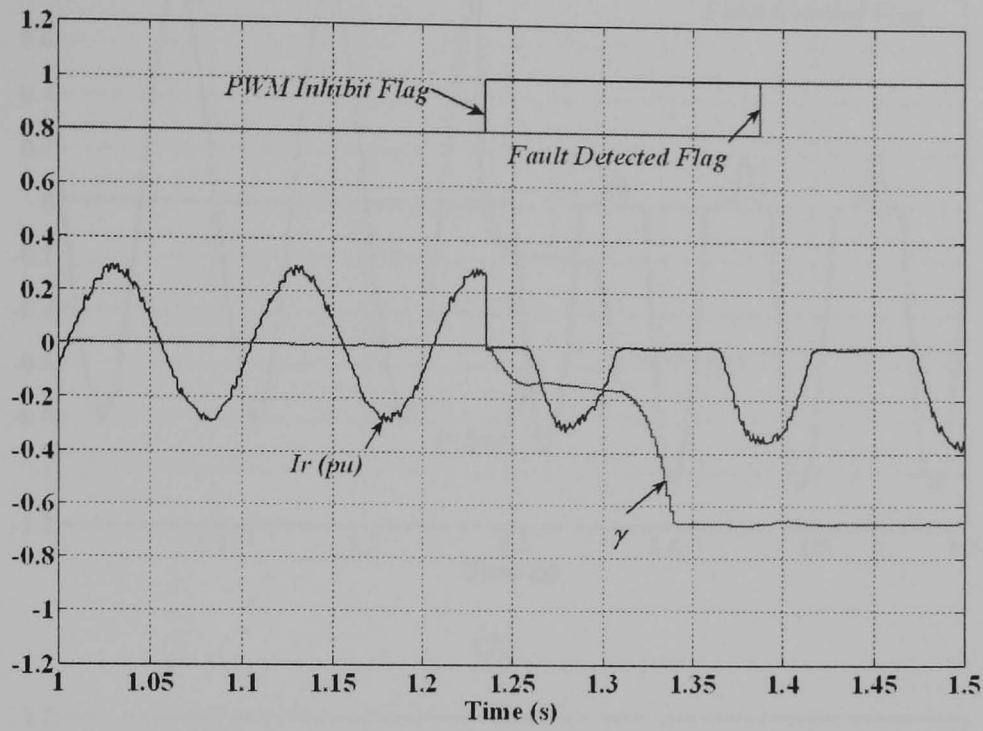
(a)
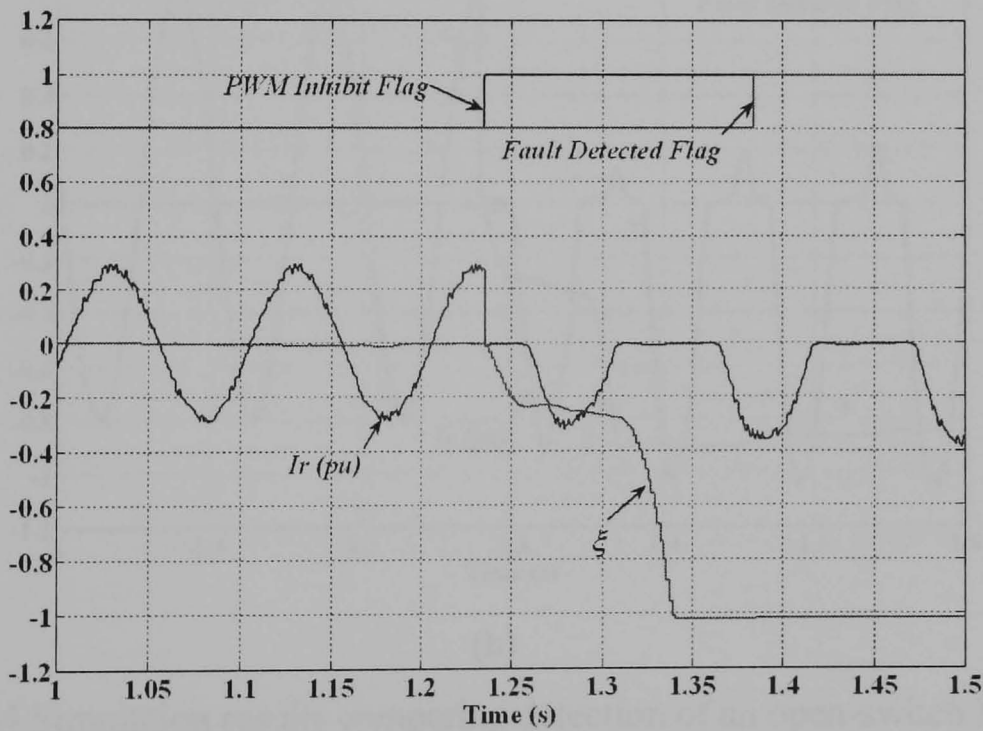
(b)

Figure 6.23 Simulation results comparing detection of an open-switch fault in the machine-side converter for sub-synchronous speed generation (a) the Modified Normalised DC Current Method and (b) the Absolute Normalised DC Current Method
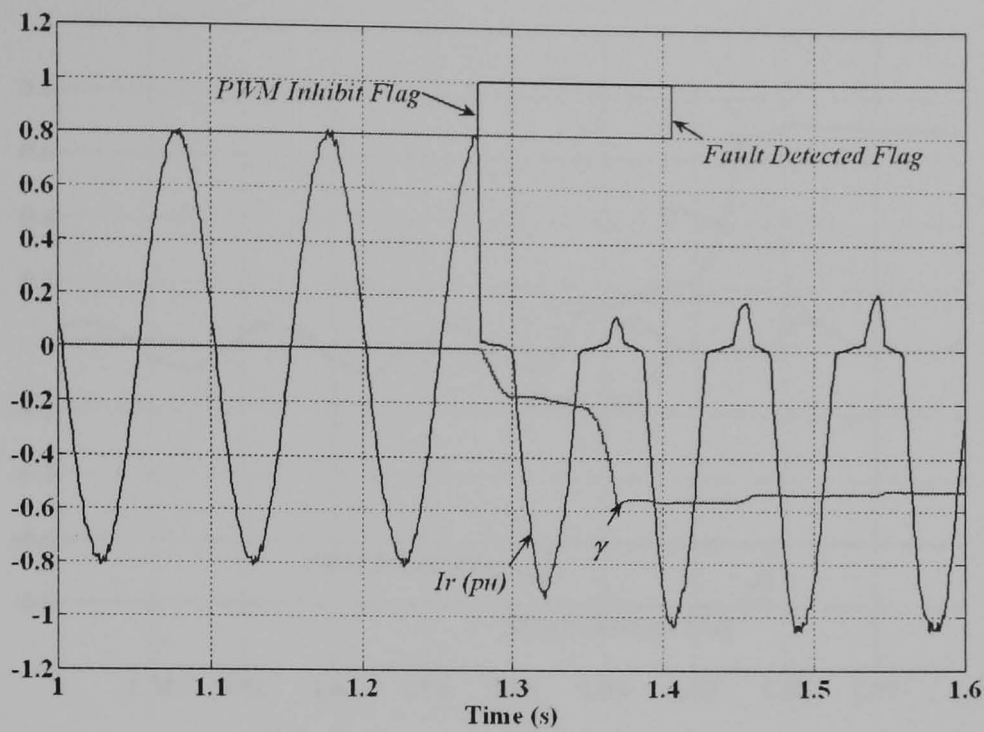
(a)
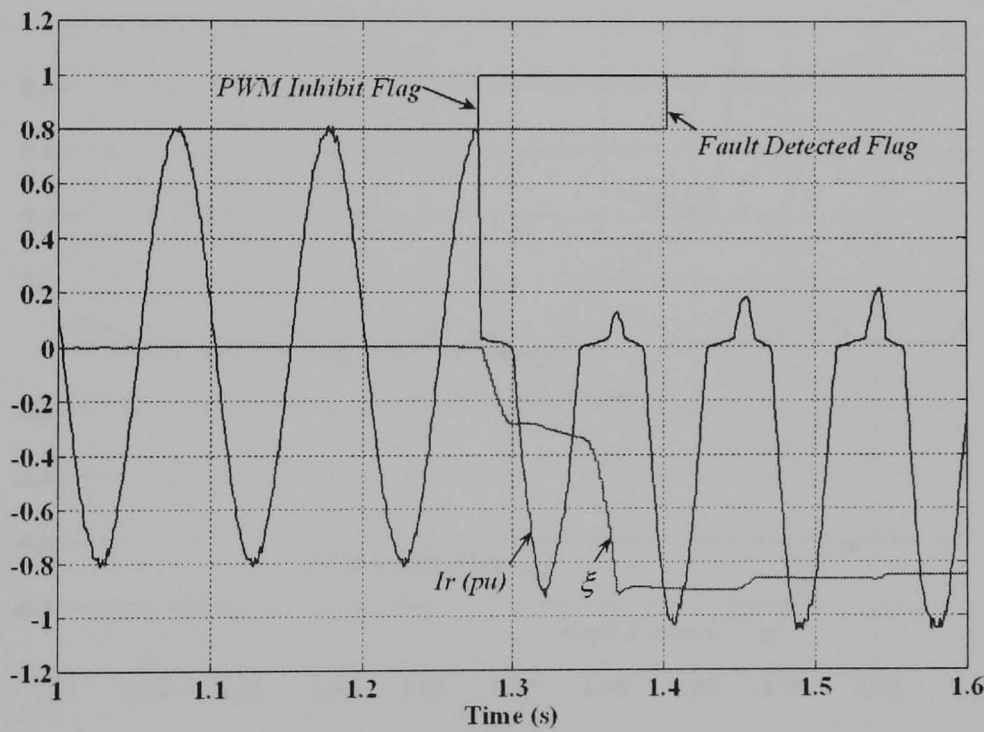
(b)

Figure 6.24 Simulation results comparing detection of an open-switch fault in the machine-side converter for super-synchronous speed generation (a) the Modified Normalised DC Current Method and (b) the Absolute Normalised DC Current Method
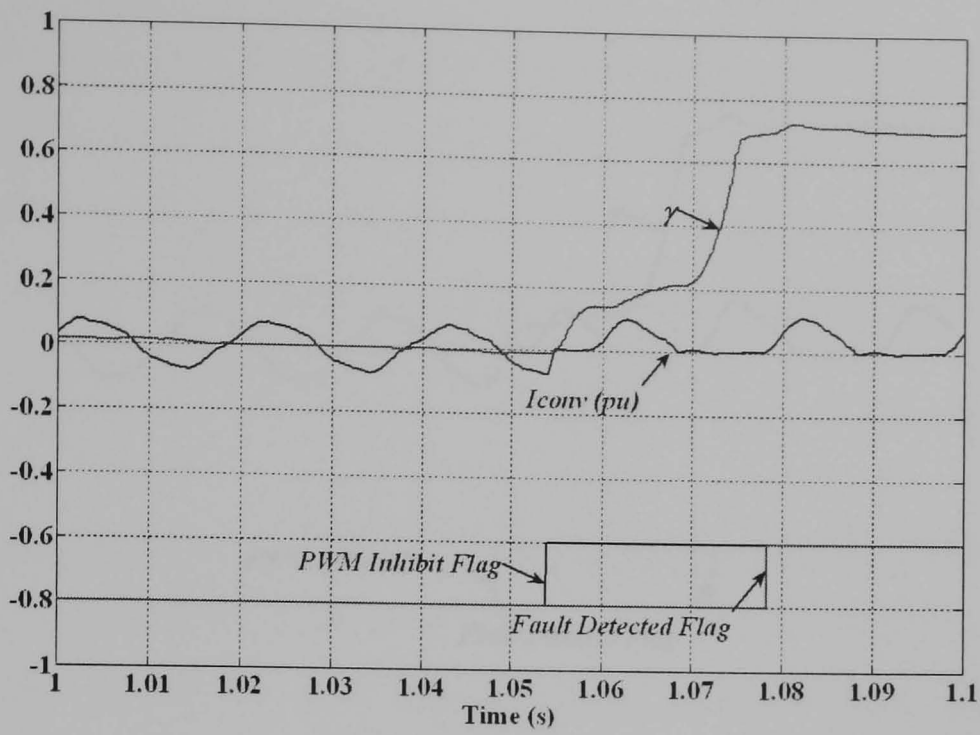
(a)
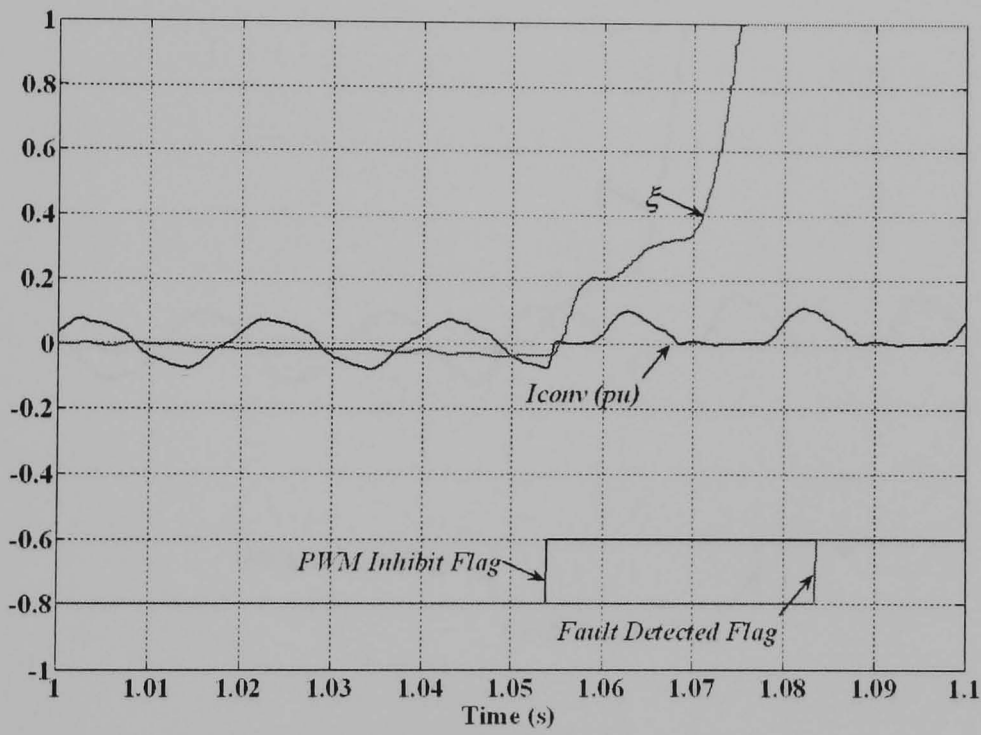
(b)

Figure 6.25 Simulation results comparing detection of an open-switch fault in the grid-side converter for sub-synchronous speed generation (a) the Modified Normalised DC Current Method and (b) the Absolute Normalised DC Current Method
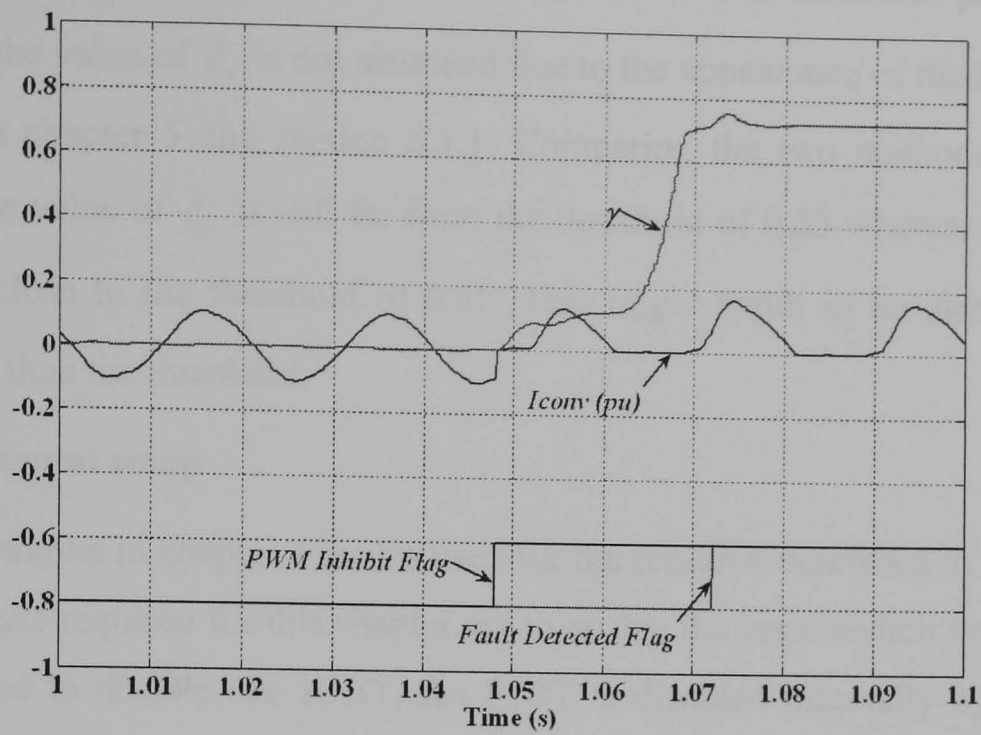
(a)
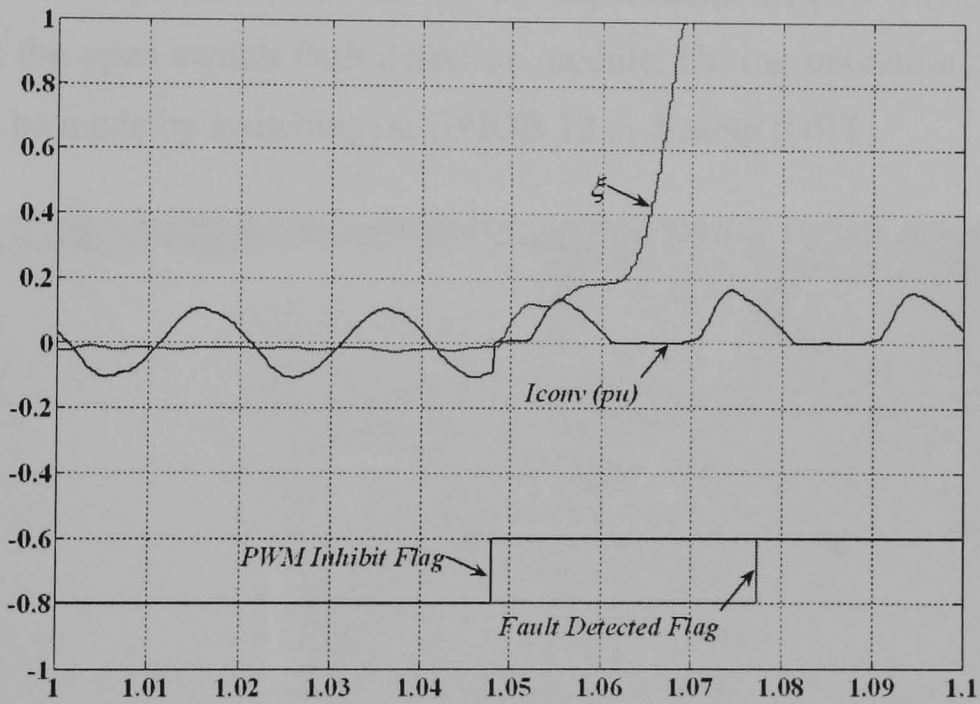
(b)

Figure 6.26 Simulation results comparing detection of an open-switch fault in the grid-side converter for super-synchronous speed generation (a) the Modified Normalised DC Current Method and (b) the Absolute Normalised DC Current Method

The simulation results in figures 6.23 to 6.26 show that the time required to detect a fault in each case is similar for the Absolute Normalised DC Current Method and the Modified Normalised DC Current Method. With the exception of the results in figure

6.24, during the fault, the value of ξ_v saturates to ± 1, as discussed previously. In figure 6.24 the value of ξ_v is not saturated due to the appearance of diode current, as discussed in chapter 5 and section 6.1.1. Comparing the two methods, under this condition the value of ξ_v is still far from the threshold of 0.65 whereas the value of γ_v is very close to the threshold of 0.45. This might result in no alarm if the γ_v became less than the threshold.

6.5 Experimental setup

The test rig shown in chapter 4 is also used for the research described in this chapter. The extra tasks required for this chapter are to enable the open-switch fault detection algorithm and to disable one IGBT. An IGBT is disabled internally by setting the PWM signal in the software to zero. This is done by a switch on GPIOB 12 as shown in figure 6.27. To operate the system for the experiment, GPIOB 8 is first switched on to enable the open switch fault detection module. During operation of the DFIG, the fault can be made by switching on GPIOB 12 to disable IGBT.
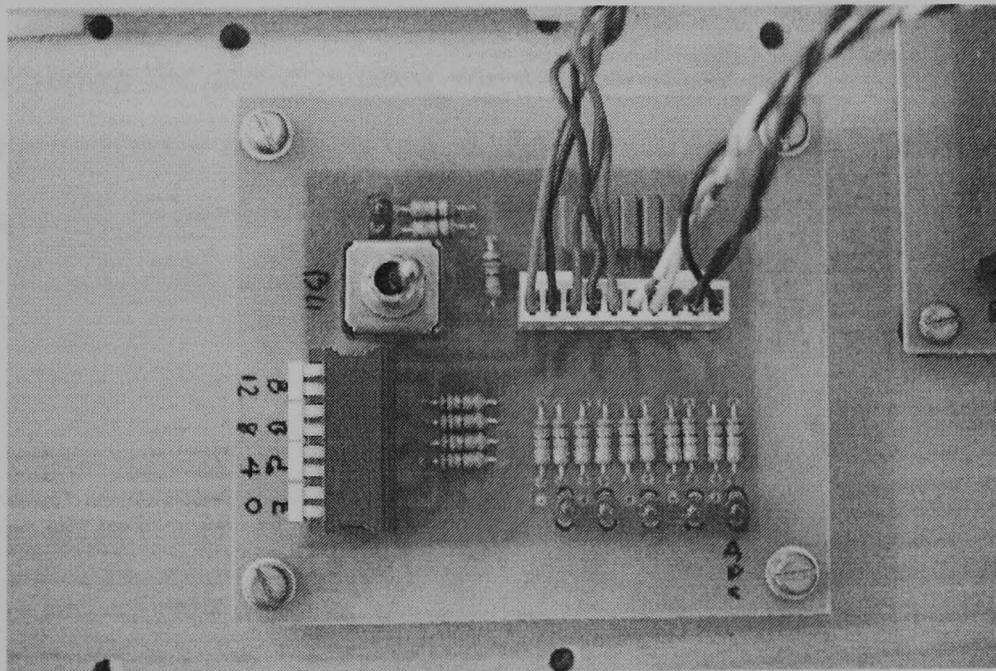
Figure 6.27 Hardware setup to generate an open-switch fault (GPIOB 12) and to enable fault detection module (GPIOB 8)

6.6 Experimental Results
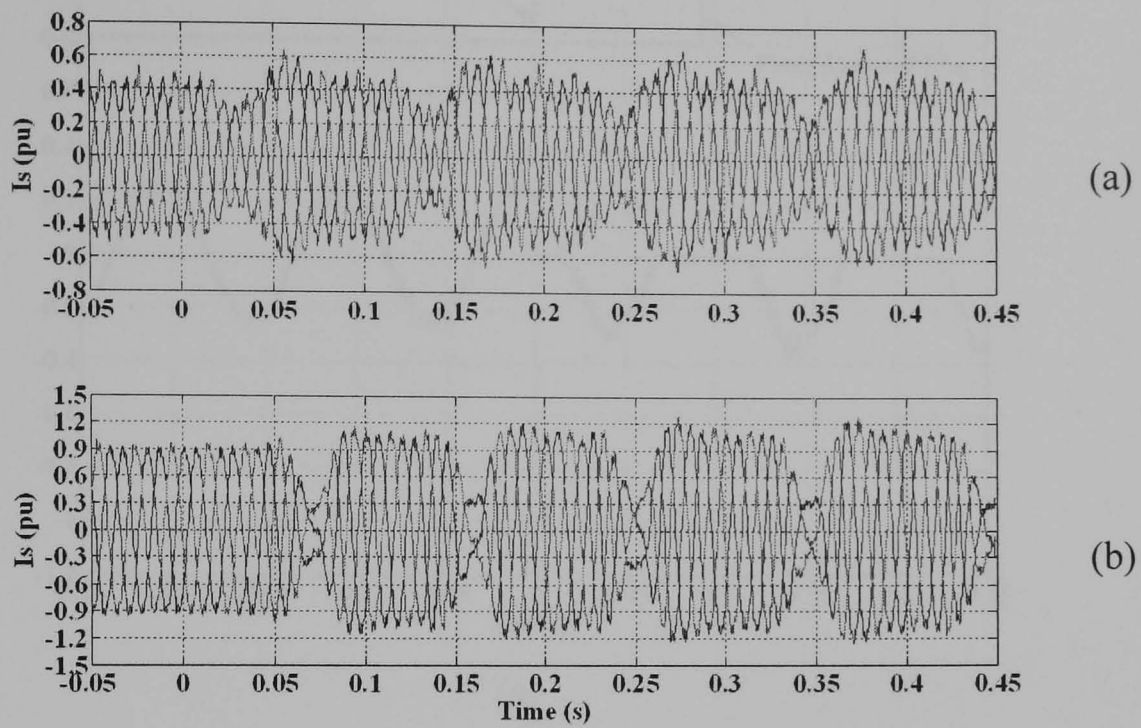
Figure 6.28 Experimental results showing the effects of an open-switch fault in the machine-side converter on stator currents at (a) sub-synchronous speed generation and (b) super-synchronous speed generation

Figure 6.28 shows the stator current waveforms under an open-switch fault in the machine-side converter at 1.2 pu speed. As shown, the stator currents are strongly oscillating at rotor frequency (10Hz) as shown in simulation results in figure 6.6.
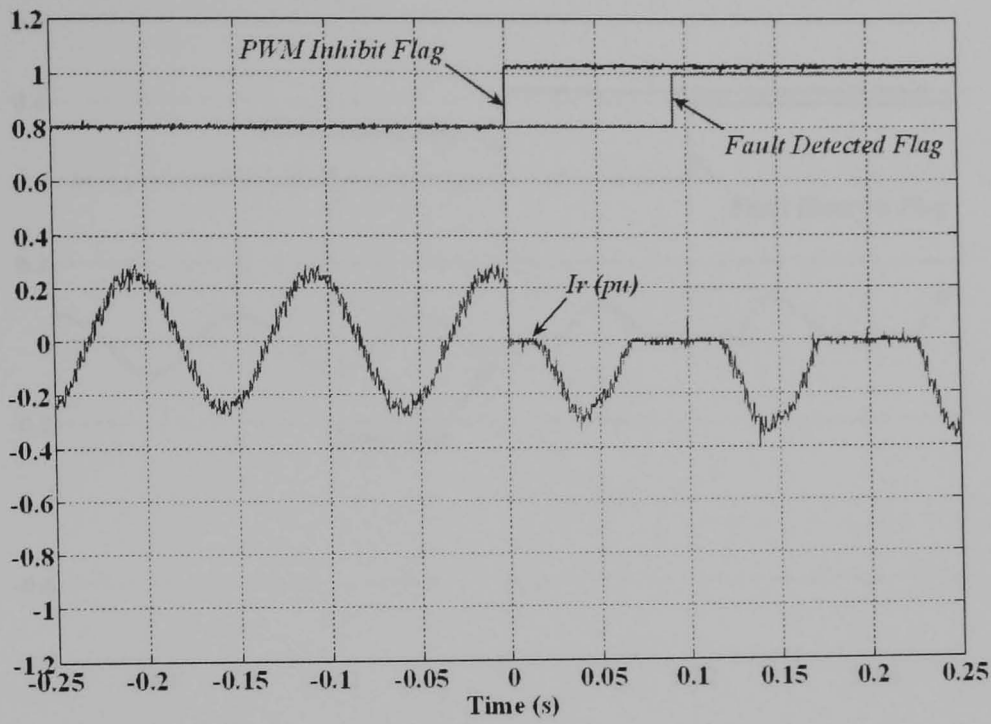
(a)
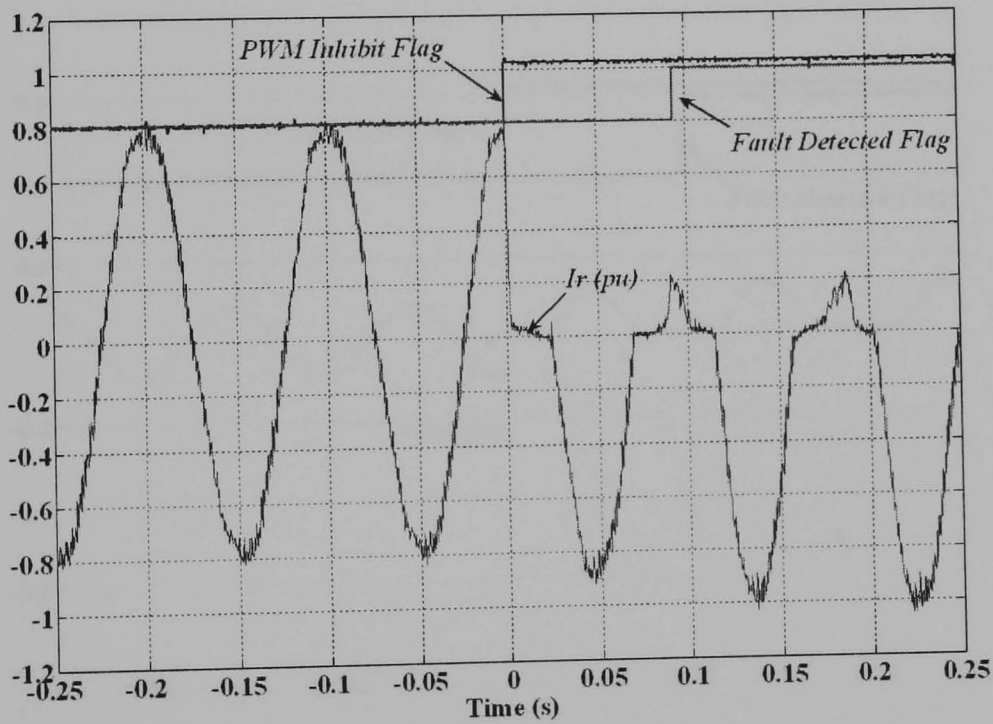
(b)

Figure 6.29 Experimental results for the Sampling Point Comparison Method to detect an open-switch fault in the machine-side converter for (a) sub-synchronous speed generation and (b) sub-synchronous speed generation
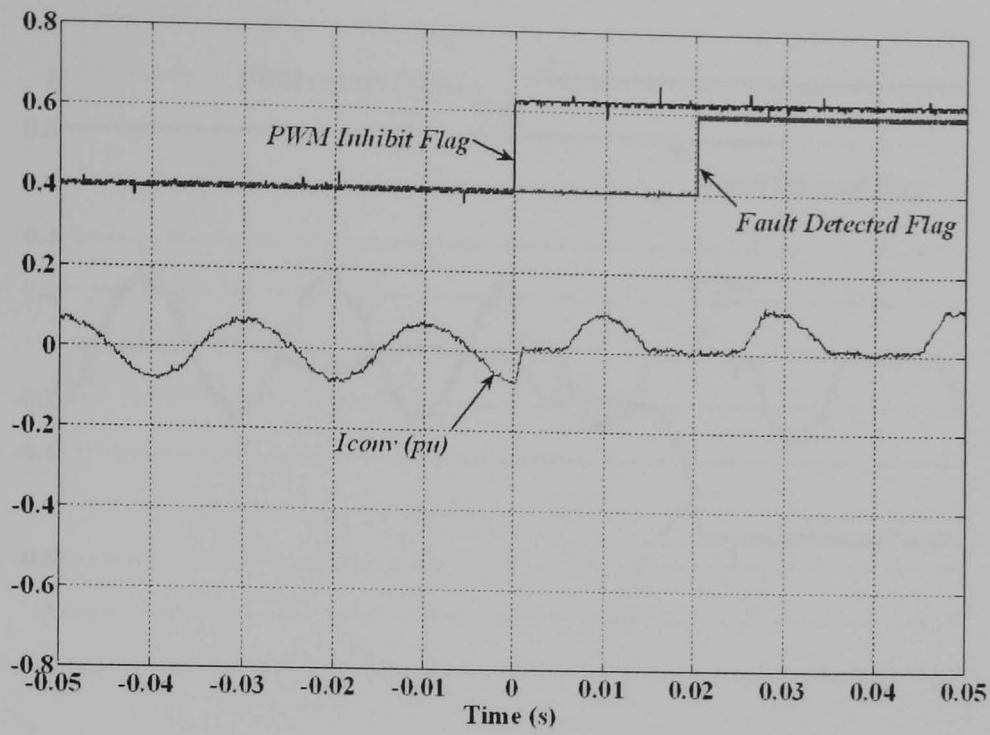
(a)
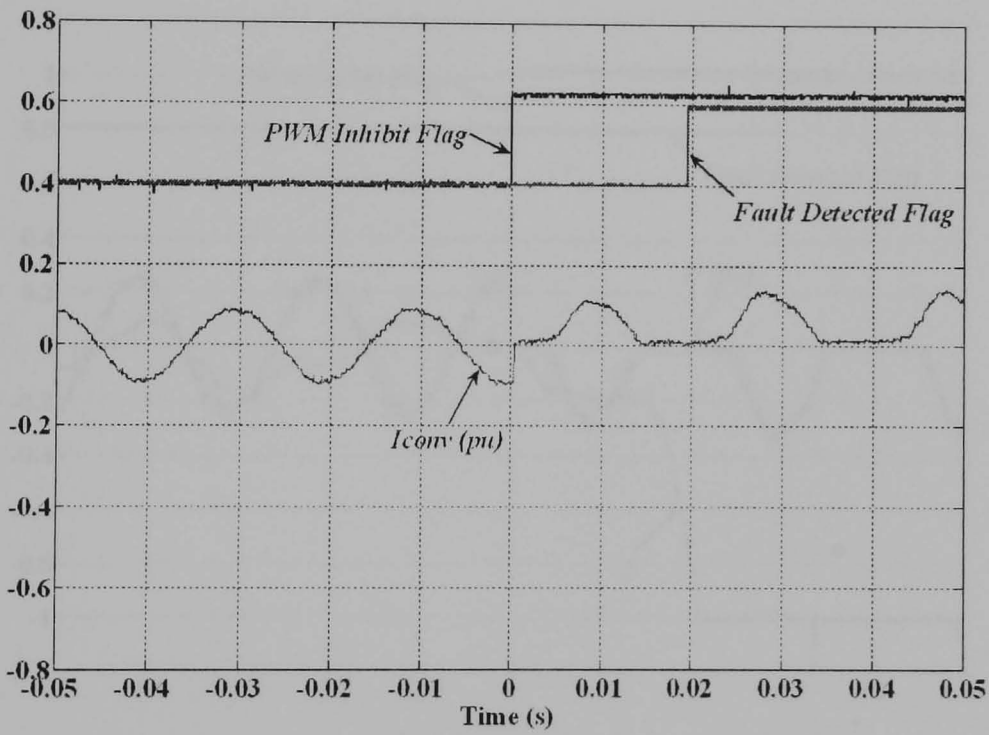
(b)

Figure 6.30 Experimental results for the Sampling Point Comparison Method to detect an open-switch fault in the grid-side converter for (a) sub-synchronous speed generation and (b) super-synchronous speed generation

Figures 6.29 and 6.30 show the results of open-switch fault detection using the Sampling Point Comparison Method. This method requires approximately one cycle to alarm after the fault occurs.
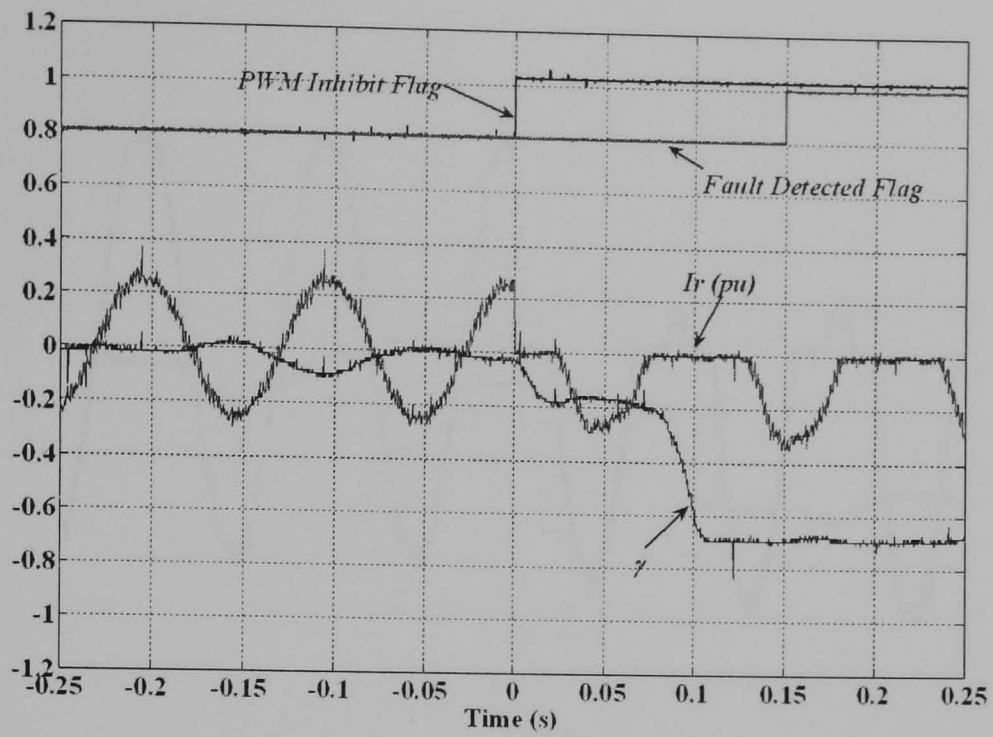
(a)
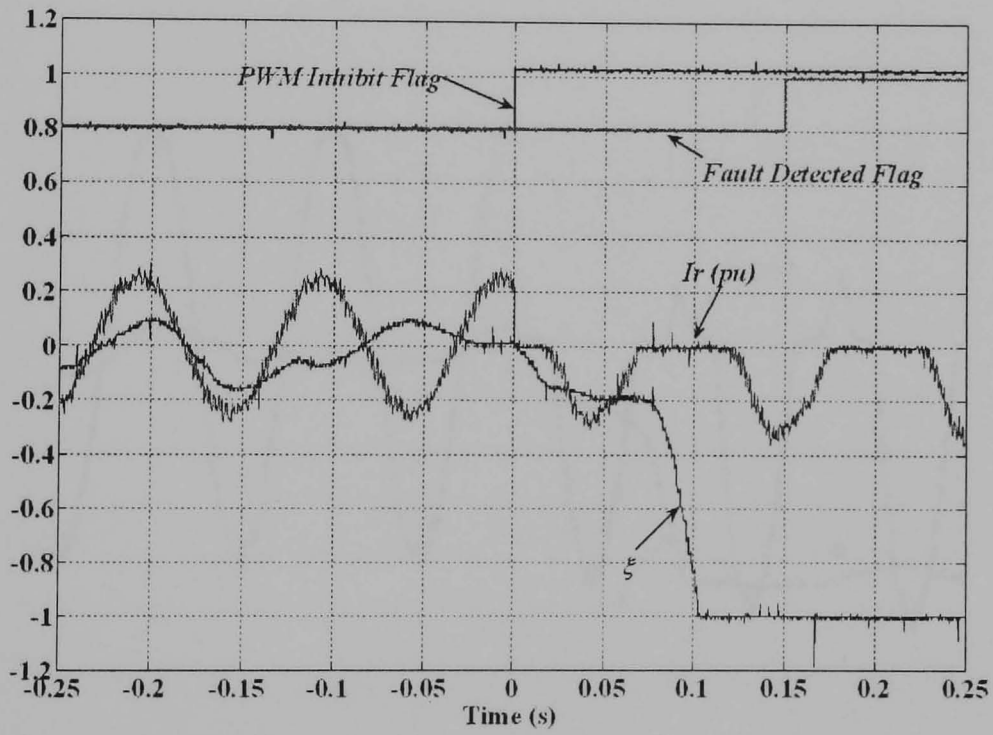
(b)

Figure 6.31 Experimental results comparing detection of an open-switch fault in the machine-side converter for sub-synchronous speed generation (a) the Modified Normalised DC Current Method and (b) the Absolute Normalised DC Current Method
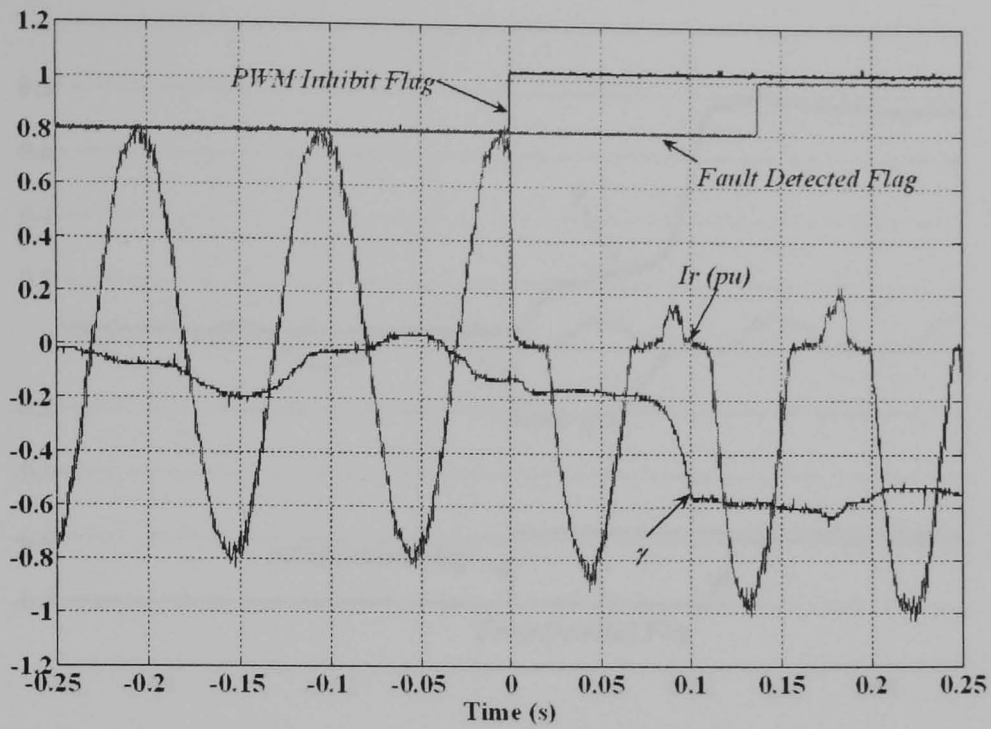
(a)
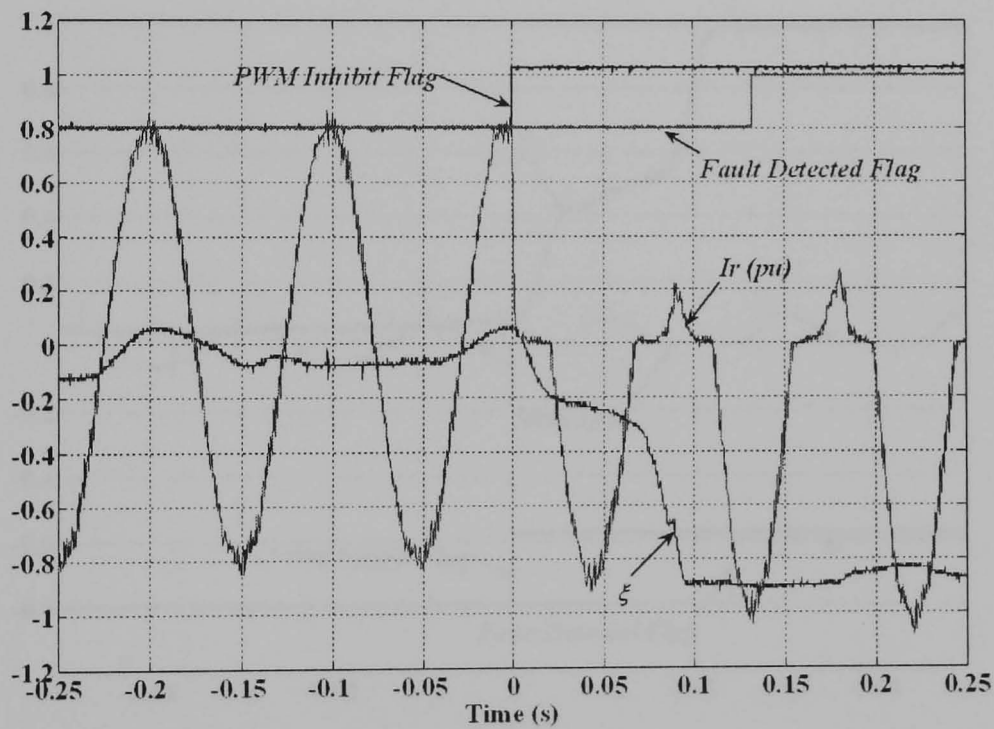
(b)

Figure 6.32 Experimental results comparing detection of an open-switch fault in the machine-side converter for super-synchronous speed generation (a) the Modified Normalised DC Current Method and (b) the Absolute Normalised DC Current Method
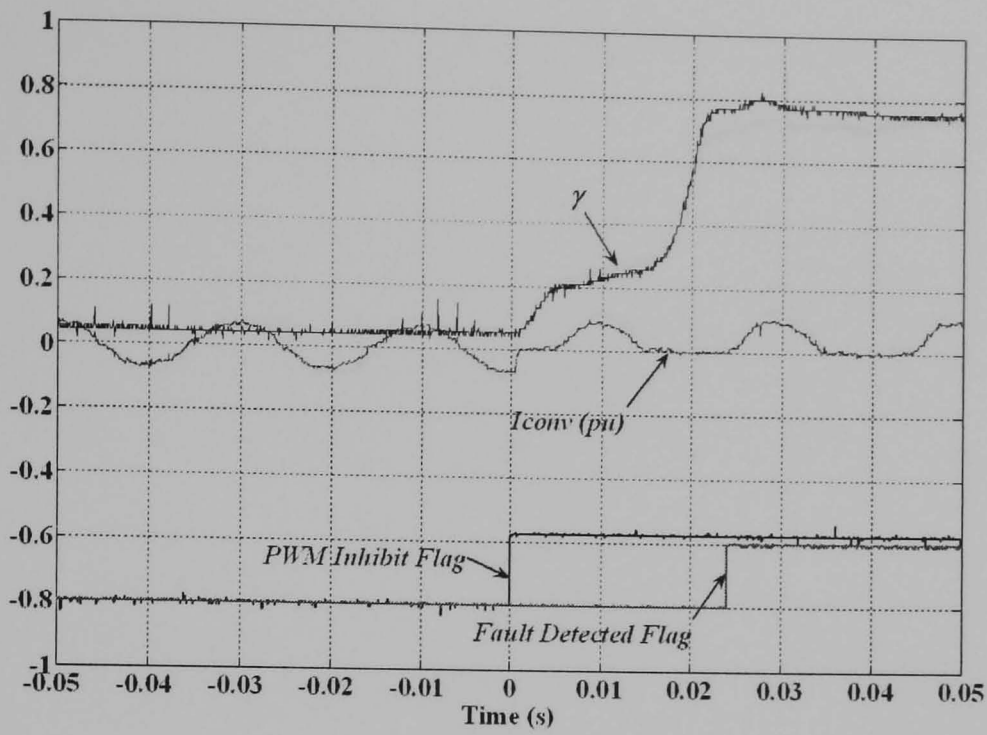
(a)
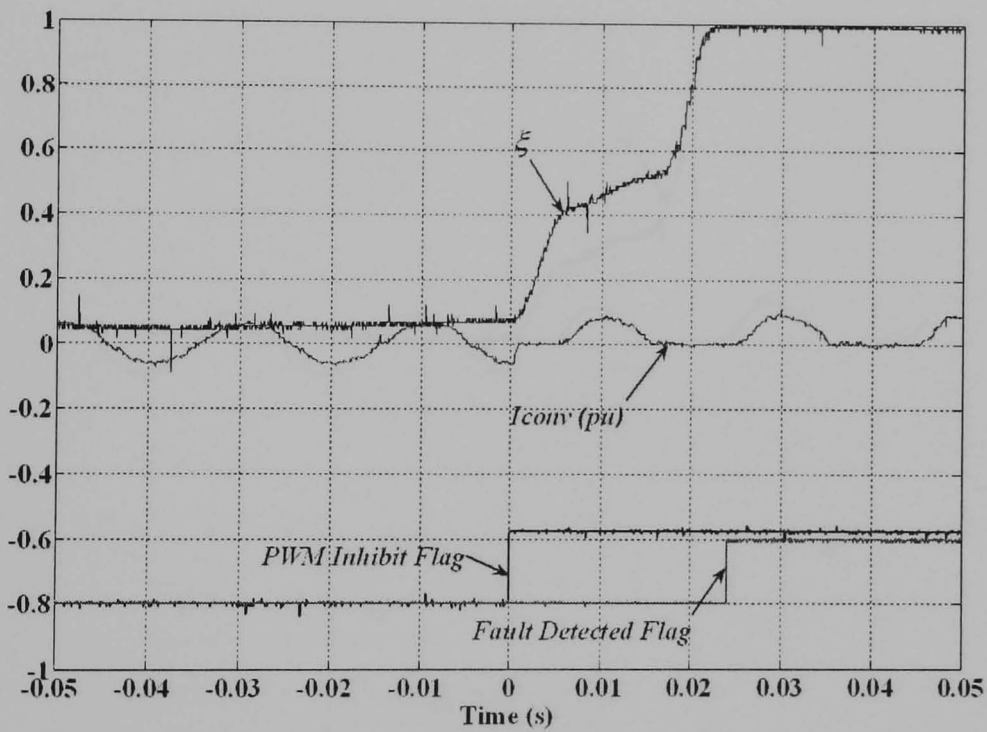
(b)

Figure 6.33 Experimental results comparing detection of an open-switch fault in the grid-side converter for sub-synchronous speed generation (a) the Modified Normalised DC Current Method and (b) the Absolute Normalised DC Current Method
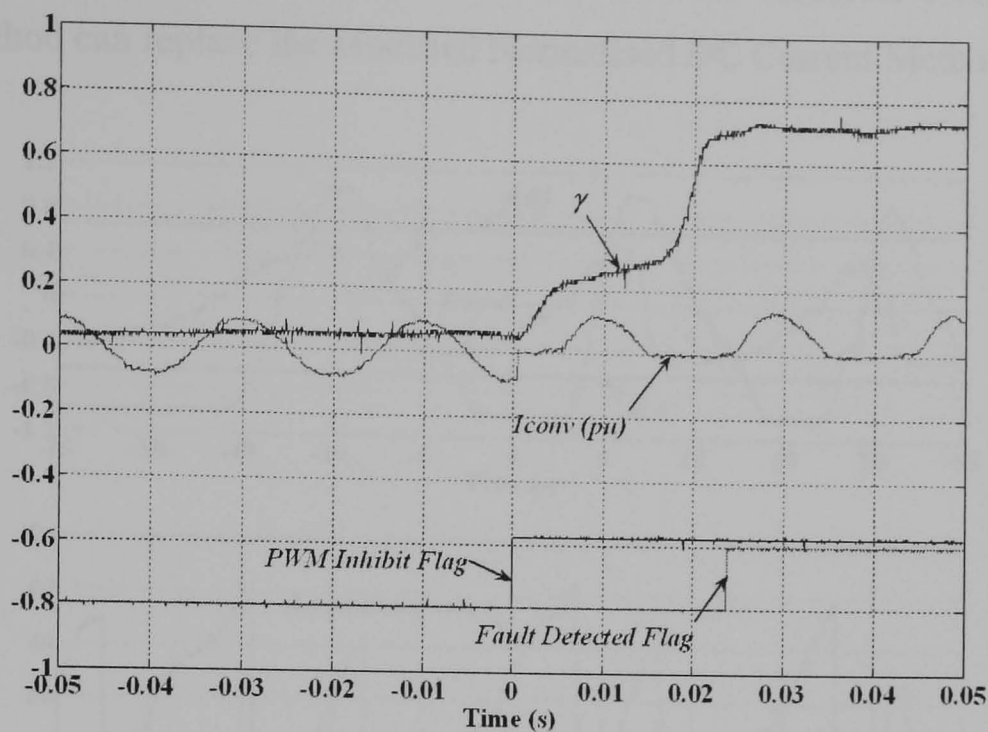
(a)
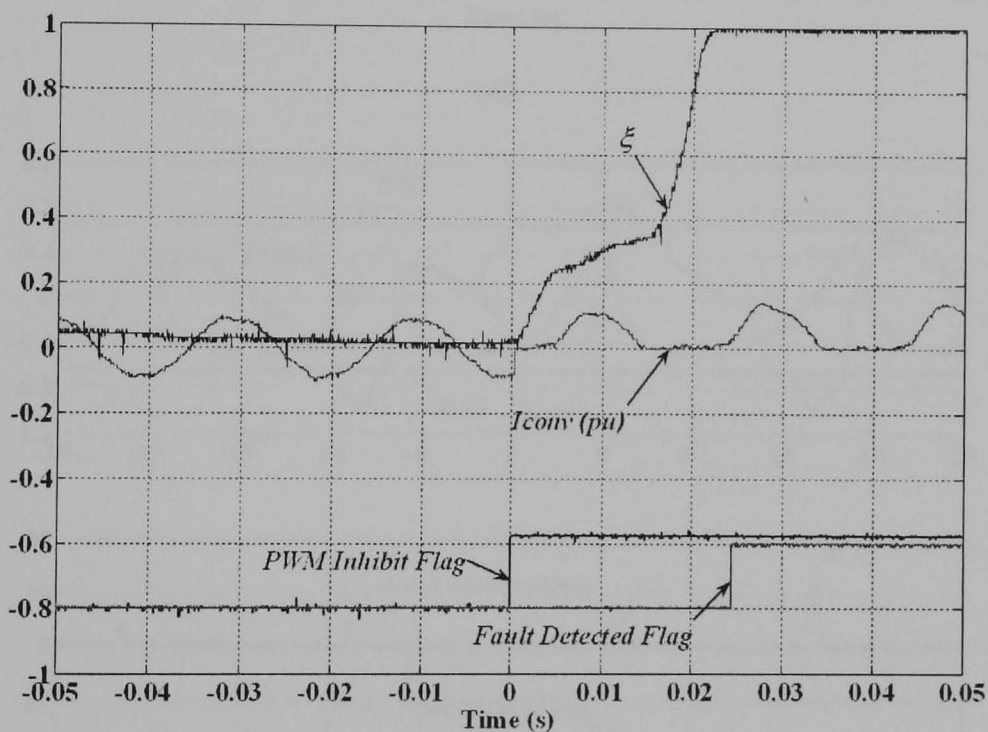
(b)

Figure 6.34 Experimental results comparing detection of an open-switch fault in the grid-side converter for super-synchronous speed generation (a) the Modified Normalised DC Current Method and (b) the Absolute Normalised DC Current Method

The results shown in figures 6.31 to 6.34 compare fault detection using the Modified Normalised DC Current Method and the Absolute Normalised DC Current Method. As shown in these figures, for the same point at which the fault appeared the

detection times are very similar which means that the Absolute Normalised DC Current Method can replace the Modified Normalised DC Current Method.

(a)

(b)
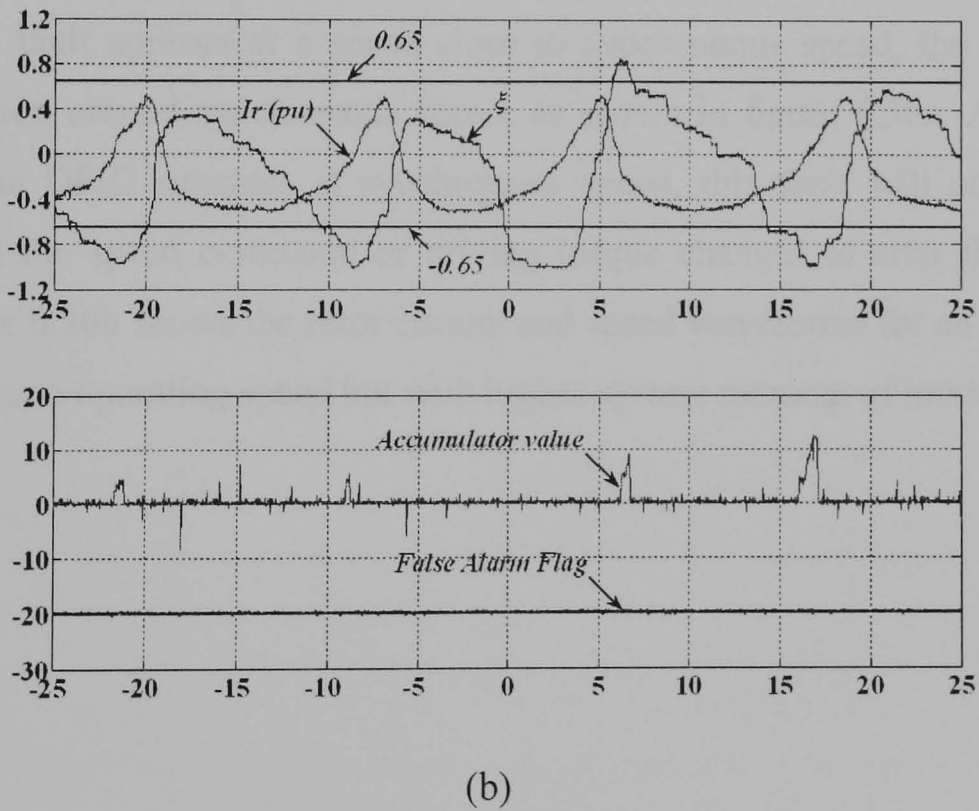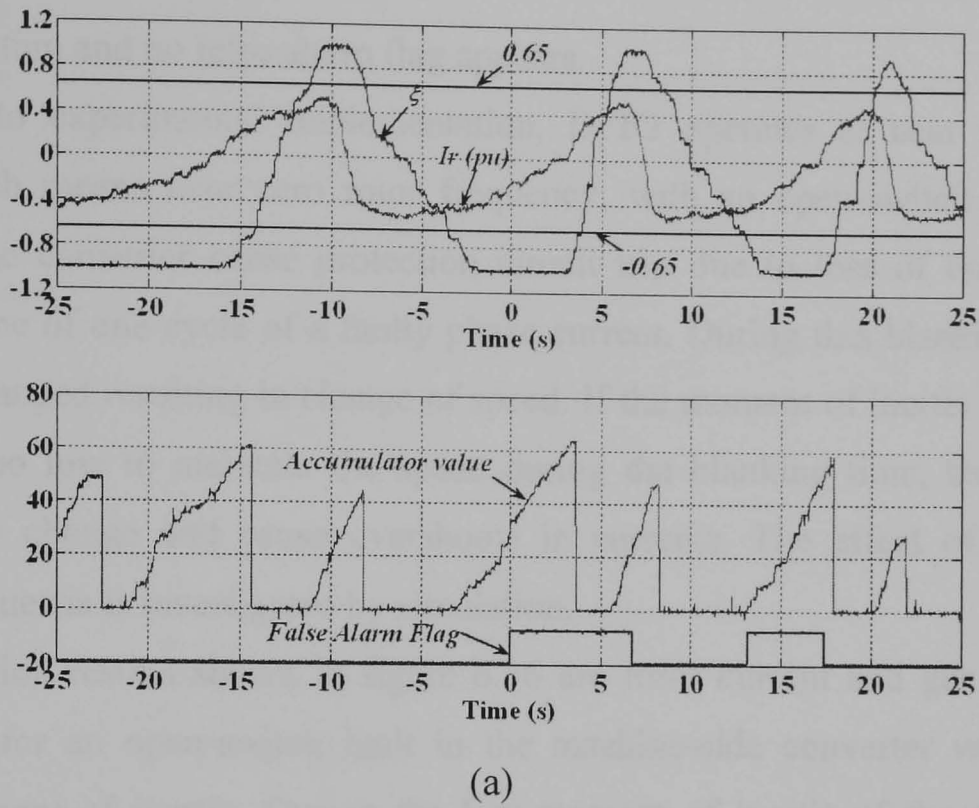
Figure 6.35 Experimental results showing the rotor currents and other necessary variables around synchronous speed (a) without false alarm suppression and (b) with false alarm suppression

In figure 6.35a, the system is operating without the false alarm suppression algorithm. The value of the accumulator when ξ_v exceeds the threshold is high and it

exceeds the limit set in the software (32 counts), causing false alarms to appear. Conversely, in figure 6.35b, the false alarm suppression algorithm has been added into the software. Although ξ_v exceeds the limit, the accumulator is still low because of the algorithm and no false alarm flag appears.

According to experimental implementation, DFIG operates at near synchronous speed, which means near zero rotor frequency, with an open-switch fault in the machine-side converter cause protection circuit trip due to loss of control during blanking time of one cycle of a faulty phase current. During this blanking time, the torque is changed resulting in change of speed. If the moment of inertia of the DFIG system is too low to maintain the speed during the blanking time, the speed will dramatically change and cause overshoots in currents. The effect of the size of moment of inertia is investigated by simulation.

The simulation results shown in figure 6.36 are rotor current and generator speed waveforms for an open-switch fault in the machine-side converter with different system moment of inertia. Due to the low moment of inertia of the experimental system, if a fault appears at a speed close to synchronous speed, the fault causes speed variation around synchronous speed, as shown in figure 6.36a. As discussed earlier, if the DFIG operates at synchronous speed, this fault will not affect the system until the speed command or driving torque changes to alter the operating speed. Figure 6.36b shows the rotor current and speed waveforms for an open-switch fault at the same operating speed but with higher system moment of inertia.

(a)

(b)
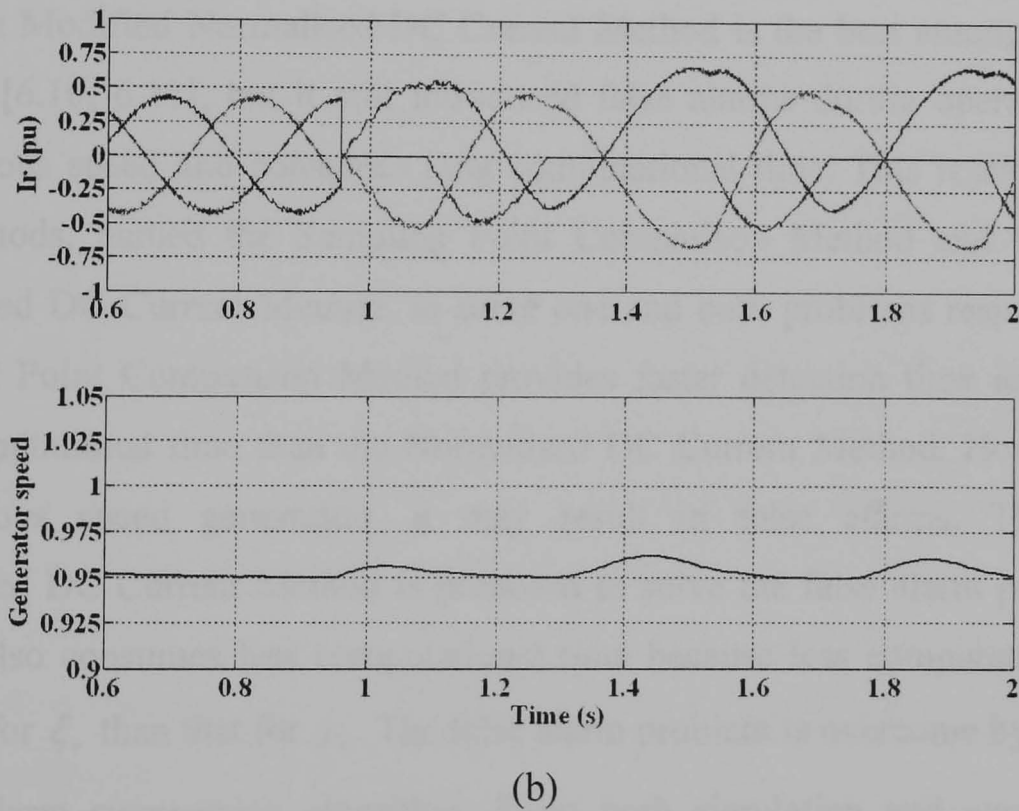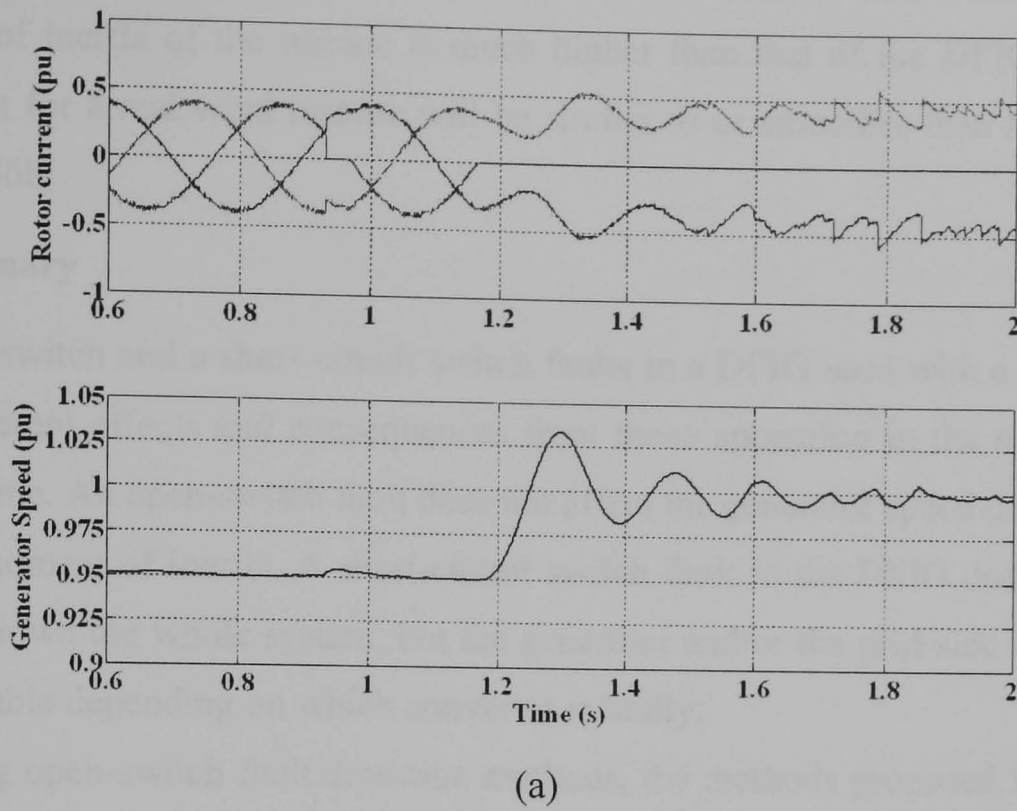
Figure 6.36 Simulation results showing rotor currents and generator speed under an open-switch fault in the machine-side converter at 0.95pu speed with different moment of inertia (a) normal moment of inertia (0.075 kg-m^2) and (b) 1 kg-m^2 moment of inertia

As shown in figure 6.36b, due to high moment of inertia the generator speed does not vary too much, so the rotor current waveforms are in the same form as for a normal

open switch in a voltage source converter. In the case of real wind turbine, the moment of inertia of the turbine is much higher than that of the DFIG. The speed waveform for a real wind turbine will be similar to or smoother than that shown in figure 6.36b.

6.7 Summary

An open-switch and a short-circuit switch faults in a DFIG used with a wind turbine have different effects and consequences from those appearing in the normal stator-fed machine. An open-switch fault does not affect the generator speed due to the high turbine moment of inertia. A short-circuit switch fault in the DFIG does not end up shutting down the whole system, but the generator and/or the grid-side converter are still operable depending on which converter is faulty.

Regarding open-switch fault detection methods, the methods proposed for stator-fed induction machines introduced false alarms and/or consumed long computational time. The Modified Normalised DC Current Method is the best among the existing methods [6.10, 6.11], but it still introduced false alarms during operating through synchronous speed and consumes long computational time. This research proposes two methods, named the Sampling Point Comparison Method and the Absolute Normalised DC Current Method, to solve one and both problems respectively. The Sampling Point Comparison Method provides faster detection time and consumes less computational time than the Normalised DC Current Method. However, under synchronous speed generation, it may result in false alarms. The Absolute Normalised DC Current Method is proposed to solve the false alarm problem. This method also consumes less computational time because less computational time is required for ξ_v than that for γ_v. The false alarm problem is overcome by introducing a false alarm suppression algorithm. From both simulation and experiment, the detection time for the Absolute Normalised DC Current Method and the Modified Normalised DC Current Method is almost identical. Therefore, the Absolute Normalised DC Current Method is the preferred choice for a DFIG used with a wind turbine.

Reference

6.1. A. Petersson, 'Analysis, Modeling and Control of Doubly-Fed Induction Generators for Wind Turbines'. Ph.D. Thesis, Chalmers University of Technology, 2005.

6.2. P. C. Krause, 'Analysis of Electric Machinery, International Editions'. McGraw-Hill Book Company, 1987

6.3. R. Peuget, S. Courtine, and J.P. Rognon, 'Two Knowledge-Based Approaches to Fault Detection and Isolation on a PWM Inverter'. Proceedings of the 1997 IEEE International Conference on Control Applications, pp. 565-570.

6.4. Raphael Peuget, St'ephane Courtine, and Jean-Pierre Rognon, 'Fault Detection and Isolation on a PWM Inverter by Knowledge-Based Model'. IEEE Trans. on Industry Applications, vol. 34, no. 6, Nov./Dec. 1998, pp. 1318-1326.

6.5. A. M. S. Mendes and A. J. Marques Cardoso, 'Voltage Source Inverter Fault Diagnosis in Variable Speed AC Drives, by the Average Current Park's Vector Approach'. Proceedings of International Conference Machine and Drives, 1999, pp. 704-706.

6.6. A. M. S. Mendes and A. J. Marques Cardoso, 'Fault Diagnosis in a Rectifier-Inverter System Used in Variable Speed AC Drive, by the Average Park's Vector Approach'. Proceedings of the 1999 EPE 8th European Conference on Power Electronics and Applications, pp. P.1-P.9.

6.7. C. Kral and K. Kafka, 'Power Electronics Monitoring for a Controlled Voltage Source Inverter'. Proceedings of IEEE Power Electronics Specialists Conference, 2000, Vol.1, pp. 213-217.

6.8. S. Abramik *et al.*, 'A Diagnostic Method for On-line Fault Detection and Localization in VSI-Fed AC Drive'. Proceedings of the 2003 EPE 10th European Conference on Power Electronics and Applications, pp. P.1-P.8.

6.9. F. W. Fuchs, 'Some Diagnosis Methods for Voltage Source Inverters in Variable Speed Drives with Induction Machines a Survey'. Proceedings of the 29th Annual Conference of the IEEE Industrial Electronics Society, 2003 Vol. 2, November 2003, pp. 1378-1385.

6.10. K. Rothenhagen and F. W. Fuchs, 'Performance of Diagnosis Methods for IGBT Open Circuit Faults in Voltage Source Active Rectifiers'. Proceedings of the 35th Power Electronics Specialists Conference, 2004, pp. 4348-4354.

6.11. K. Rothenhagen and F. W. Fuchs, 'Performance of Diagnosis Methods for IGBT Open Circuit Faults in Three Phase Voltage Source Inverters for AC Variable Speed Drives'. Proceedings of the 2005 EPE 12th European Conference on Power Electronics and Applications, pp. P.1-P.7.

6.12. W. Sae-Kok and D. M. Grant, 'Open Switch Fault Diagnosis for a Doubly-Fed Induction Generator'. Proceeding of the 7th International Conference on Power Electronics and Drive System, 2007, pp. 131-138.

Chapter Seven

System Reconfiguration

The aim of this chapter is to consider post-fault operation for a doubly-fed induction generator (DFIG) used with a wind turbine. Some possible fault isolation strategies are first reviewed and followed by the reconfiguration operation. Component-minimised topologies are discussed and applied to post-fault operation for the DFIG. The strategies to reconfigure and operate the DFIG for a machine-side converter fault or a grid-side converter fault are proposed and discussed. Simulation results show the behaviour with these strategies applied and further validation of the strategies are then demonstrated by experimental results. Moreover, another possible topology for post-fault operation is also proposed and the simulation and experimental results are presented. Finally, the advantages and drawbacks of such strategies are discussed.

7.1 Review of Post-Fault Operation Methods

The benefit of having fault diagnosis is that it can be used to apply fault-tolerant control to the system for post-fault operation. Once a fault is detected and identified, the immediate action is to isolate the fault and then operate the system under fault-tolerant control, either by a change of control mode or a change of hardware configuration. For fault isolation, several strategies have been proposed. For an open-switch fault, the isolation method is simply to turn off the complementary switch in the same leg of the converter. However, for a short-circuit switch fault, complete isolation of the faulty leg is necessary although the controller can immediately turn the complementary switch off. This is because the faulty switch still permanently connects to either the positive or negative dc bus via the short-circuit switch. A fuse becomes the essential component to isolate the faulty leg from the system. Several strategies have been proposed and explained. As shown in figure 7.1, two possible isolation topologies for a PWM converter leg are proposed. The first topology, shown in figure 7.1a, was proposed by Bolognani *et al.* [7.1]. Once the short-circuit switch fault is detected, the controller will send the command signal to trigger the thyristors in the top and the bottom of the faulty leg. The current will then flow from

the positive and negative dc bus to blow the fuses and consequently isolate the faulty leg from the system. The small capacitors are required to avoid a dc path through the thyristors, which allow the thyristors to turn off due to the open-circuit characteristic of the capacitor under fully charged condition.

(a)   (b)
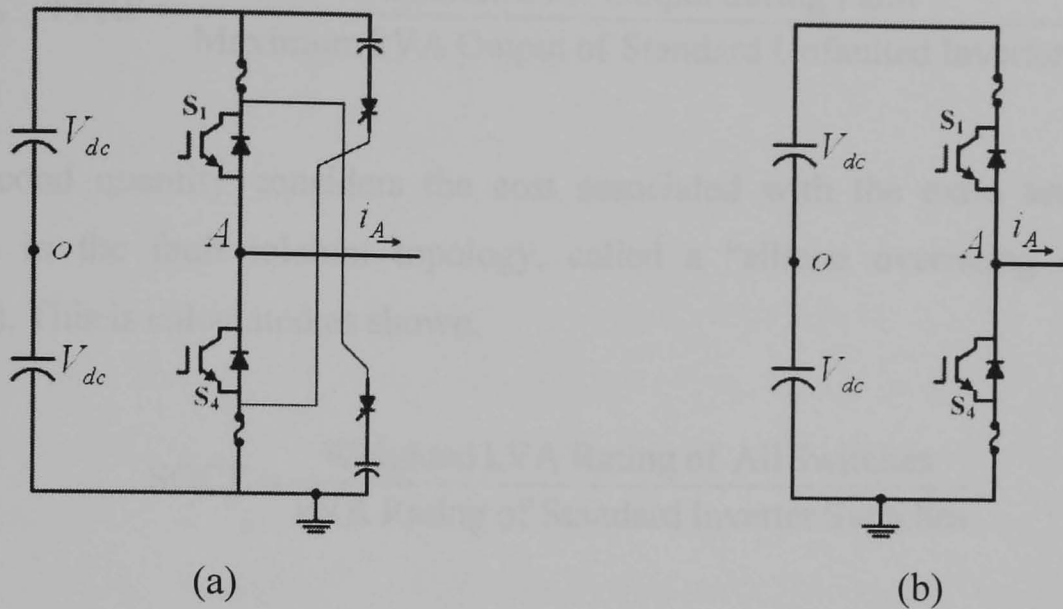
Figure 7.1 Fault isolation topologies

The second topology, shown in figure 7.1b, simply uses fuses between the dc bus and each semiconductor switch [7.2, 7.3]. This topology uses the shoot-through current to blow the fuses. However, this topology requires that the i^2t of the fuses be less than the withstand value of the semiconductor switches.

The preferred action required after isolation is to operate the system under fault tolerant conditions. Operation after reconfiguration can be either (i) operating the system as before the fault or (ii) operating the system under component-minimised topology. Several researchers in this area have proposed methods to deliver satisfactory operation. The first possible method [7.4-7.6] was applied to a voltage-fed induction motor under open-loop volts/Hz operation. It attempted to operate the system under single-phase operation by injecting odd harmonic voltages with appropriate phase angles to neutralise the low frequency pulsating torques and permit smooth drive operation. However, the results shown in [7.4-7.6] do not show satisfactory performance because the line voltage and line current waveforms contain low-order harmonics and there is negative torque appearing in the electromagnetic torque. Other possible methods are to reconfigure the faulty converter to improve system performance for post-fault operation. These are summarised by Welchko *et*

al. [7.7]. Two quantities were proposed to compare each topology. The first quantity compares the capacity of each topology with reference to the standard topology, called a "fault power rating factor" (FPRF). The equation to calculate it is as follows,

$$\text{FPRF} = \frac{\text{Maximum kVA Output during Fault}}{\text{Maximum kVA Output of Standard Unfaulted Inverter}}. \tag{7.1}$$

The second quantity considers the cost associated with the extra semiconductor devices in the fault tolerant topology, called a "silicon overrating cost factor" (SOCF). This is calculated as shown,

$$\text{SOCF} = \frac{\text{Weighted kVA Rating of All Switches}}{\text{kVA Rating of Standard Inverter Switches}}. \tag{7.2}$$

In this equation, the devices used are SCRs, TRIACs, and IGBTs. In the case of IGBTs, the free wheeling diode is included in the IGBT. The assumed relative costs of the silicon switches are as follows,

$$1\,\text{SCR} = 0.5\,\text{IGBT}, \\ 1\,\text{TRIAC} = 1\,\text{IGBT}. \tag{7.3}$$

The values of FPRF and SOCF for each topology are summarised in [7.7], which can be used to assist decision making. The first proposed topology is a switch-redundant topology, as shown in figure 7.2. This topology can be used for short-circuit switch faults, open-switch faults and open-phase faults. In the case of short-circuit switch and open-switch faults, TRIACs in all three phases are required, whereas in the case of open-phase faults, only one TRIAC is required, to connect the neutral of the machine to the dc-link midpoint. This topology is also proposed in [7.3, 7.8-7.9]. However, this topology requires access to the dc-link midpoint and dc-link voltage balancing to avoid distortion.
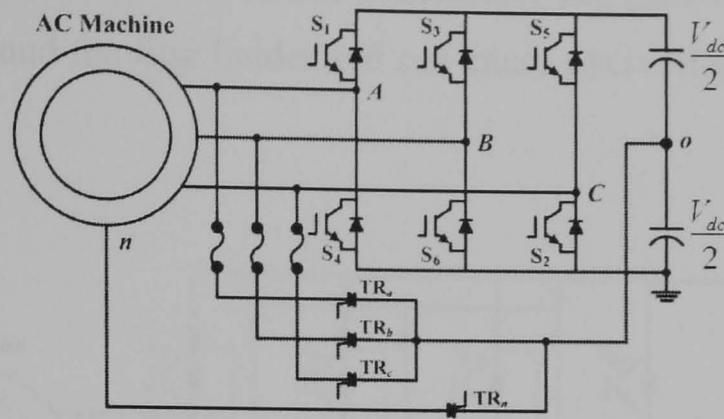
Figure 7.2 Switch redundancy topology

The next topology is a double switch-redundant topology as shown in figure 7.3. This converter leg topology was first proposed by Bolognani *et al.* [7.1] as discussed previously, and can be reconfigured by enabling the fourth leg which is permanently connected to the neutral of the machine. The advantages of this topology are that no dc-link midpoint is required, which avoids the need for dc-link voltage balancing between the two capacitors, and the control method of neutral voltage shifting, which has been developed for single-phase induction motors, can be applied to post-fault operation. This topology has the capability of dealing with a short-circuit switch, a short-circuit phase leg, an open-switch and an open-phase fault.
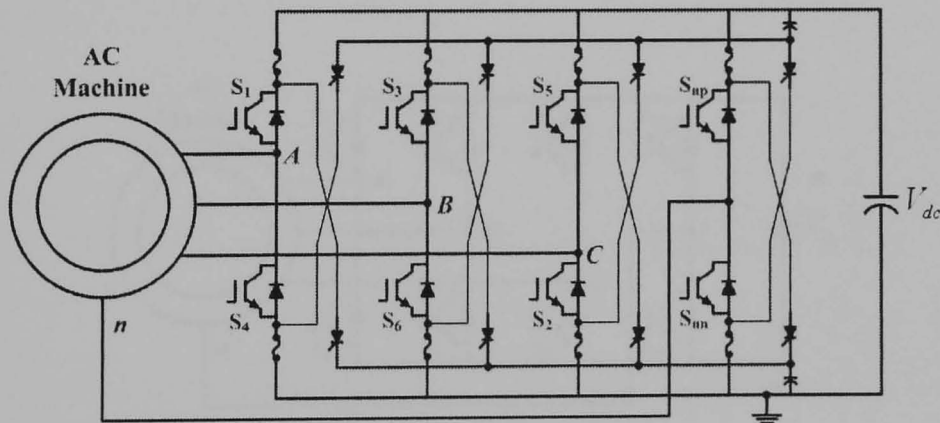
Figure 7.3 Double switch-redundant topology

The next topology, shown in figure 7.4, is called phase-redundant topology and is similar to the previous topology except that the fourth leg has no isolation circuit. The post-fault operation of this topology is to transfer from the faulty leg to the fourth leg by triggering the TRIAC of the faulty phase. This topology was experimentally demonstrated in [7.10] for the case of open-phase and open-switch faults in the inverter. It is important to note that the presence of fuses in these two

topologies leads to an increase in dc bus inductance. The parasitic inductance comes from both the fuse and the fuse holder and can cause overvoltages across the switch due to high $L\dfrac{di}{dt}$.
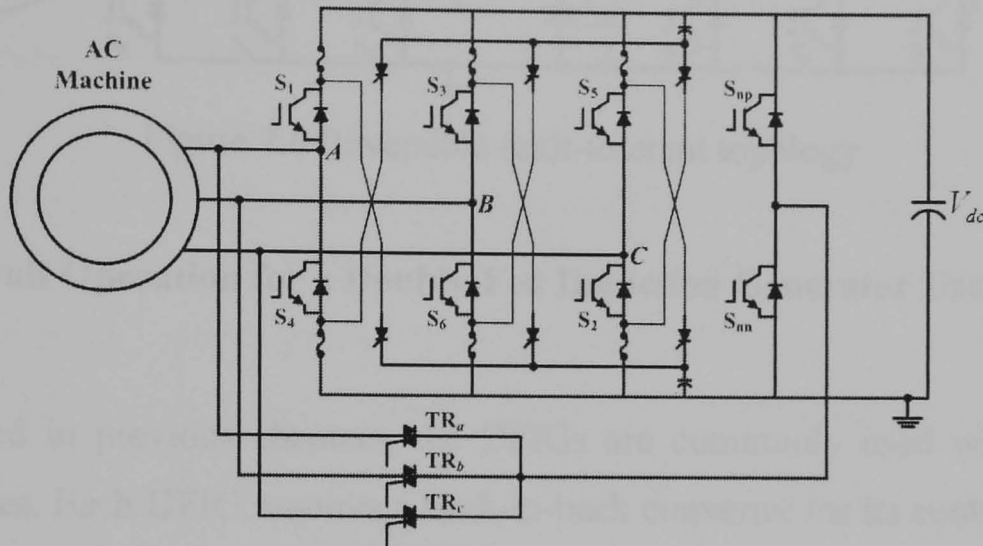
Figure 7.4 Phase-redundant topology

The four-leg topology presented in figure 7.5 was proposed by Correa *et al.* [7.11] to deal with an open-switch fault. The post-fault operation was controlled by composing the unipolar current (zero sequence component) in the post-fault current command to maintain the amplitude and phase of $\alpha - \beta$ currents.
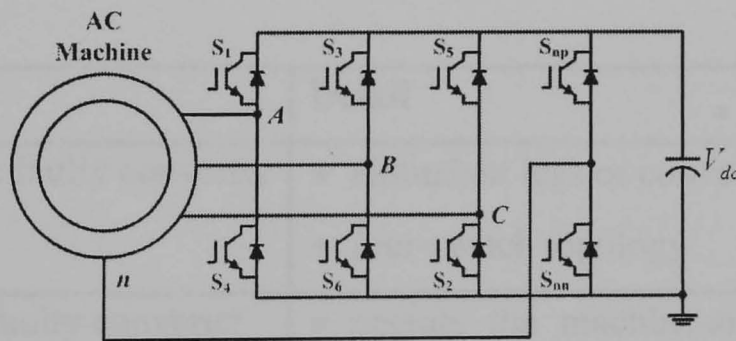
Figure 7.5 Four-leg inverter topology

Jacobina *et al.* [7.12] proposed an alternative topology applicable to back-to-back converters, as shown in figure 7.6. Once a fault appears in either converter, the TRIAC of the faulty phase will be triggered to connect the faulty leg to the same phase of the other converter. However, this topology results in common coupling between the two converters.
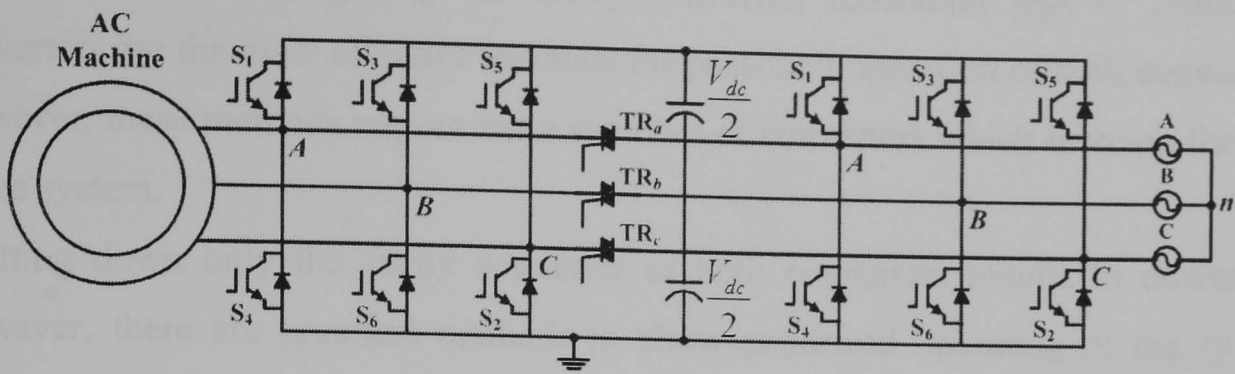
Figure 7.6 Reversible fault-tolerant topology

7.2 Post-Fault Operation for a Doubly-Fed Induction Generator Used in a Wind Turbine

As discussed in previous chapters, the DFIGs are commonly used with off-shore wind turbines. Each DFIG requires a back-to-back converter for its control. If a fault appears in either the machine-side converter or the grid-side converter, it will affect the power generated from the DFIG and possibly adversely affect the mechanical parts of the wind turbine. Possible post-fault operation is an alternative response to converter fault problems instead of shutting down the generator. Possible post-fault options for the DFIG used with wind turbine are listed in table 7.1.

Table 7.1: Summary of possible post-fault operation for the DFIG used in the wind turbine

Option	Detail
1. Reconfigure the faulty converter	• redundant legs or converters • four-switch topology
2. Shut down the faulty converter	• operate the machine-side converter with added-on components and switches • operate the grid-side converter as a STATCOM and operate the generator by aerodynamic control only
3. Shut down both converters	• operate the generator by aerodynamic control only

In the case of reconfiguring the faulty converter, redundant legs or redundant converters are the most effective methods for post-fault operation of both converters. However, these methods require extra switches or converters which increase the cost of the system.

Shutting down only the faulty converter or both converters results in downtime. However, there are practical methods to allow continued operating of the system after the fault. As discussed in chapter 2, power control for a variable-speed wind turbine can be accomplished by either aerodynamic control or generator control or both. Generally, both active power and reactive power can be controlled by the power converters. Without power converters, the DFIG can operate as a normal induction generator with active power control by aerodynamic control of turbine blade pitch angle. However, under this condition, reactive power cannot be controlled and flows only to the generator.

In this research system reconfiguration to a four-switch topology with dc-link midpoint connection is the chosen option for all open-switch faults. In the case of short-circuit switch faults two solutions are selected. For a fault in the machine-side converter, the machine-side converter must be isolated from dc bus and requires the mechanical protection device to short circuit the rotor to operate the generator as an uncontrolled induction generator or stop the generator. The grid-side converter can be controlled to operate like a STATCOM.

If the fault occurs in the grid-side converter, the grid-side converter must be isolated from both dc bus and ac bus while the machine-side converter can be controlled with add-on components and switches. Only this case is considered and implemented in this research.

7.2.1 Four-Switch Topology with DC-Link Midpoint Connection

This topology was proposed by Van Der Broeck and Van Wyk [7.13] in 1984. This system was proposed to minimise the number of semiconductor switches in the inverter and has been widely applied to small induction machine drives [7.13, 7.14]. It consists of two converter legs connected to two phases of the machine or three-phase load as shown in figure 7.7a.

(a)   (b)
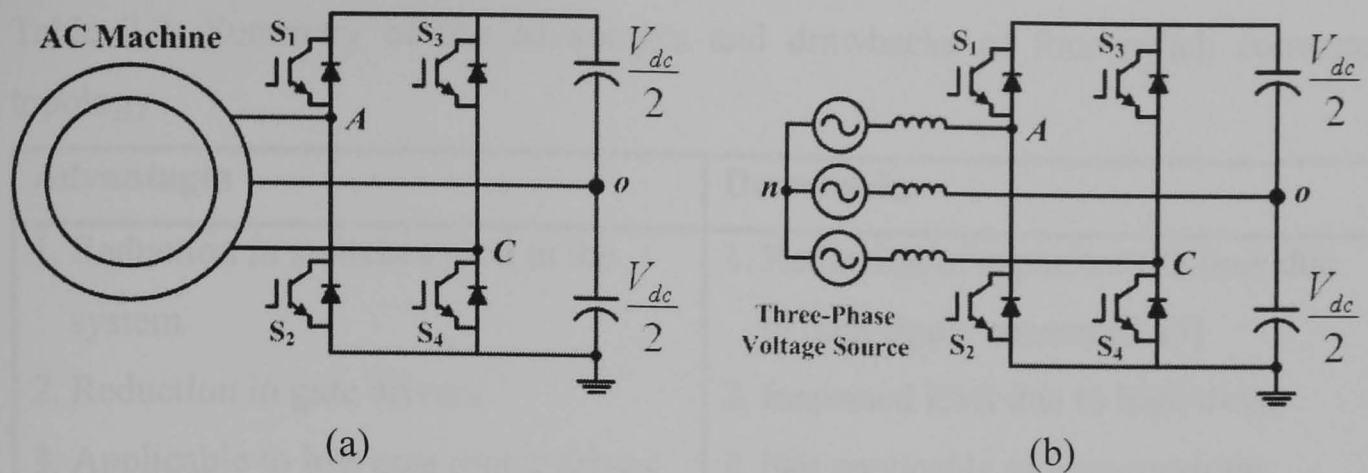
Figure 7.7 Application of four-switch topology (a) inverter, (b) PWM rectifier

The dc side of this converter requires two equal value capacitors connected in series and the midpoint is connected to the third phase of the system. The selection of which phase is connected to the dc-link midpoint is arbitrary

As well as its application to induction machine drives, this topology can also be applied to drive other machines – eg. a permanent magnet synchronous motor (PMSM) [7.15, 7.16] and a brushless dc machine (BLDC) [7.17-7.26]. The main aim of these applications is to reduce the cost of the drive system. This topology is also applicable to a PWM rectifier, as shown in figure 7.7b [7.27, 7.28], and active power filters [7.29-7.31].

Four-quadrant drives with reduced switch count have been studied by many research groups. A single-phase PWM rectifier has been proposed to drive a three-phase induction motor [7.32]. However, it can supply less energy than the three-phase supply. Kim and Lipo [7.33, 7.34] solved this problem by proposing a VSI-PWM rectifier/inverter system with reduced switch count. This system uses the topology shown in figure 7.7a on the machine side and the topology in figure 7.7b on the grid side. The advantages and the drawbacks of the four-switch topology with dc-link midpoint connection are summarised in table 7.2

Table 7.2: Summary of the advantages and drawbacks of four-switch converter topology

Advantages	Drawbacks
1. Reduction in switches used in the system	1. Reduction of capacitor life time due to high ripple current [7.45]
2. Reduction in gate drivers	2. Increased EMI due to high dv/dt
3. Applicable to low cost motor drives	3. Not applicable to four-quadrant drives

i. ***Control Requirements of Four-Switch Topology with DC-Link Midpoint Connection***

Control of this converter [7.13] can be achieved by either current control or voltage control. In the case of current control, two phase currents are controlled to have a 120 degree phase shift between them. With the assumption of a three-wire system with no zero-sequence path, the uncontrolled phase current is automatically indirectly controlled to have a value equal to the negative sum of the controlled currents. Another method is to control the voltage vectors of the controlled phase currents to have a 60 degree phase shift between them. Each vector must be shifted forwards or backwards by 30 degrees depending on which phase is connected to the dc-link midpoint, as shown in figure 7.8a, b and c respectively. The values of the new phase voltage vectors are increased by $\sqrt{3}$ from their original values.

(a)   (b)   (c)
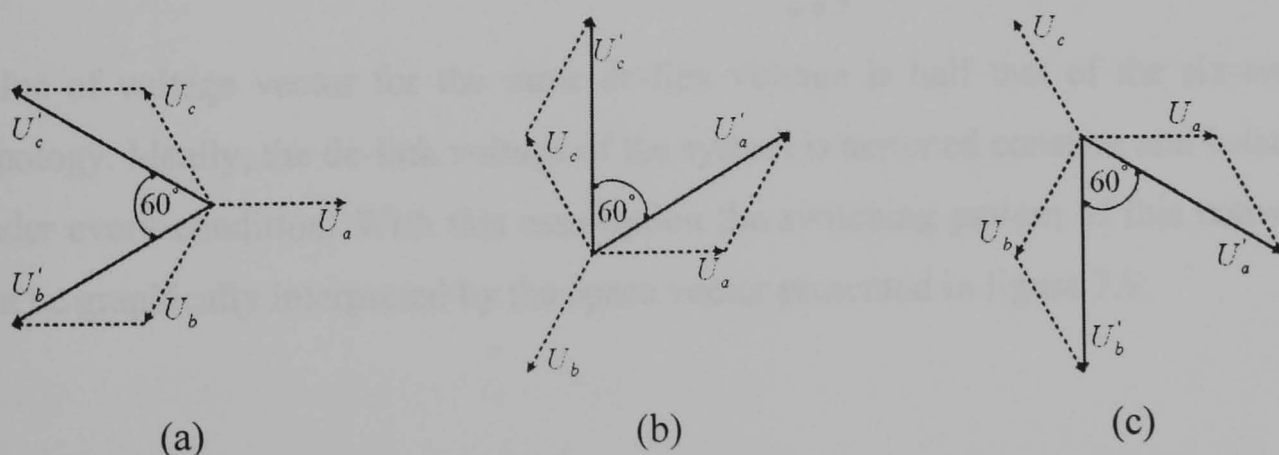
Figure 7.8 Voltage vectors of the four-switch topology with different phases connecting to the dc-link midpoint (a) phase A, (b) phase B and (c) phase C

The ripple voltage for each capacitor is used to estimate the appropriate capacitor size. The ripple voltage of each capacitor, v_{ripple}, can be calculated as follows [7.40],

$$v_{ripple} = \frac{V_{dc}/2}{f_N C (V_{dc}^2 / P_l)/2},$$

(7.4)

where C is the capacitance across half the dc bus, f_N is the supply frequency, V_{dc} is total dc-link voltage and P_l is the power transfer.

The available capacitors have a capacity of $6800\,\mu F$ for 300 V dc–link voltage, and the maximum power transfer of the machine-side converter is at 1.2 pu super-synchronous speed generation (10 Hz) which in this case $\approx 1.2 kW$. Hence the ripple voltage of each capacitor is approximately 19 % of total dc voltage.

Generally, for a six-switch converter, the minimum dc-link voltage must be higher than the peak value of the line voltage. However, the minimum value of the dc-link voltage for the four-switch topology should be at least two times the peak value of the line voltage and the voltage of each capacitor must not be less than the peak value of the line voltage to keep the system controllable [7.33, 7.34].

ii. PWM Modulation for the Four-Switch Topology

For the six-switch topology, the maximum circular trajectory of the voltage is in a hexagon and is $\frac{1}{\sqrt{3}}V_{dc}$, whereas for the four-switch topology, the maximum circular trajectory of the voltage is in a rhombus and is $\frac{1}{2\sqrt{3}}V_{dc}$. Therefore, the maximum value of voltage vector for the same dc-link voltage is half that of the six-switch topology. Ideally, the dc-link voltage of the system is assumed constant and balanced under every condition. With this assumption the switching pattern of this converter can be graphically interpreted by the space vector presented in figure 7.9.

(a)   (b)   (c)
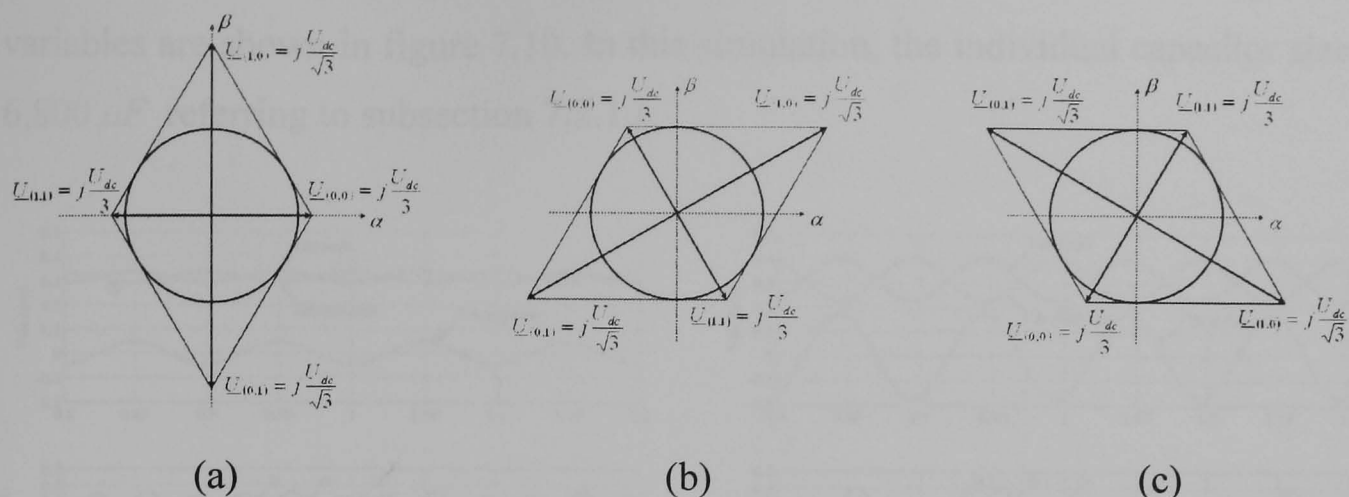
Figure 7.9 Space vector of a four-switch converter with different controlled phases

(a) phase B and C, (b) phase A and C and (c) phase A and B

As shown in figure 7.9 the magnitude of four vectors in the rhombus for each case can be summarised in table 7.3.

Table 7.3: Summarised vector of a four-switch topology with dc-link midpoint connection

Vector	Figure 7.1a	Figure 7.1b	Figure 7.1c
00	$\mathbf{v}_{00} = \dfrac{V_{dc}}{3} e^{j0}$	$\mathbf{v}_{00} = \dfrac{V_{dc}}{3} e^{j\frac{2\pi}{3}}$	$\mathbf{v}_{00} = \dfrac{V_{dc}}{3} e^{-j\frac{2\pi}{3}}$
10	$\mathbf{v}_{10} = \dfrac{V_{dc}}{\sqrt{3}} e^{j\frac{\pi}{2}}$	$\mathbf{v}_{10} = \dfrac{V_{dc}}{\sqrt{3}} e^{j\frac{\pi}{6}}$	$\mathbf{v}_{10} = \dfrac{V_{dc}}{\sqrt{3}} e^{-j\frac{\pi}{6}}$
11	$\mathbf{v}_{11} = \dfrac{V_{dc}}{3} e^{j\pi}$	$\mathbf{v}_{11} = \dfrac{V_{dc}}{3} e^{-j\frac{\pi}{3}}$	$\mathbf{v}_{11} = \dfrac{V_{dc}}{3} e^{j\frac{\pi}{3}}$
01	$\mathbf{v}_{01} = \dfrac{V_{dc}}{2} e^{-j\frac{\pi}{2}}$	$\mathbf{v}_{01} = \dfrac{V_{dc}}{2} e^{-j\frac{5\pi}{6}}$	$\mathbf{v}_{01} = \dfrac{V_{dc}}{2} e^{j\frac{5\pi}{6}}$

Another difference between the four-switch topology and the six-switch topology is that there are no zero voltage vectors in its space vector.

iii. Effect of Capacitor Voltage Oscillation

Due to the injection of alternating current into each capacitor, the voltages of the capacitors oscillate at fundamental frequency. The oscillation depends on the size of the capacitors, the amplitude of line currents and the operating frequency. The four-

switch inverter supplying a passive RL load was simulated and all significant variables are shown in figure 7.10. In this simulation, the individual capacitor size is 6,800 μF referring to subsection 7.2.1.*i*.

(a)   (b)

(c)   (d)
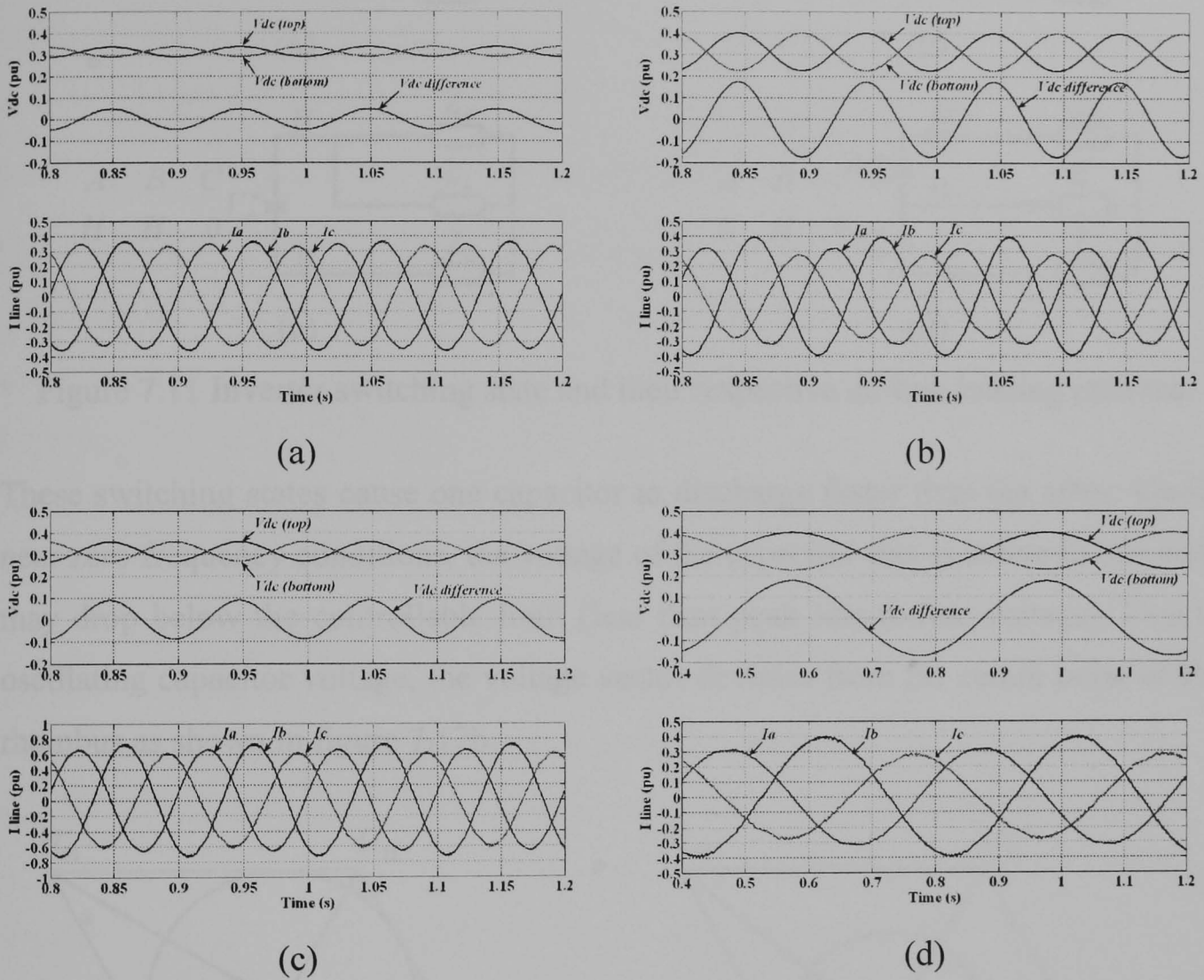
Figure 7.10 Comparison of the voltage of each capacitor, the voltage difference and the line currents for different conditions (a) 10 Hz, normal size capacitors, normal load, (b) 10 Hz, a quarter size capacitors, normal load, (c) 10 Hz, normal size capacitors, double load and (d) 2.5 Hz, normal size capacitors, normal load

It can be concluded that the oscillation of the dc–link voltage increases if the size of capacitors decreases, as shown in figure 7.10b. The larger the load the larger the oscillation as shown in figure 7.10c. Finally, decreasing the operating frequency increases the oscillation as shown in figure 7.10d. Moreover, as shown in figure 7.10, oscillation in the capacitor voltages causes unbalanced three phase currents. This problem is caused by the switching states that cause a short circuit between two controlled phases to either the positive or negative dc bus, as shown in figures 7.11a and 7.11c.
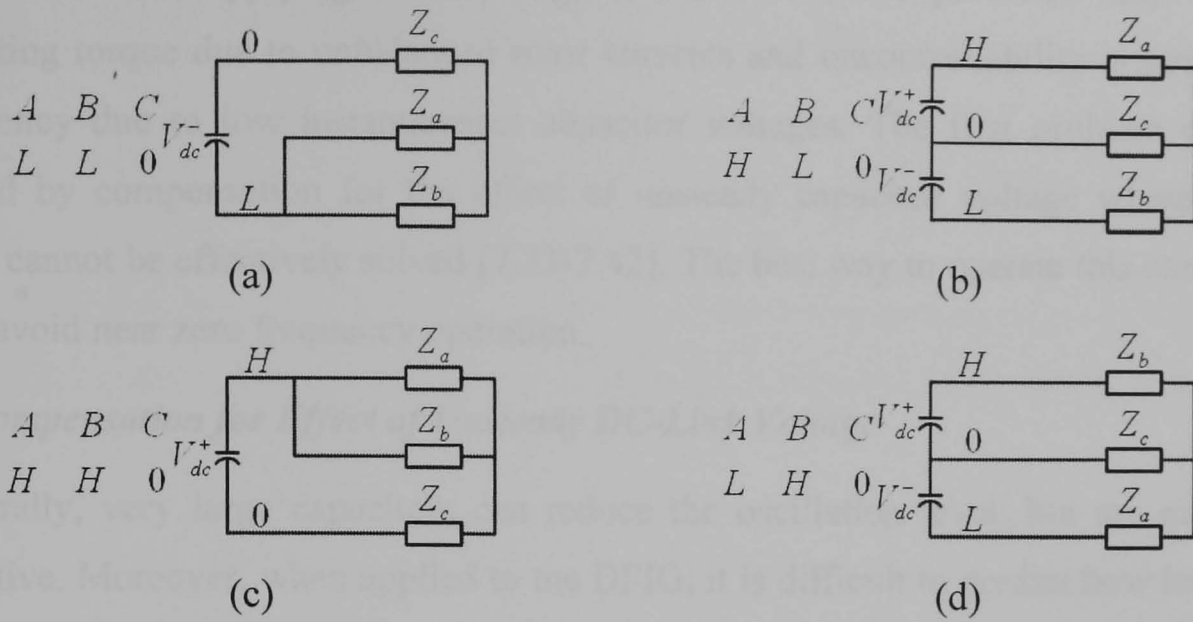
Figure 7.11 Inverter switching state and their respective dc-link loading patterns

These switching states cause one capacitor to discharge faster than the other. Under near zero frequency conditions, the voltage of the capacitor that is active in this state may drop below the controllable limit (less than peak line-to-line voltage). Due to oscillating capacitor voltage, the voltage vector deviates from the centre point of the rhombus as shown in figure 7.12b.
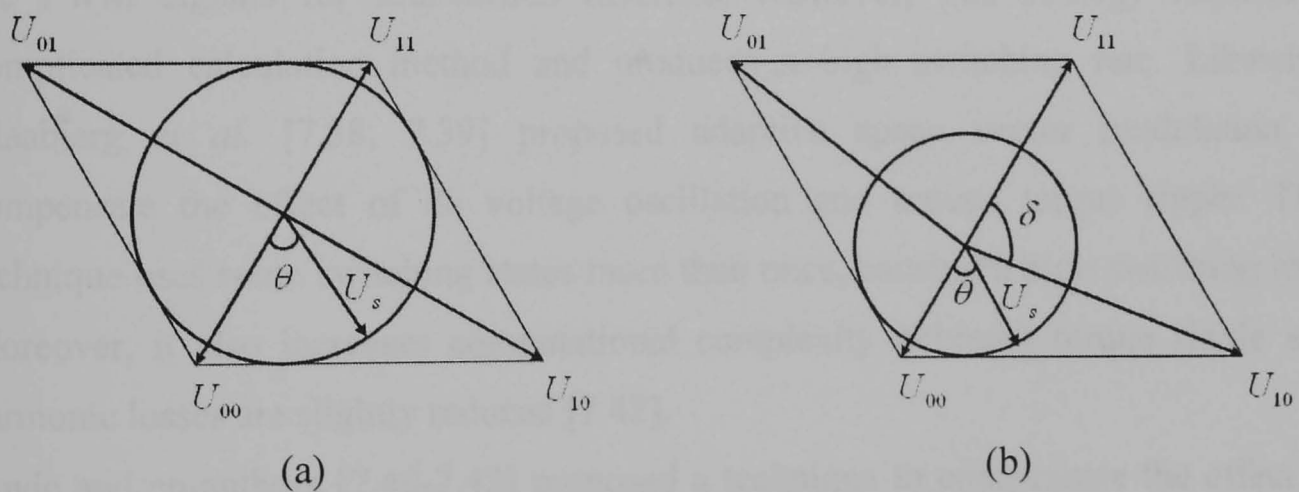
Figure 7.12 Space vector diagram of switching state space vector, with maximum circular trajectory (a) perfect dc voltages, (b) oscillating dc voltages

Figure 7.12 shows the space vector diagram of the four-switch converter under perfect and oscillating dc voltage. Under oscillating conditions, the vectors 00 and 11 have unequal length, depending on which state dominates this condition. Therefore the amplitudes of vectors 00 and 11 vary sinusoidally at fundamental frequency. As shown in figure 7.10, these oscillations also cause unbalanced line currents.

Therefore, when applying this topology to the DFIG, two problems may exist - pulsating torque due to unbalanced rotor currents and uncontrollability at near zero frequency due to low instantaneous capacitor voltages. The first problem can be solved by compensation for the effect of unsteady capacitor voltage whereas the latter cannot be effectively solved [7.33-7.42]. The best way to operate this converter is to avoid near zero frequency operation.

iv. Compensation for Effect of Unsteady DC-Link Voltage

Generally, very large capacitors can reduce the oscillation level, but are not cost effective. Moreover, when applied to the DFIG, it is difficult to predict how long the operating frequency remains very low or zero. Therefore, another solution should be investigated.

Several techniques have been proposed to compensate the effect of dc-link voltage oscillation. Kim and Lipo [7.33, 7.34] proposed scalar modulation for the four-switch inverter and hysteresis PWM for the PWM rectifier. Jacobina *et al.* [7.35-7.37] proposed digital scalar modulation to generate a PWM signal that mimics space vector modulation. In [7.37] they also proposed a general PWM pattern to generate the PWM signals for four-switch inverters. However, this strategy requires a complicated calculation method and produces a high switching rate. Likewise, Blaabjerg *et al.* [7.38, 7.39] proposed adaptive space vector modulation to compensate the effect of dc voltage oscillation and reduce torque ripple. This technique uses some switching states more than once, causing a high switching rate. Moreover, it also increases computational complexity although torque ripple and harmonic losses are slightly reduced [7.42].

Covic and co-authors [7.40-7.42] proposed a technique to compensate the effect of capacitor voltage oscillations on the line current signals. This technique requires only three switching states for each switching cycle. Because of its simplicity and its effectiveness in compensation for the dc-link voltage oscillations, this technique was selected for this research.

The relationship between the voltage across each capacitor referring to dc-link midpoint and the total dc-link voltage can be written as follows,

$$V_{dc}^{+} = (1 - \gamma)V_{dc} \qquad \text{and} \qquad V_{dc}^{-} = (-\gamma)V_{dc}, \qquad (7.5)$$

where γ represents the ratio of the lower capacitor voltage to the total dc-link voltage, which is equal to 0.5 under steady conditions.

The matrix representing the output of the converter as a function of switch states is shown in equation (7.6), where phase C is the uncontrolled phase connected to the dc-link midpoint,

$$\begin{bmatrix} L & H & H & L \\ L & L & H & H \\ 0 & 0 & 0 & 0 \end{bmatrix} = \begin{bmatrix} -\gamma V_{dc} & (1-\gamma)V_{dc} & (1-\gamma)V_{dc} & -\gamma V_{dc} \\ -\gamma V_{dc} & -\gamma V_{dc} & (1-\gamma)V_{dc} & (1-\gamma)V_{dc} \\ 0 & 0 & 0 & 0 \end{bmatrix}. \qquad (7.6)$$

Using Clarke's transform, the $\alpha - \beta$ voltage components of each voltage are shown in equation (7.7),

$$\begin{bmatrix} u_{00\alpha} & u_{10\alpha} & u_{11\alpha} & u_{01\alpha} \\ u_{00\beta} & u_{10\beta} & u_{11\beta} & u_{01\beta} \end{bmatrix} = \frac{2}{3} \begin{bmatrix} 1 & -\dfrac{1}{2} & -\dfrac{1}{2} \\ 0 & \dfrac{\sqrt{3}}{2} & -\dfrac{\sqrt{3}}{2} \end{bmatrix}$$
$$\times \begin{bmatrix} -\gamma V_{dc} & (1-\gamma)V_{dc} & (1-\gamma)V_{dc} & -\gamma V_{dc} \\ -\gamma V_{dc} & -\gamma V_{dc} & (1-\gamma)V_{dc} & (1-\gamma)V_{dc} \\ 0 & 0 & 0 & 0 \end{bmatrix}. \qquad (7.7)$$

The transformation results in the voltage space vector equations (7.8a-7.8d),

$$\mathbf{U}_{00} = V_{dc}\left[\left(\frac{-\gamma}{3}\right) + j\left(\frac{-\gamma}{\sqrt{3}}\right)\right], \qquad (7.8a)$$

$$\mathbf{U}_{10} = V_{dc}\left[\left(\frac{2-\gamma}{3}\right) + j\left(\frac{-\gamma}{\sqrt{3}}\right)\right], \qquad (7.8b)$$

$$\mathbf{U}_{11} = V_{dc}\left[\left(\frac{1-\gamma}{3}\right) + j\left(\frac{1-\gamma}{\sqrt{3}}\right)\right], \qquad (7.8c)$$

$$\mathbf{U}_{01} = V_{dc}\left[\left(\frac{-1-\gamma}{3}\right) + j\left(\frac{1-\gamma}{\sqrt{3}}\right)\right]. \qquad (7.8d)$$

In the same way, the voltage vectors where phase A or phase B is connected to the dc-link midpoint are expressed in equations (7.9a-7.9d) and (7.10a-7.10d) respectively.

$$\mathbf{U}_{00} = V_{dc}\left[\frac{2}{3}\gamma\right],$$

(7.9a)

$$\mathbf{U}_{10} = V_{dc}\left[\left(\frac{-1+2\gamma}{3}\right)+j\left(\frac{1}{\sqrt{3}}\right)\right],$$

(7.9b)

$$\mathbf{U}_{11} = V_{dc}\left[-\frac{2}{3}(1-\gamma)\right],$$

(7.9c)

$$\mathbf{U}_{01} = V_{dc}\left[\left(\frac{-1+2\gamma}{3}\right)-j\left(\frac{1}{\sqrt{3}}\right)\right],$$

(7.9d)

$$\mathbf{U}_{00} = V_{dc}\left[\left(\frac{-\gamma}{3}\right)+j\left(\frac{\gamma}{\sqrt{3}}\right)\right],$$

(7.10a)

$$\mathbf{U}_{10} = V_{dc}\left[\left(\frac{2-\gamma}{3}\right)+j\left(\frac{\gamma}{\sqrt{3}}\right)\right],$$

(7.10b)

$$\mathbf{U}_{11} = V_{dc}\left[\left(\frac{1-\gamma}{3}\right)-j\left(\frac{1-\gamma}{\sqrt{3}}\right)\right],$$

(7.10c)

$$\mathbf{U}_{01} = V_{dc}\left[\left(\frac{-1-\gamma}{3}\right)-j\left(\frac{1-\gamma}{\sqrt{3}}\right)\right].$$

(7.10d)

These voltage vectors are then used to calculate the switching time for each controlled phase. Figure 7.13 presents the four vectors of the four-switch topology, with phase C connected to the dc-link midpoint, and with unbalance occurring in the system such that $\gamma < 0.5$.
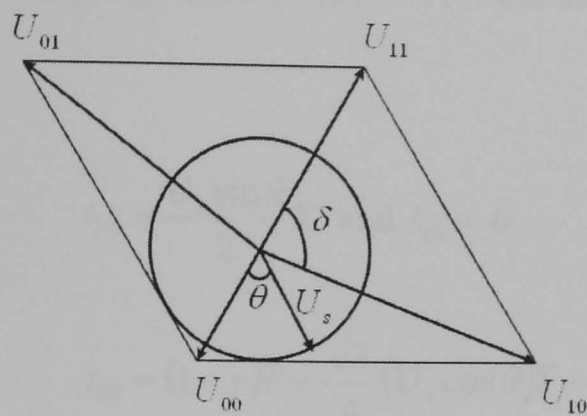
Figure 7.13 Space vector diagram of switching states, with maximum circular

trajectory under oscillating dc-link voltage $(\gamma < 0.5)$

The voltage vector shown $\mathbf{U}_s$ in figure 7.13 can be written as follows,

$$(\mathbf{U}_s \sin\theta)T = (\mathbf{U}_{10} \sin\delta)t_b, \tag{7.11}$$

$$(\mathbf{U}_s \cos\theta)T = \mathbf{U}_{00}t_{00} + \mathbf{U}_{11}t_{11} + (\mathbf{U}_{10} \cos\delta)t_{10}. \tag{7.12}$$

Placing equations (7.8a-7.8d) into equation (7.11) and (7.12), the results are shown in equations (7.13)-(7.16), as follows,

$$(\mathbf{U}_{10} \sin\delta)T = \frac{2}{3}\frac{\sqrt{3}V_{dc}}{2}, \tag{7.13}$$

$$(\mathbf{U}_{10} \cos\delta)T = \frac{2}{3}\frac{(-1+2\gamma)V_{dc}}{2}, \tag{7.14}$$

$$\mathbf{U}_{00} = \frac{2}{3}\gamma V_{dc}, \tag{7.15}$$

$$\mathbf{U}_{11} = -\frac{2}{3}(1-\gamma)V_{dc}. \tag{7.16}$$

As discussed previously, the maximum voltage in the rhombus is

$$V_{1p.u.} = \frac{V_{dc}}{2\sqrt{3}}. \tag{7.17}$$

Therefore, after per-unitising equations (7.13)-(7.16), the calculated switching times become

$$t_{10} = \frac{U_s \sin\theta}{2}T \text{ and } t_{01} = 0,$$ (7.18)

$$t_{00} = (1-\gamma)T + \frac{\sqrt{3}}{4}(U_s \cos\theta)T - \frac{t_{10}}{2},$$ (7.19)

$$t_{11} = T - (t_{00} + t_{10}).$$ (7.20)

For application in both simulation and experimental implementation, 1 per-unit time for this calculation is the switching time and the terms $U_s \cos\theta$ and $U_s \sin\theta$ are replaced by u_α and u_β respectively. However, the α-axis for this case must be rotated to align on the vector 00 position, and this procedure must be applied to other cases where another phase is connected to the dc-link midpoint.

The finalised equations, derived from equations (7.18)–(7.20) are

$$t_{10} = \frac{u_\beta}{2} \text{ and } t_{01} = 0,$$ (7.21)

$$t_{00} = (1-\gamma) + \frac{\sqrt{3}}{4}u_\alpha - \frac{1}{4}u_\beta,$$ (7.22)

$$t_{11} = 1 - (t_{00} + t_{10}).$$ (7.23)

By using $\alpha - \beta$ components as the input signals instead of the resultant command voltage vector, it is not necessary to consider the angle of the resultant vector for changing the timing from t_{10} to t_{01} if the angle exceeds $180°$. Therefore, timing t_{10} is adequate for this calculation. From simulation, when arranging the timing for the controlled phases, the timing for different controlled phases become as follows,

Uncontrolled Phase   Controlled Phase

A

$$
\begin{aligned}
T_b &= 1 - t_{10} + t_{11} \\
T_c &= T_b + t_{10}
\end{aligned}
\tag{7.24}
$$

B

$$
\begin{aligned}
T_a &= T_c + t_{10} \\
T_c &= 1 - t_{10} + t_{11}
\end{aligned}
\tag{7.25}
$$

C

$$
\begin{aligned}
T_a &= 1 - t_{10} + t_{11} \\
T_b &= T_a + t_{10}
\end{aligned}
\tag{7.26}
$$

As discussed by Covic and co-authors [7.40], and to match the switching scheme of TI DSP, the proper switching strategy that provides low switching losses and a low harmonic level is shown in figure 7.14.
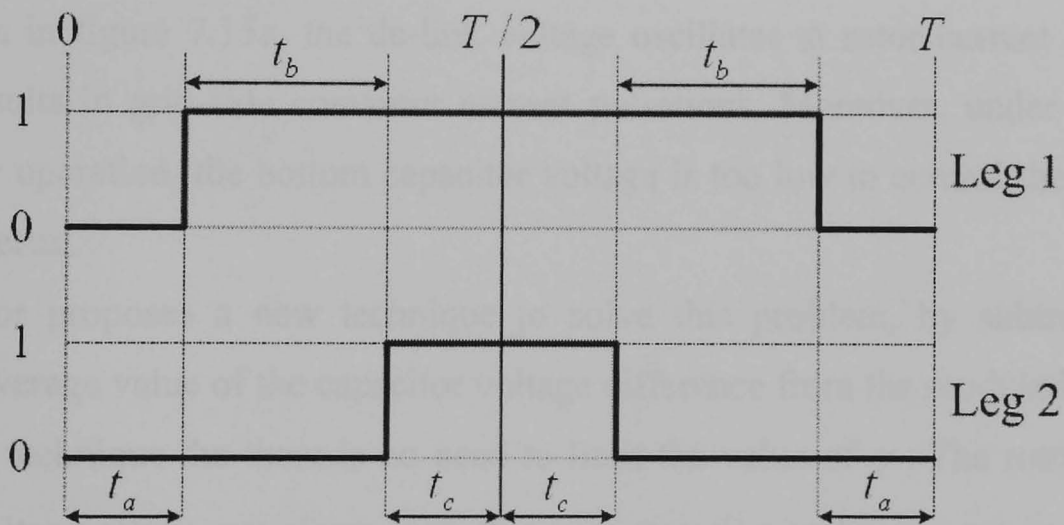
Figure 7.14 Switching strategy for the four-switch topology

The application of this algorithm to a closed-loop system results in an ever increasing difference between the dc voltages of the capacitors. During closed-loop operation of the DFIG, the top capacitor voltage increases while the bottom capacitor voltage decreases. This phenomenon is caused by the closed-loop controller which tries to control the dq-axis currents to follow the command. This action results in dc offset in the modulating signals and time-varying α and β voltage commands.

However, in the case of open-loop control of the same system, the α and β voltage commands are fixed and the unbalanced condition of the three phase currents is

worse than that of closed-loop control. This condition remains steady during the whole operating time and the mean voltage of each capacitor is constant.

From simulation results the capacitor voltages will stop diverging when the modulation index of one modulating signal exceeds one. At this point, the average values of each capacitor voltage stop changing and the rotor currents become distorted. Moreover, each modulating signal has a dc offset due to the difference between the means of the capacitor voltages. However, in the experimental system, the protection circuit trips and the system cannot operate in this state.

One possible method to solve this problem is to introduce a minimum value of γ. This limits the minimum dc voltage and avoids overmodulation. However, this method allows distortion of the rotor currents and the difference between the mean capacitor voltages can be high, depending on the limit introduced to γ as shown in figure 7.15a.

As shown in figure 7.15a, the dc-link voltage oscillates at rotor current frequency which results in grid-side converter current pulsations. Moreover, under near zero frequency operation, the bottom capacitor voltage is too low to control the machine-side converter.

The author proposes a new technique to solve this problem, by subtracting the moving average value of the capacitor voltage difference from the modulating signal. With this technique the there is no need to limit the value of γ. The rotor currents and capacitor voltage waveform with this compensation technique are presented in figures 7.15b. Comparing the results in figures 7.15a and 7.15b, the current waveforms in figure 7.15b are more symmetrical and the dc-link voltage in figure 7.15b is much smoother.
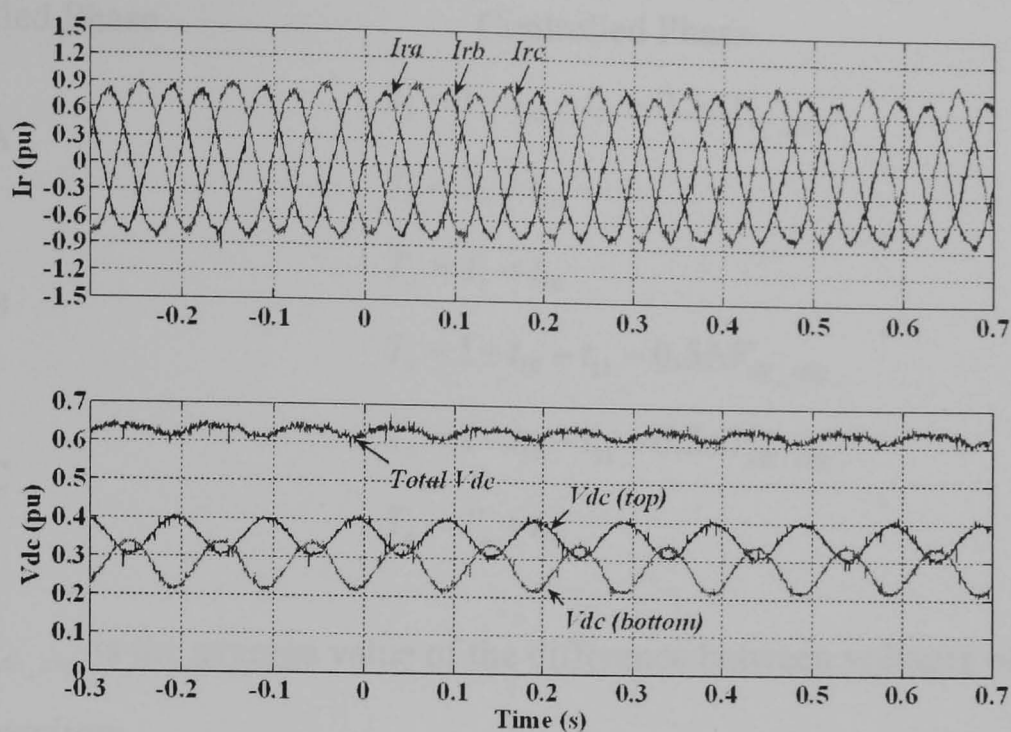
(a)
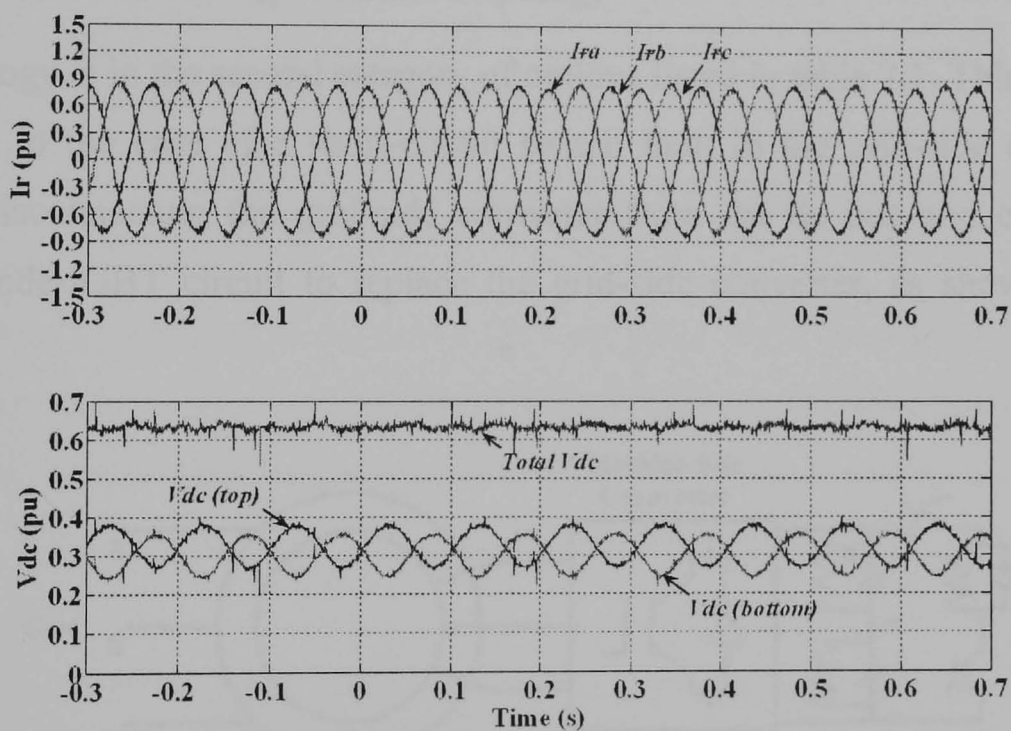
(b)

Figure 7.15 Experimental results showing rotor current waveforms, dc-link voltage and individual capacitor voltage waveforms for operation of the machine-side converter (a) with 10% limit for γ and (b) with compensation by moving average value of the dc voltage difference

The method to calculate moving average value is the same as that is used in chapter 6 for the Absolute Normalised DC Current Method. The timing calculation is modified as shown in equations (7.27)–(7.29) for each phase.

Uncontrolled Phase	Controlled Phase	
A	$T_b = 1 - t_{10} - t_{11} - 0.5\Delta V_{dc\_avg}$ $T_c = T_b + t_{10}$ $T_a = T_c + t_{10}$	(7.27)
B	$T_c = 1 - t_{10} - t_{11} - 0.5\Delta V_{dc\_avg}$ $T_a = T_c + t_{10}$	(7.28)
C	$T_a = 1 - t_{10} - t_{11} - 0.5\Delta V_{dc\_avg}$ $T_b = T_a + t_{10}$	(7.29)

where ΔV_{dc_avg} is the average value of the difference between voltages of the top and bottom capacitors.

7.2.2 Constant DC Voltage Control Topology

This topology is in the second category of options listed in table 7.1. This topology is applicable in the case of a short-circuit switch fault in the grid-side converter. It requires disconnecting the grid-side converter from the dc bus and connecting a resistor-diode-IGBT circuit to replace the grid-side converter, as shown in figure 7.16.
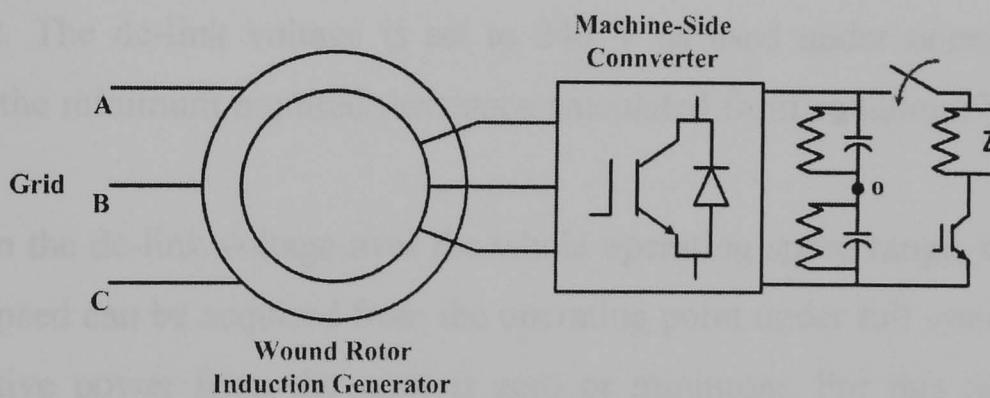
Figure 7.16 Reconfiguration system with constant dc voltage control

The dc-link voltage is fed back to the controller and using hysteresis control the IGBT regulates the dc-link voltage. This topology is generally used in motor drives with dynamic braking, where the regenerative power is dissipated in the resistor. With this topology, the machine-side converter can still be controlled by vector control and maximum power tracking is achievable provided the machine is running

in the super-synchronous speed region. During operation, power is generated from both stator and rotor, but the rotor power is dissipated in the resistor. Therefore the power generated to the grid is only stator power.

The resistance value can be calculated from rotor power at the maximum operating speed. Assuming that the rotor loss is zero, rotor power is

$$P_r = -s \cdot P_s , \qquad (7.30)$$

where s is a per-unit slip and P_s is the stator power.

The minimum resistance required can be calculated from the condition that the duty cycle of the chopper IGBT is 1. Therefore, the equation to calculate the resistance value is

$$R = \frac{V_{dc}^2}{P_r} , \qquad (7.31)$$

where P_r is the maximum power generated from the rotor at the maximum per-unit slip.

In this research, referring to chapter 4 the maximum stator power is approximately 0.775 pu which is equal to approximately 1080 W/phase and the maximum operating slip is -0.2. The dc-link voltage is set to 240 V as used under normal operation. Therefore, the minimum required resistance calculated from equation (7.31) is 53.92 Ω.

To maintain the dc-link voltage over the whole operating speed range, the minimum operating speed can be acquired from the operating point under full system operation that the active power from the rotor is zero or minimum. For this research, such operating speed is approximately 1.065 pu speed. Therefore, considering the speed fluctuation caused by wind, the minimum operating speed for this topology is set to 1.10 pu. The speed range can be increased by reducing the dc-link voltage and value of resistor bank, but the current rating of the resistor must also be increased.

This topology is designed for reconfiguration of the DFIG if a short-circuit switch fault occurs in the grid-side converter. After isolation of the faulty converter by protection systems and the disconnection of the stator from the network, the

reconfiguration can be completed off-line and the system resynchronised for super-synchronous speed generation.

7.3 Operation Requirement for System Reconfiguration

This section discusses the operations required for system reconfiguration to four-switch topology with dc-link midpoint connection after an open-switch fault in either converter. Two main operations are required – (i) fault isolation and (ii) system reconfiguration, which are discussed in sections 7.3.1 and 7.3.2 respectively.

7.3.1 Fault Isolation

After an open-switch fault is detected, the controller has to first isolate the relevant phase from the faulty converter. The isolation method is simply to disable the firing signals for both the switches in the faulty leg. This method is adequate to isolate the faulty phase while the system is operating under either inverting mode or rectifying mode. Although the anti-parallel diodes are still present in the faulty leg, current cannot flow through these diodes. Since the dc-link voltage of each capacitor must be higher than the peak value of line voltage, the top diode is reverse biased. Likewise, the midpoint has higher potential than the negative bus and the bottom diode is also reverse biased. This is shown in the schematic of figure 7.17, after reconfiguration.
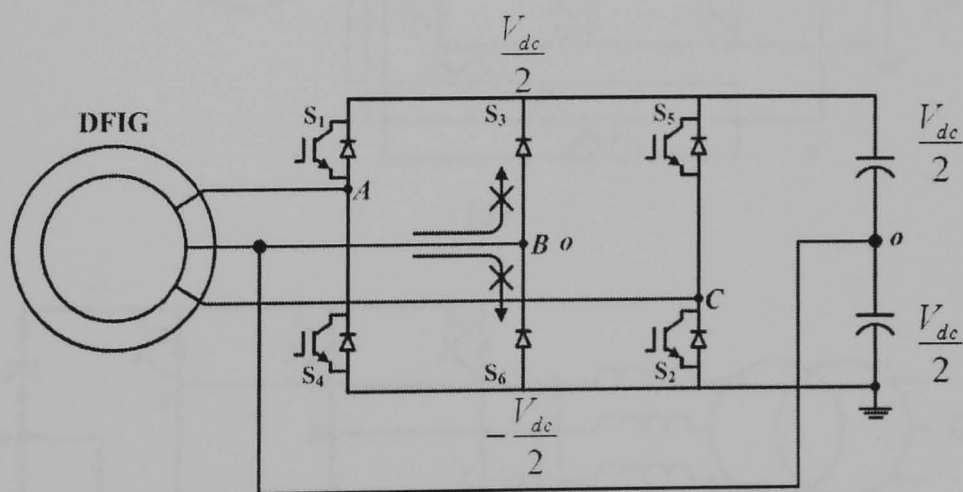
Figure 7.17 Schematic diagram after isolation of phase B, showing reverse bias of both anti-parallel diodes after reconfiguration

Therefore, after disabling the switches in the faulty leg and connecting the faulty phase to the dc-link midpoint, the system is ready to operate under either super-synchronous (rectifier) or sub-synchronous (inverter) generation.

7.3.2 System Reconfiguration

To reconfigure the system, three bi-directional switches are required, permanently connected between each phase and the dc-link midpoint. Normally, the switches are TRIACs or back-to-back thyristors. An alternative choice of bi-directional switch is from matrix converter topology, using two IGBTs with anti-parallel diodes connected in anti-series configuration, as in figure 7.18.
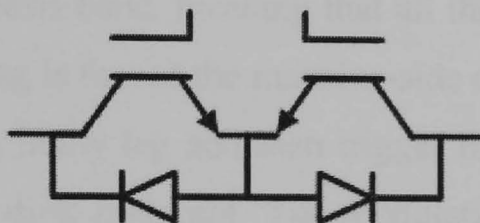
Figure 7.18 Bidirectional switch

The advantage of this topology is that it has a common emitter, which allows the use of one gate driver to turn on both switches. The switches are fit to both machine-side and grid-side converters as shown in figure 7.19.
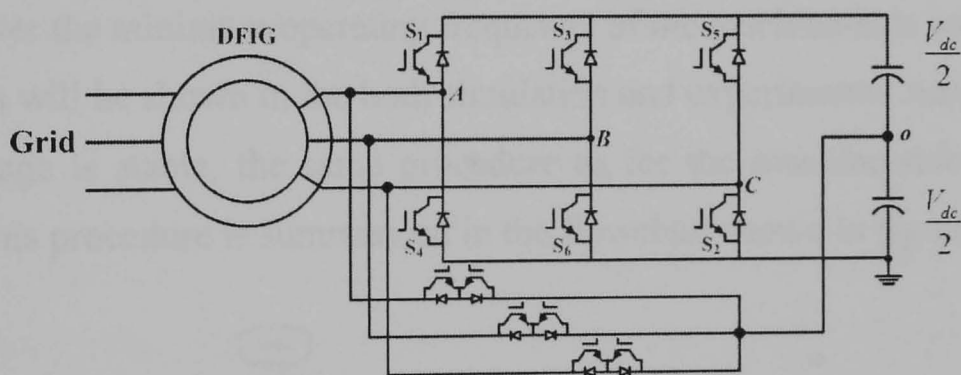
(a)
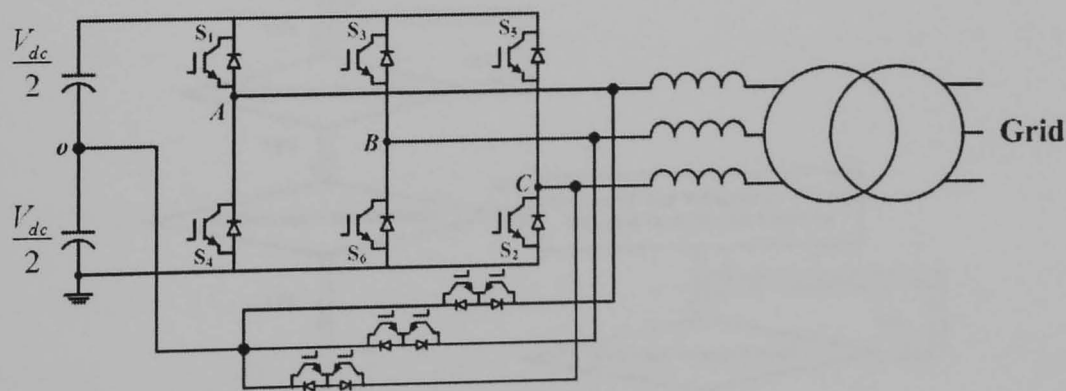
(b)

Figure 7.19 Fault tolerant topology for a doubly-fed induction generator on (a) the machine-side converter and (b) the grid-side converter

In this research, simultaneous faults in both converters are not considered. System reconfiguration for the machine-side converter and the grid-side converter are considered separately.

i. Reconfiguration Procedure

Referring to chapter 6, the proposed fault detection method recognises that an open-switch fault has occurred. The controller waits until the amplitude of each phase current is within the hysteresis band, meaning that all three phase current values are close to zero. If the fault flag is that of the machine-side converter, the controller will disable the switches in the faulty leg and then trigger the bypass switch to connect the faulty phase to the dc-link midpoint. The modulating signal will immediately change to that for control of the four-switch converter. In contrast, if the fault flag is that of the grid-side converter, the controller will increase the dc-link voltage command to be higher than twice the peak value of line-to-line voltage. This procedure is not necessary for the machine-side converter because the rotor line-to-line voltage under healthy condition is lower than half of the dc voltage. However, it can help lower the minimum operating frequency of the machine-side converter.

This process will be shown in the both simulation and experimental results. Once the dc-link voltage is stable, the same procedure as for the machine-side converter is followed. This procedure is summarised in the flowchart shown in figure 7.20.
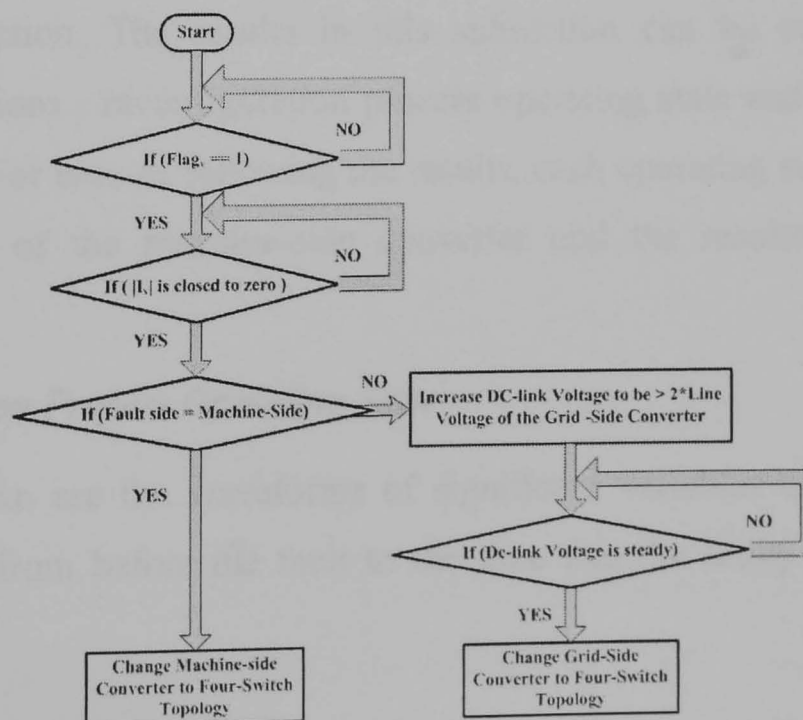
Figure 7.20 Reconfiguration flowchart

Due to the capacitor voltage oscillation problem while operating a four-switch converter at near zero frequency, if a fault occurs in the machine-side converter, the generator should continue to operate under sub-synchronous or super-synchronous generation as it was at the time of the fault.

This problem could be overcome by changing the speed command faster than the rate of change of dc-link voltage. However, this method is not possible for a wind turbine because its inertia is too high to allow fast speed change. Therefore, it is advisable to operate the generator under the mode prior to the fault. If the generator is restarted, the most suitable mode is super-synchronous speed generation as it can generate more power than sub-synchronous speed generation. The grid-side converter does not suffer from this problem because it operates at constant frequency.

7.4 Simulation Results

A MATLAB/SIMULINK program is used to simulate the whole system. The simulation can be divided into open-switch fault reconfiguration and short-circuit switch fault reconfiguration. The former is achieved by the four-switch topology with dc-link midpoint connection and the latter by the constant dc voltage control topology.

7.4.1 Open-Switch Faults

In this case, the reconfigured topology is the four-switch topology with dc-link midpoint connection. The results in this subsection can be separated into two operating conditions - reconfiguration process operating state and steady-state post-fault operation. For ease of following the results, each operating state is also divided into the results of the machine-side converter and the results of the grid-side converter.

i. Reconfiguration Process Operating State

The results shown are the waveforms of significant variables of the DFIG. Each result is shown from before the fault to the time that the faulty converter is fully reconfigured.

• *Machine-Side Converter*
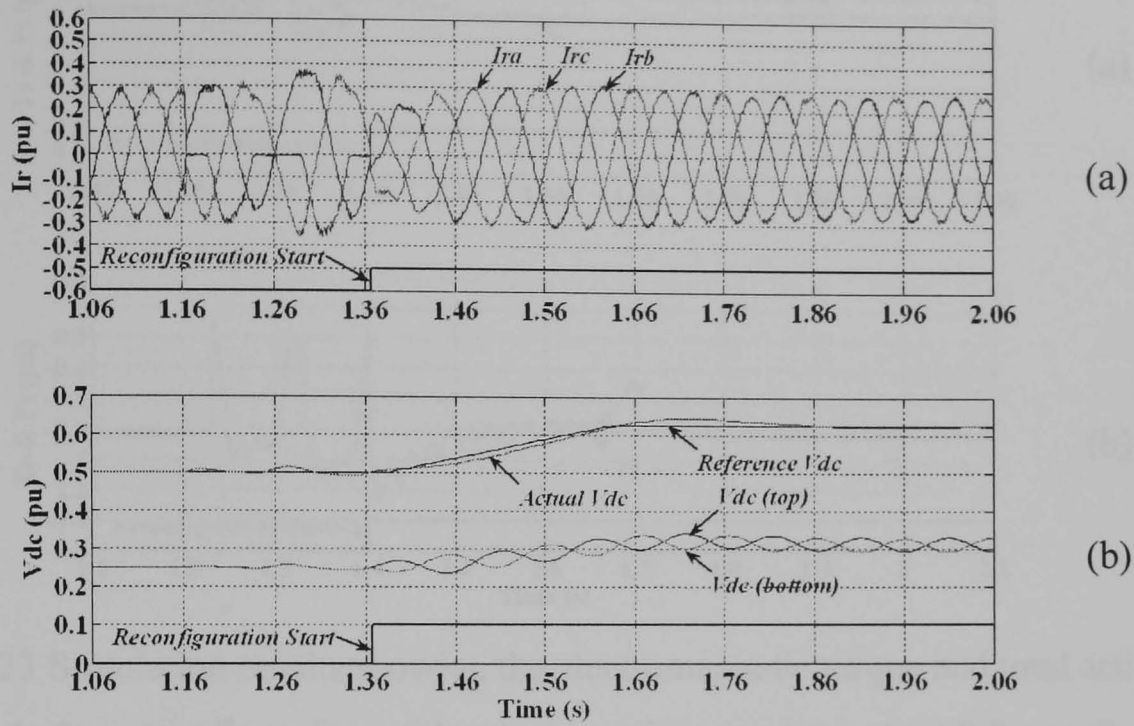
Figure 7.21 Simulation results showing (a) rotor current waveforms and (b) dc-link voltage and individual capacitor voltage waveforms during reconfiguration of the machine-side converter at 0.8 pu sub-synchronous speed generation
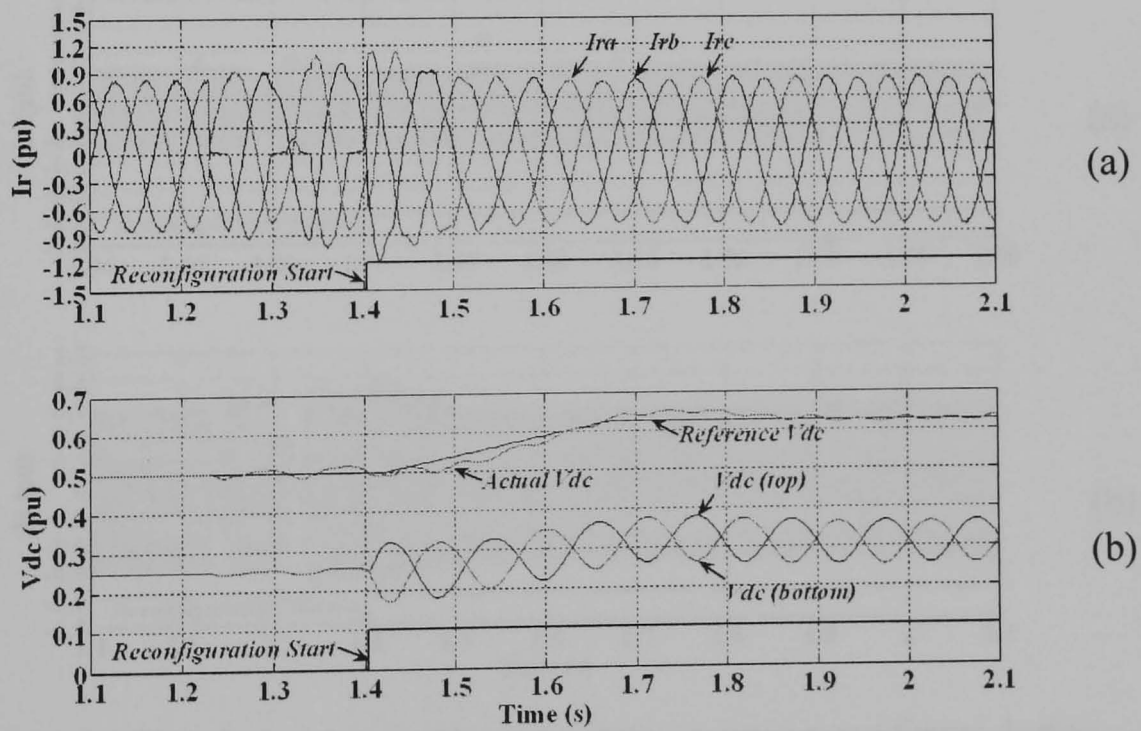
Figure 7.22 Simulation results showing (a) rotor current waveforms and (b) dc-link voltage and individual capacitor voltage waveforms during reconfiguration of the machine-side converter at 1.2 pu super-synchronous speed generation

214
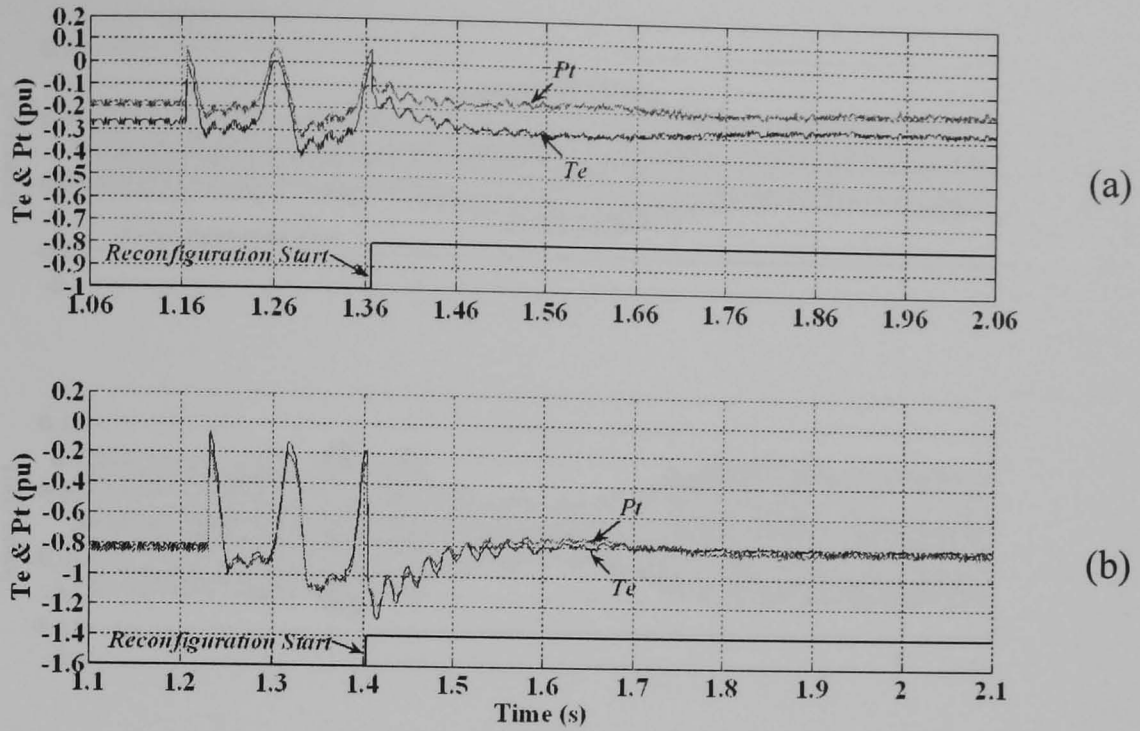
Figure 7.23 Simulation results showing the electromagnetic torque and total active power during reconfiguration of the machine-side converter at (a) 0.8 pu sub-synchronous speed generation and (b) 1.2 pu super-synchronous speed generation
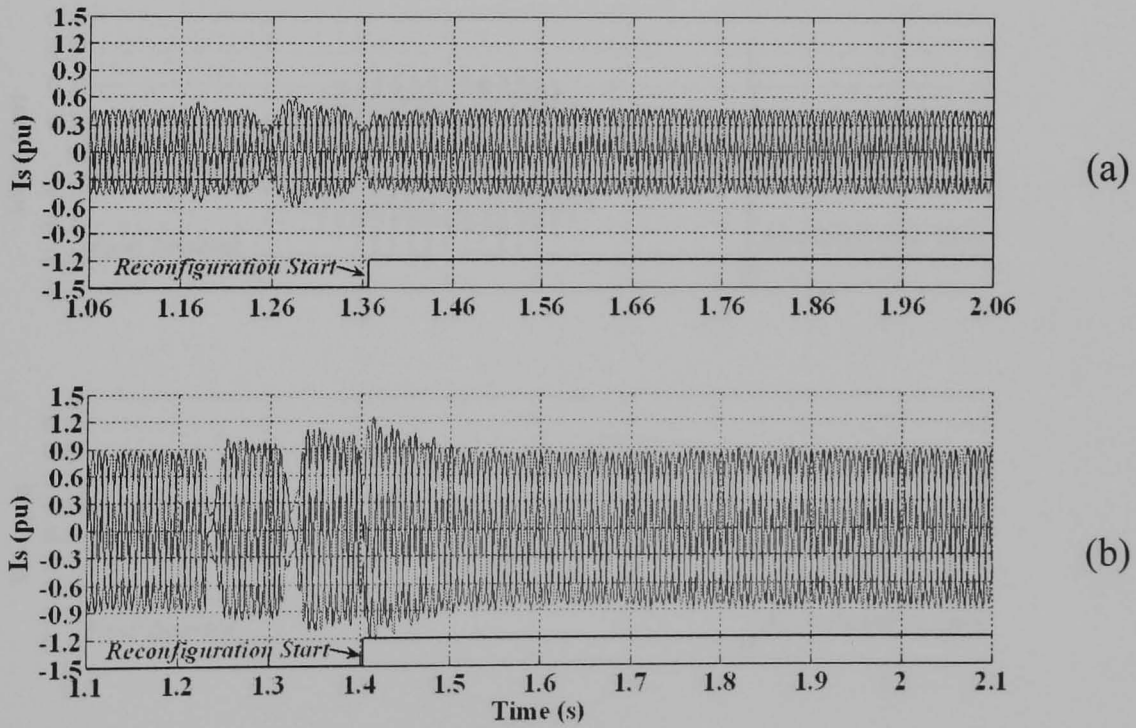
Figure 7.24 Simulation results showing stator current waveforms during reconfiguration of the machine-side converter at (a) 0.8 pu sub-synchronous speed generation and (b) 1.2 pu super-synchronous speed generation
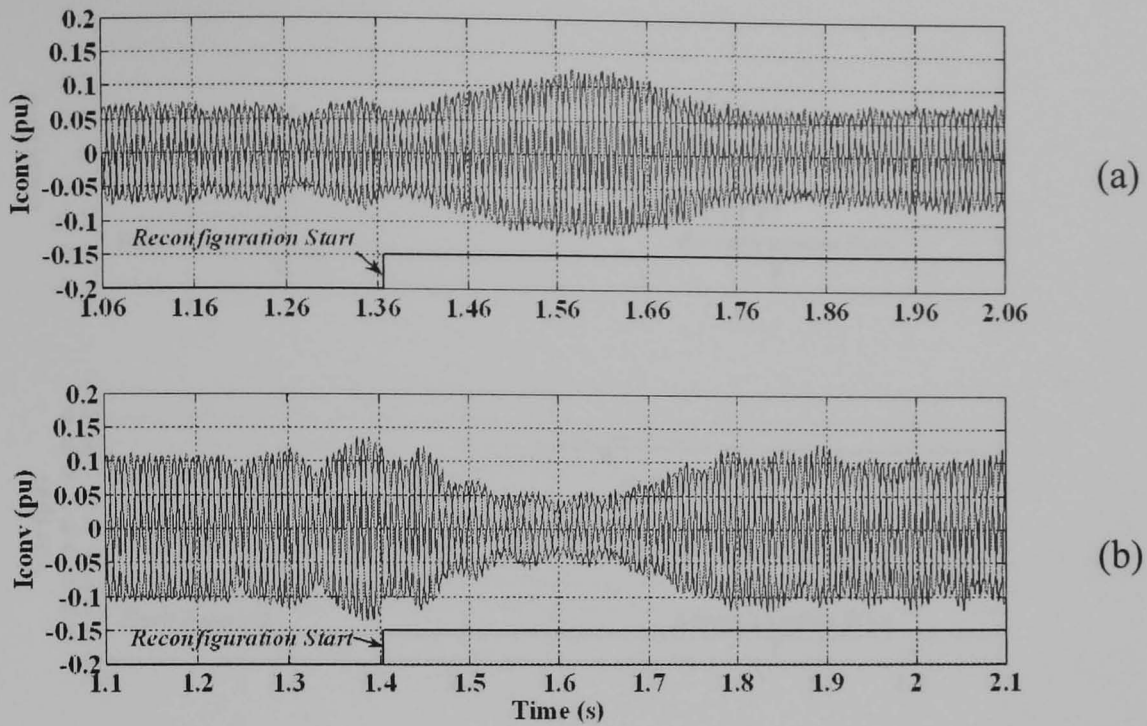
Figure 7.25 Simulation results showing grid-side converter current waveforms during reconfiguration of the machine-side converter at (a) 0.8 pu sub-synchronous speed generation and (b) 1.2 pu super-synchronous speed generation

- *Grid-Side Converter*
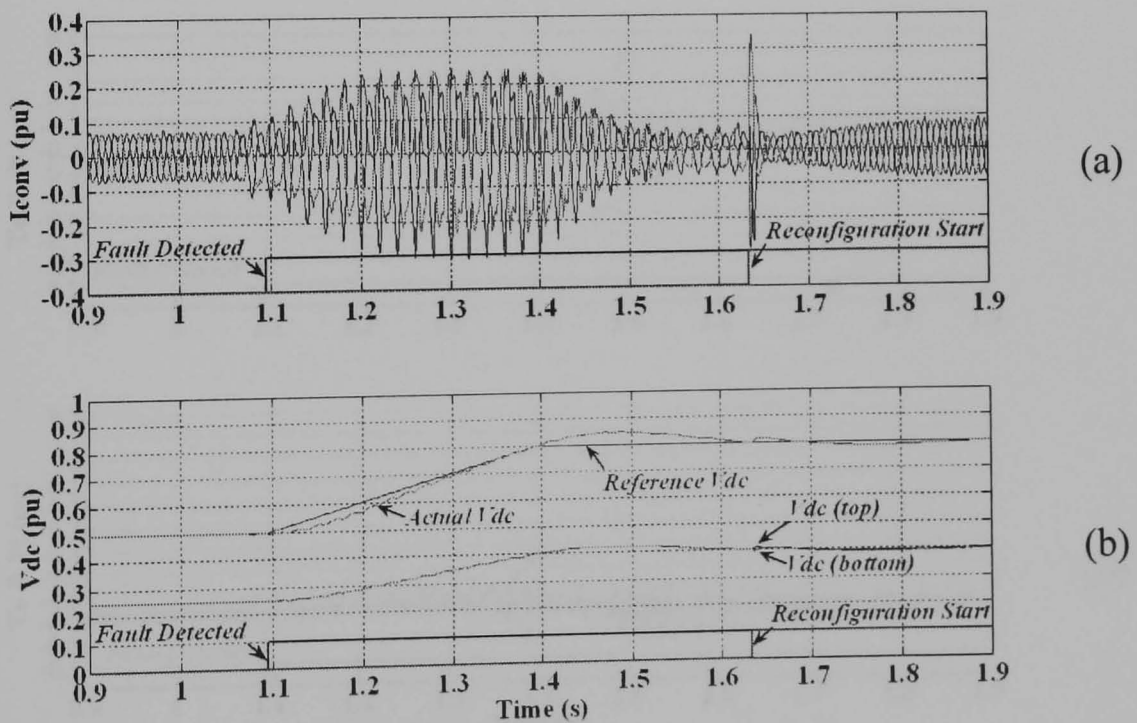
Figure 7.26 Simulation results showing (a) grid-side converter current waveforms and (b) dc-link voltage and individual capacitor voltage waveforms during reconfiguration of the grid-side converter under rectifier mode operation
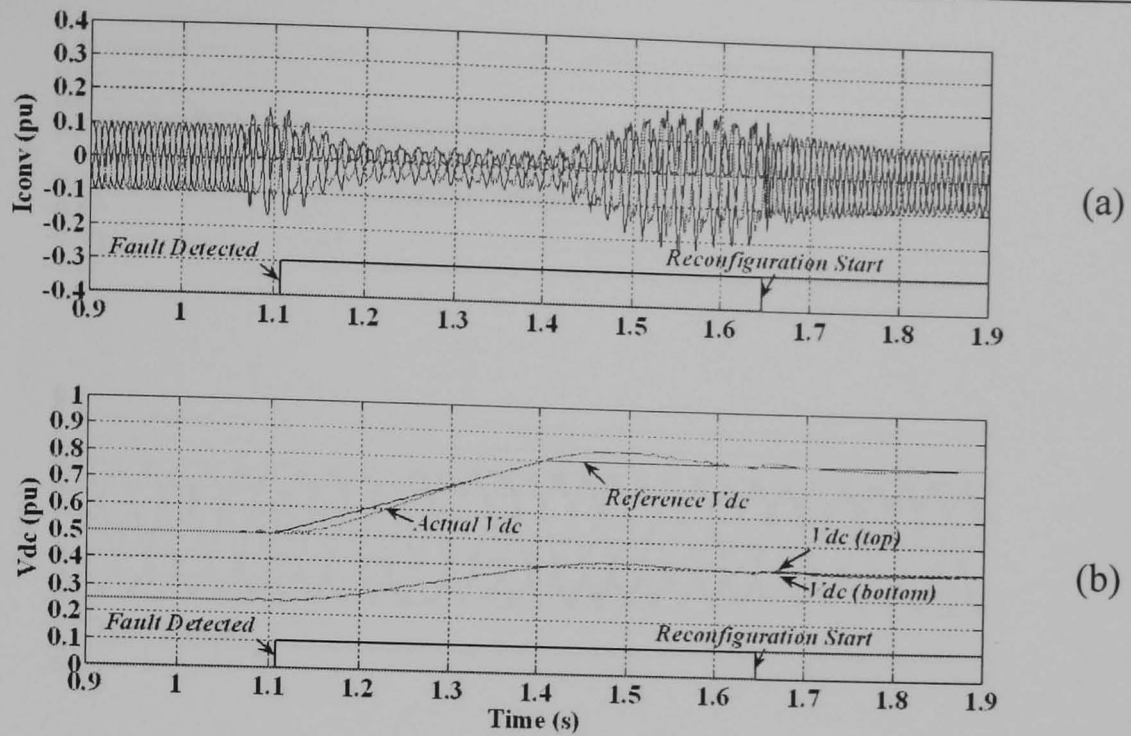
Figure 7.27 Simulation results showing (a) grid-side converter current waveforms and (b) dc-link voltage and individual capacitor voltage waveforms during reconfiguration of the grid-side converter under inverter mode operation
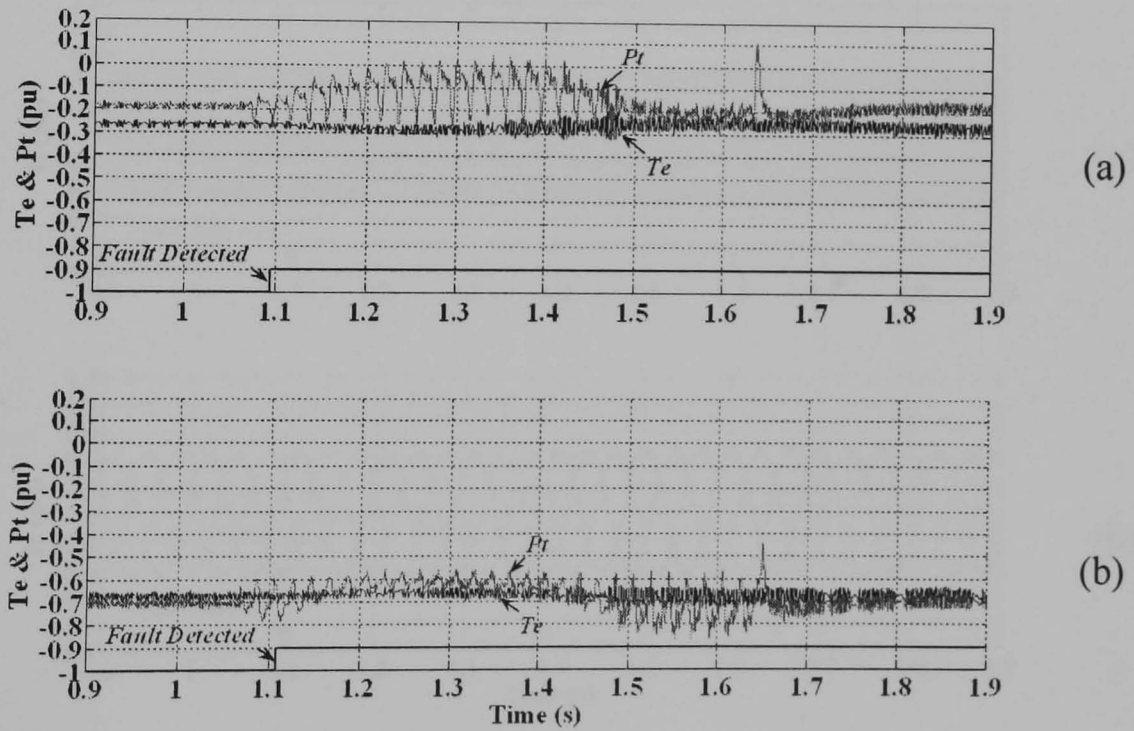
Figure 7.28 Simulation results showing the electromagnetic torque and total active power during reconfiguration of the grid-side converter under (a) rectifier mode operation and (b) inverter mode operation
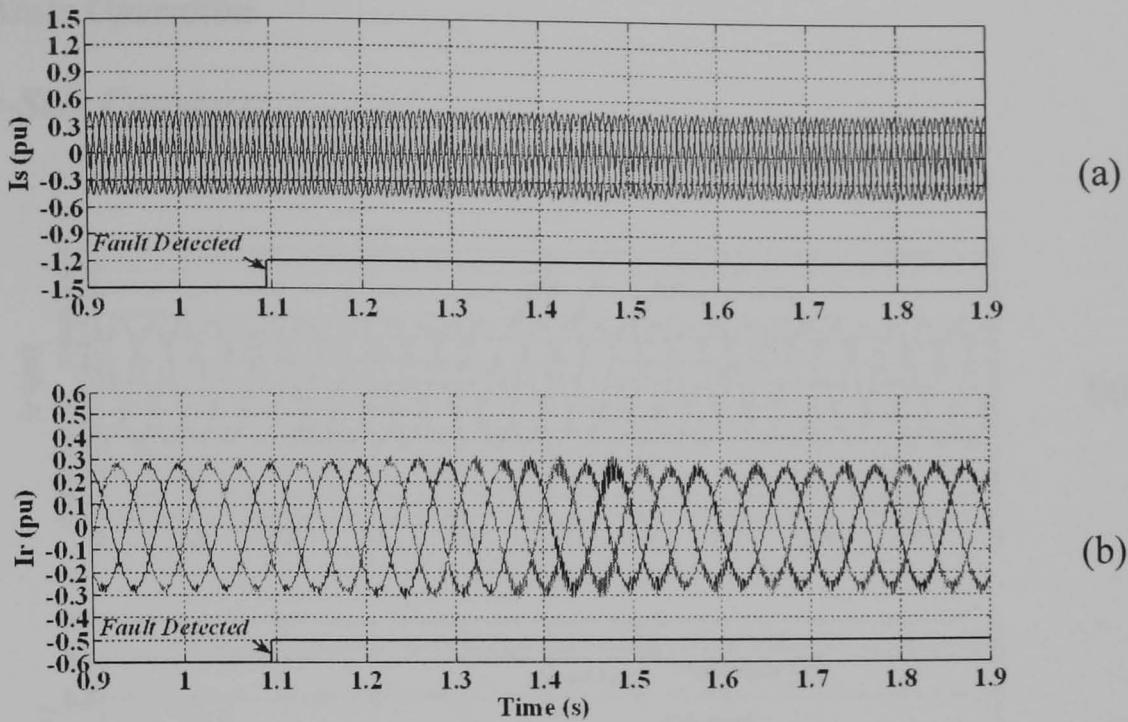
Figure 7.29 Simulation results showing (a) stator current waveforms and (b) rotor current waveforms during reconfiguration of the grid-side converter under rectifier mode operation
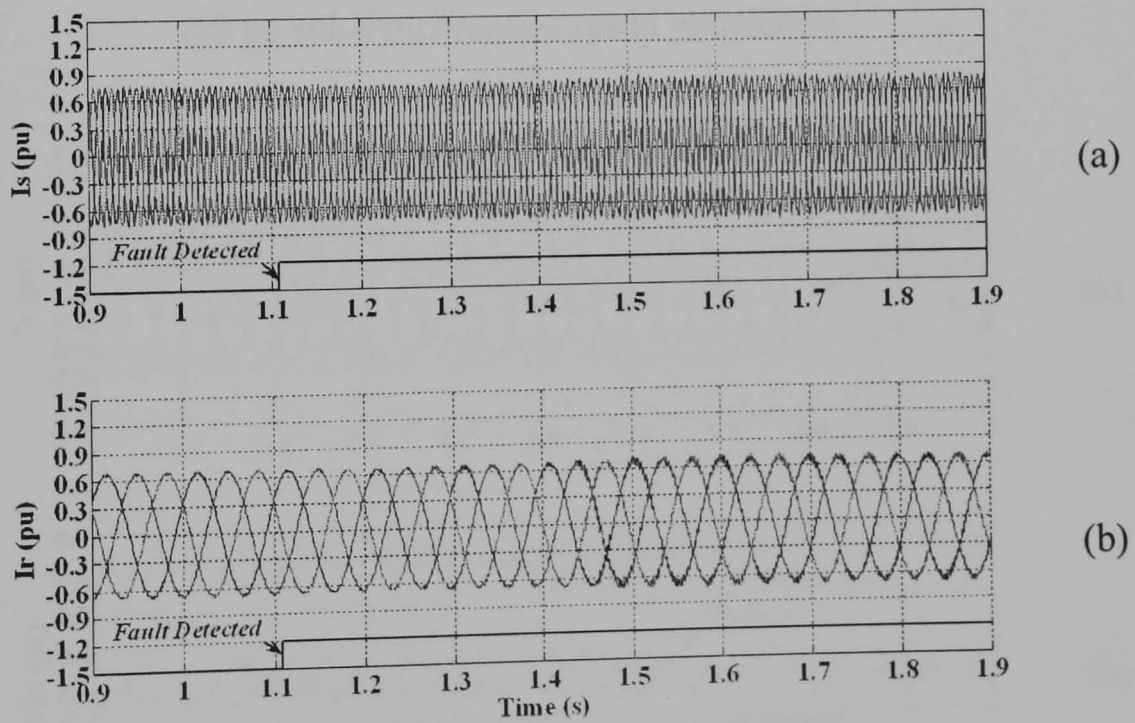
Figure 7.30 Simulation results showing (a) stator current waveforms and (b) rotor current waveforms during reconfiguration of the grid-side converter under inverter mode operation

ii. Steady-State Operation

- ● *Machine-Side Converter*
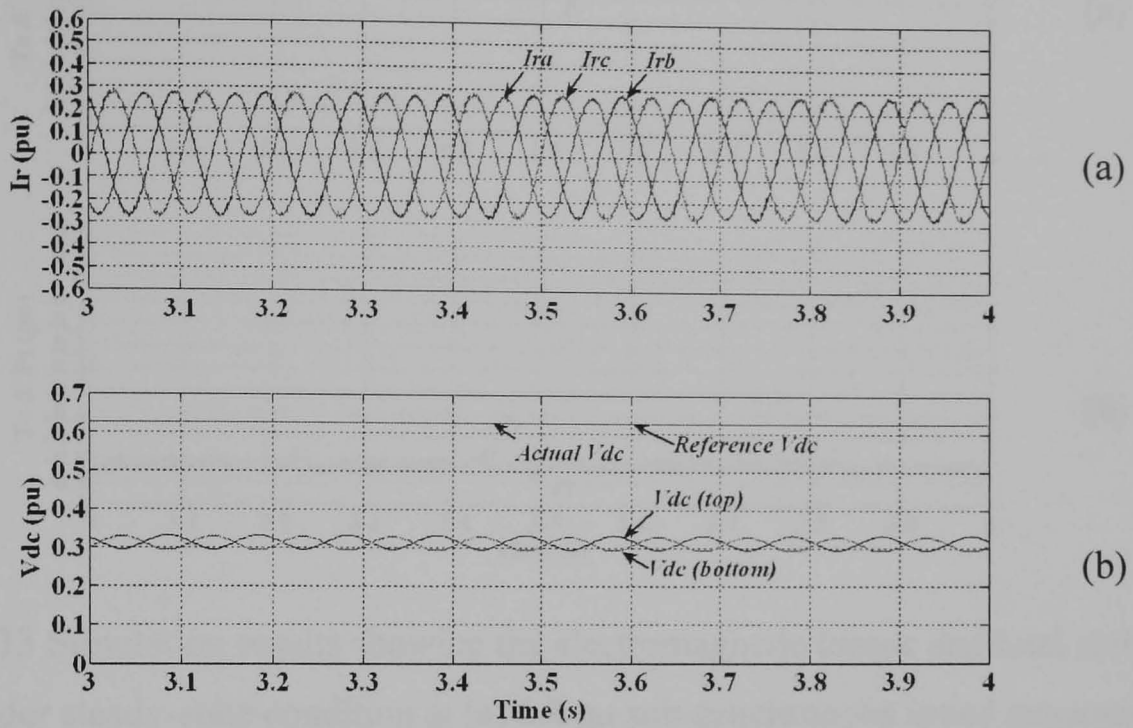
Figure 7.31 Simulation results showing (a) rotor current waveforms and (b) dc-link voltage and individual capacitor voltage waveforms under steady-state condition at 0.8 pu sub-synchronous speed generation
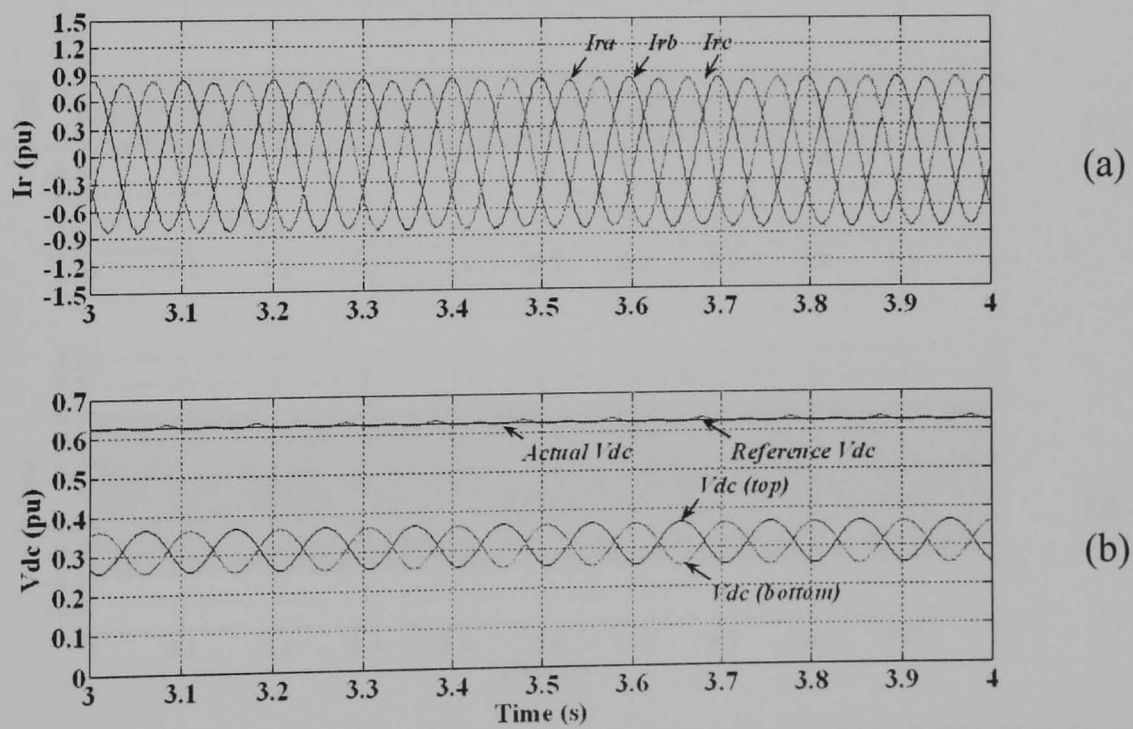
Figure 7.32 Simulation results showing (a) rotor current waveforms and (b) dc-link voltage and individual capacitor voltage waveforms under steady-state condition at 1.2 pu super-synchronous speed generation
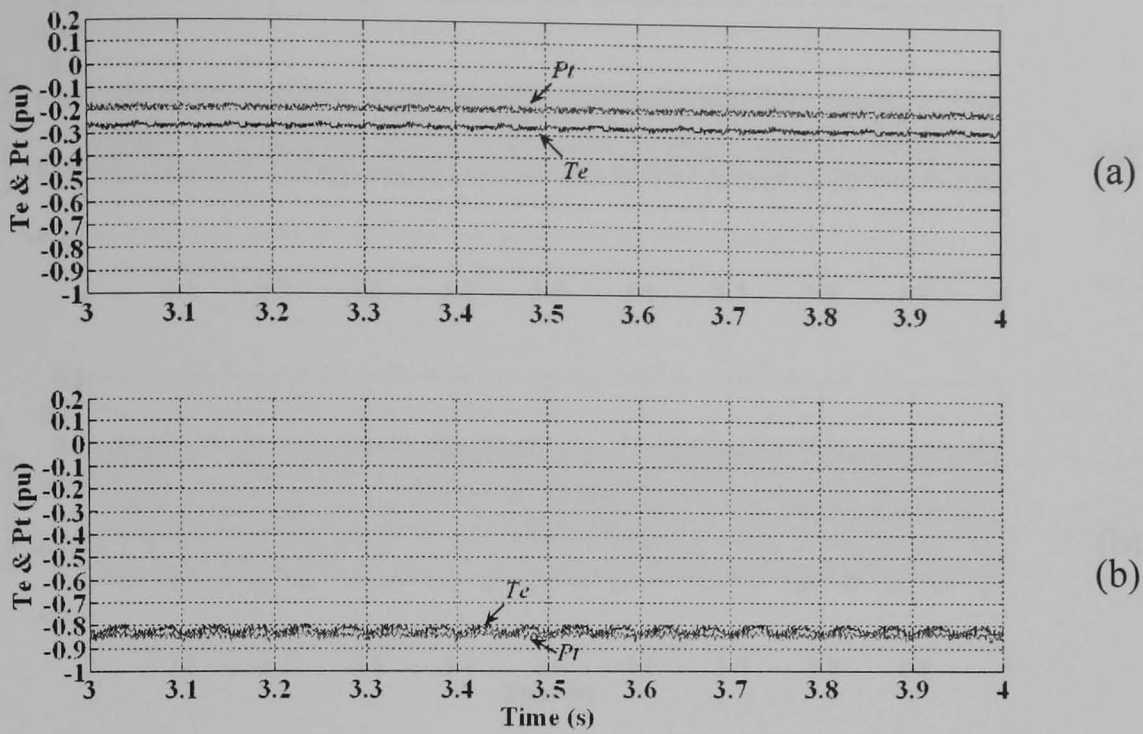
Figure 7.33 Simulation results showing the electromagnetic torque and total active power under steady-state condition at (a) 0.8 pu sub-synchronous speed generation and (b) 1.2 pu super-synchronous speed generation
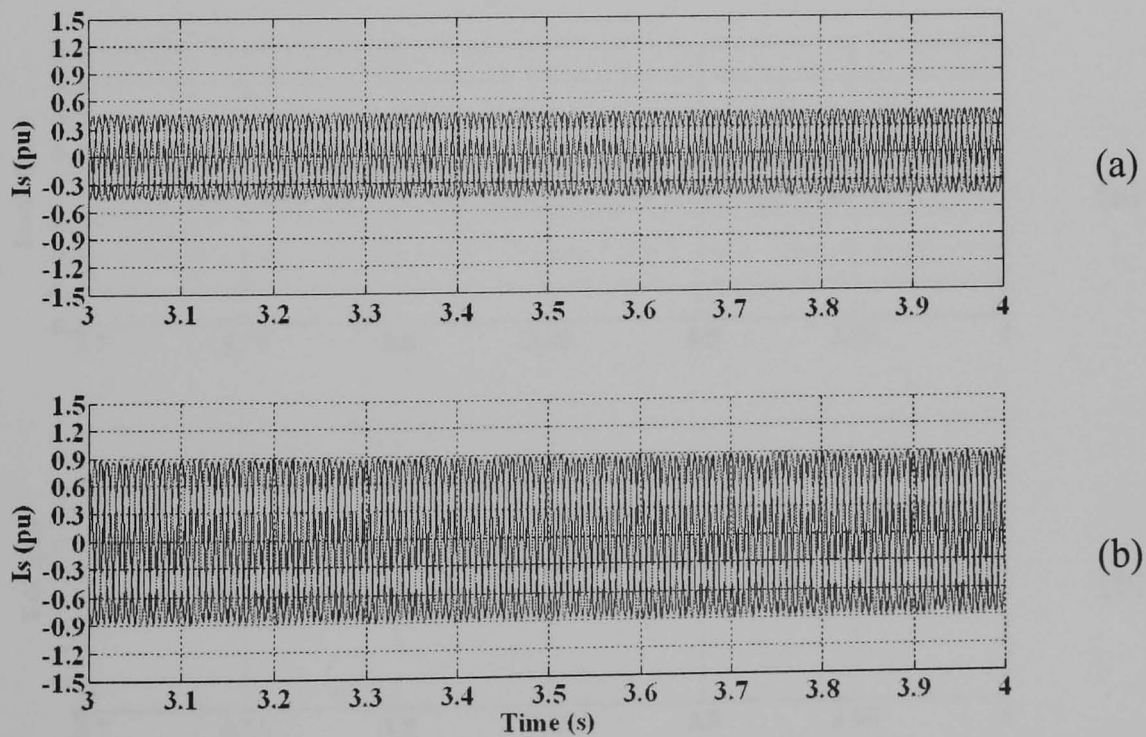
Figure 7.34 Simulation results showing stator current waveforms under steady-state condition at (a) 0.8 pu sub-synchronous speed generation and (b) 1.2 pu super-synchronous speed generation

220
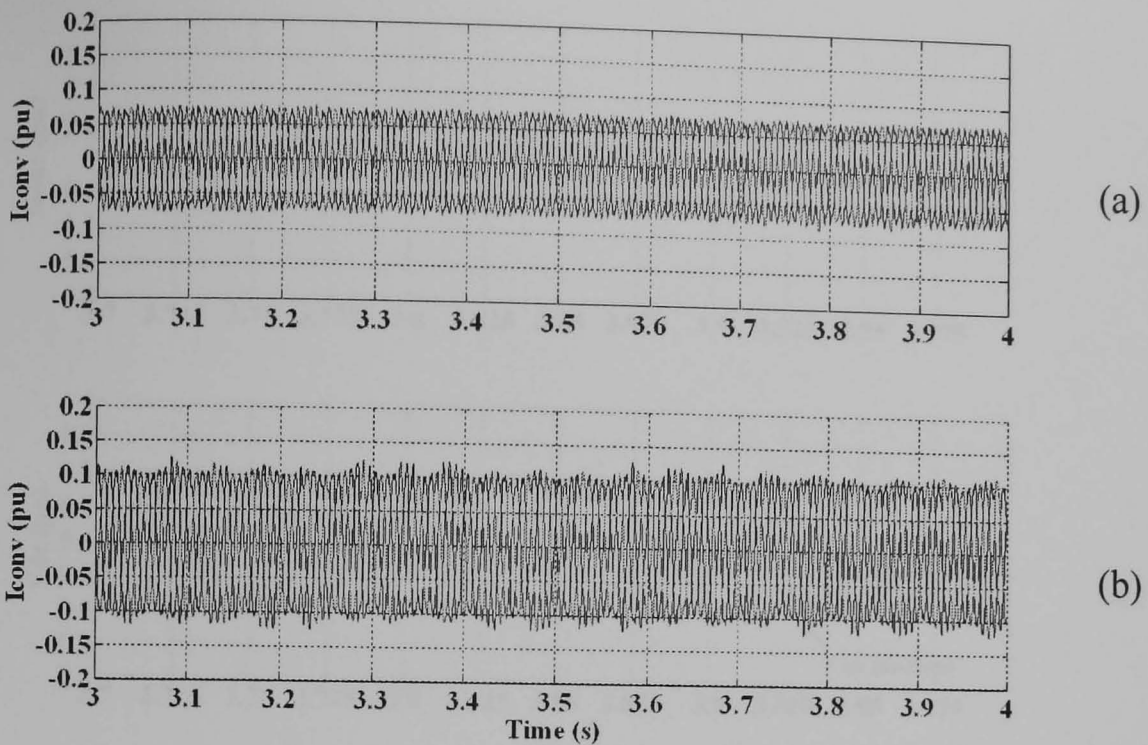
Figure 7.35 Simulation results showing grid-side converter current waveforms under steady-state condition at (a) 0.8 pu sub-synchronous speed generation and (b) 1.2 pu super-synchronous speed generation

● **Grid-Side Converter**
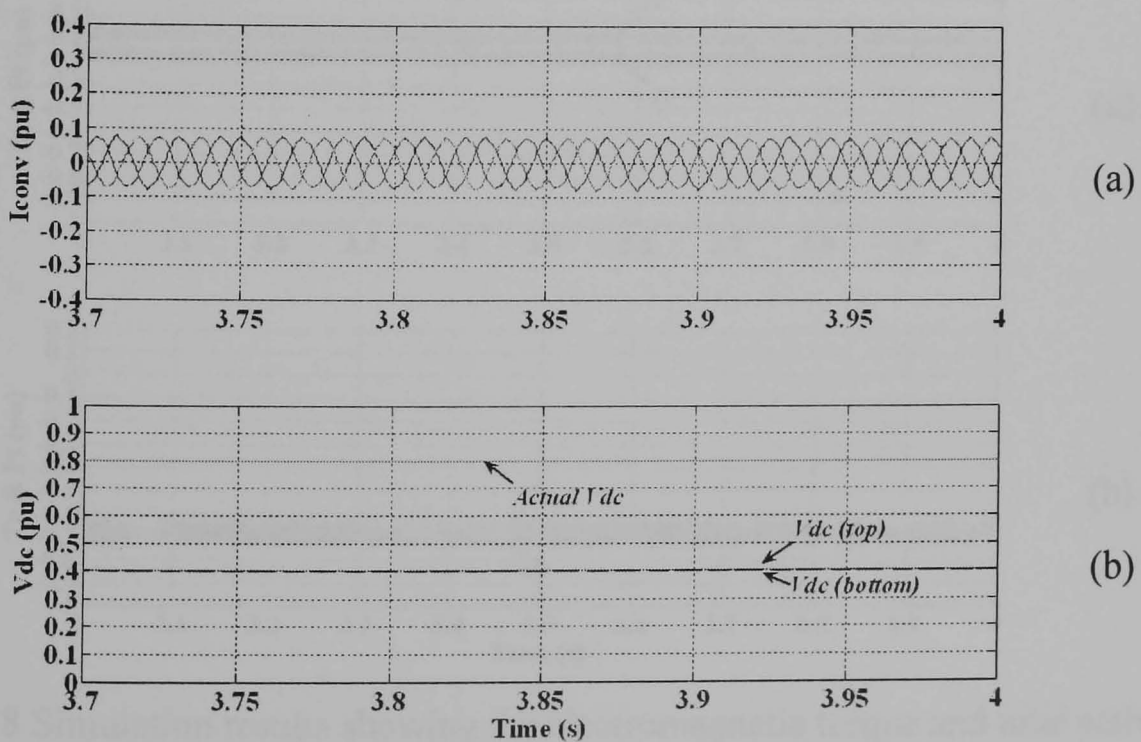
Figure 7.36 Simulation results showing (a) grid-side converter current waveforms and (b) dc-link voltage and individual capacitor voltage waveforms under steady-state rectifier mode operation
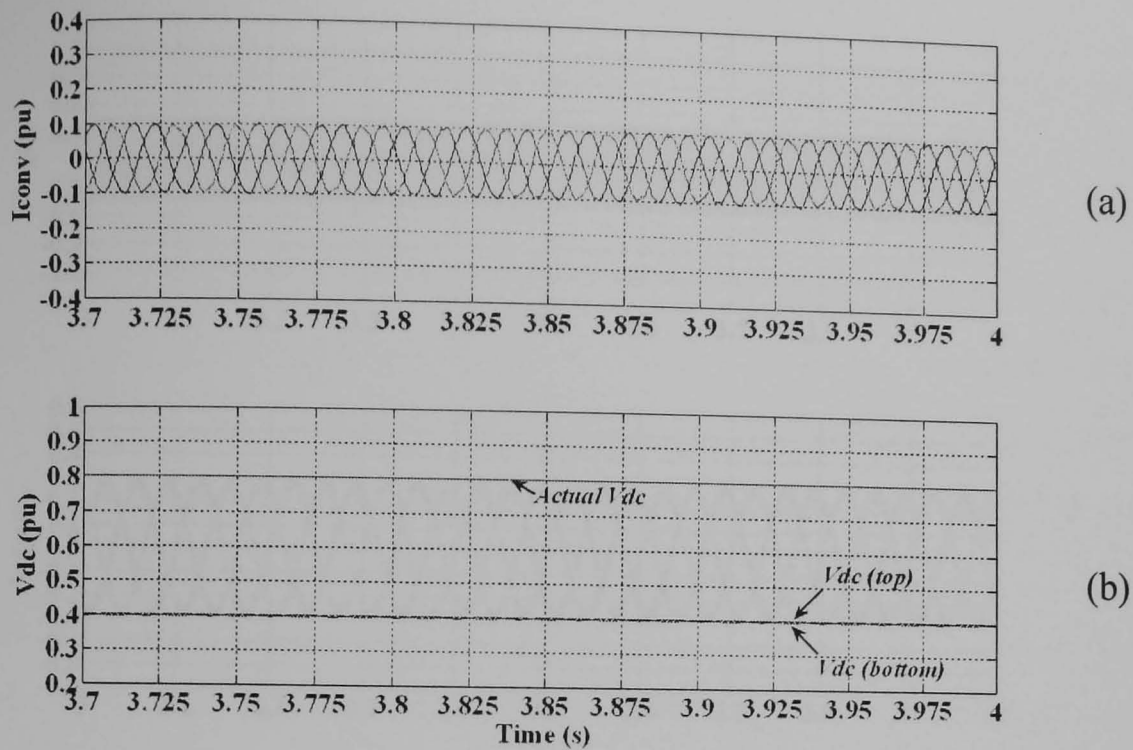
Figure 7.37 Simulation results showing (a) grid-side converter current waveforms and (b) dc-link voltage and individual capacitor voltage waveforms under steady-state inverter mode operation
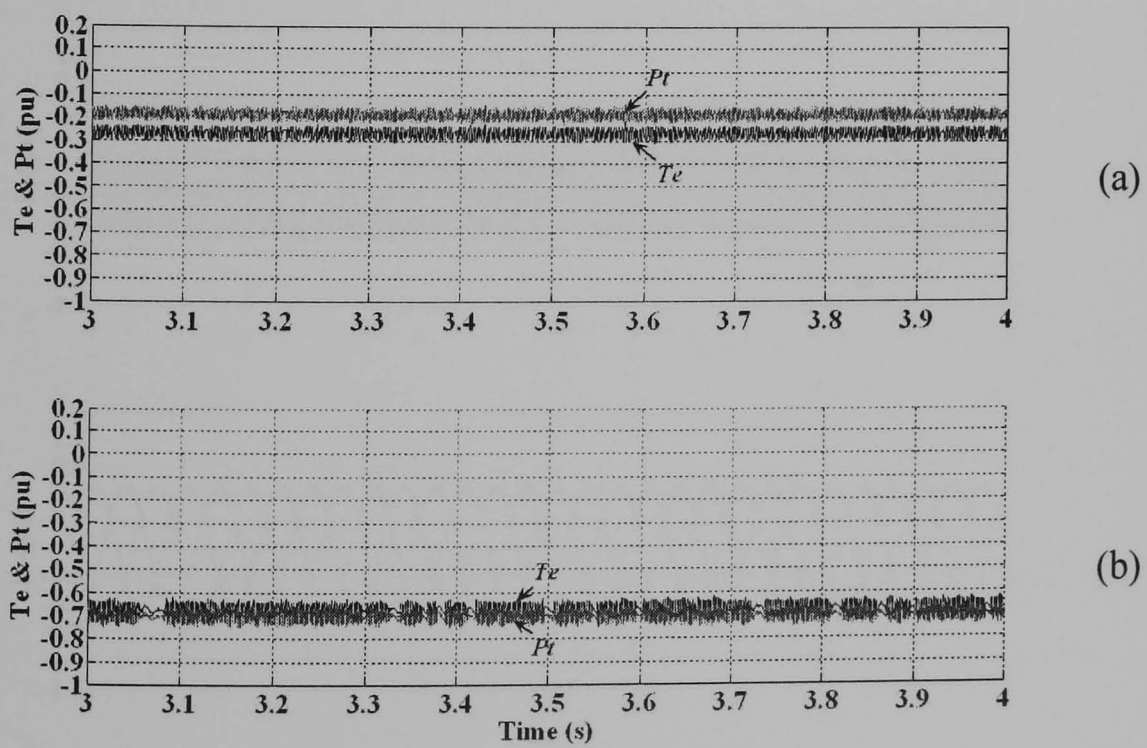
Figure 7.38 Simulation results showing the electromagnetic torque and total active power under steady-state (a) rectifier mode operation and (b) inverter mode operation of the grid-side converter
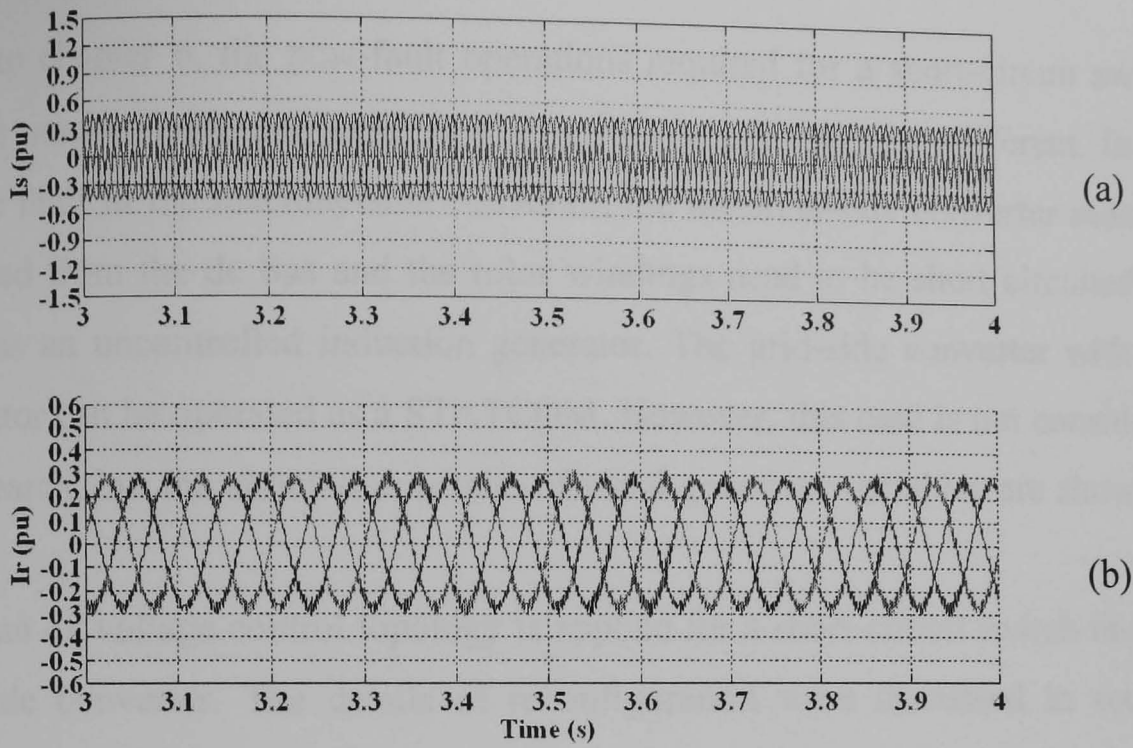
Figure 7.39 Simulation results showing (a) stator current waveforms and (b) rotor current waveforms under steady-state rectifier mode operation of the grid-side converter
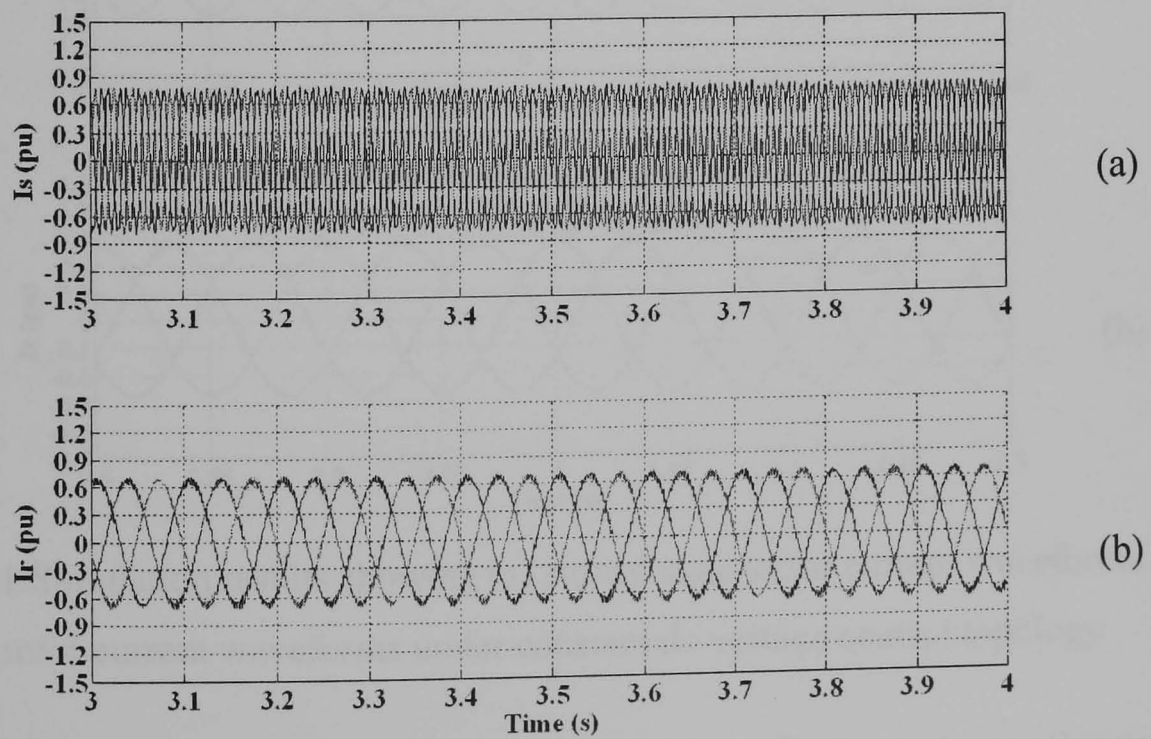
Figure 7.40 Simulation results showing (a) stator current waveforms and (b) rotor current waveforms under steady-state inverter mode operation of the grid-side converter

7.4.2 Short-Circuit Switch Faults

Referring to chapter 6, the post-fault operations required for a short-circuit switch fault in the machine-side converter and the grid-side converter are different. In the case of the fault in the machine-side converter, the machine-side converter must be disconnected from the dc bus and the rotor windings need to be short circuited for operation as an uncontrolled induction generator. The grid-side converter with dc-link capacitor can be operated as a STATCOM. However, this case is not considered in this research, but the simulation results of some generator variables are shown in chapter 6.

The constant dc voltage control topology is applied for a short-circuit switch fault in the grid-side converter. The details of reconfiguration were discussed in section 7.2.2. The simulation results in figure 7.41 are the stator and rotor current waveforms under steady-state operation.
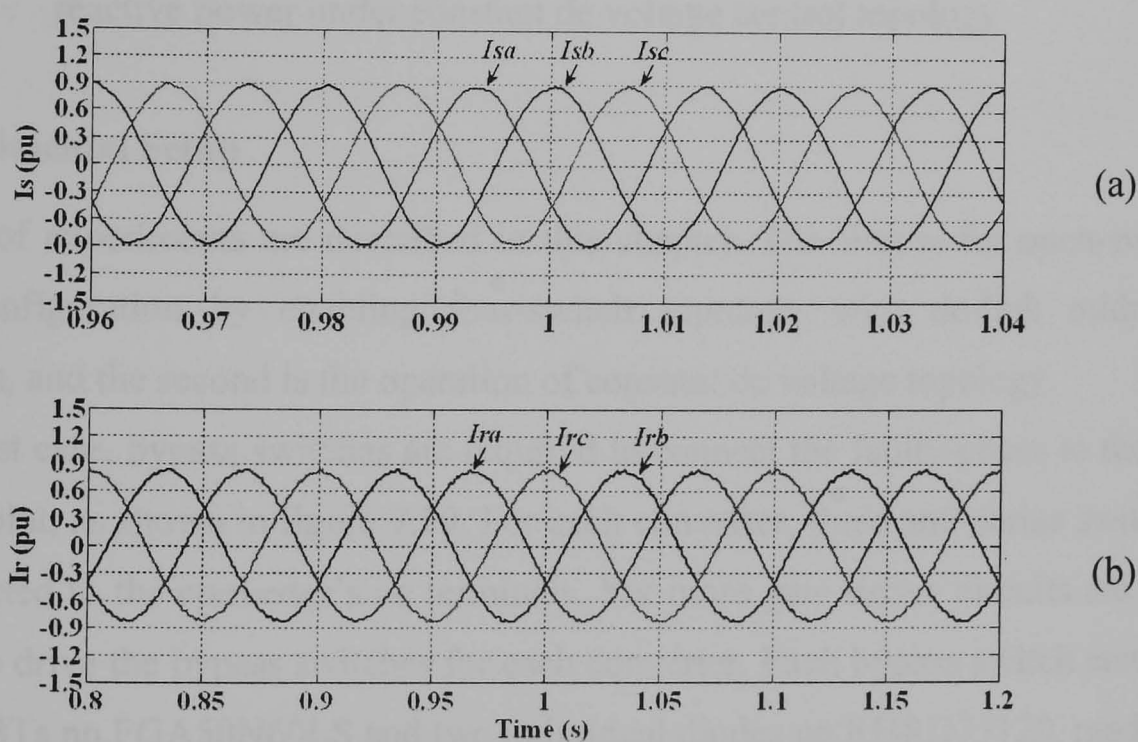
Figure 7.41 Simulation results showing (a) steady-state stator current waveforms and (b) rotor current waveforms under constant dc voltage control topology

Figure 7.42 shows the operation of this topology under step change in reactive power command. These results show that this topology is capable of operating under unity power factor at the stator.
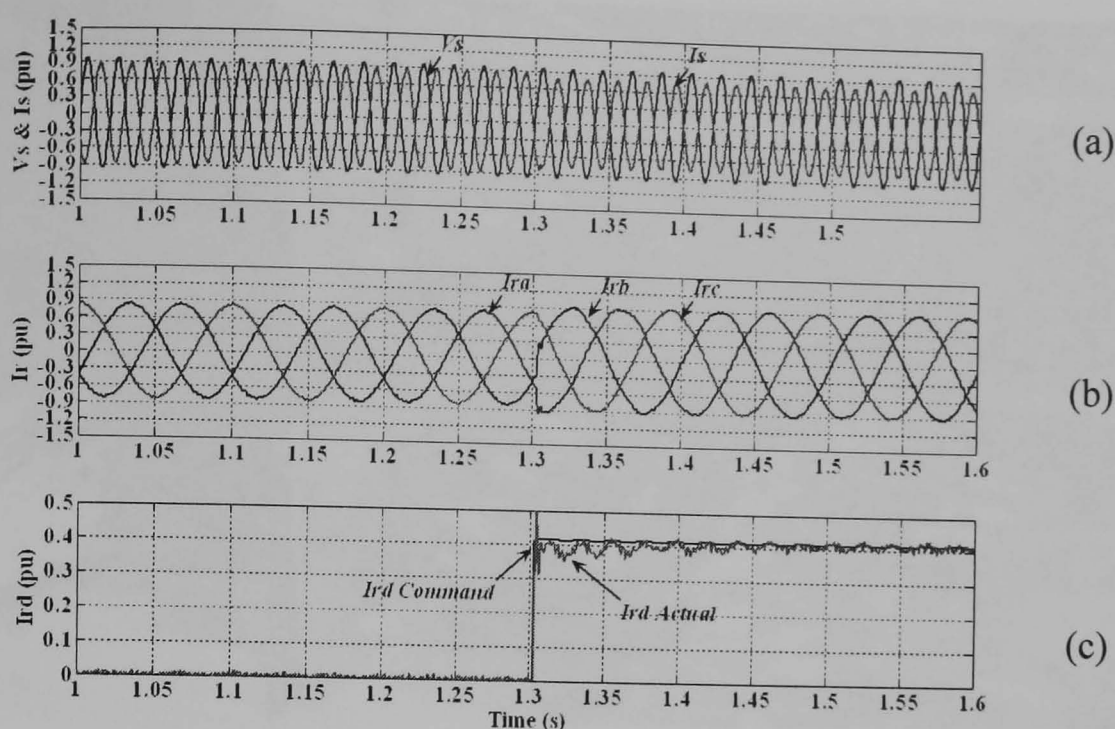
Figure 7.42 Simulation results showing (a) stator voltage and current, (b) rotor currents and (c) command and actual d-axis rotor currents for a step change in stator reactive power under constant dc voltage control topology

7.5 Experimental Setup

Two sets of experiments are described in this chapter. The first is for open-switch fault reconfiguration by enabling four-switch topology with dc-link midpoint connection, and the second is the operation of constant dc voltage topology.

For the first case, bypass switches are required to connect the faulty-phase to the dc-link midpoint, as shown in figure 7.19. For each converter, three anti-series switches are connected to the converter's ac terminals. Six more gate driver circuits are also required to drive the bypass switches for each converter. Each bypass switch consists of two IGBTs no.FGA50N60LS and two individual diodes no.RHRD75120, made by Fairchild Semiconductor [7.43] connected in an anti-series configuration as shown figure 7.18. The photograph of the bypass circuits and gate driver circuits are shown in figure 7.43.
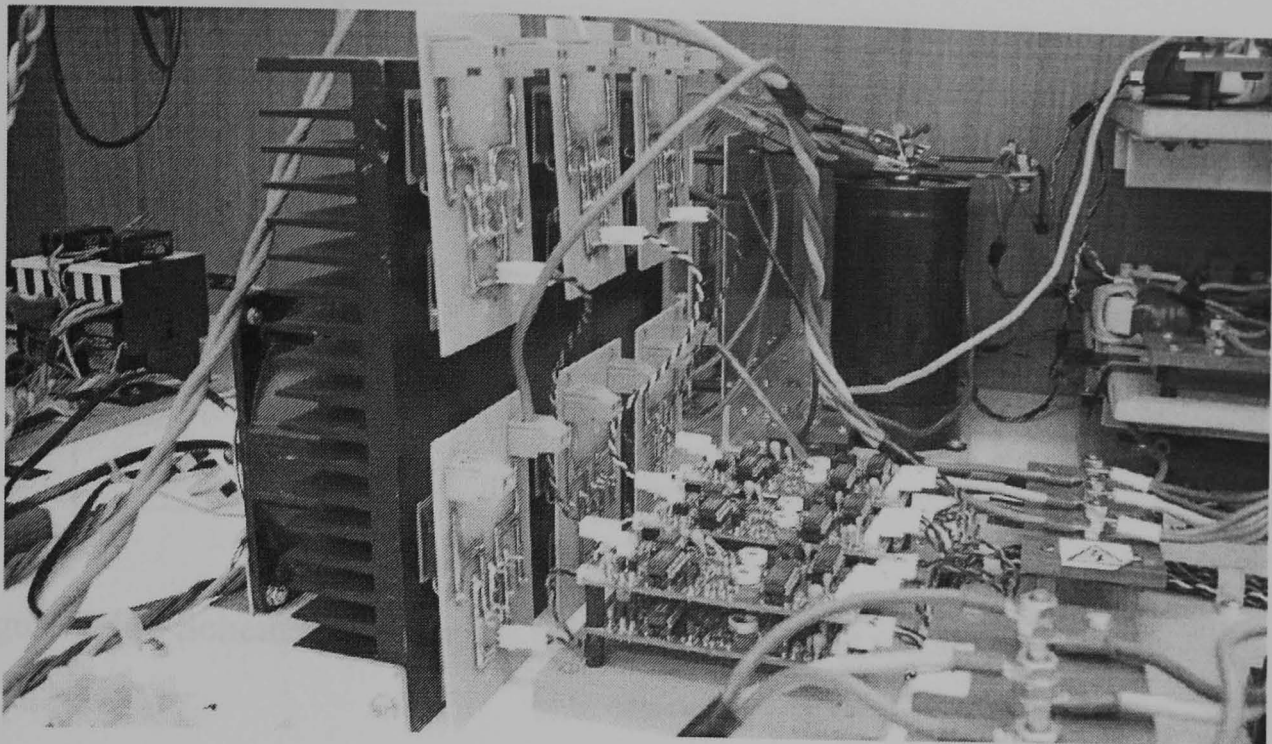
Figure 7.43 Gate driver circuits and the anti-series switches

The schematic diagrams of the full system with bypass switches are shown in figures 7.44a and 7.44b respectively.

Regarding the software, the code written in the DSP for the first experiment was added to the existing code for open-switch fault detection by the Absolute Normalised DC Current Method. As presented in the flowchart shown in figure 7.20, the code for system reconfiguration receives the output signals from fault detection module to reconfigure the system.
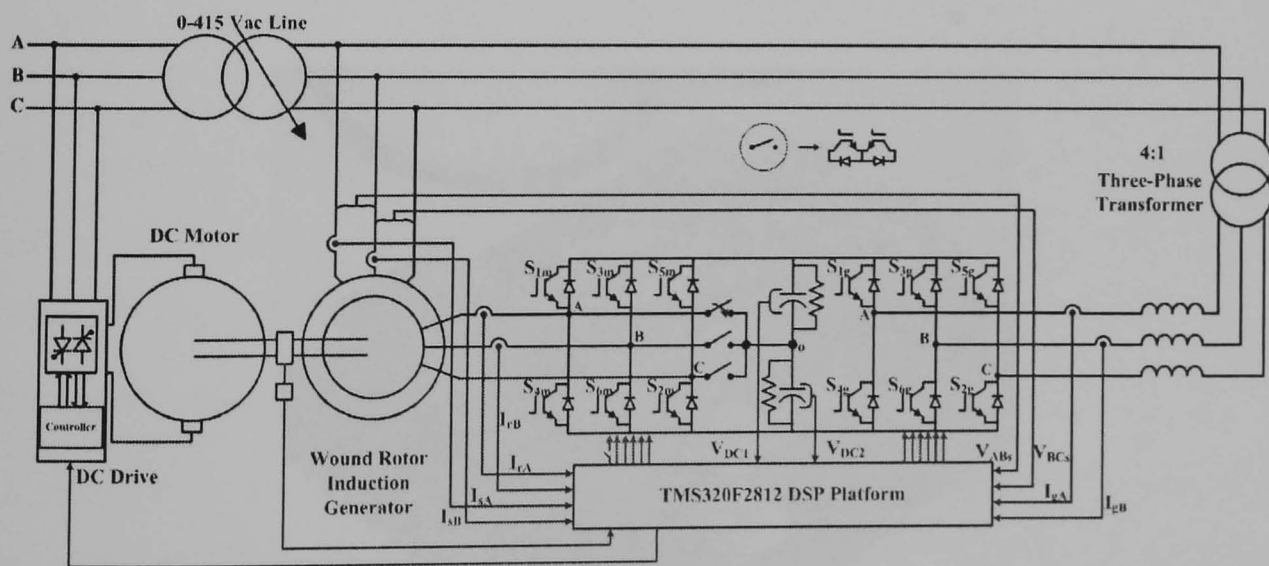
(a)

Figure 7.44a Schematic of circuits for open-switch fault reconfiguration for the machine-side converter

(b)
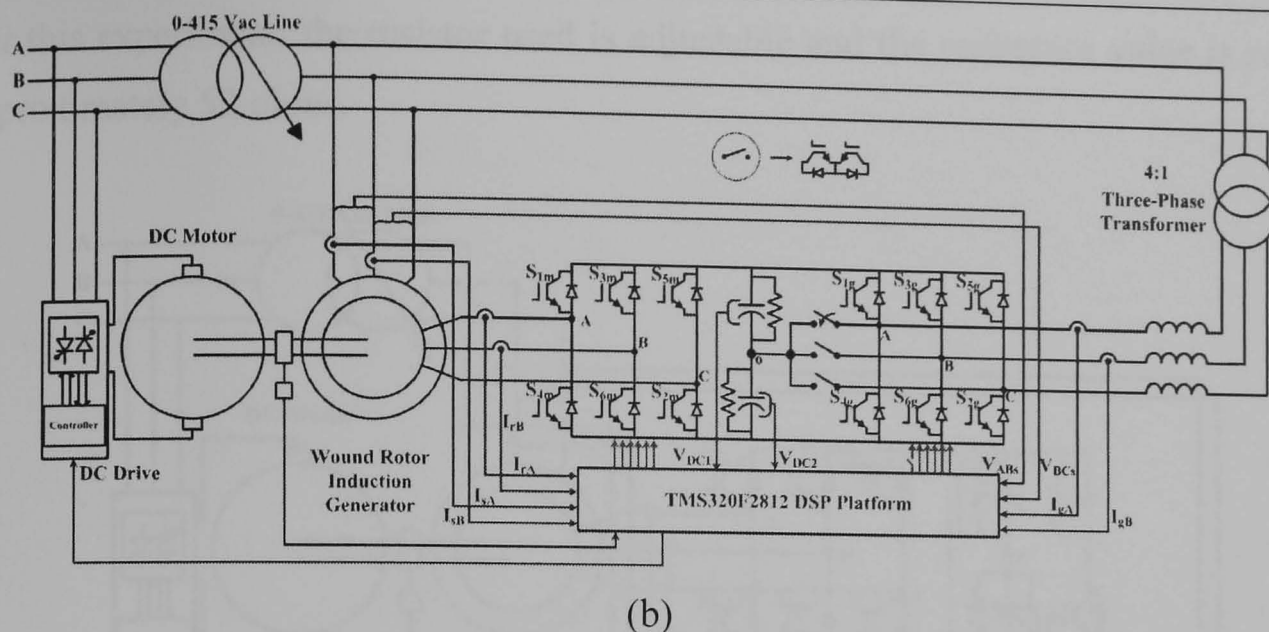
Figure 7.44b Schematic of circuits for open-switch fault reconfiguration for the grid-side converter

In the case of system reconfiguration for the constant voltage control topology, the chopper switch is a 1200V, 150A single switch with chopper diode module, number BSM150GAL120DN2 made by Siemens [7.44]. This IGBT module and a gate driver circuit are shown in figure 7.45. For this experiment, the system starts with the reconfigured topology as shown in figure 7.46. This is on the assumption that after a short-circuit switch fault in the grid-side converter is detected, the whole system is shut down and is then reconfigured to the constant dc voltage control topology. This topology can also be an alternative for the case of an open-switch fault in the grid-side converter.
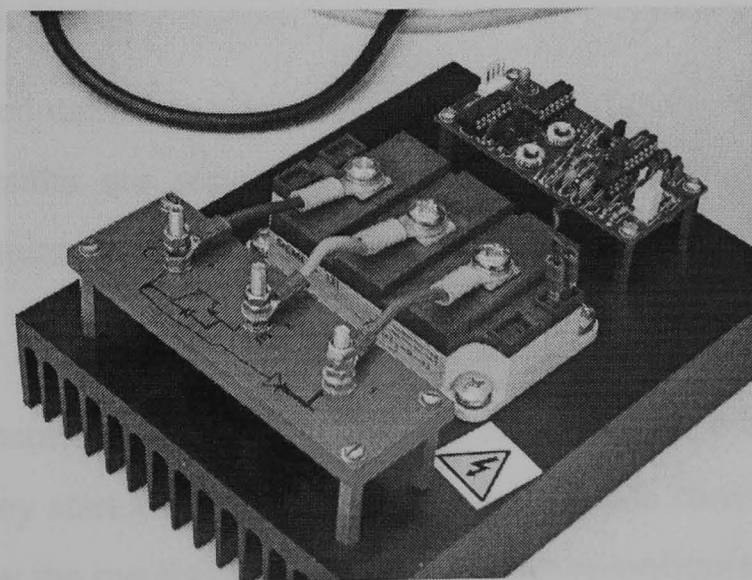
Figure 7.45 An IGBT-Diode module and a gate driver circuit used for constant dc voltage control topology

For this experiment, the resistor used is adjustable and the resistance value is set to approximately 52 ohms.
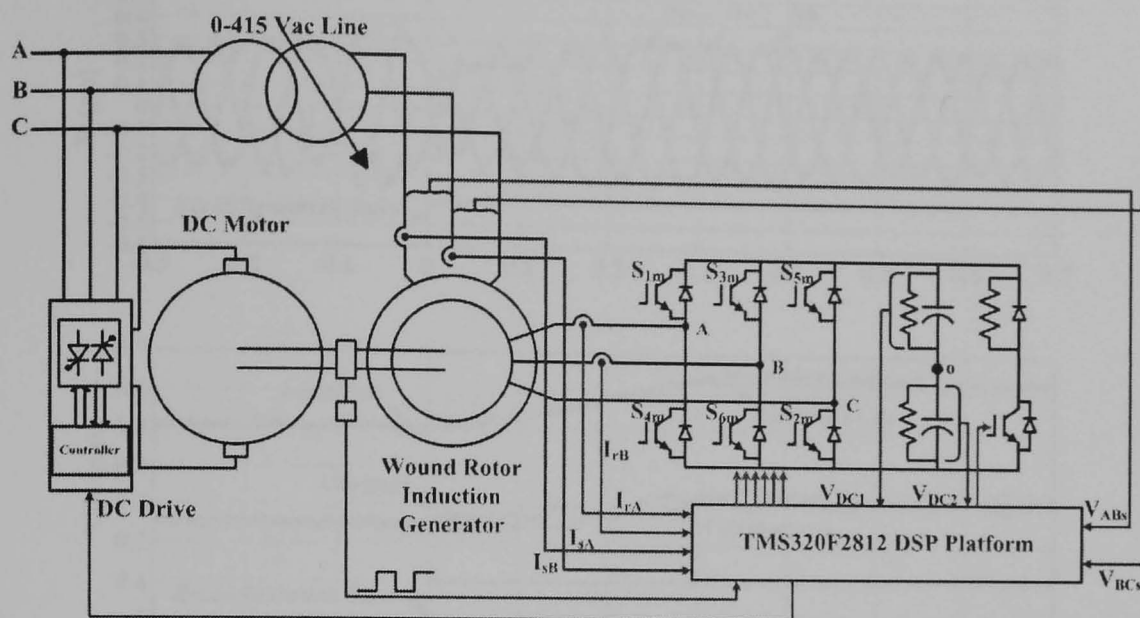
Figure 7.46 Schematic of circuits for short-circuit switch fault reconfiguration

7.6 Experimental Results

Experimental results are divided into two groups – reconfiguration by the four-switch topology with dc-link midpoint connection and operation of the constant dc voltage control topology. The former experimental results are first presented and can be divided into reconfiguration process and steady-state post-fault operation as in the simulation results. For the operation of the constant dc voltage control topology, the results show only the operation of the system under different conditions.

7.6.1 Open-Switch Faults

This subsection contains results of significant variables which affect system operation. The results are separated into the results during the reconfiguration process and the results under steady-state operation respectively.

i. Reconfiguration Process Operating State

The results are separated into the results of the machine-side converter and the grid-side converter. They start with the results of machine-side converter reconfiguration and are followed by the results of grid-side converter reconfiguration.

228

• *Machine-Side Converter*
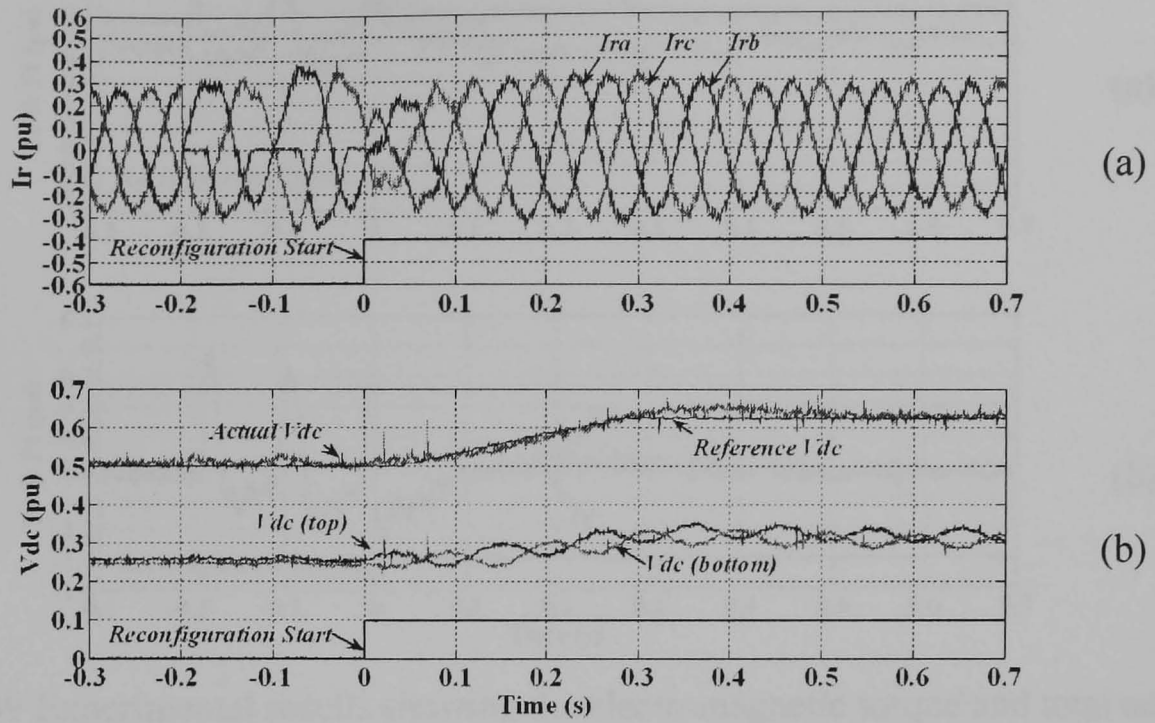
Figure 7.47 Experimental results showing (a) rotor current waveforms and (b) dc-link voltage and individual capacitor voltage waveforms during reconfiguration of the machine-side converter at 0.8 pu sub-synchronous speed generation
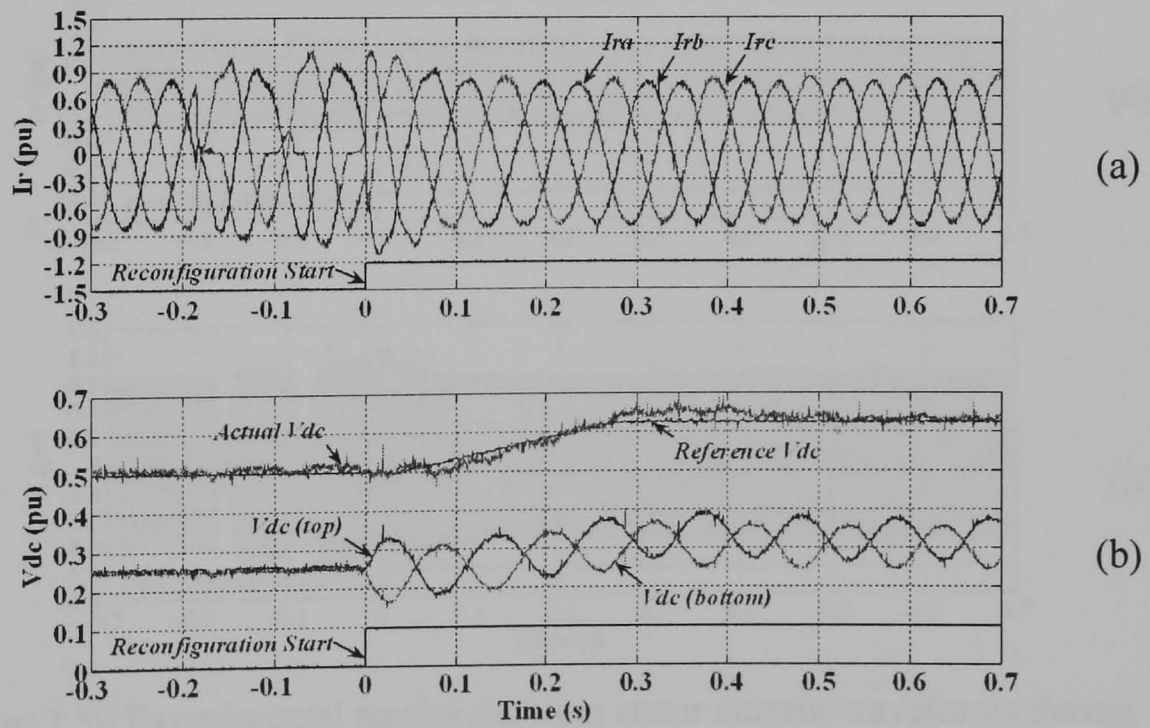
Figure 7.48 Experimental results showing (a) rotor current waveforms and (b) dc-link voltage and individual capacitor voltage waveforms during reconfiguration of the machine-side converter at 1.2 pu super-synchronous speed generation
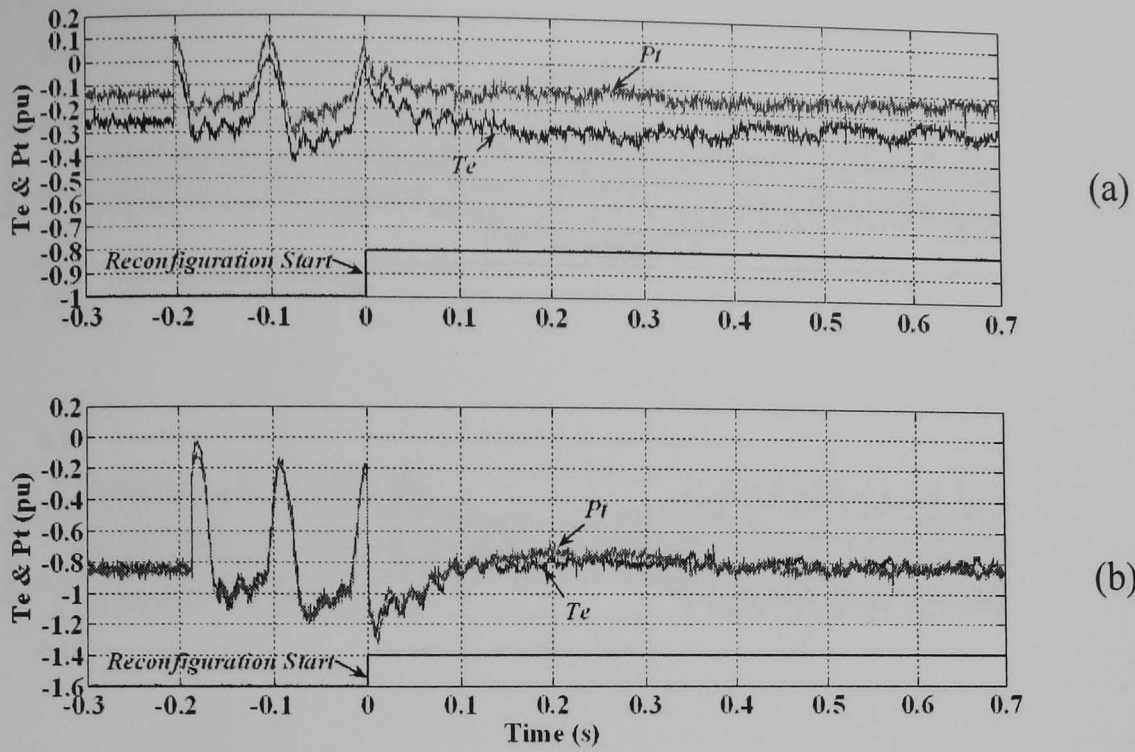
Figure 7.49 Experimental results showing the electromagnetic torque and total active power during reconfiguration of the machine-side converter at (a) 0.8 pu sub-synchronous speed generation and (b) 1.2 pu super-synchronous speed generation
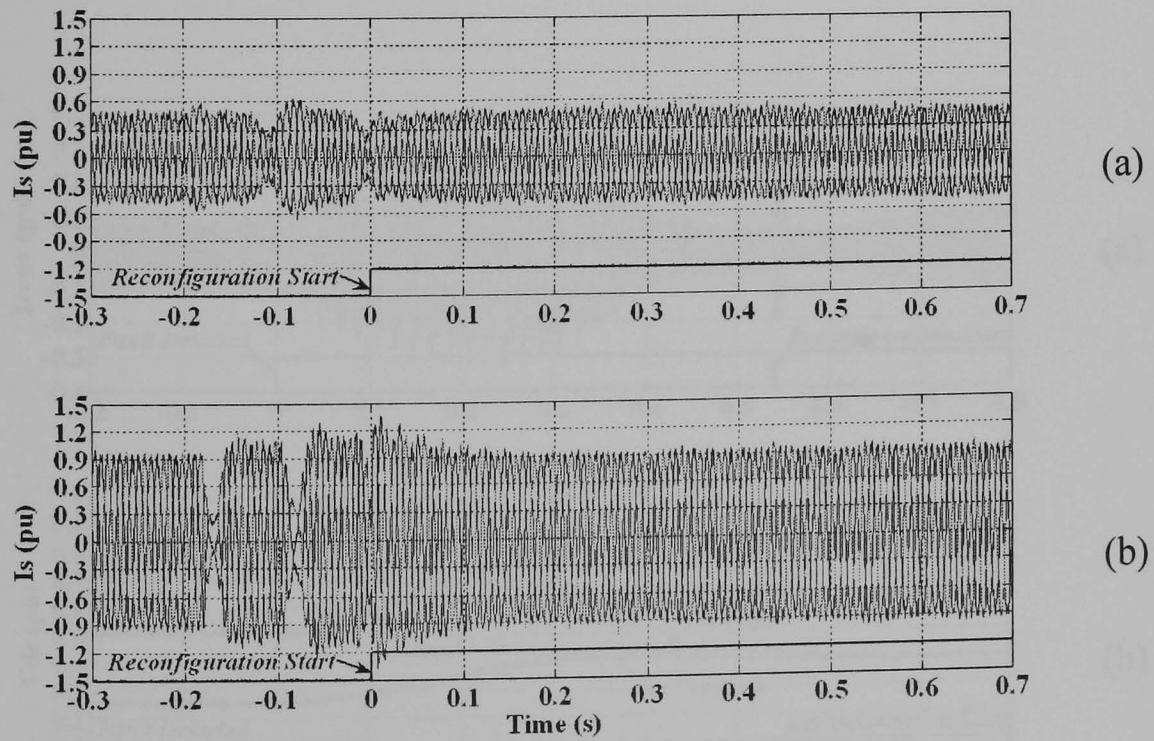
Figure 7.50 Experimental results showing stator current waveforms during reconfiguration of the machine-side converter at (a) 0.8 pu sub-synchronous speed generation and (b) 1.2 pu super-synchronous speed generation
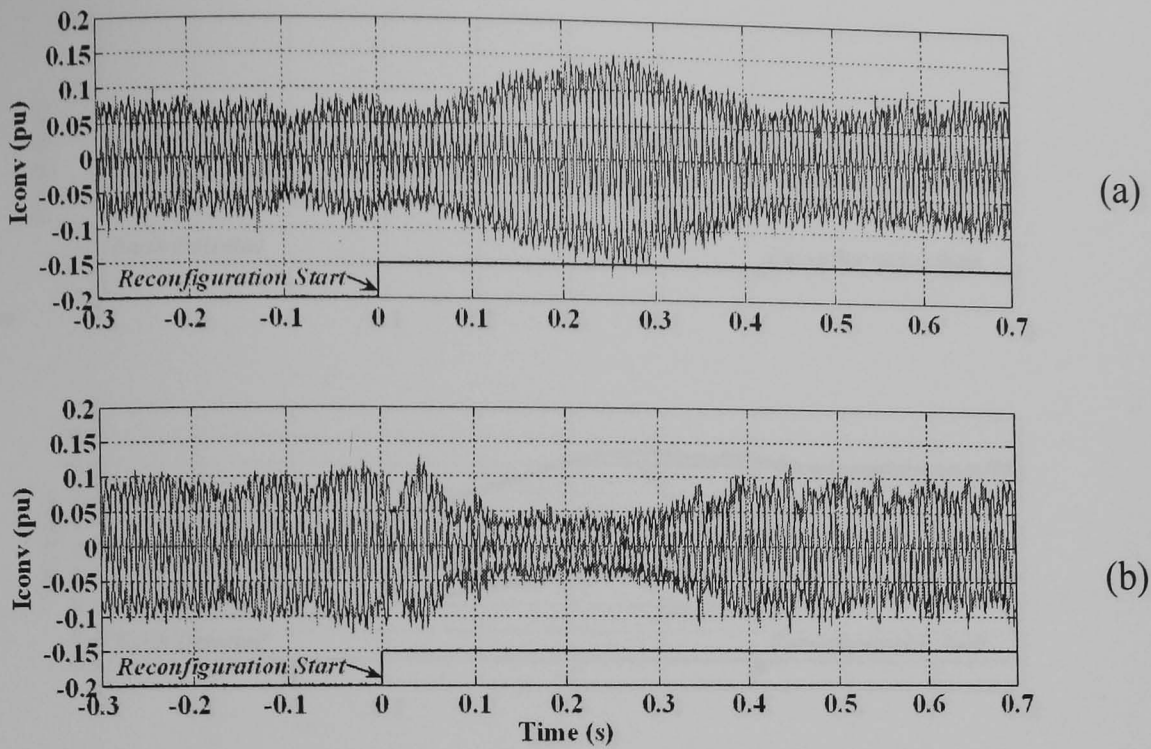
Figure 7.51 Experimental results showing grid-side converter current waveforms during reconfiguration of the machine-side converter at (a) 0.8 pu sub-synchronous speed generation and (b) 1.2 pu super-synchronous speed generation

- *Grid-Side Converter*
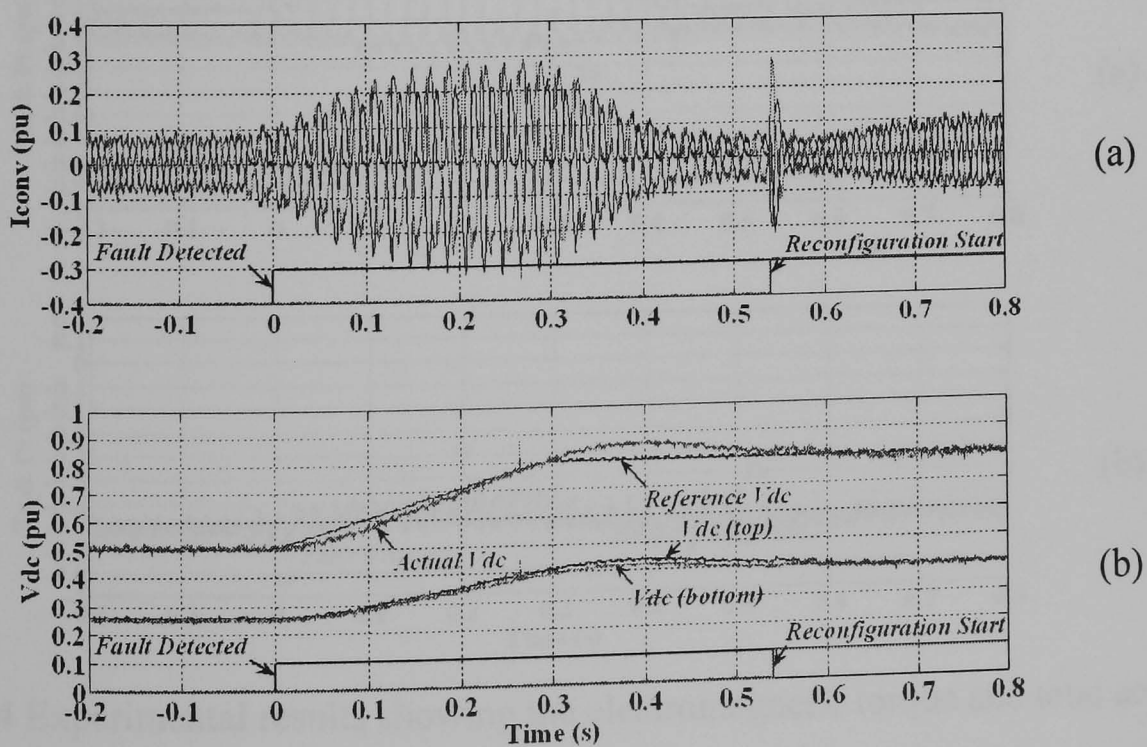
Figure 7.52 Experimental results showing (a) grid-side converter current waveforms and (b) dc-link voltage and individual capacitor voltage waveforms during reconfiguration of the grid-side converter under rectifier mode operation
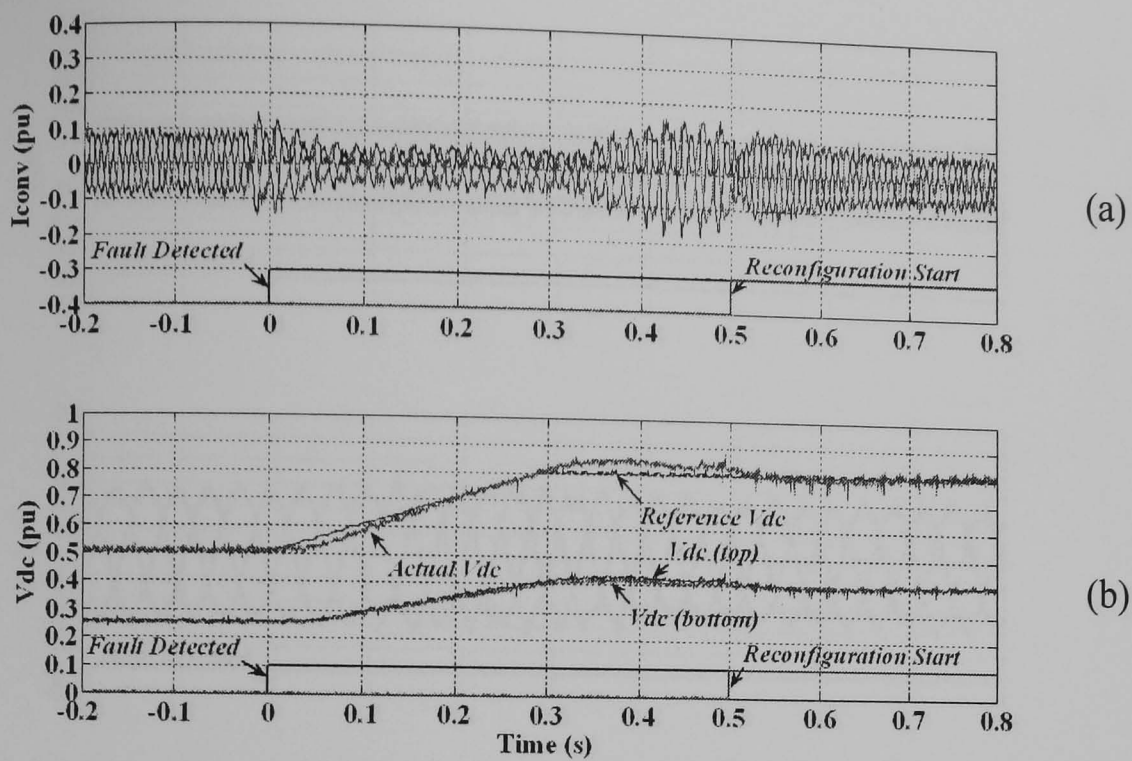
Figure 7.53 Experimental results showing (a) grid-side converter current waveforms and (b) dc-link voltage and individual capacitor voltage waveforms during reconfiguration of the grid-side converter under inverter mode operation
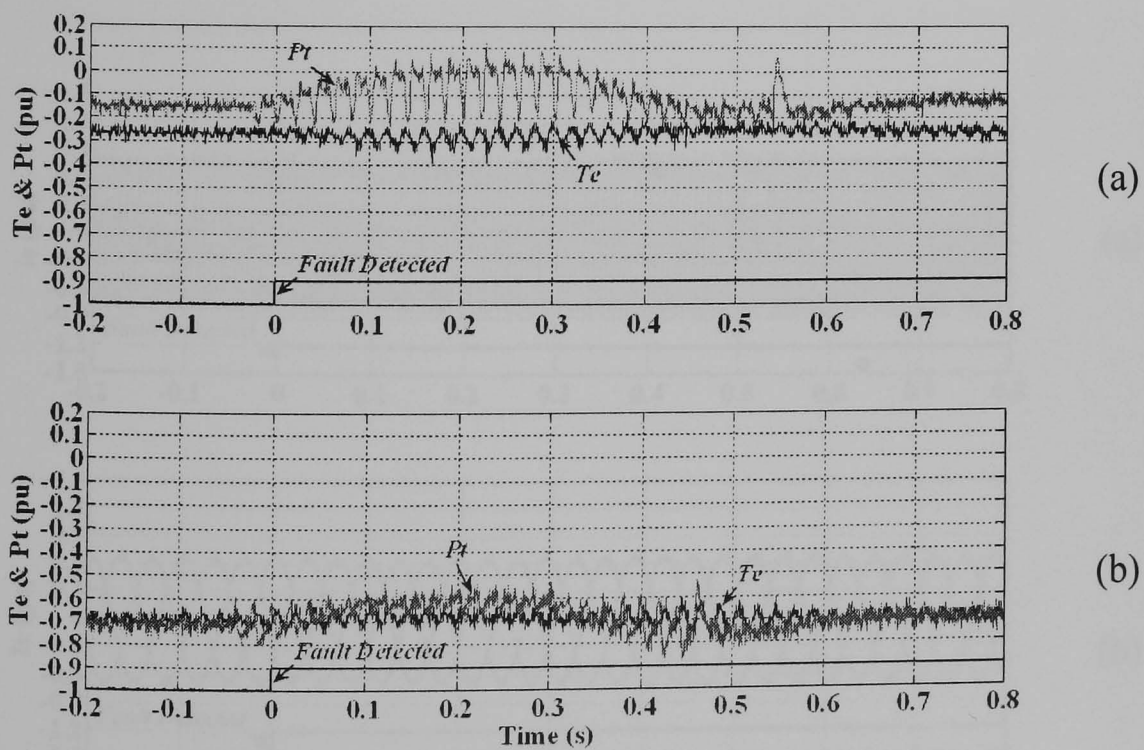
Figure 7.54 Experimental results showing the electromagnetic torque and total active power during reconfiguration of the grid-side converter under (a) rectifier mode operation and (b) inverter mode operation
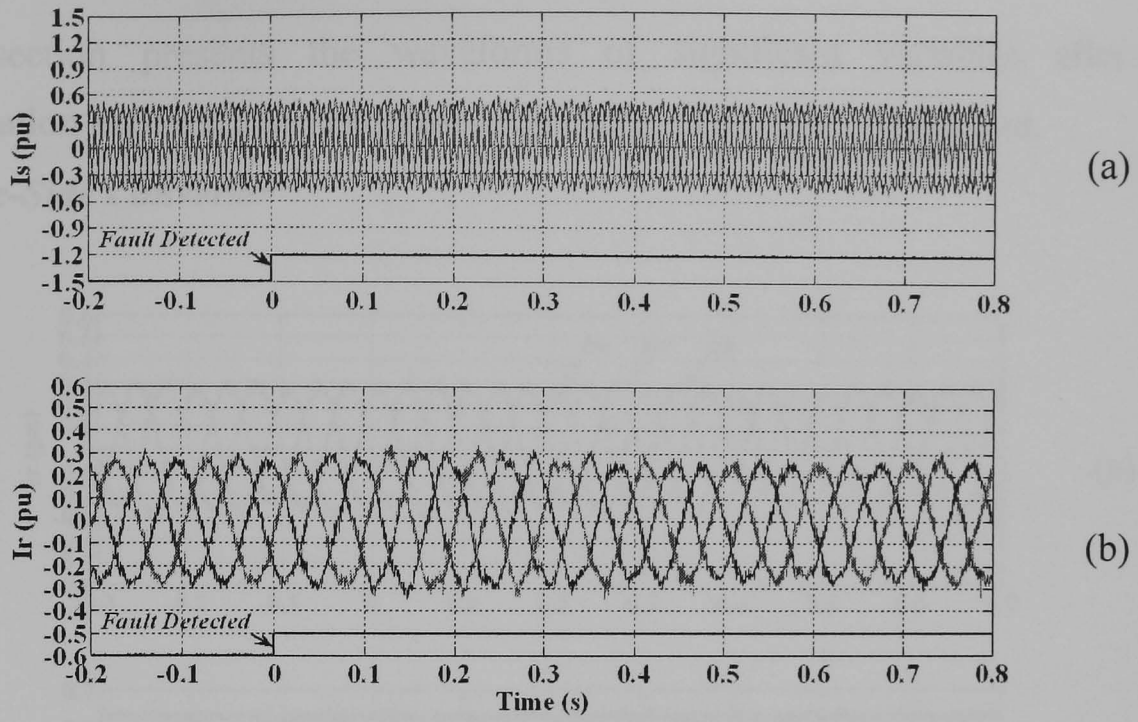
Figure 7.55 Experimental results showing (a) stator current waveforms and (b) rotor current waveforms during reconfiguration of the grid-side converter under rectifier mode operation
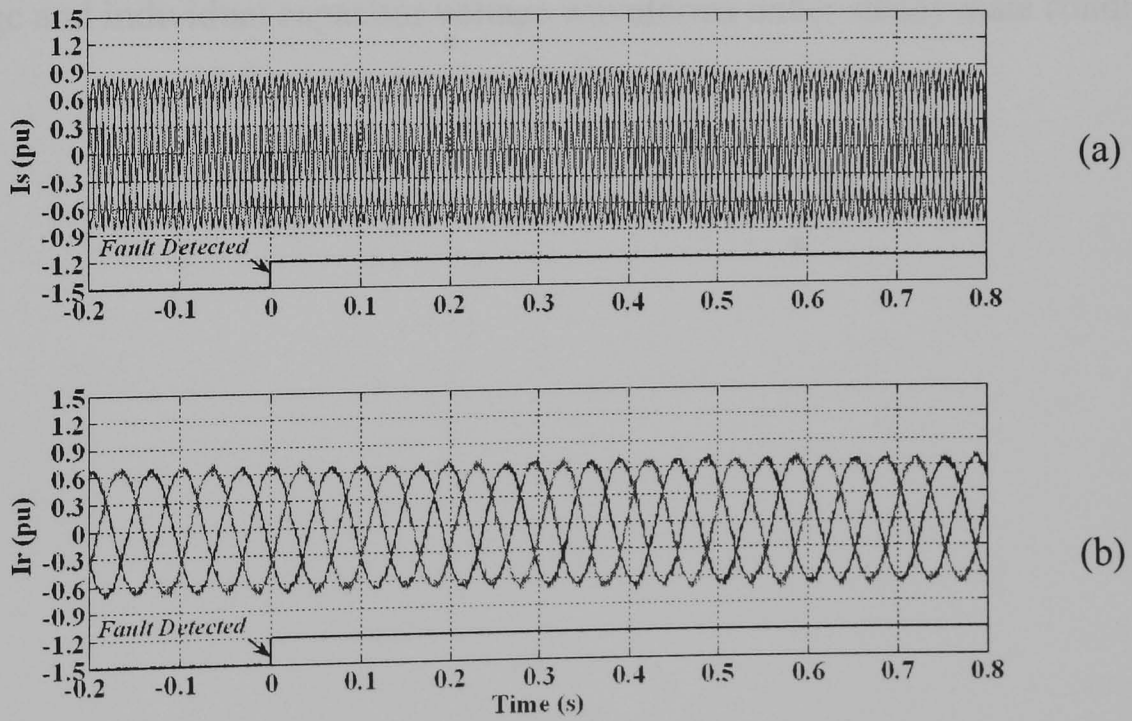
Figure 7.56 Experimental results showing (a) stator current waveforms and (b) rotor current waveforms during reconfiguration of the grid-side converter under inverter mode operation

ii. Steady-State Operation

This subsection presents the waveforms of significant variables after the reconfiguration process. The results are arranged as in previous subsection.

- *Machine-Side Converter*
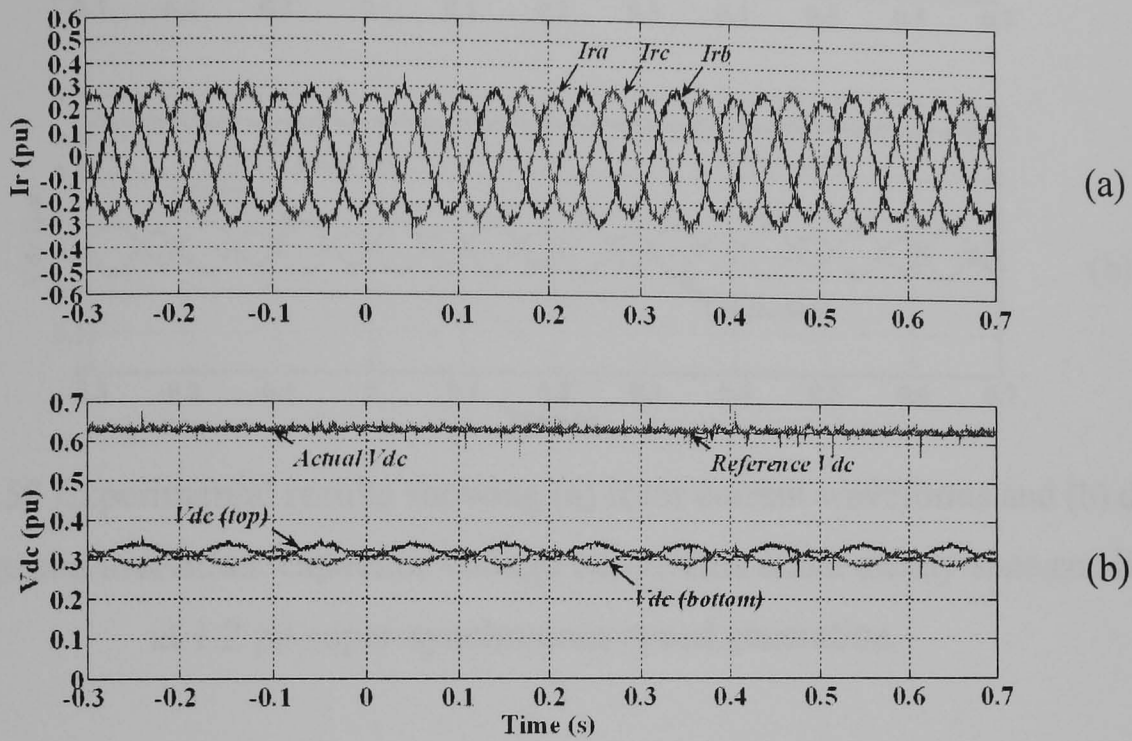
Figure 7.57 Experimental results showing (a) rotor current waveforms and (b) dc-link voltage and individual capacitor voltage waveforms under steady-state condition at 0.8 pu sub-synchronous speed generation
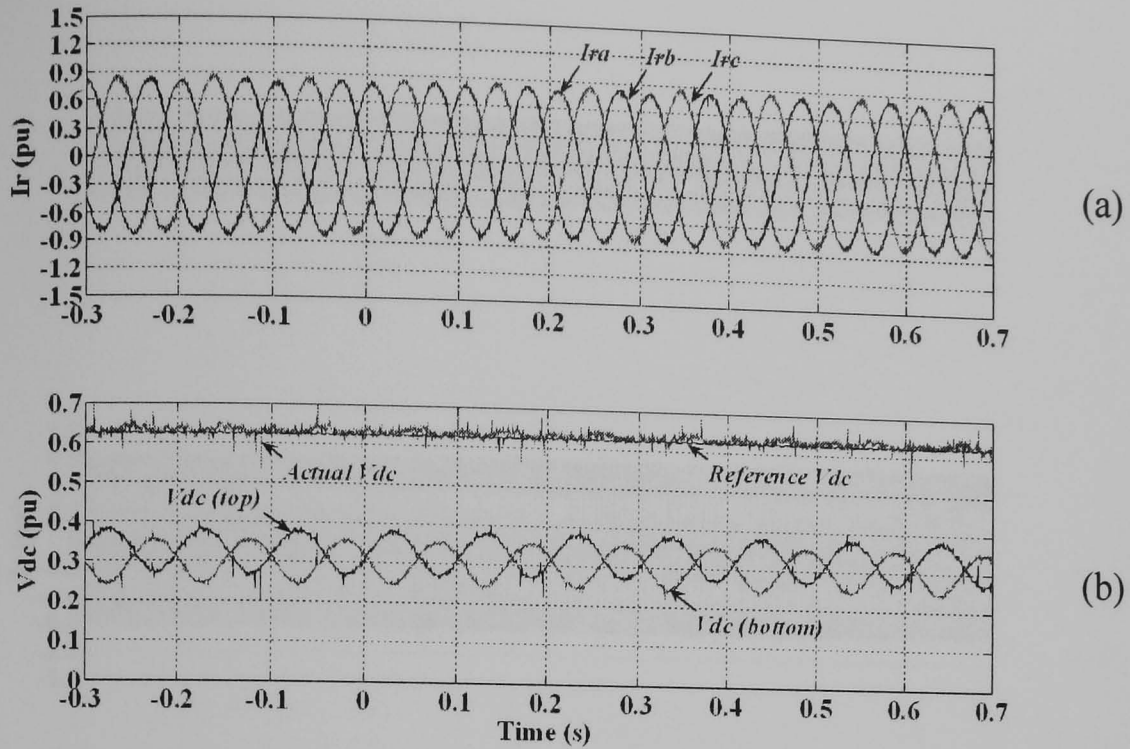
Figure 7.58 Experimental results showing (a) rotor current waveforms and (b) dc-link voltage and individual capacitor voltage waveforms under steady-state condition at 1.2 pu super-synchronous speed generation
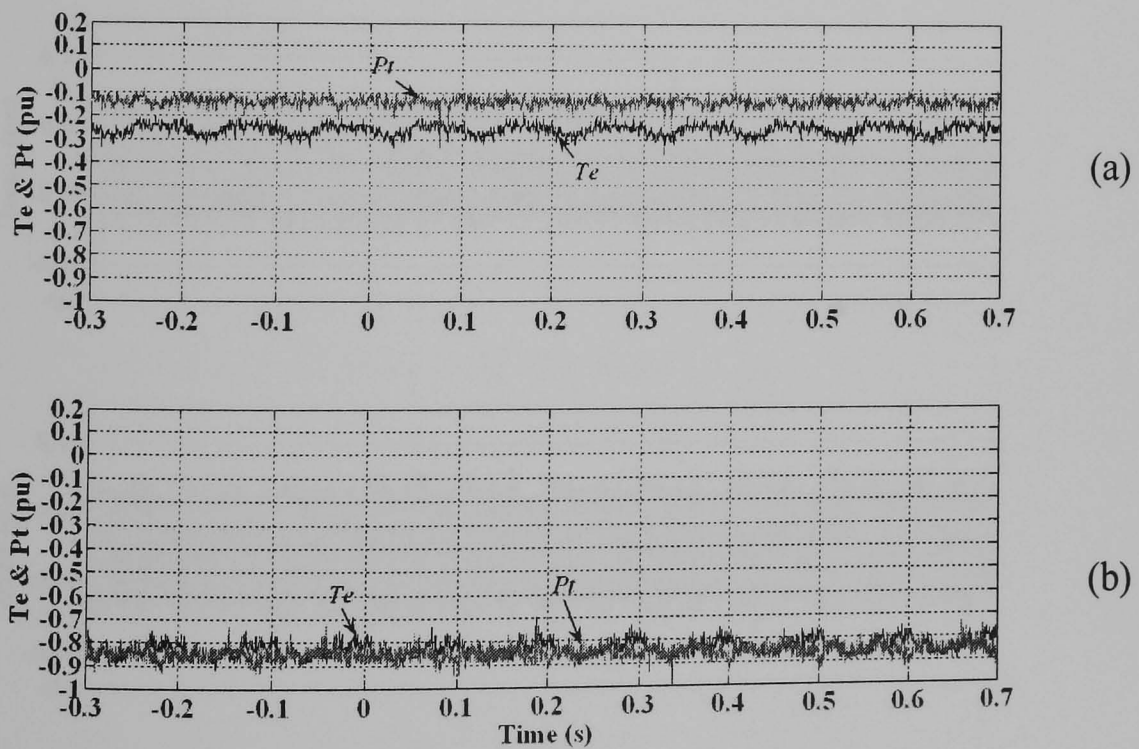
Figure 7.59 Experimental results showing the electromagnetic torque and total active power under steady-state condition at (a) 0.8 pu sub-synchronous speed generation and (b) 1.2 pu super-synchronous speed generation
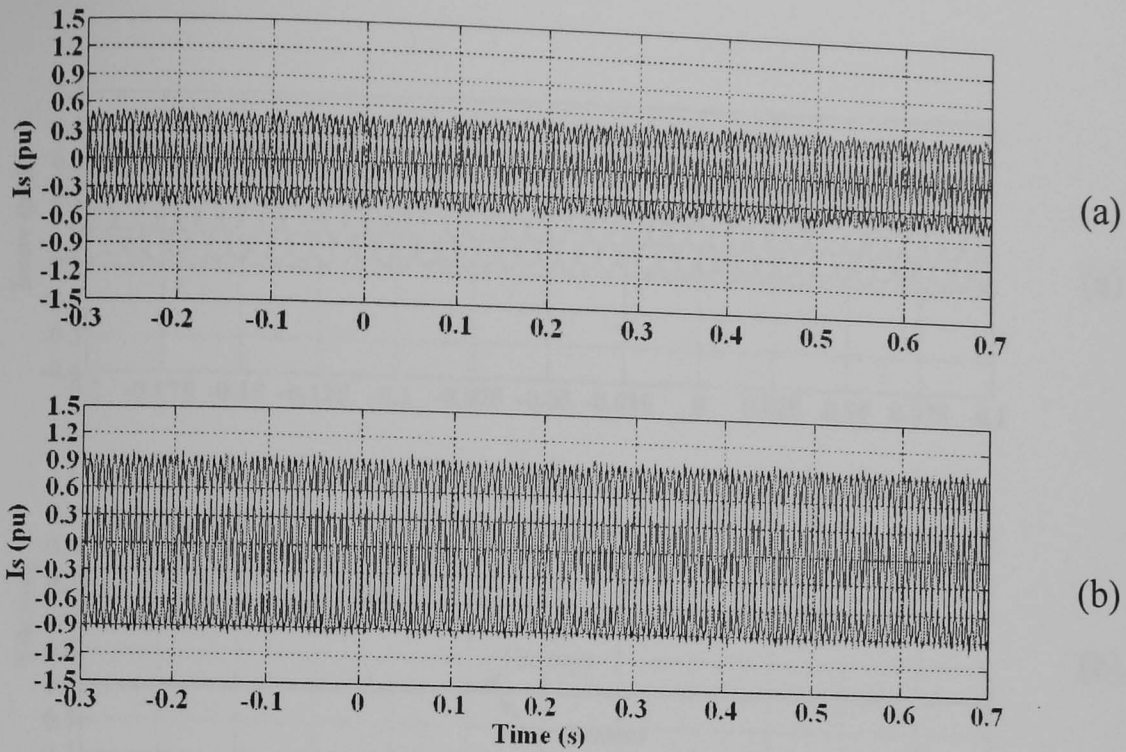
Figure 7.60 Experimental results showing stator current waveforms under steady-state condition at (a) 0.8 pu sub-synchronous speed generation and (b) 1.2 pu super-synchronous speed generation
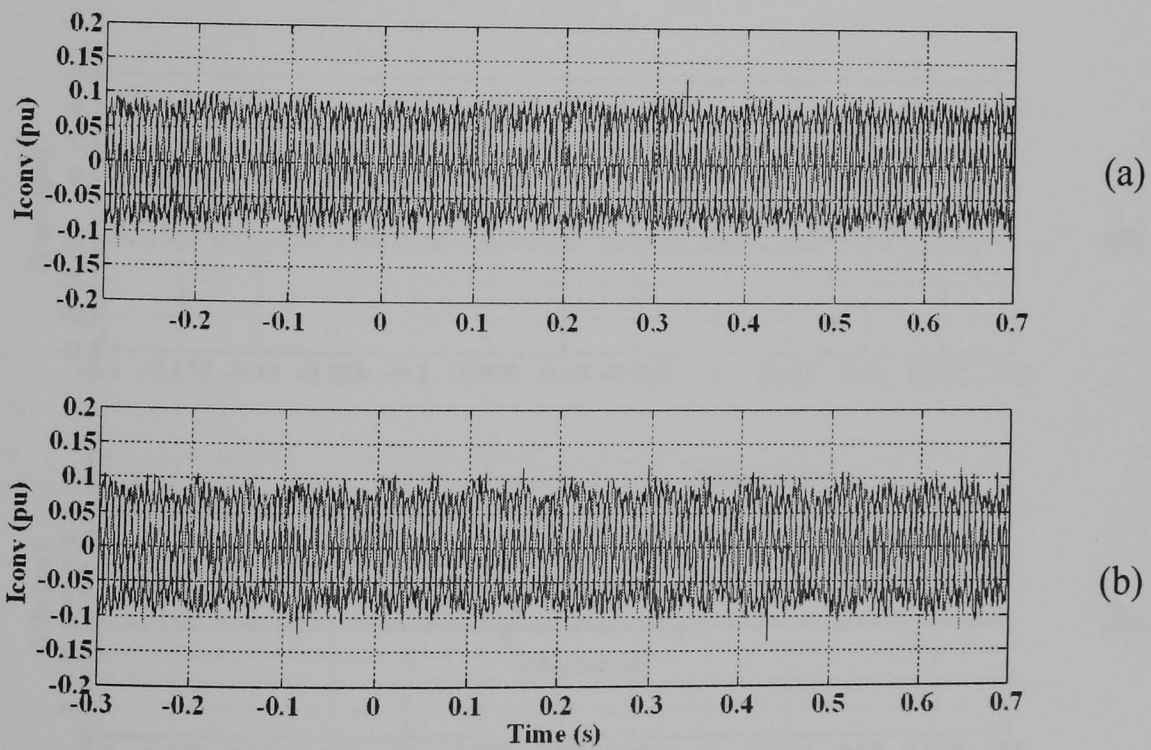
Figure 7.61 Experimental results showing grid-side converter current waveforms under steady-state condition at (a) 0.8 pu sub-synchronous speed generation and (b) 1.2 pu super-synchronous speed generation

•*Grid-Side Converter*
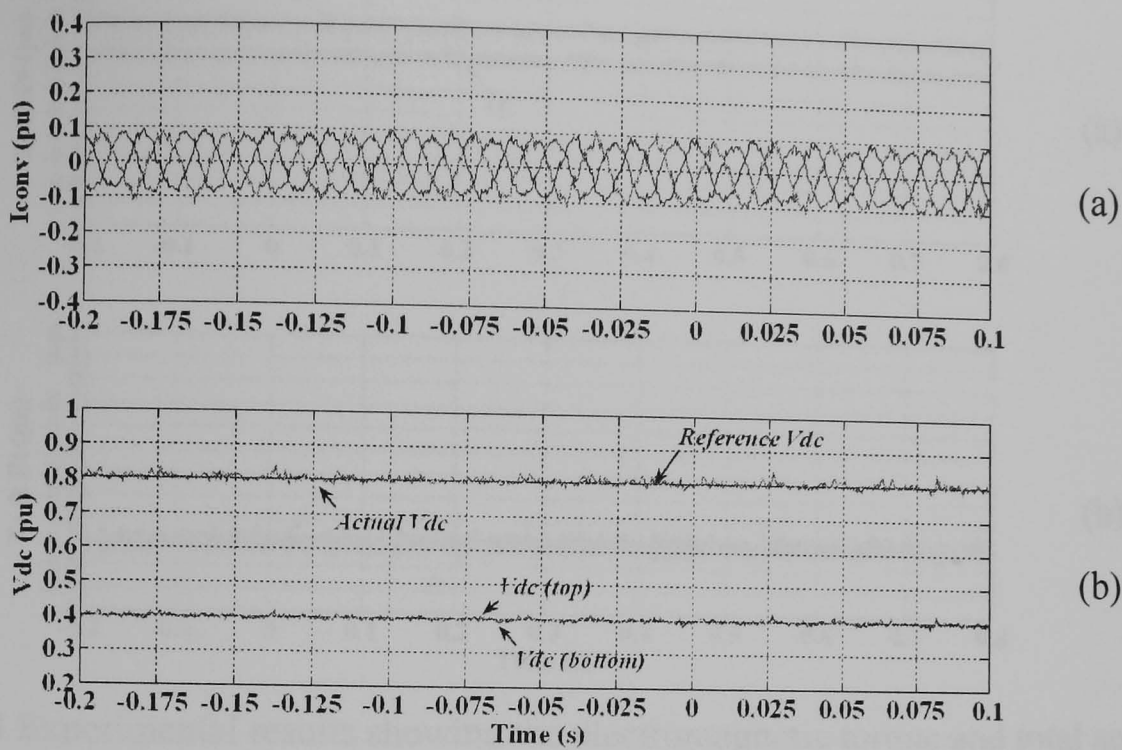
Figure 7.62 Experimental results showing (a) grid-side converter current waveforms and (b) dc-link voltage and individual capacitor voltage waveforms under steady-state rectifier mode operation
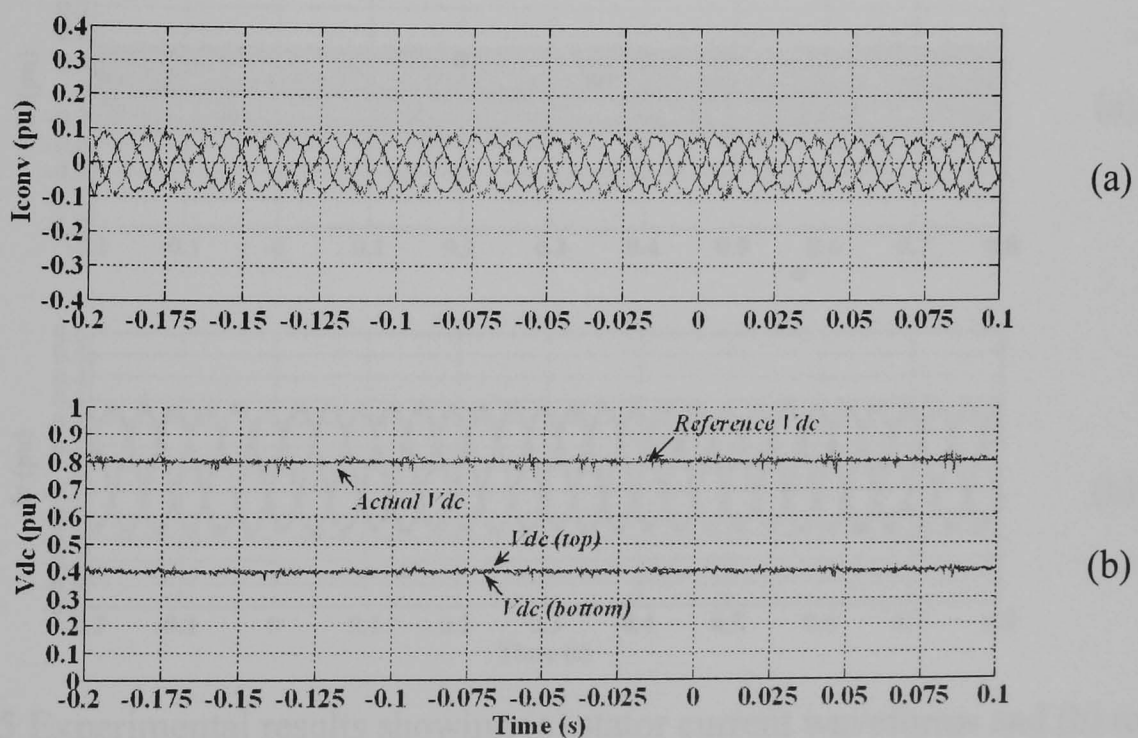
Figure 7.63 Experimental results showing (a) grid-side converter current waveforms and (b) dc-link voltage and individual capacitor voltage waveforms under steady-state inverter mode operation
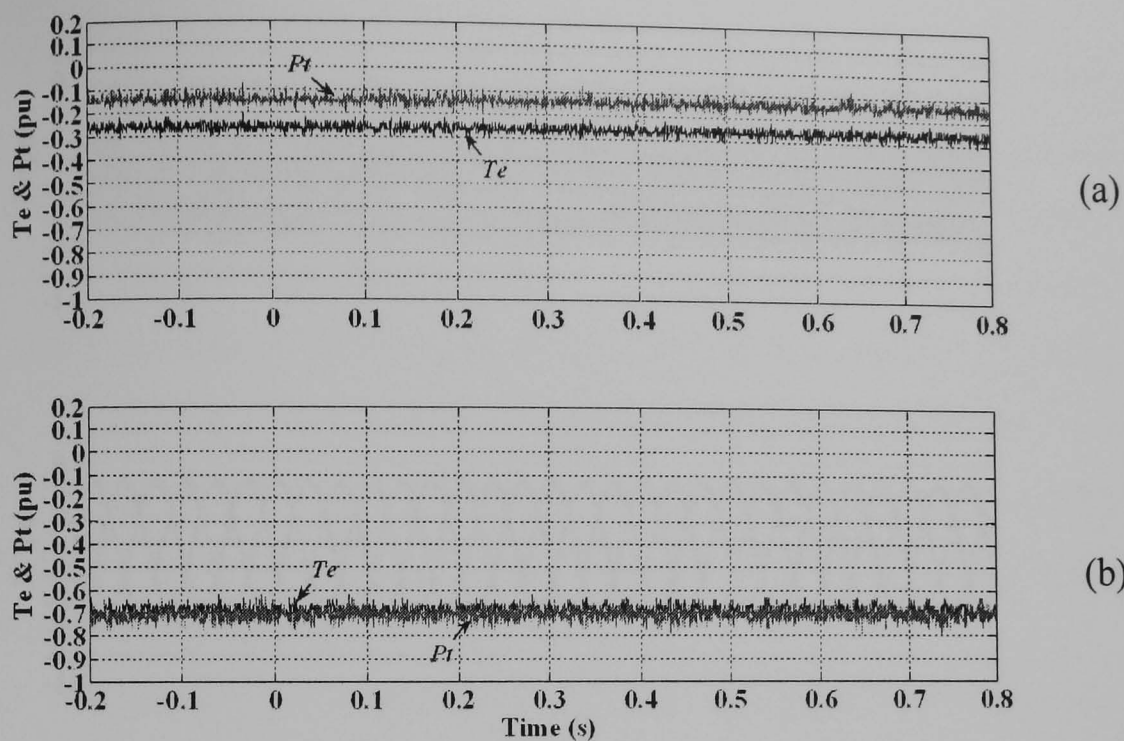
Figure 7.64 Experimental results showing the electromagnetic torque and total active power under steady-state (a) rectifier mode operation and (b) inverter mode operation of the grid-side converter
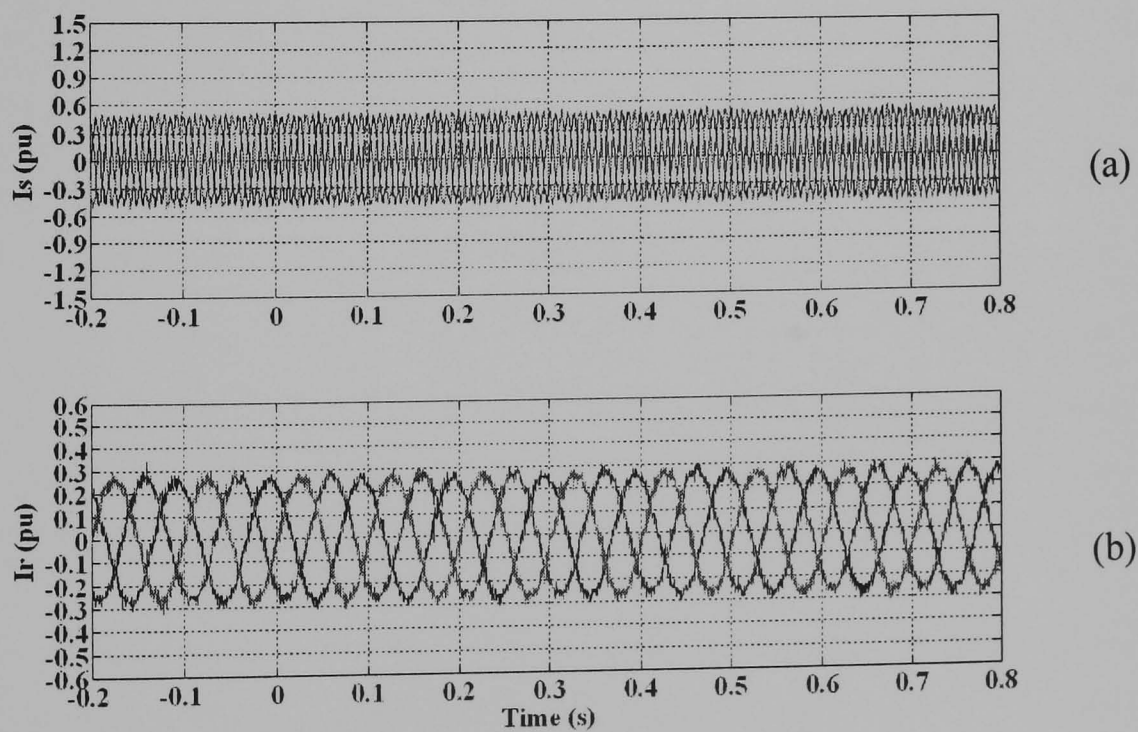
Figure 7.65 Experimental results showing (a) stator current waveforms and (b) rotor current waveforms under steady-state rectifier mode operation of the grid-side converter
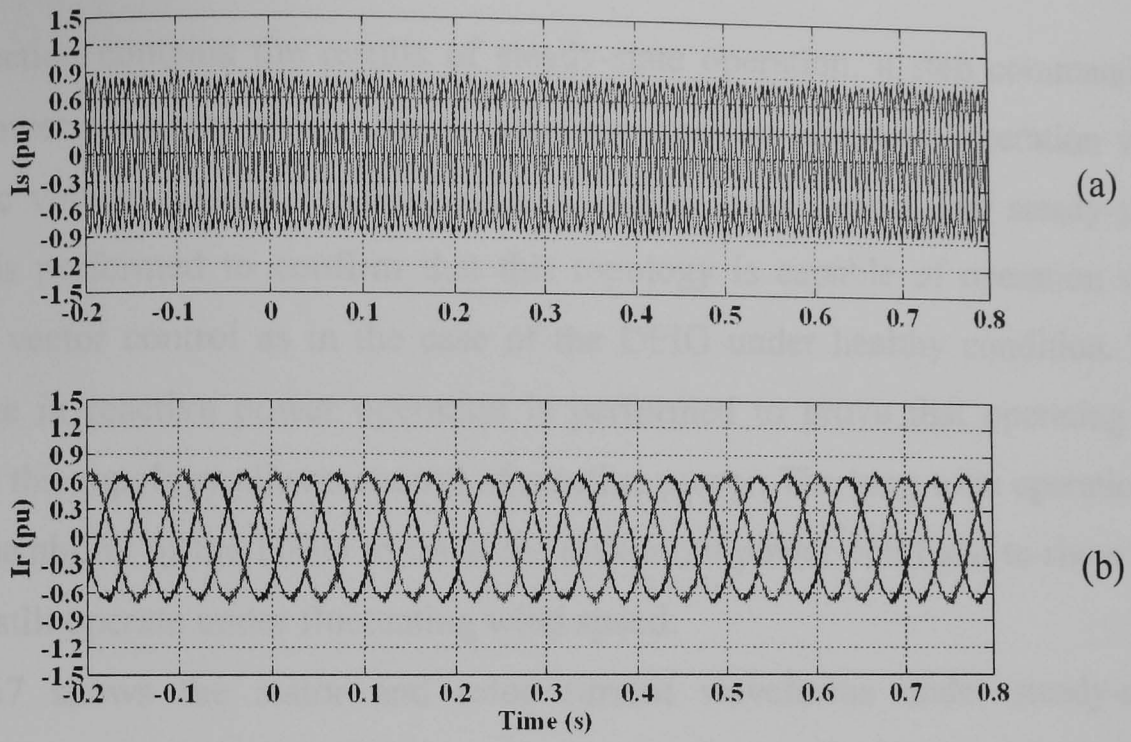
Figure 7.66 Experimental results showing (a) stator current waveforms and (b) rotor current waveforms under steady-state inverter mode operation of the grid-side converter

7.6.2 Short-Circuit Switch Faults

This subsection contains the results of steady-state operation, a step command in reactive power for unity power factor operation and the long-term operation with constant dc voltage control topology over a limited speed range. The steady-state operation is performed to confirm that this topology is capable of operation with stator-flux vector control as in the case of the DFIG under healthy condition. The step change in reactive power operation is performed to prove that operating the DFIG with this topology allows control of reactive power. The long-term operation is to prove the ability of the DFIG to track the maximum power point and to show that DFIG can still operate under fluctuating wind speed.

Figure 7.67 shows the stator and rotor current waveforms under steady-state operation. These are identical to the steady-state current waveforms of the healthy DFIG shown in figure 4.29.
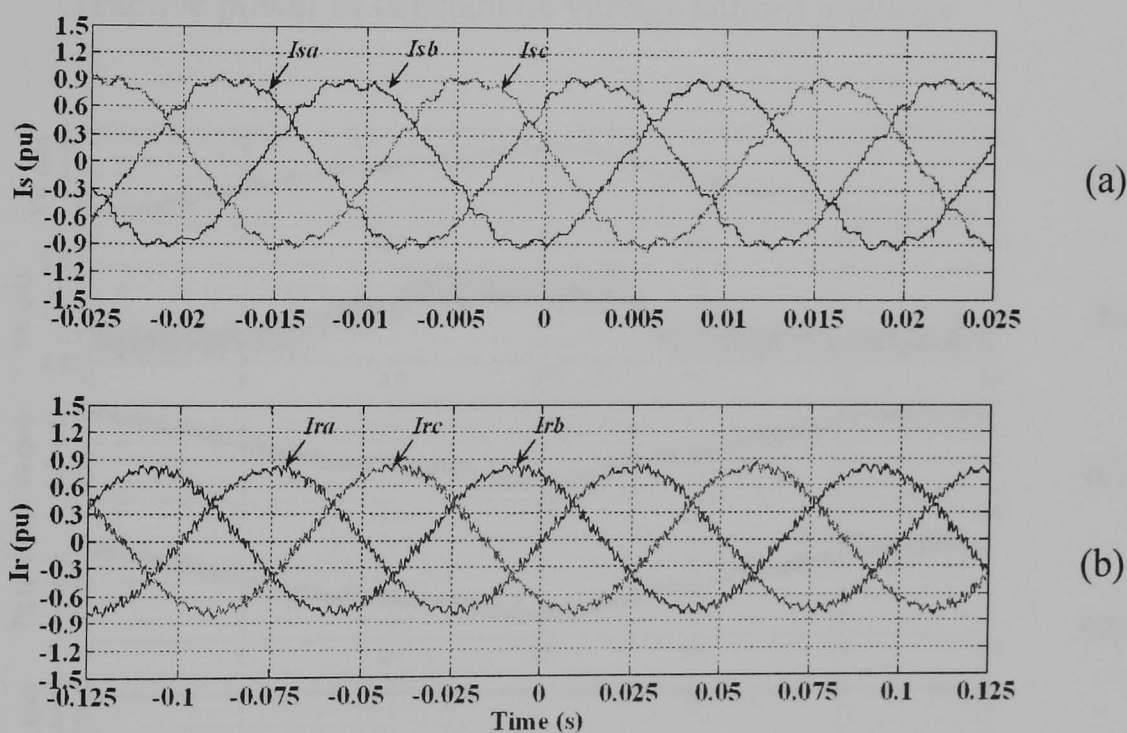
Figure 7.67 Experimental results showing (a) steady-state stator current waveforms and (b) rotor current waveforms under constant dc voltage control operation

Figure 7.68 shows the response to step change in reactive power command confirming that this topology is capable of operating under unity power factor at the stator.
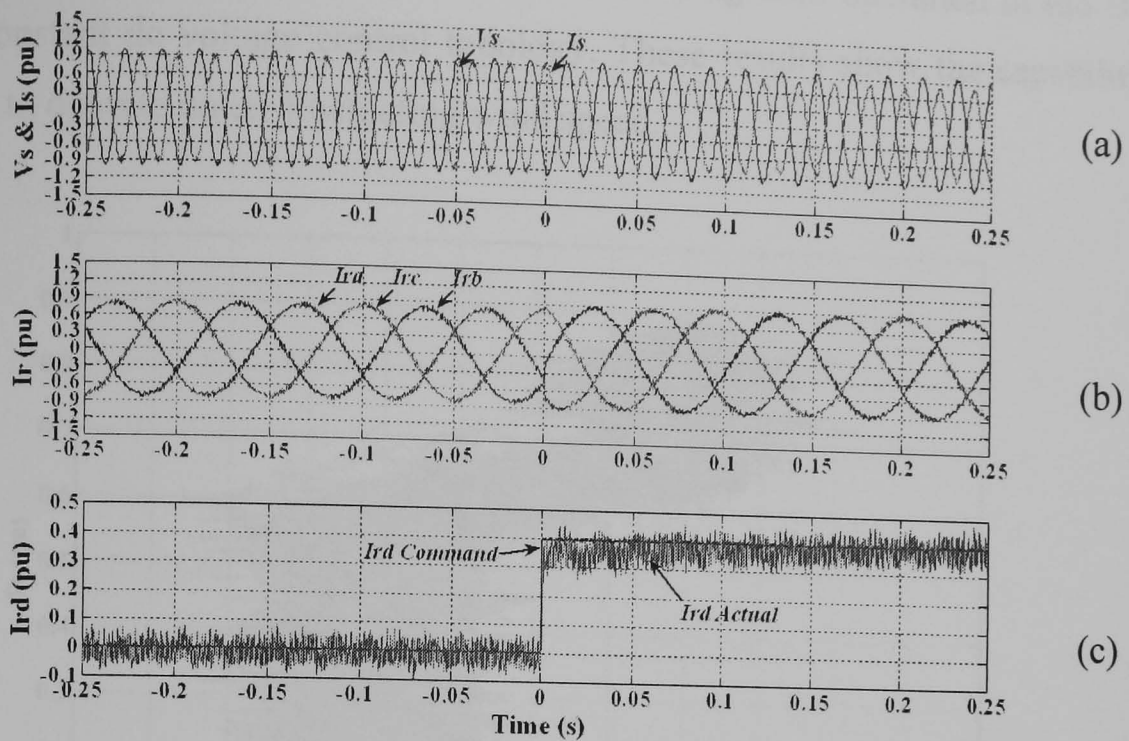
Figure 7.68 Experimental results showing (a) stator voltage and current, (b) rotor currents and (c) command and actual d-axis rotor current for step change in stator reactive power of constant dc voltage control topology
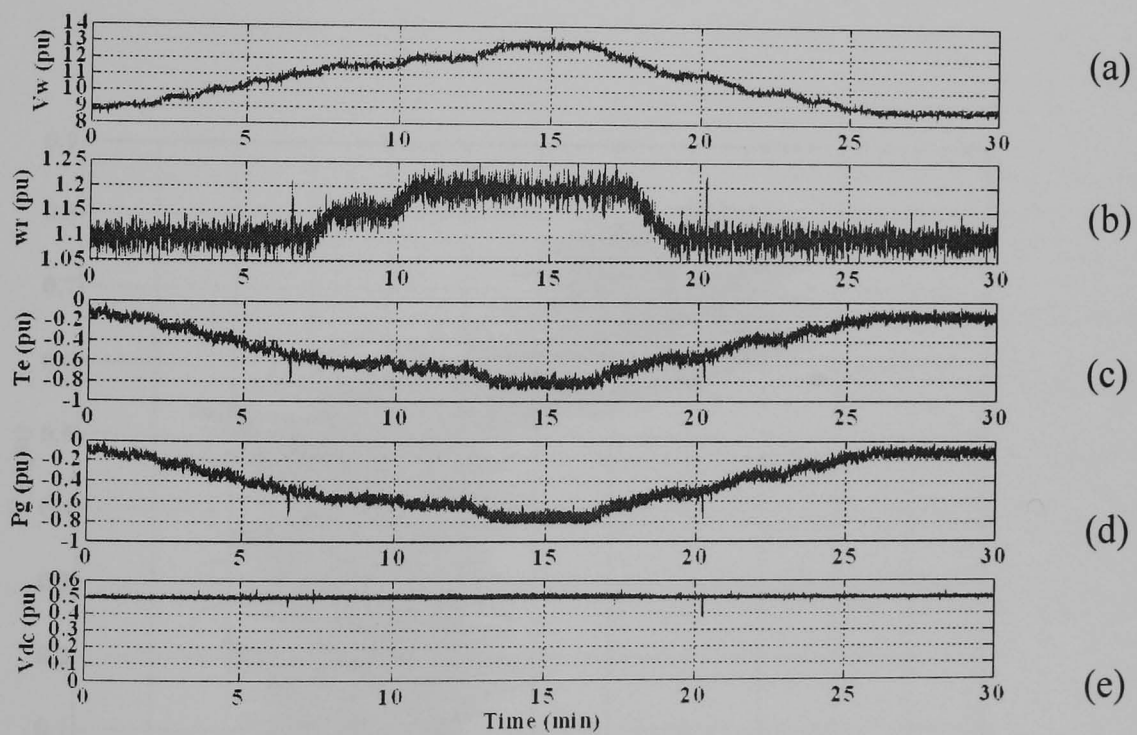
Figure 7.69 Experimental results showing (a) wind speed vs. time curve, (b) generator speed vs. time curve, (c) electromagnetic torque vs. time curve, (d) generator power vs. time curve and (e) dc-link voltage vs. time curve under the long-term operation

Figure 7.69 shows the experimental results for the long-term operation of the DFIG with the constant dc voltage control topology. These results show the capability of the system to operate under fluctuating wind speed.
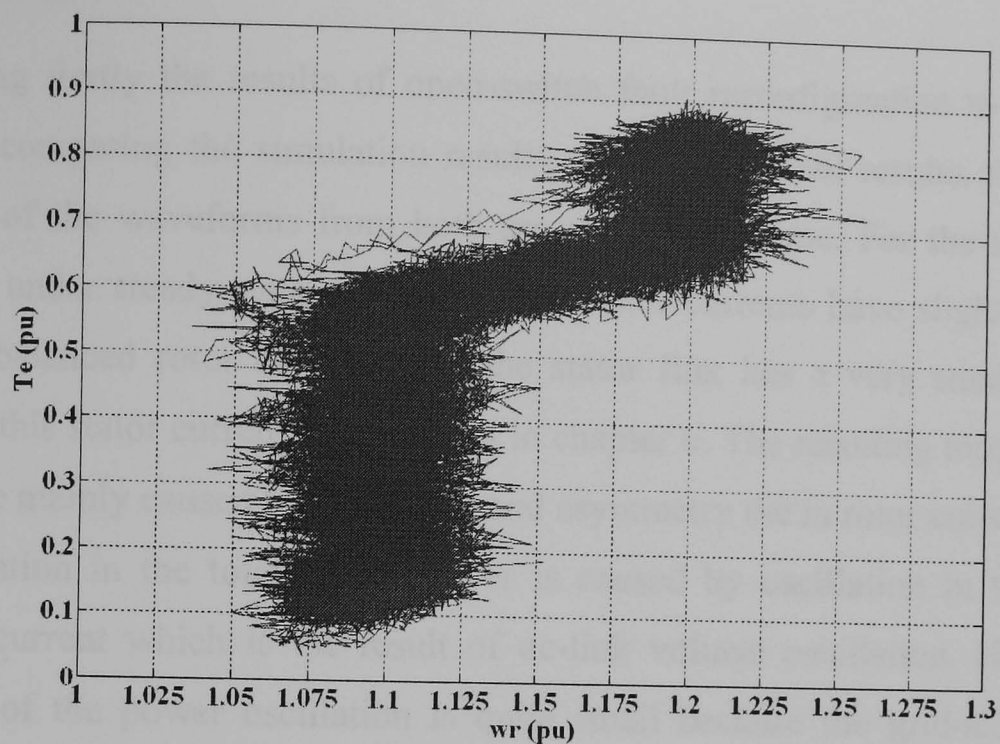
Figure 7.70 Electromagnetic torque vs. generator speed curve
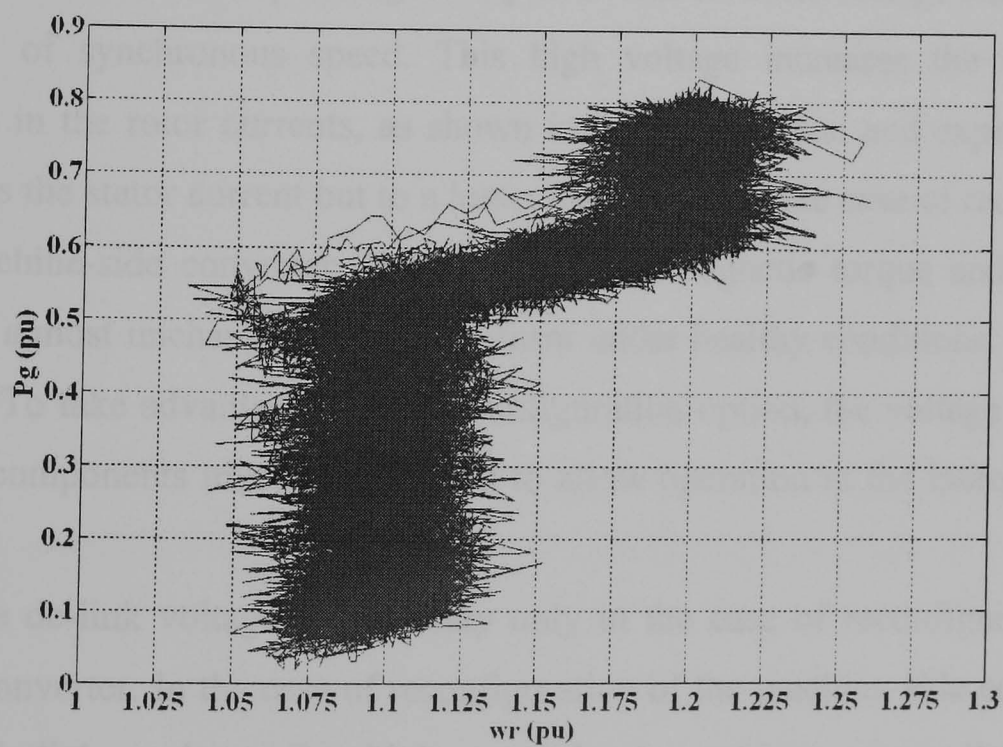
Figure 7.71 Generator power vs. generator speed curve

Figures 7.70 and 7.71 show the relationship between generator torque and generator speed and between generator power and generator speed respectively. As shown in

these figures, the minimum speed is set at 1.1 pu. For operation at speed between 1.1 pu and 1.2 pu, the speed control follows the maximum power tracking scheme as presented in chapter 4.

7.7 Discussion

Considering firstly the results of open-switch fault reconfiguration to four–switch topology, comparing the simulation results and experimental results, the trend and the shape of the waveforms from both are almost the same. For the machine-side converter, under steady-state conditions, the stator currents have slightly distortion due to unbalanced rotor currents, but the stator flux has a very small oscillation caused by this stator current as discussed in chapter 6. The resulting torque pulsation is therefore mainly caused by unbalance and asymmetry the in rotor currents.

The oscillation in the total active power is caused by oscillation in the grid-side converter current which is the result of dc-link voltage oscillation. However, the amplitude of the power oscillation is quite small because the grid-side converter power is only a fraction of stator power.

In the case of reconfiguration of the grid-side converter, the voltage is raised from 240 V to 384 V, which is quite high compared with the rotor voltage while operating at ±10% of synchronous speed. This high voltage increases the higher order harmonics in the rotor currents, as shown in both simulation and experiment. This also affects the stator current but to a lesser extent than in the case of reconfiguration of the machine-side converter. Hence, the electromagnetic torque and total active power are almost unchanged from their form under healthy conditions, as shown in chapter 4. To take advantage of this reconfiguration option, the voltage rating of all converter components must be sufficient to allow operation at the increased dc-link voltage.

Raising the dc-link voltage is necessary only in the case of reconfiguration of the grid-side converter. In the case of reconfiguration of the machine-side converter, the existing dc-link voltage is high enough to achieve controllability after reconfiguration.

In the case of operation of the constant dc voltage control topology, the steady-state waveforms of stator and rotor currents are as same as the waveforms while operating

the DFIG under healthy condition. This is due to the capability of controlling the DFIG by vector control, as under healthy condition.

7.8 Summary

System reconfiguration is required to avoid down time of the wind turbine system. For any off-shore wind turbine, system reconfiguration avoids shutting down the system with consequent loss of generated power to the grid. In this chapter, two topologies have been applied to reconfigure the system after an open-switch fault or a short-circuit switch fault occurs in the back-to-back converters - the four-switch topology with dc-link midpoint connection and the constant dc voltage control topology.

The first topology is applied to reconfigure the system after an open-switch fault is detected in either the machine-side converter or the grid-side converter. This topology provides continuous operation of the DFIG without any break in generation. A significant contribution in this chapter is the technique to eliminate the drift to a large difference in the mean voltages of individual capacitors and the explanation of the cause of this problem. The technique also smoothes the dc-link voltage which improves the quality of the power generated to the grid.

The second topology is applicable in the case of a short-circuit switch fault in the grid-side converter. This fault requires complete isolation of the faulty converter from the dc bus and from the ac side of the converter. However, after isolating the faulty converter, the machine-side converter and dc-link capacitor are still healthy. Therefore, by connecting the chopper circuit to the dc bus, the DFIG can still operate under maximum power point tracking with reactive power control, as for healthy conditions. However, the speed range is limited to the super-synchronous speed region only and the minimum operating speed must be high enough for the controller to maintain the dc-link voltage. In this configuration the power generated to the grid is reduced to stator power only, as the rotor power is dissipated in the resistor.

Reference

7.1. Silverio Bolognani, Marco Zordan, and Mauro Zigliotto, 'Experimental Fault-Tolerant Control of a PMSM Drive'. IEEE Trans. on Industrial Electronics, Vol. 47, No. 5, October 2000, pp. 1134-1141.

7.2. R. L. A. Ribeiro *et al.*, 'Compensation Strategies in the PWM–VSI Topology for a Fault Tolerant Induction Motor Drives System'. Proceeding of Symposium on Diagnostics for Electric Machines, Power Electronics and Drives, 2003, pp. 211-216.

7.3. R. L. A. Ribeiro *et al.*, 'Fault–Tolerant Voltage-Fed PWM Inverter AC Motor Drive Systems'. IEEE Trans. on Industrial Electronics, Vol. 51, No. 2, April 2004, pp. 439-446.

7.4. D. Kastha and B. K. Bose, 'Fault Mode Single-Phase Operation of a Variable Frequency Induction Drives and Improving of Pulsating Torque Characteristics'. IEEE Trans. on Industrial Electronics, Vol. 41, No. 4, August 1994, pp. 426-433.

7.5. D. Kastha and B. K. Bose, 'On-Line Search Based Pulsating Torque Compensation of a Fault Mode Single-Phase Variable Frequency Induction Motor Drive'. IEEE Trans. on Industry Applications, Vol. 31, No. 4, July/August 1995, pp. 802-811.

7.6. D. Kastha and A. K. Majumdar, 'An Improve Starting Strategy for Voltage-Source Inverter Fed Three Phase Induction Motor Drives Under Inverter Fault Conditions'. IEEE Trans. on Power Electronics, Vol. 15, No. 4, July 2000, pp. 726-732.

7.7. B. A. Welchko *et al.*, 'Fault Tolerant Three-Phase AC Motor Drive Topologies: A Comparison of Features, Cost, and Limitations'. IEEE Trans. on Power Electronics, Vol. 19, No. 4, July 2004, pp. 1108-1116.

7.8. J. R. Fu and T. A. Lipo, 'A Strategy to Isolate the Switching Device Fault of a Current Regulated Motor Drive'. Proceeding of IEEE IAS Annual Meeting 1993, Vol. 2, pp. 1015-1020.

7.9. Tian-Hua Liu, Jen-Ren Fu, and Thomas A. Lipo, 'A Strategy for Improving Reliability of Field Oriented Controlled Induction Motor Drives'. IEEE Trans. on Industry Applications, Vol. 29, No. 5 September/October 1993, pp. 449-455.

7.10. R. L. A. Ribeiro *et al.*, 'A Fault Tolerant Induction Motor Drive System by Using a Compensation Strategy on the PWM-VSI Topology'. Proceeding of IEEE Power Electronics Specialist Conference, 2001, Vol. 1, pp. 1191-1196.

7.11. M. B. de R. Correa *et al.*, 'An Induction Motor Drive System with Improving Fault Tolerance'. IEEE Trans. on Industry Applications, Vol. 37, No. 3, May/June 2001, pp. 873-879.

7.12. C. B. Jacobina *et al.*, 'Fault Tolerant Reversible AC Motor Drive System'. IEEE Trans. on Industry Applications, Vol. 39, No. 4, July/August 2003, pp. 1077-1084.

7.13. H. W. Van Der Broeck and J. D. Van Wyk, 'A Comparative Investigation of a Three-Phase Induction Machine Drive with a Component Minimized Voltage- Fed Inverter under Different Control Options'. IEEE Trans. on Industry Application, Vol. IA-20, No.2, March/April 1984, pp. 309-320.

7.14. C. B. Jacobina *et al.*, 'Induction Generator Static System with a Reduced Number of Component'. Proceeding of Thirty-First IAS Annual Meeting 1996, pp. 432-439.

7.15. M. Nask Uddin, T. S. Radwan, and M. A. Rahman, 'Performance Analysis of a 4-Switch, 3-Phase Inverter Based Cost Effective IPM Motor Drives'. Proceeding of Canadian Conference on Electrical and Computer Engineering, 2004, pp.85-88.

7.16. M. Nasir Uddin, Tawfik S. Radwan, and M. Azizur Rahman, 'Fuzzy-Logic-Controller-Based Cost-Effective Four-Switch Three-Phase Inverter-Fed IPM Synchronous Motor Drive System'. IEEE Trans. on Industry Applications, Vol. 42, No. 1, January/February 2006, pp. 21-30.

7.17. Joon-Hwan Lee, Sung-Chan Ahn, and Dong-Seok Hyun, 'A BLDCM Drive with Trapezoidal Back EMF Using Four-Switch Three Phase Inverter'. Proceeding of Conference Record of IEEE Industry Application Conference, 2000, pp. 1705-1709.

7.18. S. M. Madani, Lei Hao, and Hamid A. Toliyat, 'A Low-Cost Four-Switch BLDC Motor Drive with Active Power Factor Correction'. Proceeding of 28th IEEE Annual Conference of the Industrial Electronics Society, 2002, pp. 579-584.

7.19. B. K. Lee, T. H. Kim, and M. Ehsani "On the Feasibility of Four-Switch Three-Phase BLDC Motor Drives for Low Cost Commercial Applications: Topology and Control'. IEEE Trans. on Power Electronics, Vol. 18, No. 1, January 2003, pp. 164-172

7.20. S. H. Park *et al.*, A Simple Current Control Algorithm for Torque Ripple Reduction of Brushless DC Motor Using Four-Switch Three-Phase Inverter'. Proceeding of 34th IEEE Power Electronics Specialist Conference, 2003, pp. 574-579.

7.21. J. H. Lee *et al.*, 'A Study for Improved of Speed Response Characteristic in Four-Switch Three-Phase BLDC Motor'. Proceeding of the 30th Annual Conference of the IEEE Industrial Electronics Society, 2004, pp. 1339-1343.

7.22. Q. Fu and H. Lin, 'Sliding Mode Driving Strategy for Four-Switch Three-Phase Brushless DC Motor'. Proceeding of International Joint Conference 2006, pp. 696-701.

7.23. B. G. Park *et al.*, 'Fault Tolerant Strategies for BLDC Motor Drives under Switch Faults'. Proceeding of 41st IEEE Industry Applications Conference Annual Meeting, 2006, pp. 1637-1641.

7.24. A. Halvaei Niasar, H. Moghbelli, and A. Vahedi, 'Commutation Torque Ripple of Four-Switch Brushless DC Motor Drives, Part I: Analysis'. Proceeding of 9th IEEE International Workshop on Advance Motion Control, 2006 pp. 541- 546.

7.25. A. Halvaei Niasar, H. Moghbelli, and A. Vahedi, 'Commutation Torque Ripple of Four-Switch Brushless DC Motor Drives, Part II: Controllability and Minimization'. Proceeding of 9th IEEE International Workshop on Advance Motion Control, 2006, pp. 547- 552.

7.26. J.-J.Shieh, C.-T. Pan, and Z.-J.Cuey, 'Modelling and Design of a Reversible Three-Phase Switching Mode Rectifier'. Proceeding of IEE Electric Power Applications, Vol. 144, No. 6, November 1997, pp. 389-396.

7.27. B. R. Lin and D. P. Wu, 'Implementation of Three-Phase Power Factor Correction Circuit with Less Power Switches and Current Sensors'. IEEE Trans. on Aero Space and Electronic Systems, Vol. 34, No. 2, April 1998, pp. 664-670.

7.28. KeVoek Haddad and Geza Joos, 'Three-Phase Active Filter Topology Based on a Reduced Switch Count Voltage Source Inverter'. Proceeding of 30th Annual IEEE Power Electronics Specialist Conference, 1999, pp. 236-241.

7.29. G. Joos *et al.*, 'Four Switch Three Phase Active Filter with Reduced Current Sensors'. Proceeding of 31st Annual IEEE Power Electronics Specialists Conference, 2000, pp. 1318-1323.

7.30. R. L. A. Riberio *et al.*, 'Two-Fault Tolerant Control Strategies for Shunt Active Power Filter Systems'. Proceeding of 28th IEEE Annual Conference on the Industrial Electronics Society, 2002, pp. 792-797.

7.31. H. J. Chiu *et al.*, 'Three-Phase Active Power Filter for Power Quality Compensation'. Proceeding of 5th International Conference on Power Electronics and Drive System, 2003, pp. 1540-1542.

7.32. C. B. Jacobine *et al.*, 'Induction Motor Drive System for Low-Power Applications'. IEEE Trans. on Industry Applications, Vol. 35, No. 1, January/February 1999, pp. 52-61.

7.33. G. T. Kim and T. A. Lipo, 'VSI-PWM Rectifier/Inverter System with a Reduced Switch Count'. IEEE Trans. on Industry Applications, Vol. 32, No.6, November/December 1996, pp. 1331-1337.

7.34. G. T. Kim and T. A. Lipo, 'DC Link Voltage Control of Reduced Switch VSI-PWM Rectifier/Inverter System'. Proceeding of 23rd International Conference on Industrial Electronics, Control and Instrumentation, 1997, Vol. 2, pp. 833-838.

7.35. C. B. Jacobina *et al.*, 'Vector and Scalar Control of a Four Switch Three Phase Inverter'. Proceeding of 30th IEEE Industry Applications Conference Annual Meeting, 1995, pp. 2422-2429.

7.36. M. B. R. Correa *et al.*, 'A New Approach to Generate PWM Pattern for Four-Switch Three-Phase Inverters'. Proceeding of Annual IEEE Specialists Conference, 1999, pp. 941-946.

7.37. R. B. D. R. Correa *et al.*, 'A General PWM Strategy for Four-Switch Three-Phase Inverter'. IEEE Trans. on Power Electronics, Vol. 21, No. 6, November 2006, pp. 1618-1627.

7.38. F. Blaabjerg *et al.*, 'A New Optimized Space-Vector Modulation Strategy for a Component-Minimized Voltage Source Inverter'. IEEE Trans. on Power Electronics, Vol. 12, No. 4, July 1997, pp. 704-714.

7.39. Frede Blaabjerg, Dorin O. Neacsu, and John K. Pedersen, 'Adaptive SVM to Compensate DC-Link Voltage Ripple for Four-Switch Three-Phase Voltage-Source Inverters'. IEEE Trans. on Power Electronics, Vol. 14, No. 4, July 1999, pp. 743-752.

7.40. Grant A. Covic, Grant L. Peters, and John T. Boys, 'An Improved Single Phase to Three Phase Converter for Low Cost AC Motor Drives'. Proceeding of International Conference on Power Electronics and Drives Systems 1995, pp. 549-554.

7.41. G. A. Covic and G. L. Peters, 'DC link imbalance compensation in fourswitch inverter AC motor drives'. Electronics Letters, 19th June 1997, Vol. 33, No. 13.

7.42. G. L. Peters, G. A. Covic, and J.T. Boys, 'Eliminating Output distortion in four-switch inverters with three-phase loads'. Proceeding of IEE Electric Power Application, Vol. 145, No. 4, July 1998, pp. 326-332.

7.43. http://www.fairchildsemi.com

7.44. http://www.siemens.com

7.45. http://www.hitachiaic.com/pdf/technicalreport06.pdf

Chapter Eight

Conclusion

This research has achieved two main objectives – demonstrated converter fault diagnosis methods for a doubly-fed induction generator (DFIG) used in a wind turbine, and proved technologies for its post-fault operation. As discussed in chapter 2, multi-megawatt variable-speed wind turbines used worldwide are generally equipped with DFIGs. The DFIG consists of a wound rotor induction generator, back-to-back converters, a three-phase filter and a three-phase transformer as discussed in chapter 3. The back-to-back converters are the least reliable parts, in which the occurrence of a fault may cause serious damage to the generator and other parts of a wind turbine, leading to down time. Converter fault diagnosis and post-fault operation for the DFIG are necessary to prevent such conditions.

The simulation models and experimental system were designed, built and tested based on the theories presented in chapter 3. Control of a DFIG is generally achieved by stator-flux vector control, due to its analogy to rotor-flux vector control for a cage induction motor. The main problem of this method is stator-flux estimation when implementing in a DSP. However, this was overcome by a combination of a voltage model and a current model, in a similar way to a sensorless drive for a cage motor [8.1]. The simulated system was modeled in Matlab/Simulink [8.2]. As presented in chapter 4, the model was generated by using both built-in blocks and writing m-file s-functions. The built-in asynchronous machine model required modification because it is intended to represent only a cage machine or a wound rotor machine with a 1:1 turn ratio. The experimental system was controlled by a single TI DSP type TMS320F2812, which is used to control both a DFIG and a dc motor. The latter is torque controlled to behave like a wind turbine. The good match between the simulation and experimental results proved that the experimental system was functioning correctly and so was ready for the main objectives of this research, namely converter switch fault diagnosis and post-fault operation for the DFIG.

As discussed in chapter 5, faults in power converters may be divided into open-switch faults and short-circuit switch faults. Chapter 5 analysed and reviewed

existing methods to detect both types of switch fault. In the case of an open-switch fault, the diode current which appears in the faulty half cycle of the faulty phase current while operating the converter as a PWM rectifier was fully explained by the principle of the dc-dc boost converter. This diode current phenomenon had not been adequately explained in any reference. Following the analysis, the existing methods for open-switch fault diagnosis were compared. The best-known diagnostic indices are the line currents of the converters, because no extra transducers are required since current transducers are already installed in the system for control purposes. Other diagnostic indices such as voltages may require extra transducers or access to the neutral of the electrical machines [8.3]. The methods applied to diagnose the faults were able to be classified into model-based methods and non-model-based methods. The former required an accurate model of the system and the accurate system parameters under any operating condition. The latter are more generally applicable due to their flexibility and effectiveness. AI may also be applied to reduce the knowledge required from the expert, but a more complicated system is required. The second part of chapter 5 discussed the methods generally used for short-circuit switch fault detection in the converters of electrical drives and their protection methods. This fault requires immediate action to protect the converter, in the time scale of microseconds. The most effective method is by placing a current transducer and controller at every switch to detect overcurrent conditions and disable all the switches before the short circuit has fully developed.

Chapter 6 first analysed the effects of an open-switch fault and a short-circuit switch fault on the DFIG. An open-switch fault results in phenomena similar to the case of a stator-fed induction machine. The most serious problem is torque pulsations which can damage the mechanical parts of the generator and turbine. Reference frame theory [8.4] was applied to analyse the effect of an open-switch fault and explain how the fault transfers its effects to the stator side. Existing methods of fault diagnosis were summarised and discussed. The Modified Normalised DC Current Method was the best among them, but two problems existed when the method was applied to the DFIG – long computation time and false alarms while operating around synchronous speed. Two new methods, named the Sampling Point Comparison Method and the Absolute Normalised DC Current Method were

251

proposed to solve one or both of these problems. The first method consumes less computational time and yields shorter fault detection time. However, it is prone to false alarms if the angle and frequency estimation of the faulty signal do not match. To completely solve both problems the second method was proposed. This method also required less computational time than the Modified Normalised DC Current Method and provided the equivalent fault detecting capability but still suffered false alarms. However, it was recognised that due to the nature of the diagnostic variable, the value of ξ_v has a periodic nature like its current signal. This nature is used in the false alarm suppression algorithm and added to the Absolute Normalised DC Current Method of fault detection. With this algorithm, the Absolute Normalised DC Current Method is the preferred choice for open-switch fault diagnoses for the DFIG. With this successful fault detection method in service, once the fault is detected action must be taken to avoid, if possible, shutting down the DFIG. System reconfiguration was considered to solve this problem.

In the case of a short-circuit switch fault, it was assumed that the fault persisted after shoot-through. With this assumption, the DFIG does not need to stop, unlike the stator-fed induction machine, because its stator remains directly connected to the grid. In the case of short circuit switch fault in the machine-side converter, this converter must be isolated from the dc bus. If a mechanical contactor is fitted which short-circuits the rotor of the DFIG then the DFIG can operate as a normal cage induction generator. In this configuration the grid–side converter can operate as a static VAR compensator. In the case of a short-circuit switch fault in the grid-side converter, this converter must be isolated from both dc bus and ac bus. For this case, reconfiguration is possible which permits the DFIG to function over a wider speed range than a cage generator.

Chapter 7 presented the system reconfiguration solutions for the DFIG for both open-switch faults and short-circuit switch faults. For an open-switch fault, the four-switch topology was applied and shown to be practical. Since the neutral of rotor winding is not normally accessible, the faulty phase has to be connected to the dc-link midpoint. This topology requires a special modulation scheme to control the four-switch converter. Two problems were identified with this topology - it cannot operate at or close to zero frequency and it causes torque pulsations due to the effect of unsteady

dc voltages. The method proposed in [8.5] was used in an attempt to solve this problem but it caused divergence of dc voltages of the capacitors which could lead to loss of control. The author devised a method to prevent the divergence of the dc voltages but still maintain the capability to compensate for the effects unsteady dc voltages. The simulation and experimental results prove that the problem was completely solved by the new approach. The method of dealing with a short-circuit switch fault in the machine-side converter was described in chapter 6. For a short-circuit switch fault in the grid-side converter, the author proposed a reconfiguration topology called constant dc voltage control which maintains maximum power tracking and full reactive power control capability. This topology was demonstrated to operate successfully in steady-state and long-term operation in both simulation and experiments.

8.1 Author's Contribution

The experimental system in chapter 4 was designed, built and shown to be fully functional and full simulation models of a wind turbine driven DFIG were designed and tested. Since the main objectives of this research are fault diagnosis and post-fault operation, the author's contributions are

- analysis of the cause of diode current during the faulty half cycle of the faulty phase current under rectifier mode operation of a three-phase PWM converter,

- application of the reference frame theory to analyse unbalance caused by an open-switch fault in the machine-side converter,

- proposing and proving an alternative method to detect an open-switch fault in a three-phase converter, a method which can also be applied to normal electrical drives,

- proposing and proving an algorithm to suppress false alarms caused by existing detection methods while operating the DFIG around synchronous speed,

- proposing and proving an algorithm to prevent divergence in capacitor dc voltages in the four-switch topology without degrading the effectiveness of the original compensation method to suppress torque oscillation,

- applying a dynamic braking circuit as a post-fault topology for a wind turbine driven DFIG.

8.2 Recommendation for Further Research

Recommendations for further research include:

- The four-switch topology proposed for reconfiguring the system is only for short-term operation, not for permanent use, because with this topology low frequency currents flow into each capacitor, resulting in a reduction in capacitors' life time. It would be useful to investigate the maximum possible operating time of the capacitor with this topology;

- Operation at zero frequency with four-switch topology has not been achievable, but it would be valuable to investigate possible switching methods to operate the system under this frequency without loss of controllability;

- Since faults can occur in the transducers, such as incremental encoder or current transducer or voltage transducer circuits, the post-fault operation with sensorless control should be investigated;

- Adaptive control could be investigated to help improve system performance after increasing the dc-link voltage command for four-switch topology.

Reference

8.1. Cristian Lascu, Ion Boldea, and Frede Blaabjerg, 'A Modified Direct Torque Control for Induction Motor Sensorless Drive'. IEEE Trans. on Industry Application, Vol. 36, No. 1, January/February 2000, pp. 122-130.

8.2. http://www.mathworks.com

8.3. R. L. D. A. Ribeiro *et al.*, 'Fault Detection of Open-Switch Damage in Voltage-Fed PWM Motor Drive Systems'. IEEE Trans. on Power Electronics, Vol. 18, No. 2, March 2003, pp. 587-593.

8.4. P. C. Krause, Analysis of Electric Machinery, International Editions, McGraw-Hill Book Company, 1987

8.5. G. L. Peters, G. A. Covic, and J. T.Boys, 'Eliminating Output distortion in four-switch inverters with three-phase loads'. Proceeding of IEE Electric Power Application, Vol. 145, No. 4, July 1998, pp. 326-332.

Appendix A

Hardware and Detailed System Implementation

This appendix presents the details of the hardware design for the experimental system

A.1 Base Values and Parameters

For machine control, two line-to-line stator voltages, two stator phase currents and two rotor phase current are measured and then per-unitised by the base values shown in table A.1.

Table A.1: Base values for the DFIG system

Base Volt-Ampere (VA)	6970
Base Stator Voltage (V)	$240\sqrt{2}$
Base Stator Current (A)	$9.7\sqrt{2}$
Base Rotor Voltage (V)	$120\sqrt{2}$
Base Rotor Current (A)	$19.4\sqrt{2}$
Stator-Rotor Turn Ratio (N_s / N_r)	2:1

The base values used for control of the grid-side converter are listed in table A.2

Table A.2: Base values for transformer and dc-link voltage

Base Transformer Secondary Voltage (V)	$62.5\sqrt{2}$
Base Transformer Secondary Current (A)	$37.2\sqrt{2}$
Transformer Turn Ratio	3.84:1
Base DC-Link Voltage (V)	480

Tables A.3 and A.4 shows the parameters of the induction machine and other apparatus used in the experimental system

Table A.3: Parameters of the wound rotor induction machine

Stator resistance R_s (Ω)	1.097200
Stator inductance L_s (H)	0.196620
Rotor resistance R_r (Ω) (referred to stator)	1.930000
Rotor inductance L_r (H) (referred to stator)	0.196620
Magnetising inductance L_m (H) (referred to stator)	0.190017
Pole Number	4

Table A.4: Parameters of dc-link capacitors, filter and transformer

Individual DC-Link Capacitor C (μF) (2 in series)	6800
Filter Resistance R_f (Ω)	0.08070
Filter Inductance L_f (H)	0.0408
Transformer Primary Resistance R_{pri} (Ω)	1.2
Transformer Primary Leakage Inductance L_{lpri} (H)	0.00296
Transformer Magnetising Inductance L_{mt} (H)	1.92087
Transformer Secondary Resistance R_{st} (Ω) (referred to primary side)	5.4172
Transformer Secondary Leakage Inductance L_{lst} (H) (referred to primary side)	0.00296

Control of the dc motor is achieved by a commercial dc drive [A.1]. The motor parameters and its ratings are listed in tables A.5 and A.6 respectively.

Table A.5: Parameters of the dc motor

Armature Resistance R_a (Ω)	2.1
Field Resistance R_b (Ω)	129.7

Table A.6: Rating of the dc motor

Rated Power (kW)	7.2
Rated Voltage (V) (Armature v_a)	460
Rated Voltage (V) (Field v_f)	360
Rated Current (A) (Armature)	18.5
Rated Current (A) (Field)	1.9
Rated Speed (rpm)	1500

A.2 System Layout

This section shows the layout of the main parts of the experimental system.

Figure A.1 The complete experimental system

[1]	DC drive controller	[4]	Three-phase choke
[2]	Three-phase variac	[5]	By-pass switches
[3]	Three-phase transformer	[6]	DC power supply

257
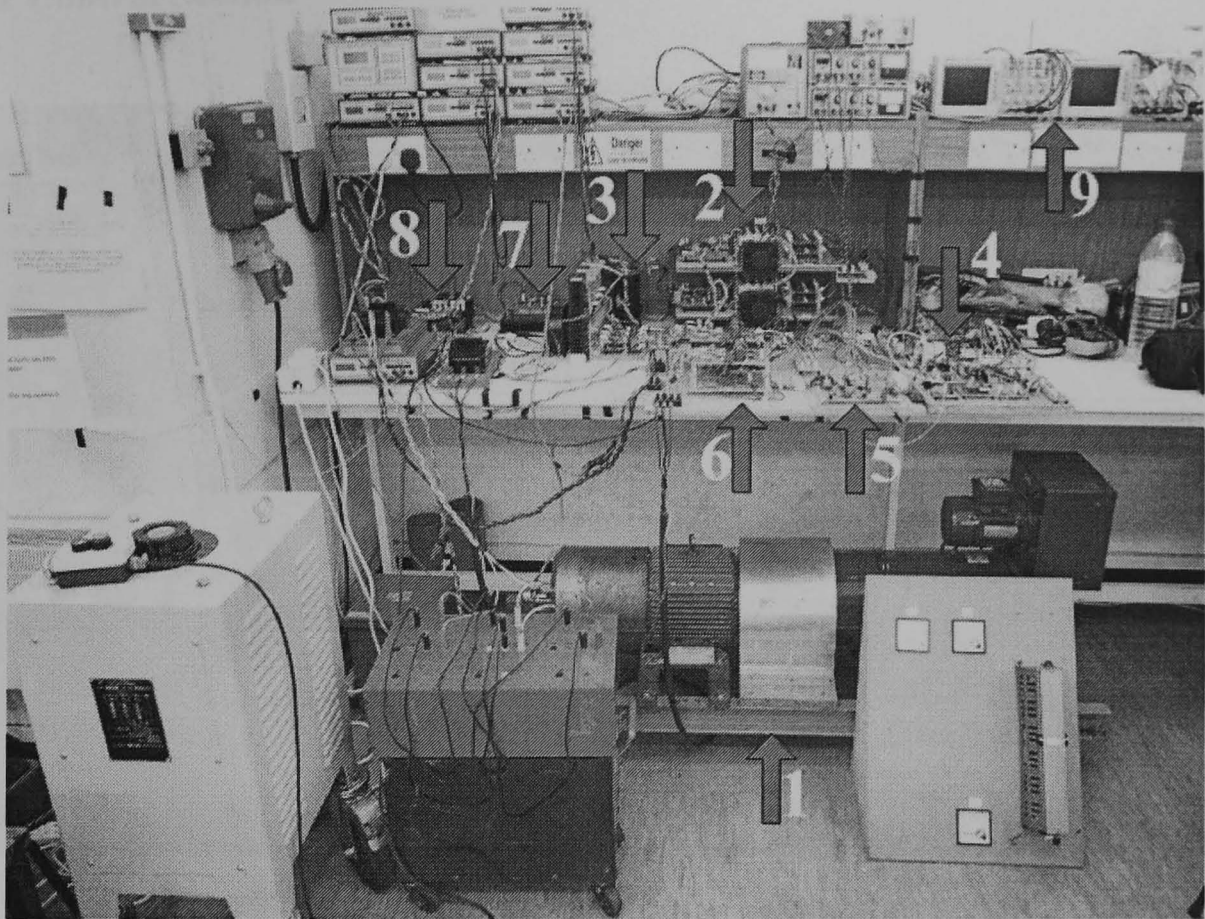
Figure A.2 Front view of the experimental system

[1]	DFIG-DC motor set	[6]	Transducer circuits
[2]	Back-to-back converters	[7]	Chopper circuit
[3]	DC-link capacitors	[8]	Magnetic contactors
[4]	Control section	[9]	4-channel oscilloscopes
[5]	Protection circuits		

The electronic circuits used in experimental system are shown in the following subsections

A.2.1 Control Section
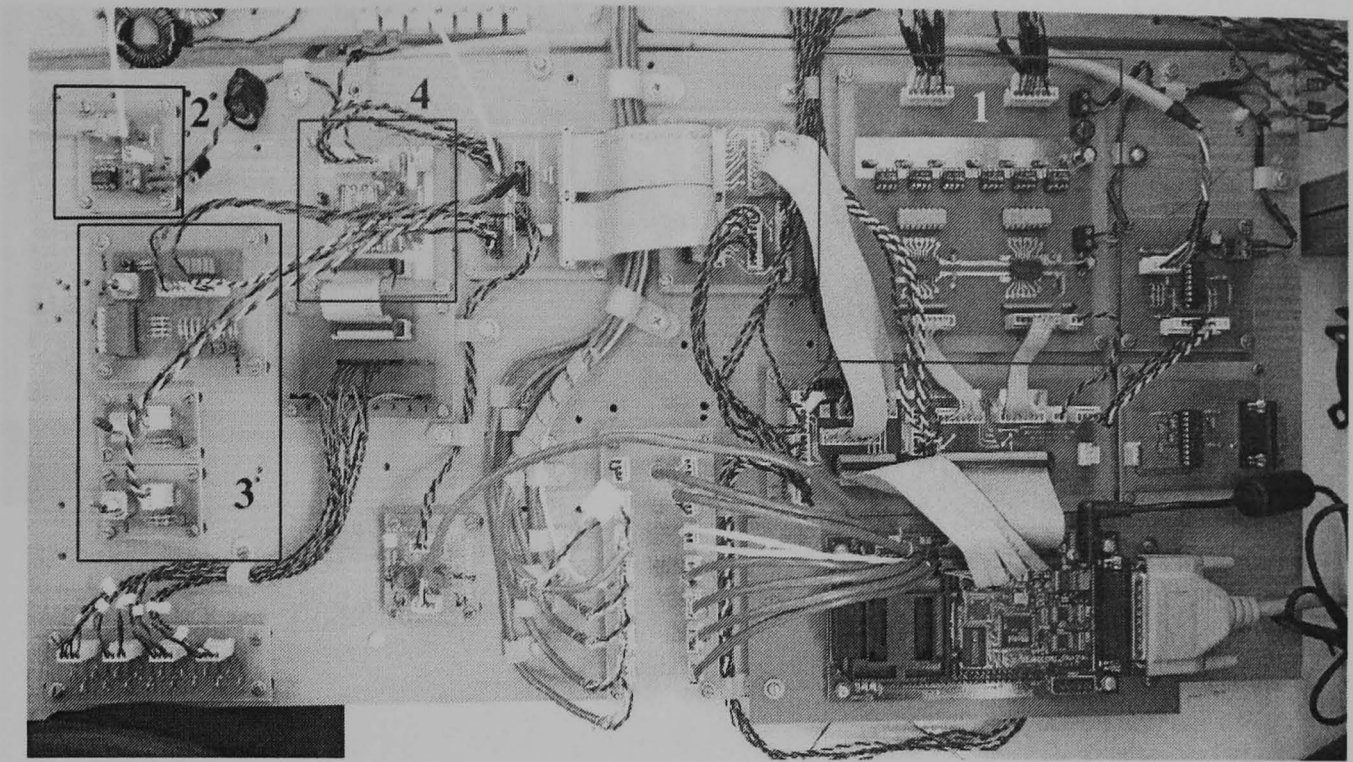
(a)
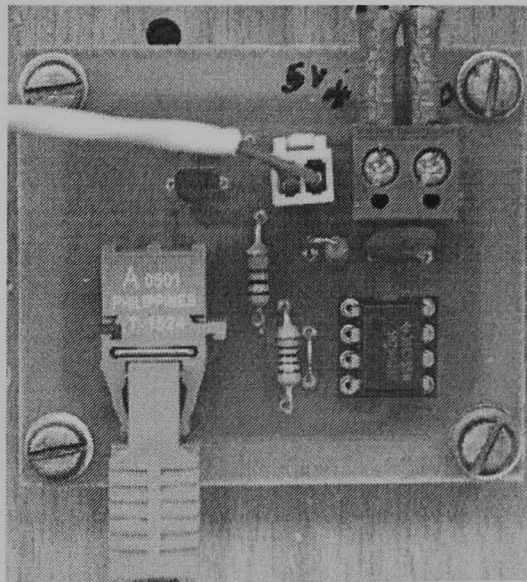
(b)

Figure A.3 (a) The main control section (b) transmitter circuit for fibre optic transmission of dc motor control signal

[1]   PWM isolating circuits

[2]   Transmitter circuit for fibre optic transmission

[3]   GPIO switches

[4]   8-channel digital-to-analogue converter circuit

A.2.2 Measurement Circuits

(a)   (b)
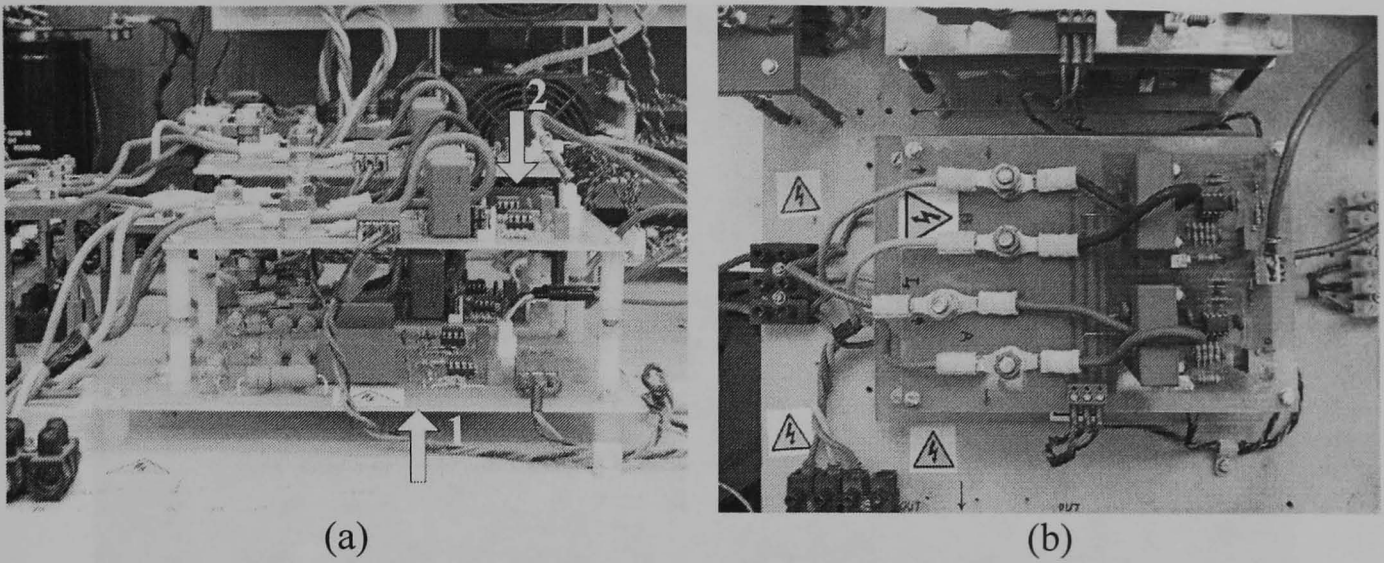
Figure A.4 Example of (a) voltage and current transducer circuits (b) top view of current transducer circuit

[1]   Voltage transducer circuits

[2]   Current transducer circuits

A.2.3 Display Section
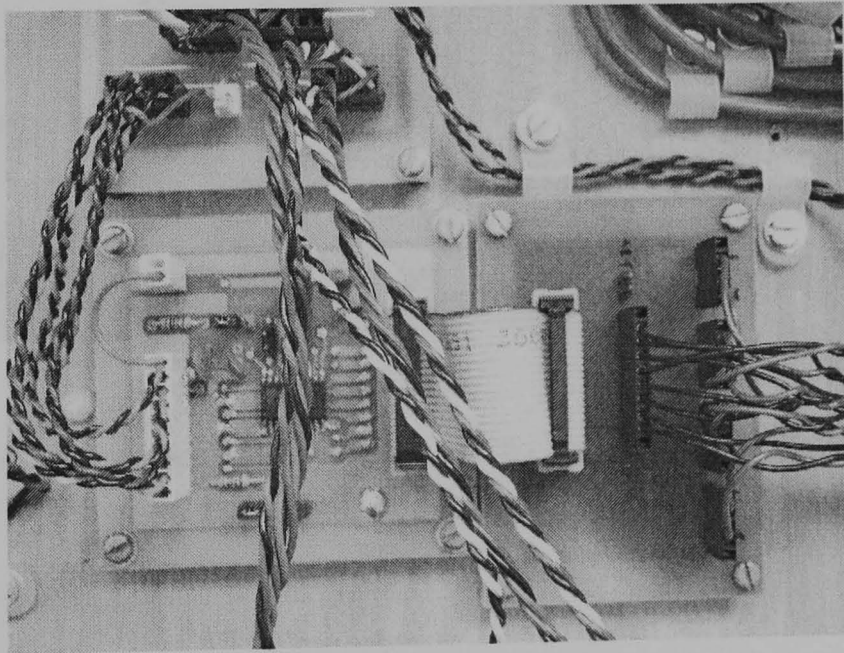
Figure A.5 The 8-channel digital-to-analogue converter circuit

A.2.4 Protection Section
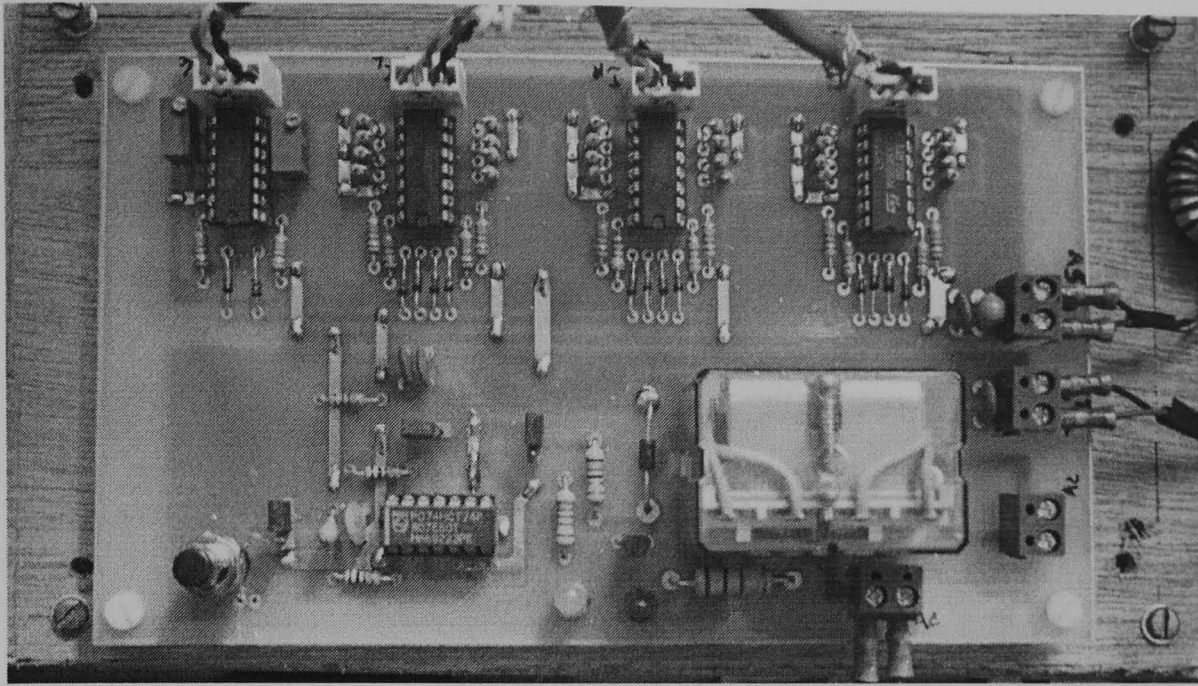
(a)
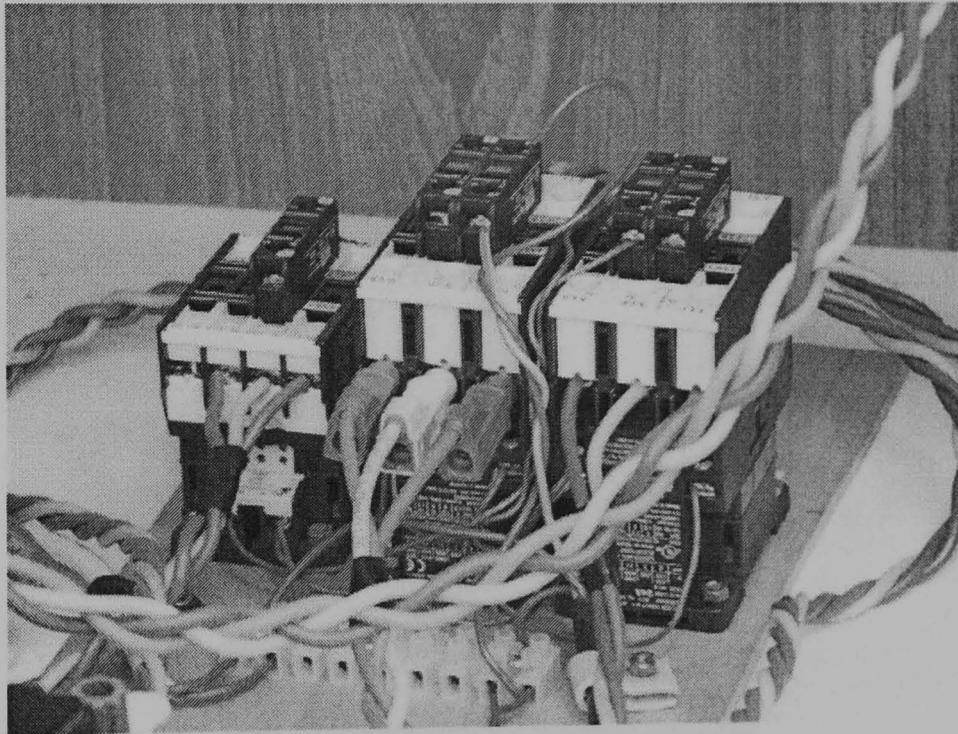
(b)

Figure A.6 (a) Over current detection circuit (b) magnetic contactors for protection circuit

A.2.5 Power Apparatus Section
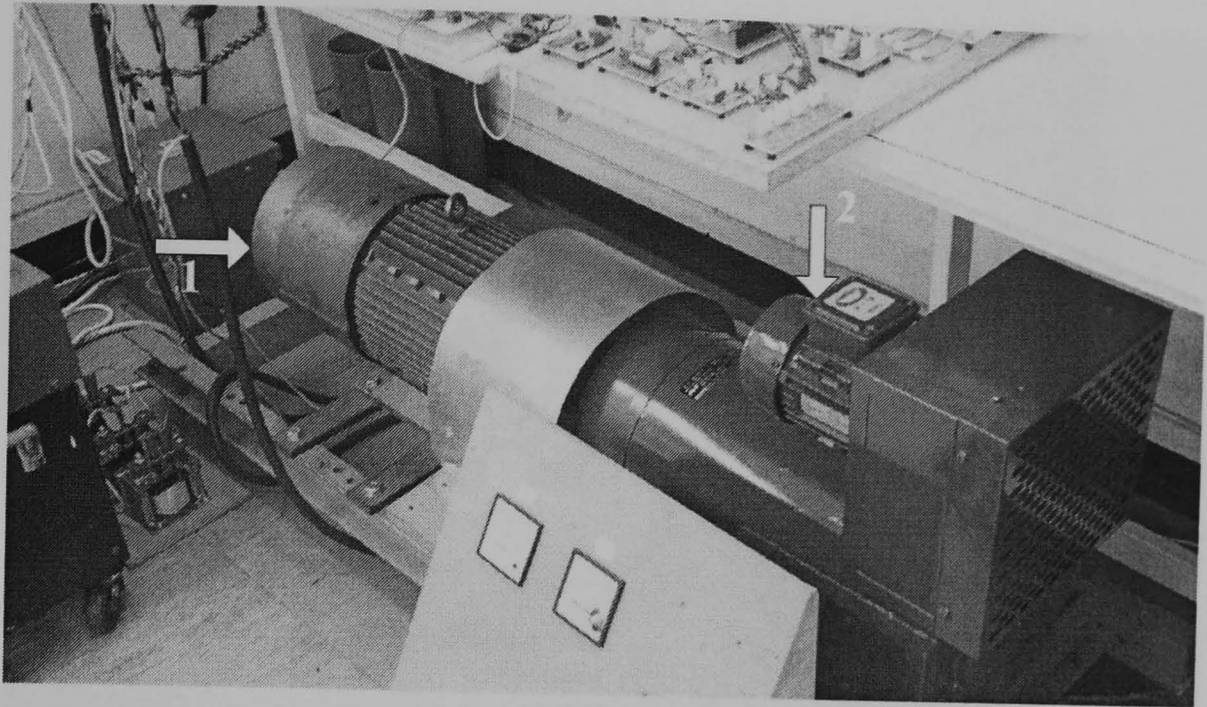
Figure A.7 Motor-generator set

[1]   Wound rotor induction generator

[2]   DC motor
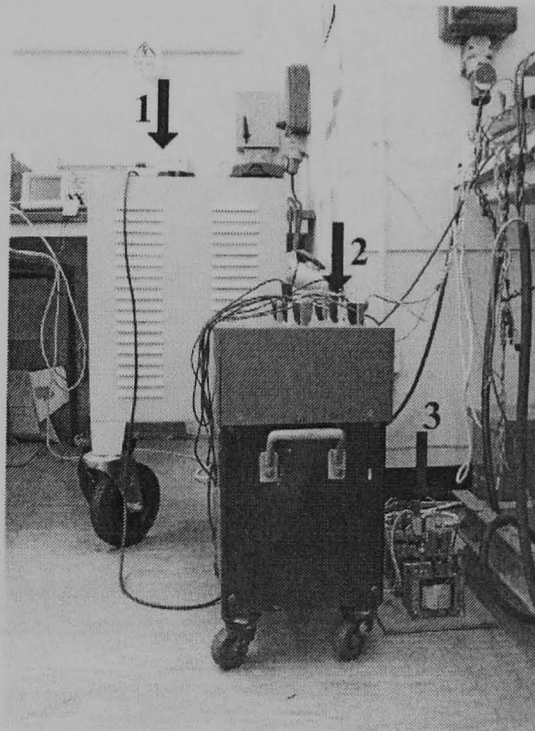
Figure A.8 Variable supply transformer, converter supply transformer and ac chokes

[1]   Three-phase variac

[2]   Three-phase transformer

[3]   Three-phase choke

A.2.6 DC Drive Section
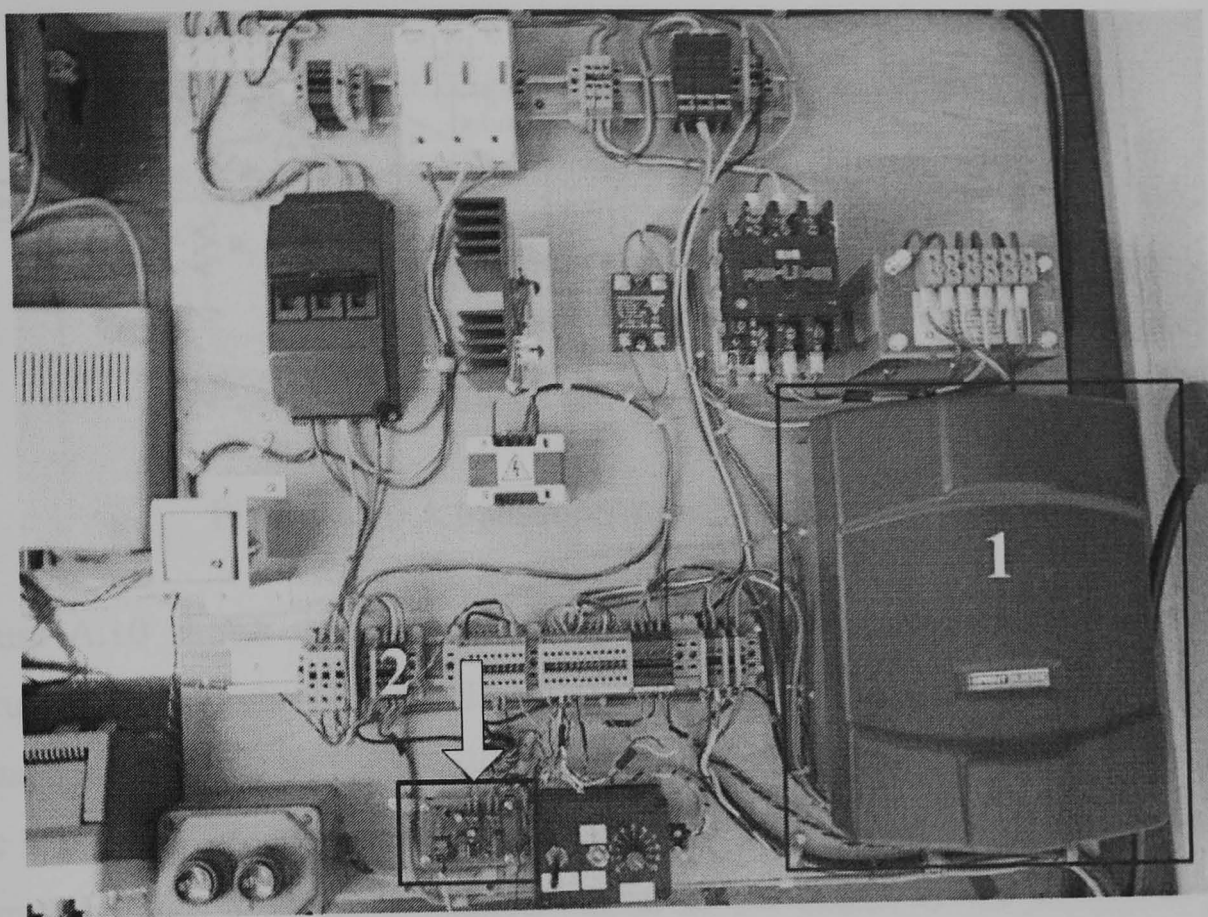
(a)
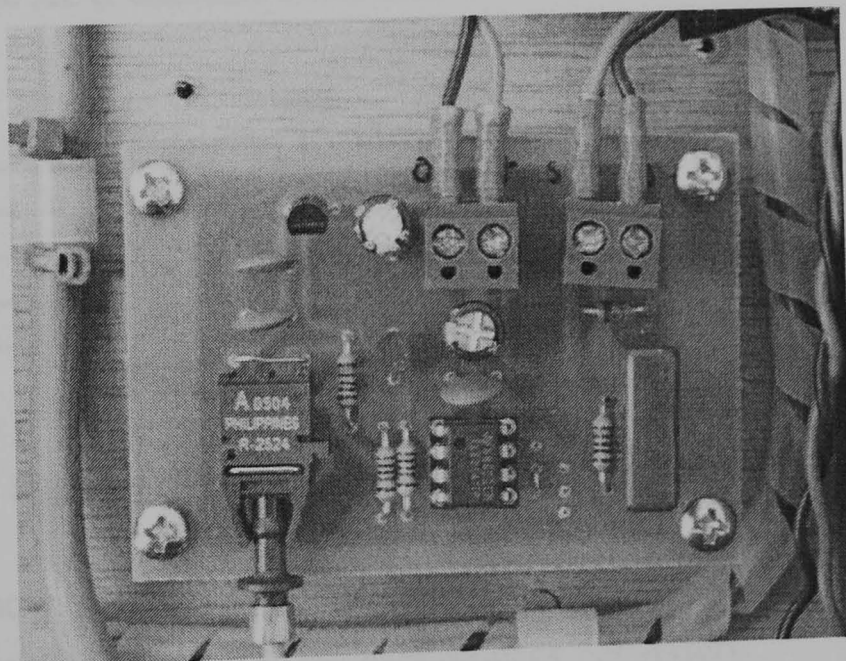
(b)

Figure A.9 (a) DC drive control circuits (b) receiver circuit for fibre optic transmission

[1]   Commercial dc drive

[2]   Receiver circuit for fibre optic transmission

A.3 Schematic Diagrams of Some Important Circuits
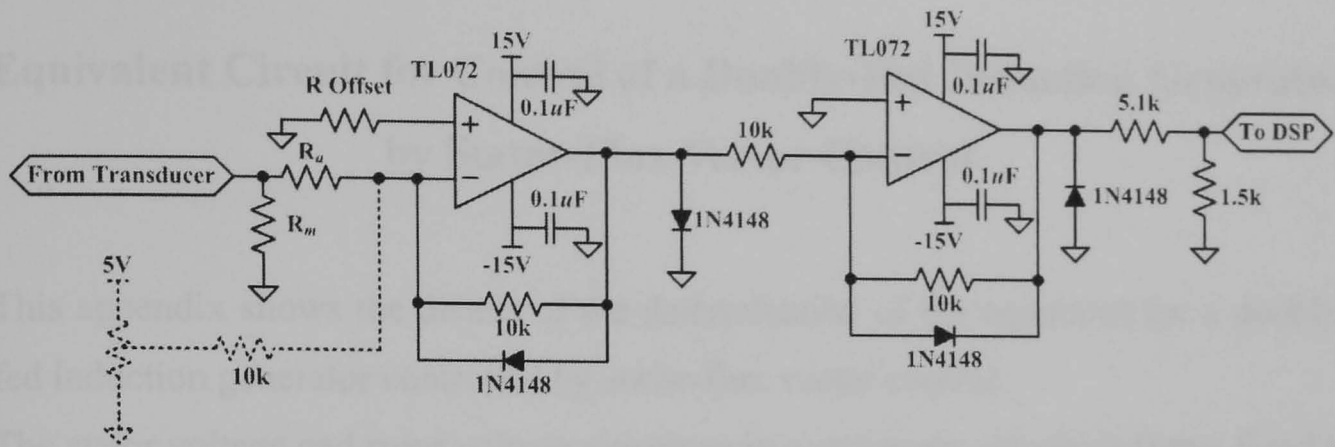
Figure A.10 A transducer signal conditioning circuit

Figure A.10 shows the schematic diagram of the transducer signal conditioning circuit used for both voltage and current measurement. The input of the circuit is the voltage signal from either a voltage transducer or a current transducer. The dotted line is used in cases where the signal is bipolar and requires a dc offset to change it from a bipolar signal to a unipolar signal at the output of the circuit, to permit connection to the ADC channels of the DSP.
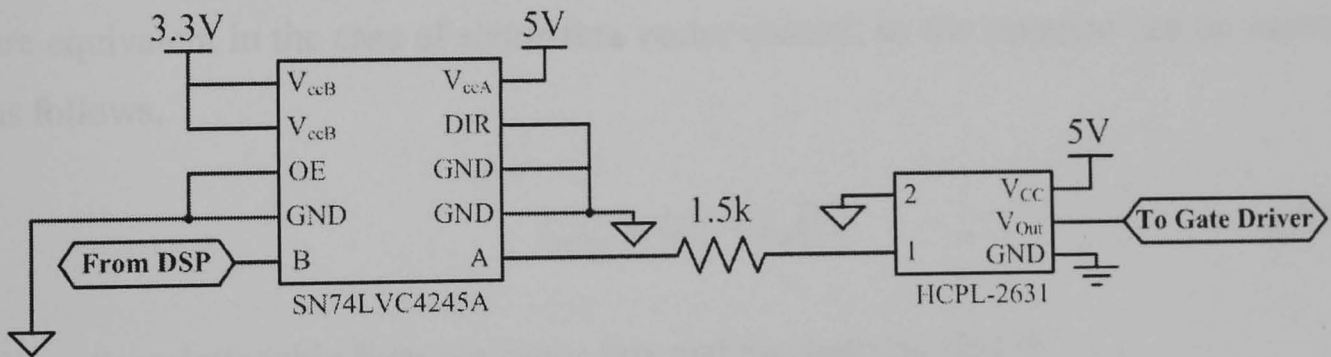
Figure A.11 An opto-isolation circuit for PWM signal

Figure A.11 shows a simplified schematic diagram of the opto-isolation circuit for each of the PWM signals driving the back-to-back converters.

Reference

A.1. http://www.sprint-electric.com/download/tech/slemanual.pdf

Appendix B

Equivalent Circuit for Control of a Doubly-Fed Induction Generator by Stator-Flux Vector Control

This appendix shows the details of the determination of the equations for a doubly-fed induction generator controlled by stator-flux vector control.

The stator voltage and rotor voltage equations in a stationary reference frame fixed to stator are written as follows,

$$\overline{u}_s^s = R_s \overline{i}_s^s + \frac{d\overline{\lambda}_s^s}{dt},$$ (B.1)

$$\overline{u}_r^s = R_r \overline{i}_r^s + \frac{d\overline{\lambda}_r^s}{dt} - j\omega_r \overline{\lambda}_r^s.$$ (B.2)

The stator flux linkage in equation (B.1) can be written in the form of either stator magnetising current or combination of stator flux and rotor mutual flux. Both forms are equivalent in the case of stator-flux vector control, so the equation can be written as follows,

$$L_m \overline{i}_{ms}^s = L_s \overline{i}_s^s + L_m \overline{i}_r^s.$$ (B.3)

Since the relationship between stator flux and magnetising flux is

$$L_s = L_m(1 + \sigma_s),$$ (B.4)

where $\sigma_s = \dfrac{L_{ls}}{L_m}$ is the stator leakage factor, equation (B.1) can be rewritten in terms of equations (B.3) and (B.4) as follows,

$$\overline{u}_s^s = R_s \overline{i}_s^s + \frac{L_s}{(1 + \sigma_s)} \frac{d\overline{i}_{ms}^s}{dt}.$$ (B.5)

Considering the rotor voltage equation (B.2),

$$\overline{u}_r^s = R_s \overline{i}_r^s + \frac{d\overline{\lambda}_r^s}{dt} - j\omega_r \overline{\lambda}_r^s ,$$ (B.6)

the rotor-flux linkage from equation (B.6) is

$$\overline{\lambda}_r^s = L_r \overline{i}_r^s + L_m \overline{i}_s^s .$$ (B.7)

From equation (B.3),

$$\overline{i}_s^s = \frac{\overline{i}_{ms}^s - \overline{i}_r^s}{(1+\sigma_s)},$$ (B.8)

therefore equation (B.7) is

$$\overline{\lambda}_r^s = (1+\sigma_r)L_m \overline{i}_r^s + \frac{L_m}{(1+\sigma_s)}(\overline{i}_{ms}^s - \overline{i}_r^s).$$ (B.9)

Rearranging equation (B.9) results in

$$\overline{\lambda}_r^s = \frac{L_m}{(1+\sigma_s)}\overline{i}_{ms}^s + \frac{[L_s(1+\sigma_r)-L_m]}{(1+\sigma_s)}\overline{i}_r^s .$$ (B.10)

From equation (B.10), the rotor voltage equation (B.6) becomes

$$\overline{u}_r^s = R_s \overline{i}_r^s + \frac{L_m}{(1+\sigma_s)}\frac{d\overline{i}_{ms}^s}{dt} + \left[\frac{L_s(1+\sigma_r)-L_m}{(1+\sigma_s)}\right]\frac{d\overline{i}_r^s}{dt}$$
$$- j\omega_r \left[\left(\frac{L_m}{(1+\sigma_s)}\right)\overline{i}_{ms}^s + \frac{[L_s(1+\sigma_r)-L_m]}{(1+\sigma_s)}\overline{i}_r^s\right].$$ (B.11)

Since $L_m = \dfrac{L_s}{1+\sigma_s}$, equation (B.11) is rewritten as follows,

$$\bar{u}_r^s = R_r \bar{i}_r^s + \frac{L_s}{(1+\sigma_s)^2} \frac{di_{ms}^s}{dt} + L_s \left[\frac{(1+\sigma_s)(1+\sigma_r)-1}{(1+\sigma_s)^2} \right] \frac{di_r^s}{dt}$$

$$- j\omega_r \left[\left(\frac{L_s}{(1+\sigma_s)^2} \right) \bar{i}_{ms}^s + L_s \frac{[(1+\sigma_s)(1+\sigma_r)-1]}{(1+\sigma_s)^2} \bar{i}_r^s \right]$$

(B.12)

Multiplying equation (B.12) by $(1+\sigma_s)$ results in

$$(1+\sigma_s)\bar{u}_r^s = (1+\sigma_s)R_r\bar{i}_r^s + \frac{L_s}{(1+\sigma_s)} \frac{di_{ms}^s}{dt} + L_s \left[\frac{(1+\sigma_s)(1+\sigma_s)-1}{(1+\sigma_s)} \right] \frac{di_r^s}{dt}$$

$$- j\omega_r \left[\left(\frac{L_s}{(1+\sigma_s)} \right) \bar{i}_{ms}^s + L_s \frac{[(1+\sigma_s)(1+\sigma_r)-1]}{(1+\sigma_s)} \bar{i}_r^s \right]$$

(B.13)

and then rearranging equation (B.13), results in

$$(1+\sigma_s)\bar{u}_r^s = (1+\sigma_s)^2 R_r \frac{\bar{i}_r^s}{(1+\sigma_s)} + \frac{L_s}{(1+\sigma_s)} \frac{di_{ms}^s}{dt} + L_s[(1+\sigma_s)(1+\sigma_r)-1]\frac{d\frac{\bar{i}_r^s}{(1+\sigma_s)}}{dt}$$

$$- j\omega_r \left[\left(\frac{L_s}{(1+\sigma_s)} \right) \bar{i}_{ms}^s + L_s[(1+\sigma_s)(1+\sigma_r)-1]\frac{\bar{i}_r^s}{(1+\sigma_s)} \right]$$

(B.14)

Since $\bar{u}_R^s = (1+\sigma_s)\bar{u}_r^s$, $\bar{i}_R^s = \frac{\bar{i}_r^s}{(1+\sigma_s)}$, $R_R = (1+\sigma_s)^2 R_r$, and $\frac{\sigma}{1-\sigma} = (1+\sigma_r)(1+\sigma_s)-1$

equation (B.14) becomes

$$\bar{u}_R^s = R_R \bar{i}_R^s + \frac{L_s}{(1+\sigma_s)} \frac{di_{ms}^s}{dt} + L_s \frac{\sigma}{1-\sigma} \frac{di_R^s}{dt} - j\omega_r \left[\left(\frac{L_s}{(1+\sigma_s)} \right) \bar{i}_{ms}^s + L_s \frac{\sigma}{1-\sigma} i_R^s \right].$$ (B.15)

Equation (B.15) can be written in term of rotor flux as follows,

$$\bar{u}_R^s = R_R \bar{i}_R^s + \frac{L_s}{(1+\sigma_s)} \frac{d\bar{i}_{ms}^s}{dt} + L_s \frac{\sigma}{1-\sigma} \frac{d\bar{i}_R^s}{dt} - j\omega_r \bar{\lambda}_R^s, \tag{B.16}$$

where

$$\bar{\lambda}_R^s = \left(\frac{L_s}{(1+\sigma_s)} \right) \bar{i}_{ms}^s + L_s \frac{\sigma}{1-\sigma} \bar{i}_R^s \tag{B.17}$$

The voltage equations of both the stator and rotor in stator flux reference frame are as follows,

$$\bar{u}_s^s = R_s i_s^s + \frac{L_s}{(1+\sigma_s)} \frac{d\bar{i}_{ms}^s}{dt}, \tag{B.18}$$

$$\bar{u}_R^s = R_R \bar{i}_R^s + \frac{L_s}{(1+\sigma_s)} \frac{d\bar{i}_{ms}^s}{dt} + L_s \frac{\sigma}{1-\sigma} \frac{d\bar{i}_R^s}{dt} - j\omega_r \bar{\lambda}_R^s, \tag{B.19}$$

and the equivalent circuit of a doubly-fed induction generator following equation (B.18) and (B.19) is shown in figure B.1
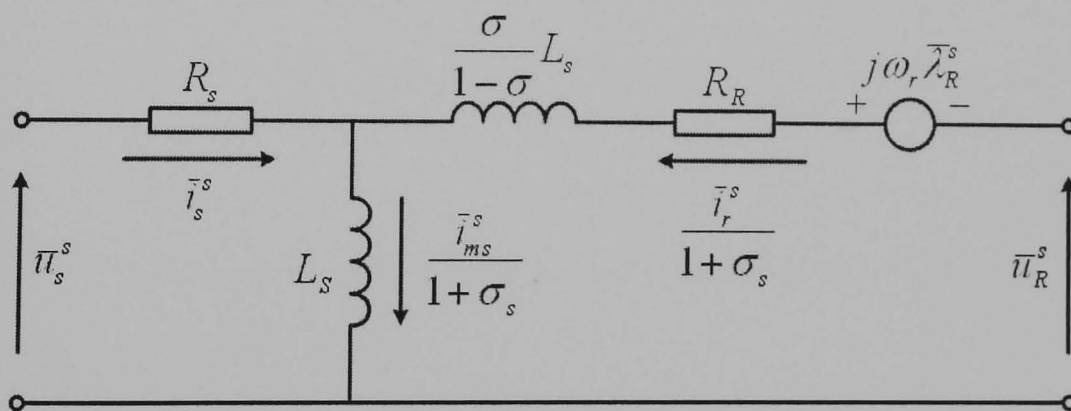
Figure B.1 The T representation of a doubly-fed induction generator for stator-flux vector control

Reference

B.1. A. Petersson, "Analysis, Modeling and Control of Doubly-Fed Induction Generators for Wind Turbines" Ph.D. Thesis, Chalmers University of Technology, 2005.

B.2. G. R. Slemon, "Modeling of Induction Machines for Electric Drives," IEEE Trans. on Industry Applications, Vol. 25, No. 6, Nov/Dec 1989, pp. 1126-1131.

Appendix C

List of Figures

Page

286

Appendix D

List of Tables

290

Appendix E

List of Author's Publications

[1]   Warachart Sae-Kok, Douglas M Grant, "TMS320F2812 DSP to Non-Invasive Health Monitoring and Fault Diagnosis for Doubly-Fed Induction Generator Systems," in *Proc. European DSP Education & Research Symposium, EDERS2006*, Munich, Germany

Abstract – This paper describes the use of the TM320f2812 DSP for vector control and for health monitoring and fault diagnosis of a doubly-fed induction generator of the type used in wind generator systems. The first task of the DSP is to control two converters in the doubly-fed induction generator. Stator flux vector control and voltage vector control are respectively implemented for the machine-side converter and line-side converter. The IQMath and Digital Motor Control Library are applied to control the generator as described above. Moreover, relating to the generator system control, a wind turbine is simulated by a dc motor driven by a commercial thyristor drive. The control signal is also generated from the same controller. A second DSP is applied to monitor health and locate internal faults of the generator system. For the sake of simplicity, toolboxes from TI such as FFT toolbox will be applied. The faults that can appear in this system and the applications of the DSP after the faults occur are briefly explained.

[2].   W. Sae-Kok and D. M. Grant, "Open Switch Fault Diagnosis for a Doubly-Fed Induction Generator," Proceeding of the 7th International Conference on Power Electronics and Drive System, Thailand, 2007, pp.131-138.

Abstract – This paper addresses the analysis and detection of open switch faults in back-to-back PWM converters used in doubly-fed induction generators (DFIG). Several methods have previously been proposed to detect open switch faults in either the machine-side or line-side converter. The operating conditions that can cause

possible false alarms with these methods are investigated. The proposed method detects open switch faults more reliably than any of the existing methods and hence improves overall system reliability. The performance of the existing methods and proposed methods has been verified by both simulation and experiment.

292